Modelling the surface energetics of patchy arctic tundra snowcover

Wiltshire, Andrew John.

UNIVERSITY OF DURHAM
CENTRE FOR ECOLOGY AND HYDROLOGY

MODELLING THE SURFACE ENERGETICS OF PATCHY ARCTIC TUNDRA SNOWCOVER

ANDREW JOHN WILTSHIRE
B.A. (Hons), M.A. (Cantab.)

SUBMITTED IN PARTIAL FULFILLMENT FOR THE DEGREE OF DOCTOR OF PHILOSOPHY
AUGUST 2006

Declaration

None of the material presented here has previously been submitted for a degree in this, or any other university. All of the work described is my own, except where otherwise stated.

Andrew John Wiltshire
August 2006

The author can be contacted at: a.j.wiltshire@cantab.net

Acknowledgements

I would like to thank Robert Baxter, Richard Harding and Brian Huntley for giving me the opportunity to undertake this work and their supervision throughout. My deepest thanks must go to Colin Lloyd, without whom I would still be trying to wire loggers and understand micro-met. Eleanor Blythe offered help and assistance throughout.

Richard Essery provided source code and much needed advice. My field assistants David Wiltshire, Sarah Taylor, Natalie McCurrach and Rachael Turton duly commenced battle in all weathers in the pursuit of data.

I am grateful to the past and present members of the Environmental Change Research Group for their friendship and assistance throughout.

Most of all I need to thank my fellow STEPPS fieldworkers James Cook and Dave Sayer and my friends at the Abisko Naturvetenskapliga Station for making my time in the field a pleasure.

Also more than worthy of a note are the many friends who helped and encouraged me to undertake this PhD.

This work was funded by Natural Environment Research Council Studentship NER/S/A/2002/10352 and a scholarship awarded by Kungliga Vetenskapsakademien (The Royal Swedish Academy of Sciences) through Abisko Naturvetenskapliga Station (Abisko Scientific Research Station). I would especially like to thank Colin Lloyd and Richard Harding of the Centre for Ecology and Hydrology, Wallingford, Oxon. for the loan of the equipment necessary for this study.

Abstract

MODELLING THE SURFACE ENERGETICS OF PATCHY ARCTIC TUNDRA SNOWCOVER

Andrew John Wiltshire

August 2006

A combination of field observations and measurements were used to study the energy-balance of a patchy arctic tundra snow-cover during the winter of 2003/2004 at a mountain tundra site in Northern Sweden. To quantify the effect of patchy snow-cover on surface energetics, the Met. Office Surface Exchange Scheme (MOSES 2) was employed to simulate surface snow dynamics.

Surface snow patchiness was controlled by the interaction of blowing snow with surface topography and vegetation, with deep drifts forming in topographic hollows and tall shrub beds. Some exposed ridge tops remained exposed for the majority of the winter.

The surface patchiness was found to significantly alter the surface energetics, and the interaction between snow and snow-free surfaces was critical to accurately numerically simulating snow-cover ablation. The assumption of uniform snow-covers in large-scale atmospheric models may lead to significant errors in model simulations. It was found that for large-scale models, heterogeneous snow-covers can be adequately represented by the use of separate energy-balances for snow and snow-free surfaces respectively with a single underlying soil layer. The proportions of each surface can be represented using a snow covered fraction which is a parameterisation of the distribution of snow depths. Simulated surface fluxes, particularly surface runoff and heat and water vapour, were found to be highly sensitive to the exact form of this parameterisation. No field evidence was found for the advection of turbulent energy between snow and snow-free surfaces.

TABLE OF CONTENTS

NOMENCLATURE AND CONVENTIONS

The symbols given here are those used in the thesis. They are arranged in alphabetic order into the Roman and Greek alphabets. Subscripts are given separately. Flux densities are given in bold throughout. Units are given according to the Système International d'unités (SI). Some of the symbols are universally accepted, others are common in the micro-meteorological literature and others are devised for consistency. A brief description of each symbol is given, and a value is given for constants. The sign convention follows standard micro-meteorological practice. Radiative fluxes are considered positive towards the surface, and turbulent and conductive fluxes away from the surface.

Abbreviations:

ANS	Abisko Naturventenskapliga Station (Research Station)
GCM	General Circulation Model
RCM	Regional Circulation Model
JULES	Joint UK Land Environment Simulator
MOSES	Met. Office Surface Exchange Scheme version 2.2
NWP	Numerical Weather Prediction
SWE	Snow Water Equivalent

Symbol	Description	SI Unit
Roman Alphabet		
$\boldsymbol{C}$	Flux density of energy due to convection	W m^{-2}
C_H	Surface heat exchange coefficient	-
C_{Hn}	Neutral surface heat exchange coefficient	-
c_p	Specific heat capacity of dry air at standard pressure	J kg^{-1} K^{-1}
d	Displacement height	M
d_0	Mass of snow required to reset snow albedo	Kg m^{-2}
E	Vapour pressure	Pa
$\boldsymbol{E}$	Flux density of water vapour in air	Kg m^{-2} s^{-1}
e_s	Saturated vapour pressure	Pa
f_H	Dimensionless surface exchange scalar	-
f_{snow}	Snow covered fraction	-

Symbol	Description	SI Unit
f_z	Dimensionless surface exchange scalar	-
$\boldsymbol{G}$	Flux density of heat due to conduction	W m^{-2}
g	Gravitational constant (9.81)	m s^{-2}
G_r	Grain growth rate for snow crystals	m^2 s^{-1}
h	Relative humidity	Pa Pa^{-1}
$\boldsymbol{H}$	Flux density of heat due to convection in air	W m^{-2}
$\boldsymbol{H_{sm}}$	Snowmelt heat flux density	W m^{-2}
k	Von Kármán's Constant (0.41)	-
$\boldsymbol{L}$	Latent heat of vaporisation of water/ice	J kg^{-1}
L	Monin stability length	m
L_c	Latent heat of condensation (2.511E6)	J kg^{-1}
L_f	Latent heat of fusion (3.34E5)	J kg^{-1}
$\boldsymbol{L_{incident}}$	Incoming longwave radiation flux density	W m^{-2}
$\boldsymbol{L_{net}}$	Net longwave radiation flux density	W m^{-2}
$\boldsymbol{L_{net}}$	Net longwave radiation flux density	W m^{-2}
$\boldsymbol{M}$	Snowmelt flux density	kg m^{-2} s^{-1}
P	Atmospheric pressure	Pa
Pr	Prandtl Number	-
$\boldsymbol{P_r}$	Rainfall flux density	kg m^{-2} s^{-1}
$\boldsymbol{P_s}$	Snowfall flux density	kg m^{-2} s^{-1}
q	Specific humidity (mass of water vapour per unit mass of moist air)	kg kg^{-1}
q_{sat}	Saturated specific humidity	kg kg^{-1}
R	Gas Constant (8.31)	J mol^{-1} K^{-1}
r	Snow grain size	μm
r_a	Aerodyamic resistance	s m^{-1}
r_{fresh}	Grain size of fresh snow	μm
Ri	Richardson Number	-
r_{max}	Maximum snow crystal grain size	μm
r_s	Aerodyamic resistance to water vapour	s m^{-1}
S	Lying Snow	kg m^{-2}
$\boldsymbol{S_{incident}}$	Incoming shortwave radiation flux density	W m^{-2}
$\boldsymbol{S_{net}}$	Net shortwave radiation flux density	W m^{-2}

Symbol	Description	SI Unit
T	Temperature at a given height (z)	°C,K
T_*	Skin Temperature	°C,K
T_m	Melt point (273.15)	K
u	Horizontal component of wind speed in direction of mean wind	m s^{-1}
u_*	Friction velocity	m s^{-1}
w	Vertical wind speed	m s^{-1}
z	Measurement height	m
z_0	Momentum roughness length	m
z_{soil}	Depth of surface soil layer	m
Greek Alphabet		
α	Surface albedo	-
α_0	Snow-free surface albedo	-
α_{snow}	Snow albedo	-
γ	Psychrometric constant	Pa K^{-1}
Δ	Change in saturation vapour pressure with temperature	Pa K^{-1}
Δt	Model timestep	s
ε	Ratio of water vapour and air (0.622)	-
ε	Surface emissivity	-
θ_{soil}	Soil moisture as fraction of saturation	-
λ	Conductivity	W m^{-2} s^{-1}
π	Pi constant (3.141)	-
ρ_{air}	Density of air at standard pressure	kg m^{-3}
ρ_{snow}	Snow density	kg m^{-3}
σ	Stefan-Boltzmann constant (5.67E-8)	W m^{-1} K^{-4}
τ	Momentum flux density	kg m^{-2} s^{-1}
Ψ	Surface resistance factor	-
Subscripts		
air	Denotes reference to air	-
effective	Denotes the use of a variable aggregated across different layers/surfaces	-
h	Denotes reference to heat	-
m	Denotes reference to momentum	-
q	Denotes reference to water vapour	-

Symbol	Description	SI Unit
snow	Denotes reference to a snow surface	-
snow-free	Denotes reference to a snow-free surface	-
soil	Denotes reference to model soil layer	-

Chapter 1

Introduction

1 Introduction

Snow-cover is well recognised to influence the climate on global and local scales (e.g. Cess *et al.*, 1991; Ellis and Leathers, 1998; Groisman and Davies, 1999; Langham, 1981; Ling and Zhang, 2005; Randall *et al.*, 1994; Segal *et al.*, 1991a; Segal *et al.*, 1991b; Taylor *et al.*, 1998). Terrestrial snow-cover is the most prominent transient feature of the land surface (Cohen and Rind, 1991) covering up to 40% of the land surface of the Northern hemisphere (Hall, 1988). The snow covered seasonal extent varies from 40-50 million km^2 in February to less than 1 million km^2 in August when snow-cover is typically at its minimum (Ramsay, 1998; Robinson, 1993). The effects of snow-cover on weather and climate are manifest in its interactions with energy exchange at the earth's surface. The principle effect of snow-cover is to increase the surface albedo, leading to a decrease in the absorption of solar radiation, the main source of energy in global circulation. Secondary effects include the suppression of air temperatures, insulation of soils, provision of a source of atmospheric moisture and sink for energy, and a delay in surface runoff all of which are critical to global and local climates.

Recent satellite evidence has shown that the extent of global snow-cover is decreasing, with Northern hemisphere snow-cover declining by approximately 10% since 1972 (Groisman *et al.*, 1994b; Serreze *et al.*, 2000). Groisman *et al.*, (1994a; 1994b) suggest the decline in snow-cover accounts for part of the observed increase in spring temperatures. In equilibrium, doubled CO_2, global circulation model (GCM) experiments, snow and sea-ice albedo feedback contributed to approximately half of simulated northern hemisphere warming (Hall, 2004). However, some of the GCM simulations showed a weak or negative feedback, associated with effects on cloud cover and the emission of long-wave radiation, leading to considerable uncertainty (Cess *et al.*, 1991; Randall *et al.*, 1994). Recent model intercomparison studies have also shown snow-cover to be a difficult quantity to model accurately and consistently (Boone and Etchevers, 2001; Bowling *et al.*, 2003; Essery *et al.*, 1999b; Etchevers *et al.*, 2004; Slater *et al.*, 2001). There is clearly a need for a better understanding of the physical processes controlling snow-cover and parameterisations for large-scale climate simulations.

Arctic tundra snow-covers are generally shallow and spatially very variable (Pomeroy *et al.*, 1998; Sturm *et al.*, 1995). Heterogeneous snow-covers are associated with complex topography subject to periglacial processes and a diverse vegetation community. Climate conditions are generally below freezing and windy. In an attempt to develop a snow-cover classification, Sturm *et al.* (1995) describe tundra snow-cover as 'a thin, cold, wind-blown snow,' with a maximum depth of 0.75 m and consisting of a basal layer of depth-hoar overlain by multiple wind slabs. The spatial variation in snow depth leads to patchy snow-cover during the melt phase of the seasonal cycle. The role of horizontal transfer of energy during ablation is one of some uncertainty, but model predictions suggest the horizontal energy exchange is an important process (Essery *et al.*, 2006). Spatially variable snow-cover is currently not included in most land surface models.

The requirement for better representation of snow processes in GCMs and uncertainty of the processes controlling snow distribution and ablation is set against an increasing consensus that climate change is occurring, and increasing evidence of climate associated environmental change in the high latitudes. Three successive Scientific Assessment Reports from the Intergovernmental Panel on Climate Change (IPCC) have shown anthropogenic influenced climate change, and an increased certainty of change during the 21st Century (IPCC, 1990, 1996, 2001). The most recent report of the IPCC predicted a global surface average warming of 1.4 to 5.8°C (IPCC, 2001). More recent work with grand ensembles GCM runs suggest a greater range of change of 1.9 to 11.5°C associated with parameter uncertainty and varying initial conditions (Stainforth *et al.*, 2005). A general consensus exists that the Northern hemisphere snow covered extent will decrease over the next 100 years (Walsh *et al.*, 2005). Considerable environmental evidence is also accumulating: lake and river ice is forming later in the autumn and melting earlier in the spring (Magnuson *et al.*, 2000); sea-ice is at record minimums and thinning (Vinnikov *et al.*, 1999); permafrost is warming and in some cases melting (Lachenbruch and Marshall, 1986); and arctic vegetation is becoming greener and shrubs and trees are extending their range (Jia *et al.*, 2003; Kullman, 2002; Sturm *et al.*, 2001b; Tape *et al.*, 2006).

This thesis presents the results of an investigation into the representation of patchy arctic tundra snow-cover in the UK Met Office Surface Exchange Scheme (MOSES), part of the latest Hadley Centre GCM (HadCM3), based on observations from a tundra site in Northern Sweden. Both parameter uncertainty and model engineering are investigated in the context of complex patchy snow-covers. The broad aim of this thesis is to make recommendations of how the representation of snow covered surfaces can be improved in the Hadley Centre GCM.

1.1 Study Background

This research forms part of STEPPS (Snow in Tundra Environments: Patterns, Processes and Scaling), a Natural Environment Research Council (NERC) funded project jointly hosted at the University of Durham and the Centre for Ecology and Hydrology, Wallingford with collaborators from the University of Uppsala, Sweden, the University of Sheffield and Abisko Naturventenskapliga Station, Sweden. The remit of STEPPS was to investigate the hydrology, micrometeorology and ecology across a low arctic tundra field site associated with spatially variable, shallow snow-covers. The broad research aim was to improve understanding on winter processes operating in tundra environments with a specific view of their improved representation in the land surface scheme of the UK Meteorological Office.

1.2 Aims and Objectives

The research presented in this thesis aims to develop and suggest parameterisations of heterogeneous snow-cover for use in large-scale atmospheric models such as those used in climate simulations and numerical weather prediction. Subgrid heterogeneity is currently treated in MOSES by dividing a 2.5° by 2.75° GCM gridbox into nine different surfaces (Broadleaf deciduous trees, Needleleaf trees, C3 Grass, C4 Grass, Shrubs, Urban, Bare Soil, Water and Ice), with a single soil layer for the entire gridbox. Figure 1-1 shows schematically the levels of subgrid heterogeneity for a typical GCM gridbox relevant to snow modelling. As can be seen only one level of heterogeneity is currently represented. Additional

unrepresented levels include the effect of elevation on snowfall and ablation, slope and aspect on radiation receipt and the differential accumulation within each of the nine surface types associated with snow redistribution. This study focuses on the patch scale of heterogeneity associated with complex topography and small-scale vegetation interaction.

Within MOSES each of the nine surface types are treated as having a uniform snow-cover. Furthermore, the physical representations of snow processes, such as thermal hydrologic conductivity, are described in a simplistic manner (see **2.2**). Model improvements may therefore include improved representation of snowpack processes and a parameterisation to describe the snow-cover heterogeneity. In MOSES simulations of the Abisko valley (meso-scale) would separate the tundra above the treeline into one surface and the forest into a second surface. The tundra would be classified as 'shrub' and the birch forest as 'broadleaf deciduous trees,' each having a separate energy-balance. This study focuses on the tundra above the treeline.

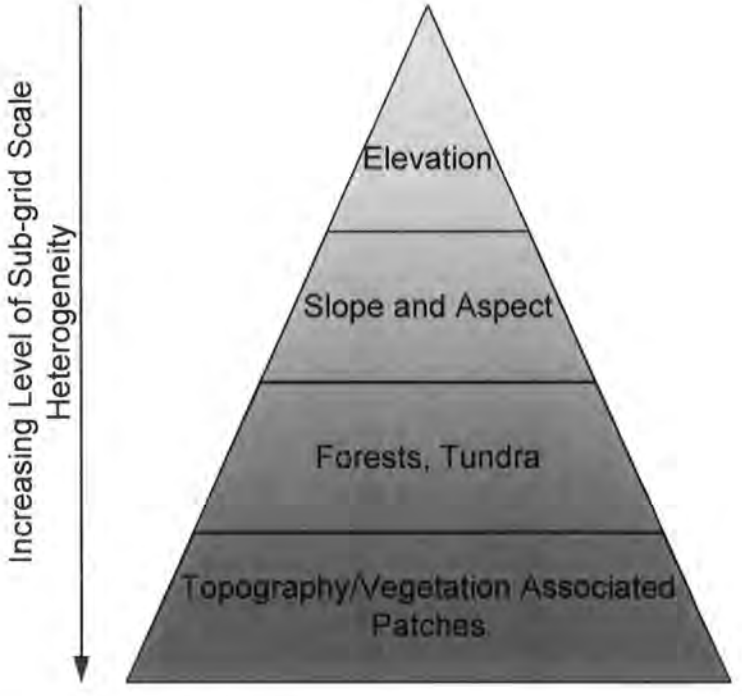

Figure 1-1: Associated landscape phenomena with increasing level of sub-grid scale heterogeneity (2.5° by 2.75° HadCM3 GCM gridbox).

The approach in this study is to use multi-scale measurements linked with numerical modelling using the MOSES model to gauge which physical processes need to be included in large-scale modelling endeavours. This relationship between scale, research questions, field measurements and numerical modelling is shown schematically in Figure 1-2. The key to appropriately addressing this up-scaling is to start at the process scale (individual patches; snow and snow-free) and up-scale to the landscape scale. This requires detailed observations over a fairly small area of tundra in Northern Sweden, particularly during the winter and melt-period. These observations include the evolution of the snowpack (accumulation and ablation) and measurements of snowpack profiles. These data are coupled with measurements of turbulent and radiative fluxes made over individual patches and landscape scale measurements of the aggregate fluxes over multiple patches. Advection of energy between patches is a complicating factor when undertaking such up-scaling schemes. Advection can lead to heterogeneous melt patterns, and thus complex snow-cover evolution. Advected energy is difficult to measure, particularly over smooth snow surfaces. Attempts are made to directly quantify this process for a typical snow patch. The aims of the field measurements are to constrain the physical processes operating.

The MOSES model is first validated at the patch scale for both snow and snow-free patches, and subsequently at the landscape scale using eddy correlation and a parameterised snow distribution. These tests are used to define the appropriate level of representation of physical processes required in the MOSES model to accurately simulate boundary conditions for atmospheric models. Subsequently, a new tiling scheme is developed to represent heterogeneous snow-covers. The tiling scheme works by aggregating all snow-free patches into a snow-free tile and a snow tile for the snow patches. An important result is that this new tiling scheme, on the basis of field-based evidence and numerical simulations, does not require a parameterisation of advection to accurately simulate surface energetics. This greatly simplifies the problem of parameterising patchy snow. However, the difficulty remains of how to parameterise the distribution of snow-cover; two versions of the tiled model are further developed, the first uses local topography to

redistribute snow-cover into hydrologically similar units (appropriate to use at the landscape to meso-scale), and the second uses a probability distribution model more appropriate for use in global simulation. Subsequently, the sensitivity of soil moisture and surface runoff to the inclusion of heterogeneous snow-cover are examined.

Although, this study focuses on the above treeline tundra, there may well be an interaction between the snow-lie on the tundra and the forest areas. To put this study in context extra measurements of snow depth are therefore made along an elevation transect covering the tundra and treeline. In addition some analyses are made of whether there exists an meso-scale circulations in the form of snow-breezes. Thus, treating the meso-scale heterogeneity as non-interacting land-surface units may thus lead to significant inaccuracies in MOSES simulations.

Throughout this thesis reference is made to a number of different scales. In some cases these relate to process scales, and in other cases to the scales resolved by regional and global atmospheric models (i.e. GCMs). For clarity four scales are consistently referred to: the 'patch scale' refers to individual patches of snow and snow-free areas, these are typically of the order of 50 m; the 'landscape scale' refers to a collection of snow and snow-free patches and is used mainly in relation to the main survey grid (**3.2**) and footprint of the eddy correlation tower. The length scale is typically 250-500 m. The 'landscape scale' therefore relates to the tundra area above the treeline. The 'meso-scale' refers to the Abisko valley and includes not only the tundra area, but also to the forest and higher mountains. The length scale is typically 2-10 km. The 'global scale' refers to the length scales that can be resolved in global climate simulations. The length scale is typically 2-3° of latitude.

1.3 Thesis Outline

Following the aims and objectives described above this thesis is divided into chapters addressing separate questions. Initially, a background to land surface models and the physics employed is given (Chapter 2), followed by a description of the study site and methods used (Chapter 3). The subsequent two chapters present

field data. Chapter 4 describes the distribution of snow-cover and associated phenomena in detail. Chapter 5 presents the climate data used for data modelling, some technical details about micrometeorological instruments, and derives the important micro-meteorological parameters used in the numerical simulations. In addition, evidence for meso-scale circulations are also presented. The following two chapters present the results from MOSES simulations including new model developments. Chapter 6 deals with the energetics of a patchy snow-cover and discusses methods by which patchy snow energetics can be up-scaled to the landscape scale in numerical models, for a given distribution of snow. Chapter 7 follows on from the previous chapter to present methods by which distribution can be modelled and used in the parameterisations developed in Chapter 6, at both the meso and global scales. The improved representation of soil moisture and surface hydrology is also detailed. In the final chapter the major conclusions and recommendations are outlined. Subsequent appendix chapters deal with some of the more technical aspects of this thesis and are referred to in the text.

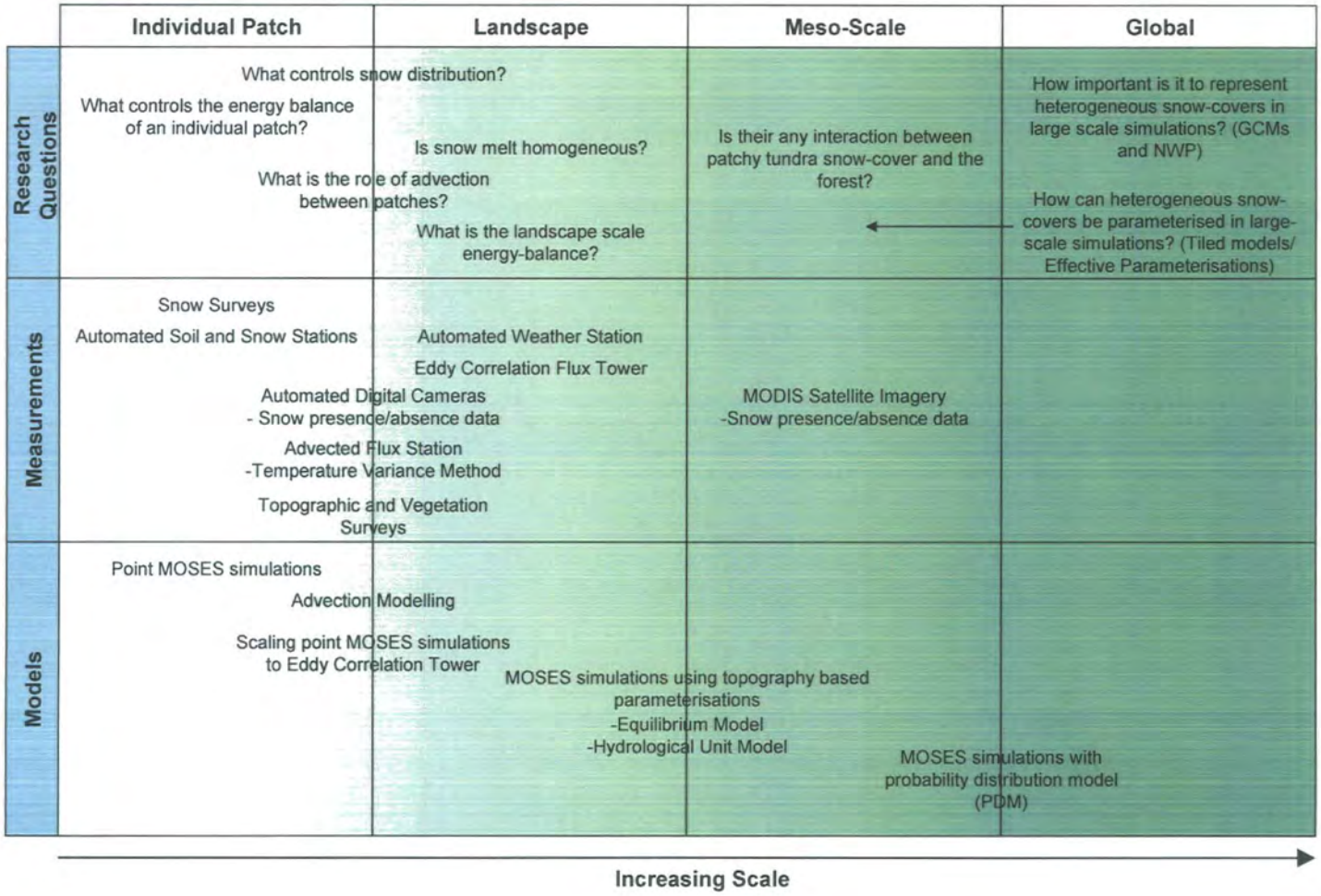

Figure 1-2: Relationship between scale, research questions, measurements and modelling used in this thesis.

Chapter 2

Background

2 Background

2.1 Introduction

This chapter presents a review of land surface model engineering and parameterisation of sub-grid heterogeneity and snow. The basic physics employed in this thesis and within the MOSES model are outlined. Subsequently, the role and feedbacks of snow-vegetation interactions are discussed.

2.2 Land Surface Models

Land surface schemes are essential components of numerical weather prediction (NWP) and global circulation models (GCM). These schemes provide the surface boundary conditions and mass calculations for the atmospheric component of NWP and GCMs as well as simulating the surface response to changing atmospheric and hydrological conditions. Land surface schemes consist of non-linear differential equations that are integrated over short time intervals to produce fluxes of momentum, mass and energy to the atmosphere and state changes in the land surface. The spatial length scales are necessarily large, and the equations are discretized to suit.

The current land surface scheme used in the latest Hadley Centre coupled climate model (HadCM3) is the Met. Office Surface Exchange Scheme (MOSES) version 2.2 (Cox *et al.*, 1999; Essery *et al.*, 2001). The GCM makes use of a 19 layer atmosphere model (HadAM3) (Pope *et al.*, 2000), a 20 layer ocean model and a 4 level soil model. The land surface is represented by 2.5° by 2.75°, or approximately 105 by 305 km, grid boxes at 68° north (study site latitude), and the model integrates over a 30 minute timestep (Gordon *et al.*, 2000). MOSES is also implemented in Regional Climate Models (RCM) typically using a cell size of approximately 50 km. HadAM3 uses a hybrid vertical coordinate system related to atmospheric pressure, the lowest atmospheric level is thus typically 10-20 m (Pope *et al.*, 2000). Providing this height is above the blending height surface heterogeneity can be parameterised into separate 'tiles' with separate energy balances (Avissar and Pielke, 1989; Claussen, 1991).

Land surface models are by necessity fairly simple, due to the need to couple them to large grid boxes and the need for computational efficiency. For instance, it would be counter-intuitive to couple a complex 1D multi-layer snow model, such as CROCUS (Brun *et al.*, 1992; Brun *et al.*, 1989) or SNTHERM (Jordan, 1991), to a GCM with a 30,000 km^2 grid box with no reference to spatial variation. Land surface models are therefore constrained by their need to be regionally applicable. The aim in this thesis is not to generate a more complex model, as this could be easily achieved using one of the models above, but define what processes need to be included in land surface models and provide suitable parameterisations of how they might be included.

2.2.1 SUBGRID SCALE HETEROGENEITY

The first land surface schemes to include processes at the land surface were simple 'bucket' models (Carson, 1982). These 'bucket' models included a surface store of moisture, from which evaporation could take place as a function of its potential rate and runoff occurred when the store filled. Subsequent model developments have included calculation of energy, water and CO_2 fluxes as with the MOSES scheme (Cox *et al.*, 1999), and the identification of distinct vegetation and soil types at the sub-grid scale. Modern land surface models generally consist of a soil model, vegetation and canopy model, coupled with a snow model.

The land surface is heterogeneous at the landscape scale, which leads to unresolved sub-grid heterogeneity when implemented in global simulations. Land surface models therefore take into account sub-grid parameterisations of both horizontal and vertical heterogeneity. This can be achieved by three main methods: (*i*) aggregate models using effective parameters, e.g. averaging albedo across snow covered and snow-free surfaces, to calculate grid box averages, (*ii*) tile models which further subdivide the land surface into separate tiles, e.g. snow and snow-free surfaces, to calculate grid box averages according to their relative cover (Avissar and Pielke, 1989; Claussen, 1991), and (*iii*) dual source models resolve vertical heterogeneity allowing separate surfaces to interact, e.g. fluxes of sensible heat from vegetation canopy to snow covered surface. In practice most models including MOSES use a combination of the above methods according to the scale

of the process in question. Correspondingly, snow models can be implemented in a number of different guises within the land surface model relating to how the thermal and radiative components are treated (Figure 2-1). MOSES treats snow as a composite snow-soil layer with an effective thermal conductivity calculated as the average of the thermal conductivity of the depth of snow and soil. Surface albedo is treated as a function of the snow covered fraction. More complex models have snow layers separate from the soil, and may use multi-layers in the modelling of thermal, hydrologic and albedo properties. These models may also include separate energy-balances for snow and snow-free surfaces.

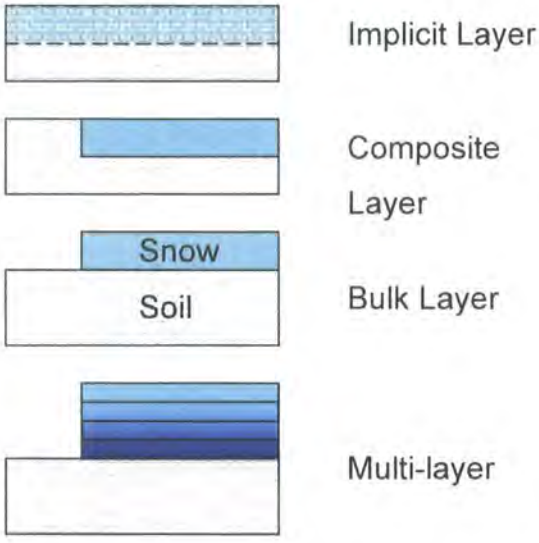

Figure 2-1: Structure of the thermal and radiation component of snow in models representing the land surface. Modified from Slater et al. (2001)

The current MOSES snow model is relatively simple compared to the range of models available (Etchevers *et al.*, 2004). The reasons for this are twofold; the first is the need for models to be computationally efficient when used in GCMs, and secondly, the accounting of spatial variation in surface conditions is very poor, a more complex model may therefore be more precise, but may not be more accurate. MOSES is under constant development and improvement as part of a new initiative: Joint UK Land Environment Simulator (JULES). Currently, JULES and MOSES are virtually the same model. This study forms part of the development of JULES which will embrace a new snow tiling scheme and multi-layered snow model. The main difference between the models is within the soil thermal and

hydrological component; MOSES uses an explicit scheme, whilst JULES uses an implicit scheme. These differences are expected to make little difference to modelled runoff. MOSES is a substantial development of the UKMO model (Warrilow and Buckley, 1989). The snow model is essentially the same but whereas UKMO used a bulk surface layer temperature, MOSES uses a separate skin temperature. This results in a greater transfer of turbulent energy in MOSES and correspondingly faster melt rates (Slater *et al.*, 2001). Model structure and engineering therefore plays a large role in simulated processes.

To allow experimentation with tiling and for ease of use the actual model used here is a cut-down version of the full MOSES model. The basic code used was supplied by R. Essery (2005) and modified as required. The main difference between the full and cut-down versions is the absence of an interactive canopy resistance to vapour transport r_s and canopy heat capacity. This was modelled using the full version and used as a driving variable in the cut-down version. The model consists of the MOSES snow model and the four layer soil model, and is executed over a single tile assuming a C3 grass surface and organic peat soil (**12.1.5**). MOSES uses a prescribed snow density and thermal conductivity, a prognostic snow albedo model and bulk aerodynamic model of turbulent exchange. For a full description of the MOSES model see Cox *et al.* (1999) and Essery *et al.* (2001). Appendix 12 gives a description of the surface exchange and snow components of the cut-down MOSES version.

Of key importance to this study is the way the model treats spatial variation in snow-cover. MOSES includes a simple parameterisation of the effective albedo to account for exposed vegetation as the snowpack melts out. The snow covered fraction f_{snow} is given as:

$$f_{snow} = \frac{S\rho_{snow}^{-1}}{S\rho_{snow}^{-1} + 10z_0}$$

Equation 2.1

where S is the lying snow mass, ρ_{snow} is the density of snow and z_0 is the surface roughness length. The snow covered fraction is in turn used to generate an effective albedo that is used in the surface energy balance.

$$\alpha_{effective} = f_{snow}\alpha_{snow} + (1 - f_{snow})\alpha_0$$

Equation 2.2

where α_0 is the snow-free albedo and α_{snow} is the simulated snow albedo. The use of such a parameterisation reduces the surface albedo for very shallow snow-covers and helps with the documented tendency for models to retain very shallow snow-covers (Slater *et al.*, 2001). However, such a parameterisation is not appropriate to account for spatially heterogeneous snow-covers where significant depths of snow exist at comparatively low snow covered fractions. A number of formulations of snow covered fraction are used in various land surface models (Table 2-1 and Figure 2-2).

Table 2-1: Formulations of Snow covered Fraction used in various land surface models

MODEL	Snow covered Fraction Formulation
ECHAM4	$f_{snow} = \frac{S}{S + 0.01\rho_s}$
BATS	$f_{snow} = 0.95\tanh\left(\frac{S}{100}\right)$
CLASS	$f_{snow} = \frac{S}{0.1\rho_s}$ $\quad 0 \le f_{snow} \le 1$
BASE	$f_{snow} = \sqrt{\frac{S\rho_s^{-1}}{0.038 + 0.000144\rho_s}}$ $\quad 0 \le f_{snow} \le 1$

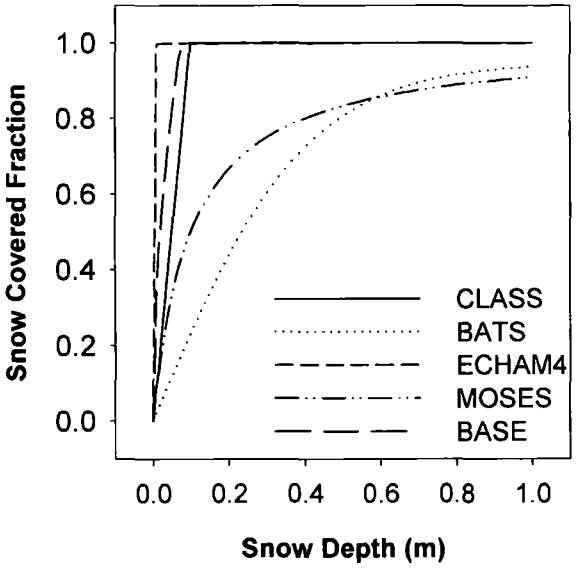

Figure 2-2: Snow covered Fraction Parameterisations used in various land surface models, given a snow-free aerodynamic roughness length of 0.01 m, and a snow density of 250 kg m^{-3}. CLASS (Verseghy, 1991; Verseghy *et al.*, 1993), BATS (Yang *et al.*, 1997), ECHAM4 (Roesch *et al.*, 2001), BASE (Slater *et al.*, 1998).

Several processes controlling snow distribution have been identified as important at the sub-grid scale, including elevation effects on snowfall and ablation (e.g. Essery, 2003; Hartman *et al.*, 1999; Moore *et al.*, 1999), topographic control on radiation and turbulent fluxes (e.g. Pohl *et al.*, 2006a; Pohl *et al.*, 2006b), snow redistribution (e.g. Elder *et al.*, 1989; Gray and Male, 1981; Gray and Prowse, 1993; Liston and Sturm, 1998; Pomeroy *et al.*, 1993) and small-scale advection leading to heterogeneous melt rates (e.g. Essery *et al.*, 2006; Marsh *et al.*, 1999; Neumann and Marsh, 1998; Pohl and Marsh, 2005).

Recent work by Déry (2004) and Liston (2004) have proposed methods to incorporate spatial variation into land surface models. Déry (2004) proposed the use of two snow tiles (deep and shallow) and a snow-free tile. The tile extent defined by analysis of a digital terrain model (DTM) and parameterised fractional coverage, with the deep snow tiles accumulating snow at a rate ten times greater than the shallow tile to account for wind redistribution. Liston (2004) proposed that a log-normal probability distribution of snow-cover can be used to define separate

energy-balances for snow and snow-free surfaces defined by a specified coefficient of variance (Liston, 2005). The result of these parameterisations compared to the assumption of uniform snow-cover are improved simulations of momentum, energy and moisture fluxes (Déry *et al.*, 2004; Liston, 2004). Two very similar methods are used in this thesis.

2.3 The Surface Energy and Mass Balance

The theoretical basis behind this study and NWP is centred on the conservation of mass and energy. The sun releases shortwave radiation which is absorbed by the atmosphere and land surface leading to a warming. The land surface warms and loses heat to the overlying atmosphere in the form of sensible and latent heat (evaporation/condensation) as well as re-radiating energy. Sensible heat is transferred from the warm land surface to the overlying ambient atmosphere in the form of turbulent eddies and is released through mixing with the ambient air. The transfer of latent heat is associated with the passage of water vapour in the eddies. Latent heat is released when water condenses or freezes leading to a warming of the ambient air. The interaction of radiation with the land surface directly controls the air temperature and water availability in the atmosphere, crucial to weather. Energy is also conducted into the soil surface and some energy used in photosynthesis, although these terms are usually small. The sum of these fluxes leads to an energy balance at the land surface.

These fluxes of sensible and latent heat are known to be dependent on the surface temperature and moisture content, windspeed, humidity and temperature of the overlying boundary layer and the roughness of the surface itself. Different surfaces have different properties. A snow covered surface exhibits a high surface albedo, a surface temperature limited to the melting point of water and a smooth surface. A snow covered surface will also melt and produce runoff introducing an additional energy sink in the energy balance. A snow-free vegetated patch exhibits an unrestricted surface temperature with a low albedo, a rough surface, and restricted water availability through stomatal and soil pore resistance. These two surface types exhibit substantially different surface characteristics and the energy partitioning can be expected to be considerably different. In fact, it can be

envisaged that the direction of fluxes could be opposite between the two surfaces. A warm well mixed boundary layer may be warmer than a snow covered surface but cooler than a low albedo, vegetated surface. The sensible heat flux will then be upwards over the snow-free surface and downwards over the snow covered surface. In which case, air temperature is directly controlled by the sensible heat flux from snow-free ground, and thus if melt is controlled by sensible heat then the rate of snowmelt may be a function of the snow-free area. Should wind advect heat energy laterally then spatially heterogeneous melt may occur.

Stefan's law states that any surface with a temperature above absolute zero will emit radiation as a function of the fourth power of its absolute temperature. Thus the atmosphere and the land surface emit a radiation known as long-wave radiation (L) (3.0 to ~100 μm) (Oke, 1987). The net long-wave radiation at the surface is correspondingly a function of the difference in the surface temperature, and the temperature of surrounding topography and the atmosphere. Radiative terms by convention are positive when directed towards the surface. The net radiation available at the surface can be expressed as:

$$Rn = (1-\alpha)S_{incident} + L_{incident} + L_{emitted}$$

Equation 2.3

The emitted long-wave radiation can be calculated by Stefan's law:

$$L_{emitted} = -\varepsilon\sigma T_*^4$$

Equation 2.4

where T_* is the surface temperature in Kelvin, σ is the Stefan-Boltzmann constant, and ε is the emissivity of the surface, equal to unity for a black-body radiator, and appropriate for the land surface.

In addition to the radiative heat fluxes are the turbulent fluxes associated with convection and mixing in the lower atmosphere and the conductive fluxes of heat energy through the substrate. Any molecule with a temperature above absolute zero has an associated energy in the form of sensible heat. The magnitude of this energy is the product of the heat capacity and absolute temperature. Correspondingly any liquid or gaseous molecule has an associated latent energy associated with its state.

Latent heat is the energy released or required during a change of state. A parcel of air will therefore have a sensible heat associated with its absolute temperature and a latent heat associated with the mass of water vapour present. An exchange of water vapour or sensible heat between the surface and overlying atmosphere leads to a flux of energy. The surface energy-balance can correspondingly be given as:

$$Rn = H + LE + G$$

Equation 2.5

where H is the sensible heat flux, LE is the latent heat flux and G the ground heat flux. For the case of a melting snowpack an additional melt heat flux (H_{sm}) associated with the latent heat of fusion has to be included:

$$H_{sm} = H + LE - G - Rn$$

Equation 2.6

The movement of an air mass over a rough surface applies a drag to the passage of air, which in turn sets up turbulence in the air mass. Turbulence can be either enhanced or damped by thermal buoyancy within the boundary layer. Turbulence leads to a mixing of the boundary layer between the surface and the blending height. The vertical movement of a parcel of air thus leads to a flux of momentum (τ), sensible (H) and latent heat (LE) in the direction of movement. In particular, the land surface acts a boundary to the atmosphere across which both mass and energy can pass, thus vertical fluxes of energy across this boundary are of importance to atmospheric models. The instantaneous flux of momentum can be calculated as (Monteith and Unsworth, 1990):

$$\tau = -\rho w$$

Equation 2.7

where ρ is the density of air in kg m^{-3} and w is the vertical windspeed in m s^{-1}. By convention the flux of momentum is negative when directed towards the surface.

Similarly, the instantaneous sensible heat flux can be calculated as:

$$H = \rho c_p w T$$

Equation 2.8

where c_p is the specific heat capacity of air in J kg m^{-3}, T is the absolute air temperature in Kelvin, and w is the vertical windspeed in m s^{-1}. Similarly, the latent heat flux is given as:

$$LE = \rho L w q$$

Equation 2.9

where L is the latent heat of vaporisation or sublimation in J kg^{-1} depending on the surface state and q is the specific humidity of the air in kg kg^{-1}. By convention the sensible and latent fluxes are positive when directed away from the surface.

By measuring air temperature, specific humidity and vertical wind velocity the instantaneous fluxes of momentum, latent and sensible heat can be measured. This is the principle behind the Eddy Correlation (sometimes known as Eddy Covariance) method of measuring turbulent fluxes.

Difficulties exist in modelling and measuring the vertical wind velocity. Turbulent fluxes are correspondingly parameterised in the form of a potential difference between the surface and the overlying air at height z, and a resistance to the transfer of energy. This form known as the bulk aerodynamic method relates the fluxes directly to the surface properties and is used in modelling applications. The momentum flux can be expressed in the following form (Garatt, 1992):

$$\tau = \frac{\rho u}{r_{a_m}}$$

Equation 2.10

where u is the wind velocity at height z, and r_{am} the aerodynamic resistance to momentum in s m^{-1}. The aerodynamic resistance is a parameterisation of the turbulent diffusion (mixing efficiency) and is a function of wind speed and thermal stability of the boundary layer. Correspondingly the sensible heat flux can be expressed as:

$$H = \frac{\rho c_p (T_* - T)}{r_{ah}}$$

Equation 2.11

where T_* is the surface temperature, T the temperature at height z, and r_{ah} the aerodynamic resistance to heat. Similarly, the latent heat flux can be calculated as:

$$LE = \frac{\rho L(q_* - q)}{r_{a_q} + r_s}$$

Equation 2.12

where q_* is the specific humidity at the surface, q the specific humidity at height z, r_{aq} the aerodynamic resistance to water vapour and r_s the surface resistance to water transfer associated with the mechanisms of water use in vascular plants, bryophytes and soil.

The aerodynamic resistance to momentum can be estimated during stable conditions as (Monteith and Unsworth, 1990):

$$r_{a_m} = \frac{1}{u_* k^2}\left[\ln\left(\frac{z-d}{z_{0m}}\right) + 5\left(\frac{z-d}{L}\right)\right]$$

Equation 2.13

and during unstable conditions as:

$$r_{a_m} = \frac{1}{u_* k^2}\left[\ln\left(\frac{z-d}{z_{0m}}\right) + 4\left(\frac{z-d}{L}\right)\right]$$

Equation 2.14

where u_* is the friction velocity in m s^{-1}, k is the von Kármán constant, z_{0m} is the aerodynamic roughness length for momentum in metres, d is the displacement height in metres and L is the Obukhov stability length (Obukhov, 1971) in metres. The aerodynamic resistance and displacement for momentum, vapour and heat are known to vary but are often assumed equal (Garatt, 1992). The roughness length for heat and moisture is poorly defined but commonly assumed to be a tenth of the roughness length for momentum.

$$z_{0m} \approx 10 z_{0h}$$

Equation 2.15

This is however an area of debate; a full discussion of the implication of this assumption can be found in **6.3.1a)**. A useful rule of thumb suggests z_{0m} and d can be estimated as a tenth and two-thirds of vegetation height respectively.

The Obukhov length (Obukhov, 1971) is a measure of thermal and mechanical turbulence. The Obukhov length is:

$$L = \frac{-\rho c_p T u_*^3}{kgC}$$

Equation 2.16

where g is the gravitational constant in m s^{-2}, and **C** is the heat flux due to heat convection. Conventionally, the Obukhov length is expressed as a dimensionless value scaled by the height above the zero-plane displacement, $\left(\frac{z-d}{L}\right)$ known as the Obukhov stability parameter. This has a value of zero during neutral conditions, positive during stable and negative during unstable conditions.

Surface resistance to evaporation is a function of water availability, the surface resistance to evaporation from a snow covered or wet surface is zero, however evaporation from the soil is a function of stomatal resistance and pore-water pressure in the soil. The Penman-Monteith equation (Monteith, 1981; Penman, 1948) provides a link between the availability of energy for evaporation, the aerodynamic resistance and surface resistance to evaporative heat flux, independent of the surface temperature.

$$LE = \frac{\Delta(L_{net} + S_{net} - G) + \dfrac{\rho c_p [e_s - e]}{r_a}}{\Delta + \left[\dfrac{\gamma(r_a + r_c)}{r_a}\right]}$$

Equation 2.17

where Δ is the change in saturation vapour pressure with temperature in Pa K^{-1} and γ is the psychrometric constant (not actually constant, but a function of atmospheric pressure) in Pa K^{-1}. The assumption made by the Penman-Monteith equation is that the sources and sinks of the turbulent fluxes are the same.

2.3.1 ADVECTION AND PATCHY SNOW-COVER

Clearly the energy-balances of snow and snow-free surfaces are dissimilar and parameterising these differences in terms of an effective albedo may lead to significant errors. Neither does it necessarily make sense to treat snow and snow-free surfaces separately using tiles, particularly when the patch extent is small relative to the blending height and the turbulent fluxes are in opposite directions. In these situations the 'difference in the vertical transfer of energy, in the forms of latent, sensible and radiative heat across heterogeneous surfaces creates horizontal inhomogeneity in the temperature, humidity and momentum fields. This in turn leads to a horizontal exchange of heat, moisture and momentum and is defined as advection' (Philip, 1959). Where the patch size is large compared to the blending height, advected energy is a much smaller component of the energy-balance. For instance, Essery (1997) using numerical simulations with a tiled and boundary-layer scheme that use the same flux parameterisation, showed that although tile schemes perform less well, they still give reasonable estimates of average and local fluxes over snow and snow-free surfaces where the patch size is of the order of 500 m. The performance of the tile model degraded as the differences in surface stability increased. The question thus remains whether advection is important at the patch scale of real snow-covers.

Advection is particularly important with heterogeneous snow surfaces due to the potentially large differences in surface temperature and differences in sensible heat flux. A melting snow surface is limited to 0°C, whilst a dark snow-free surface will have a higher surface temperature, particularly under high solar insolation. For instance, Liston (1995) observed surface temperatures as high as 42°C for black lichen during snow melt. The extra energy available for melt will be greatest at the edge of a snow patch leading to faster melt rates and exposing lower albedo surfaces at an increased rate than if melt was homogeneous. Conceptually, this process could be very important, especially where snow patches are small and patchiness is high as is the case with complex arctic snow-covers.

The theory of small-scale advection centres on the formation of internal boundary layers corresponding to the point of flux divergence. This is shown schematically in Figure 2-3.

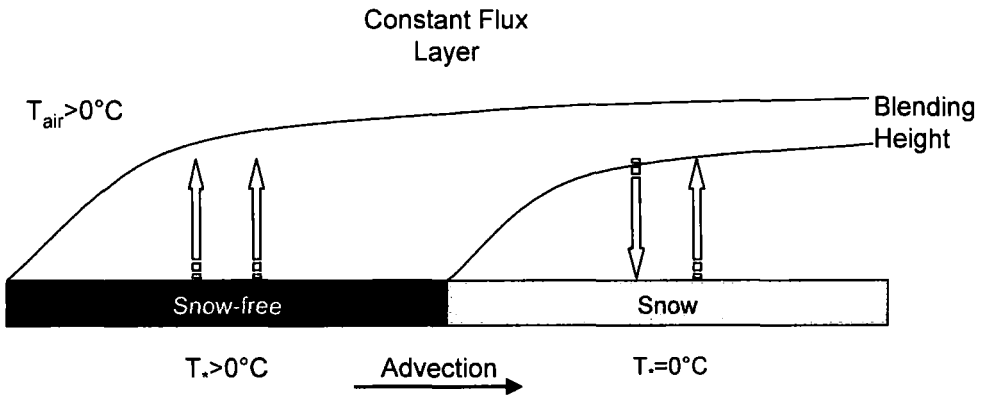

Figure 2-3: Schematic diagram of advection between snow-free and snow patches. Red and blue arrows indicate sensible heat and latent heat flux respectively. Black curves indicate the position of internal boundary layers tending towards the blending height.

At the point of transition between the surfaces, the internal boundary layer is close to the snow surface. Thus relatively warm air is near the surface leading to high sensible heat fluxes. Further downwind the internal boundary layer is higher and the fluxes conform to those controlled by the blending height. The formation of these internal boundary layers has been shown through field experimentation (Granger *et al.*, 2006) and numerical simulation (Essery *et al.*, 2006). Observations of peaks in air temperature over melting snowpacks have generally been put down to radiative heating of moisture in the lower atmosphere, but may in fact be evidence of internal boundary layer formation (Casiniere, 1974; Halberstam and Schieldge, 1981). Shook and Gray (1997a) observed temperatures measured at 0.02 m responding more quickly than those at 0.4 m due to the presence of snow patches, with both stabilizing within to 2 to 5 m of fetch suggesting the effects of advection are very localised and depend on the surface conditions. Theoretically the same process works for the transfer of latent heat, however the differences in vapour pressure between the surfaces are lower than the differences in temperature. Much work has thus concentrated on the advection of sensible heat.

The contribution of advection to snowmelt is relatively poorly understood. Advected energy is highly dependent on the size, extent and distribution of the patches, which are constantly evolving with time due to continuing accumulation,

redistribution and ablation. Snow-cover heterogeneity occurs at a number of scales and relates to a number of different types of heterogeneity, for instance patchiness could relate to a few large snow drifts surrounded by interconnected snow-free areas, or *vice versa*, or a combination of both. Furthermore, a patchy landscape could consist of a large number of small patches. Particularly crucial to advection is the degree of gappiness or lacunarity of the landscape. Referring to a distribution of snow as patchy thus refers to a variety of potential landscape patterns.

Part of the scope of this thesis is to test the importance of advection in the surface energy balance and to provide recommendations of how this might be included in future releases of the JULES model. Observations from the boreal forest showed a inverse covariance between SWE and melt rates associated with canopy effects such that shallower snow melted quicker. Fitting the covariance into the energy balance improved the simulation (Faria *et al.*, 2000). Marsh (1996) defined an advection efficiency, which Neumann (1998) subsequently used to parameterise advected heat fluxes. The use of an efficiency term is independent of patch size and distribution which are clearly important. These approaches are all unsatisfactory for use in large scale simulations. The challenge thus remains to develop parameterisations for use in large-scale hydrological models.

2.4 Snow, Climate and Vegetation Feedbacks

Tundra covers a vast swath of the northern hemisphere (5.6 million km^2) and tundra soils contain approximately 11-14% of total global soil carbon (121-191 Tg) (Wookey, 2002). The greater than average warming in the high latitudes predicted by GCMs has consequently promoted much interest in the carbon balance of tundra soil. There is evidence suggesting tundra soils are switching from a sink of atmospheric carbon to a source (Oechel *et al.*, 1993; Oechel *et al.*, 2000). Current climate change scenarios suggest a warming of 2.1°C (Figure 2-4) and a reduced precipitation of -0.09 mm day^{-1} (Figure 2-5) by 2050 for northern Sweden (IPCC Scenario B2a – medium to low emissions), suggesting that not only will these processes continue but that they may potentially occur at an increased rate.

At the landscape scale tundra demonstrates strong heterogeneity associated with topographic relief (Walker, 2000). Difference in sharpness of relief and direction of slope exposure associated with these features operate to influence soil drainage, soil depth, surface isolation, snow depth and duration, wind velocity and other environmental phenomena (Walker, 2000). The micro-zonation of species and communities along the topographic gradient is largely a function of soil moisture and the depth and duration of snow-cover (Billings and Bliss, 1959; Walker, 2000). Snow-cover influences plant distribution and abundance by affecting establishment, growth, reproduction and phenology of plants (Heegaard, 2002). Snow-cover determines the length of the growing season (Billings and Bliss, 1959), and protects from extreme cold (Billings and Bliss, 1959), water stress, desiccating winds and influences nitrogen availability (Fahnestock *et al.*, 2000). Observational evidence shows shrubs are increasing their range (Sturm *et al.*, 2001b; Tape *et al.*, 2006), and the treeline is advancing into snow-bed communities (Kullman, 2002).

A changing climate has potentially large consequences for arctic vegetation composition and structure, particular shrubs, which in turn affect snow-cover extent and duration. The expansion of shrub beds acts to trap more snow, reduce sublimation and increase the snow lie despite a reduced solid precipitation. Deeper drifts act to moderate soil temperature, which if the snow falls early in the season maintains warmer soils over the winter. This in turn promotes faster rates of nutrient cycling and the corresponding expansion of shrub communities (Liston *et al.*, 2002; Sturm *et al.*, 2001a). Model simulations of snow-cover depth and duration with a blowing snow model have shown a great deal of sensitivity to the distribution of shrubs (Liston *et al.*, 2002). The potential for snow-cover to feedback to shrub abundance has been shown by experiment by artificially increasing snow-cover depth and duration, with deciduous shrubs increasing in abundance and height with increased snow-cover (Wahren *et al.*, 2005). Although the feedbacks between snow, vegetation and biogeochemical cycles are not dealt with in this thesis, it is clear that snow plays an important role in the climate and a great deal of uncertainty remains as to how tundra landscapes will respond to a changing climate. A more complete understanding and representation of snow within numerical models will help elucidate some of these important feedbacks.

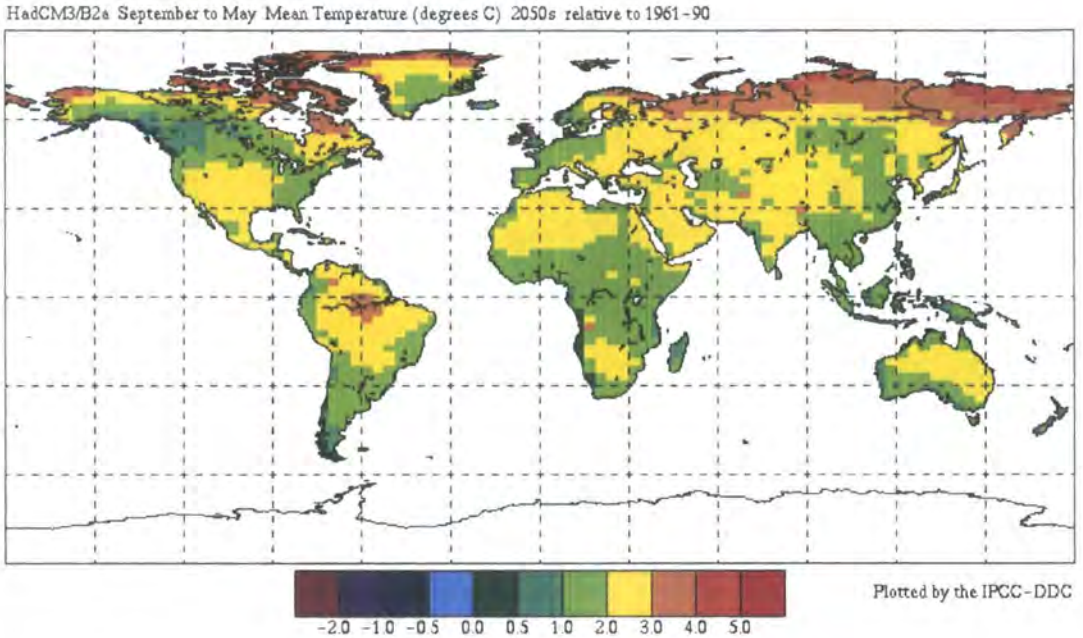

Figure 2-4: Global change in mean Temperature (°C) between 2050 and 1961-1990 for the winter months of September - May, as predicted by HadCM3 under IPCC scenario B2a. Source: IPCC Data Distribution Centre http://ipcc-ddc.cru.uea.ac.uk

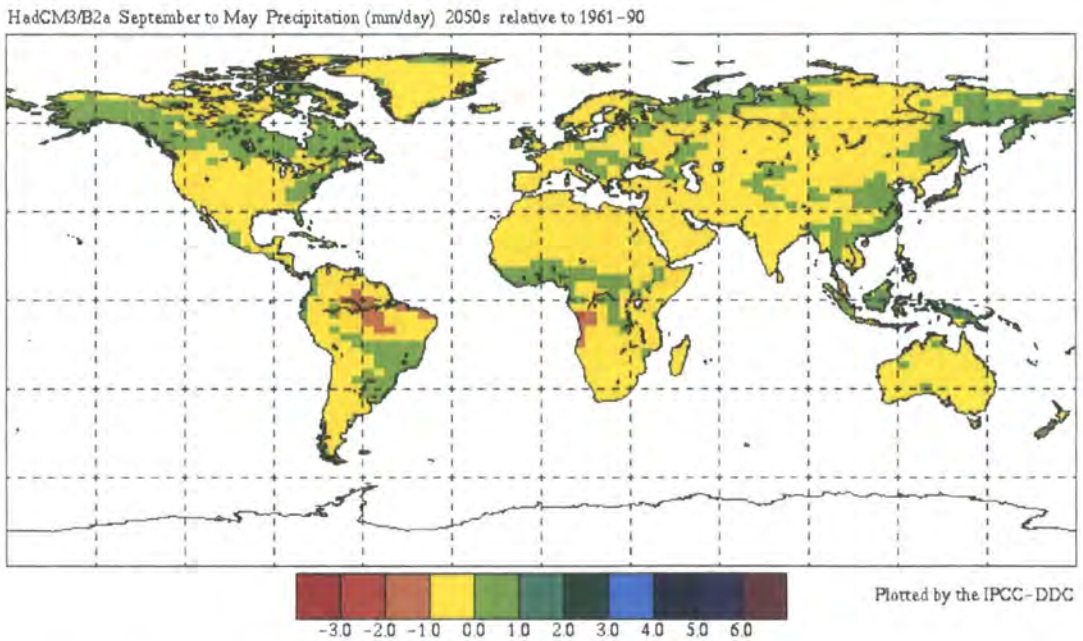

Figure 2-5: Global change in Precipitation (mm/day) between 2050 and 1961-1990 for the winter months of September - May, as predicted by HadCM3 under IPCC scenario B2a. Source: IPCC Data Distribution Centre http://ipcc-ddc.cru.uea.ac.uk

Chapter 3

Study Site Description and Experimental Design

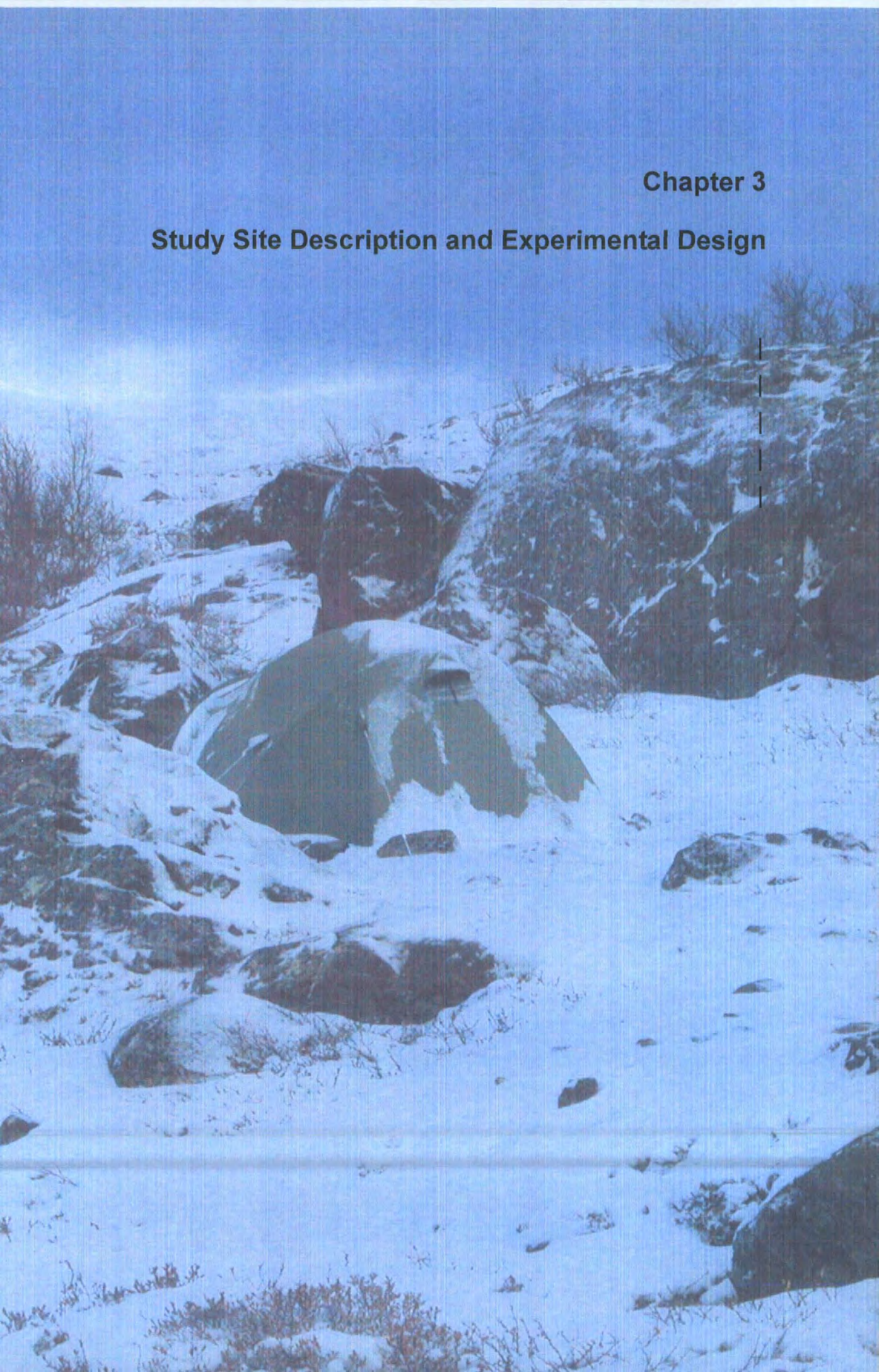

3 Study Site Description and Experimental Design

3.1 Introduction

Data for this study comes from a small area of Arctic tundra in northern Sweden and is typical of the large expanse of Arctic tundra in the high latitudes covering approximately 5.6 million km^2 (Wookey, 2002). This study rather than being extensive aims to investigate the small-scale dynamics that control snow distribution and their implications on a global basis. This chapter outlines the study site and the experimental design.

3.2 Study Site Description

The study site is based at the Abisko research station in northern Sweden and is approximately 200 km north of the Arctic Circle (Figure 3-1). The research station is sited at 385 m a.s.l., and the study site at approximately 750 m a.s.l. on a predominantly north-facing hillslope, slightly beyond the tree-line (68°18'N, 18°51'E) (Figure 3-2). The bedrock in the area belongs to the Scandes mountain range and is mainly hard shale (Nils-Åke Andersson, *personal communication*). The study site is an area of known discontinuous permafrost (King, 1986), although it is thought unlikely that permafrost underlies the study site but this remains unknown. Cold based perennial snow drifts can be found on sheltered north facing slopes at a similar altitude.

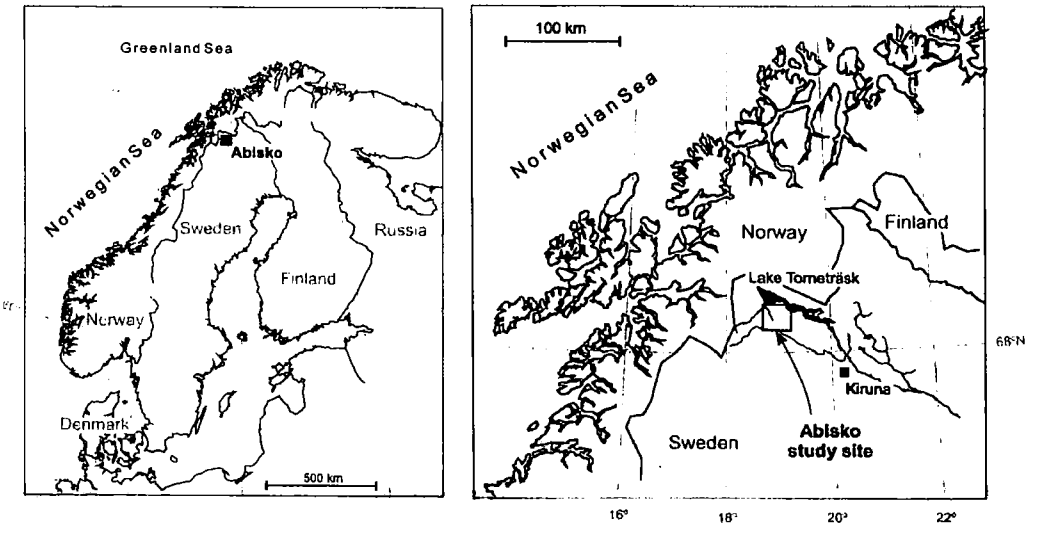

Figure 3-1: Location map (Modified from Dean, 2003)

The STEPPS research area covers an area of approximately 1 km^2, however data for this study comes from a smaller gridded area 500 by 320 m in extent (Figure 3-3). The study site demonstrates considerable complex topography associated with periglacial processes. Permafrost has been much more extensive in the past, and relic landforms especially patterned ground are widespread. These periglacial landforms were probably last active during the Little Ice Age, and have shown significant degradation and can now be considered inactive (Nyberg and Lindh, 1990). Figure 3-3 shows rock arrangement associated with the formation of patterned ground. Soils vary in depth from exposed bedrock to mineral glacial tills overlain by peat accumulations. The variation in depth and type of soil undoubtedly leads to a high degree of spatial variation in soil thermal and hydrologic conductivity. The MOSES representations of soil hydrology and thermodynamics are known to be poorly constrained, particularly for organic soils and were the subject of a separate research project. Vegetation type and size also varies across the gridded area associated with topography induced changes in abiotic processes.

The gridded studied site was chosen as typical of the co-variation in topography and vegetation of the area and of mountain tundra at the global scale. The extent was limited to allow for meaningful observation of process with the available equipment and manpower.

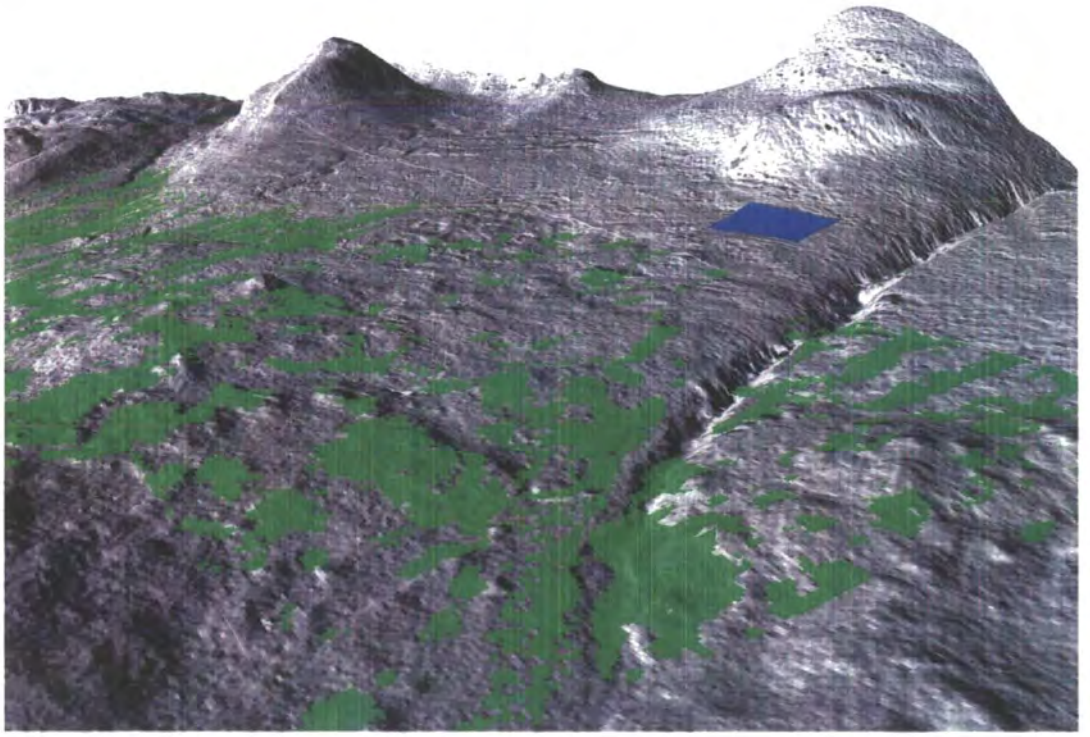

Figure 3-2: 3-D projection of the study site viewed from the North-west, at a distance of 6 km and elevation of 925 m. The blue region marks the 500 by 320 m study site, and the birch forest is marked in green. Based on data from Dean (2003).

Figure 3-3: Oblique aerial photograph of the study site, with approximate extent of gridded area marked. View North-East during peak biomass (mid-June) (Image courtesy of Anders Eriksson).

The topography of the study site is highly variable, consisting of exposed soil-free ridges and deep soil hollows. The elevation of the study site varies from 725 m in the north-west to 780 m a.s.l. in the south-east (Figure 3-4a).

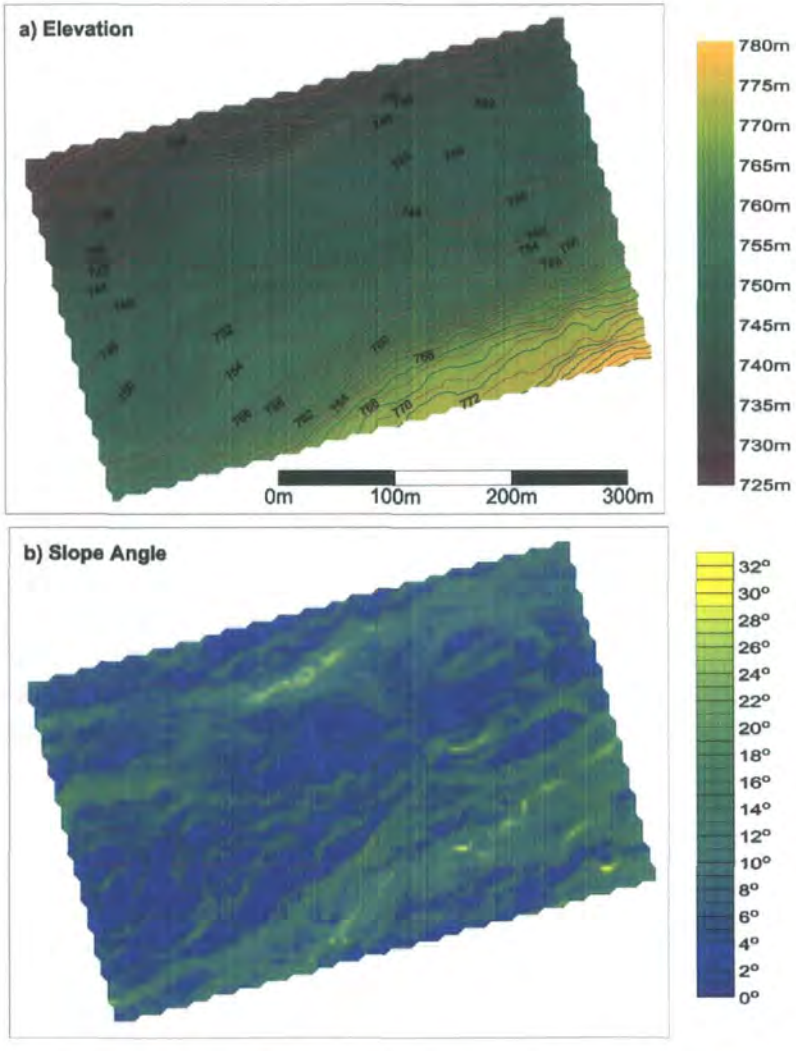

Figure 3-4: Elevation and Slope angle for study site. Elevation data are from krigged differential GPS observations. Slope angle data are calculated using the method of Zevenbergen and Thorne (1987). Contours are at 0.5 m intervals in figure a.

Slope angle varies enormously from level ground to a maximum of 32° over a distance of 5 m (Figure 3-4b). The steepest slope angles are found on two steps running approximately north-east across the study site. Shallower slope angles are associated with small formations linked to frost action. The effect of these small formations can clearly be seen on local aspect and curvature (Figure 3-5).

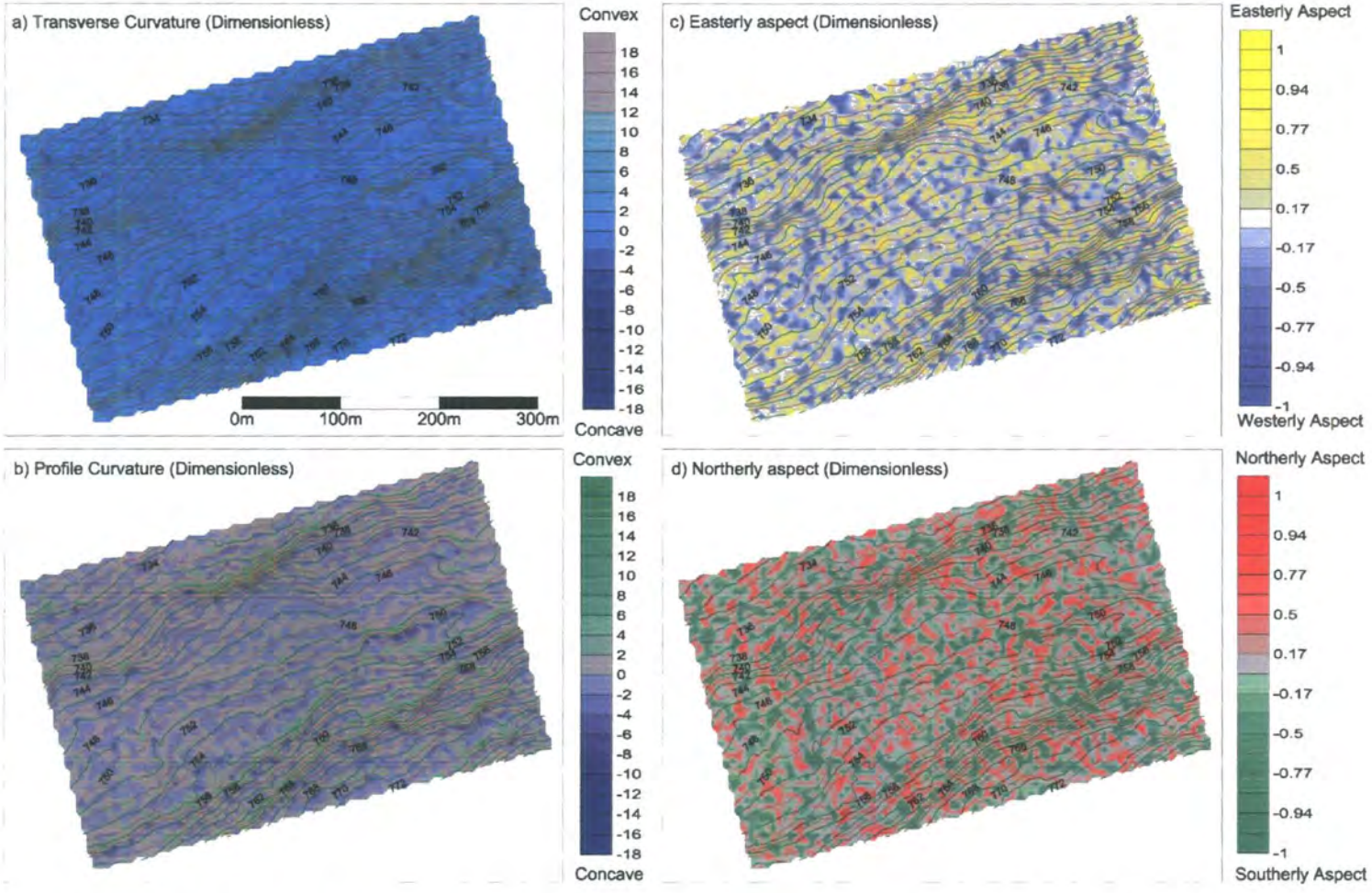

Figure 3-5: Topographic Indices of Curvature and Aspect for study site. Profile curvature is calculated in the direction of aspect, and transverse is perpendicular to aspect. Figures are contoured with elevation. Terrain indices are calculated using the method of Zevenbergen and Thorne (1987) Contours are at 0.5 m intervals.

3.2.1 CLIMATE

No long term climate measurements were made at the study site, but standard meteorological measurements are made at the Abisko research station (385 m a.s.l.). The average annual temperature at the research station is approximately -1.0°C and corresponds to -3.4°C at 700 m a.s.l. assuming a standard lapse rate of 6.5°C km^{-1}. Over a 30-year mean, July is the warmest month (mean temperature +11°C), and January the coldest (-11.9°C) (Nils-Åke Andersson, unpublished data). The Abisko valley is located in a pronounced orographic precipitation shadow, precipitation measurements thus vary considerably. The long term mean annual uncorrected precipitation is 304 mm in Abisko within 60 km annual precipitation in excess of 1000 mm is observed (*ibidem*).

3.2.2 VEGETATION

The study site is located at an altitude above the *Betula pubescens* ssp. *tortuosa* treeline and below the sparsely vegetated mountain tops (Figure 3-2). The vegetation conforms to the prostrate sedge-dwarf-shrub tundras typical of the low Arctic (Bliss and Matveyeva, 1992; Walker, 2000). The vegetation across the study site is a complex mosaic associated with terrain-influenced abiotic factors including snow depth and duration, soil moisture and soil nutrients (Figure 3-3). Vegetation distribution across the study site is classified according to its structure and subsequent capacity to retain snow (Figure 3-6). The sheltered hollows are dominated by larger shrubs such as *Salix* spp., *Betula nana* and *Juniperis communis* characterised by greater snow accumulation, subsequent longer duration of snow-cover and relatively greater soil moisture (Cook, 2005). This large shrub community accounts for approximately 20% of the study site. The exposed ridge tops retain little snow-cover during the winter and are largely devoid of higher plants and are sparsely vegetated with bryophytes and lichens. This bare ground community accounts for approximately 5% of the study site. The rest of the vegetation is a gradient of communities between these two extremes dominated by the evergreen *Empetrum hermaphroditum* with varying degrees of *B. nana* which are broadly classified into a tall (>0.2 m) and short (<0.2 m) *Empetrum* spp. dominated communities, accounting for 25 and 50% of the study site. In very wet

areas *Empetrum* heath is replaced by low sedges (*Carex spp.*, and *Eriophorum* spp.), and exhibits similar snow-retaining structural characteristics as the low *Empetrum* heath and is subsequently classified similarly. Table 3-1 lists the typical species found in each community. Vegetation height and structure bear a close relationship to the distribution of snow-cover.

Table 3-1: Typical species found in dominant communities (from Cook, 2005)

	Species
Sedge Community	*Carex* spp.
	Poa spp.
Heath Community	*Arctostaphylos alpinus*
	Betula nana
	Cassiope tetragona
	Diapensia lapponica
	Dryas octopetala
	Empetrum hermaphroditum
	Loiseleuria procumbens
	Vaccinium myrtillus
	Vaccinium uliginosum
	Vaccinium vitis-idaea
Large Shrub Community	*Betula nana*
	Juniperus communis
	Salix spp.
Bare Ground	Lichens and Bryophytes

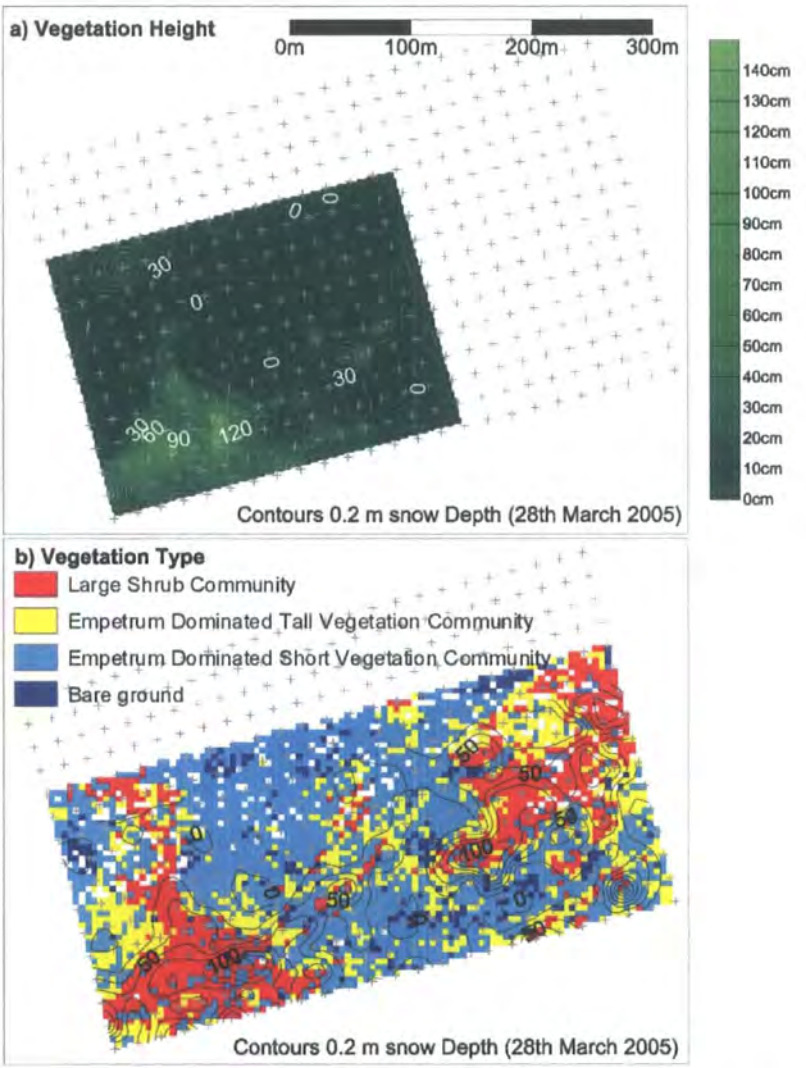

Figure 3-6: Vegetation composition across the study site classified by structure.

3.3 Experimental Design

A combination of field observations and numerical modelling is employed in this study. Field observations are centred on making measurements of snow distribution and energy exchange across the study site. To facilitate this and to enable repeat measurements an observation grid was established. The grid was laid out in a regular 20 m pattern using a Trimble Total Station (TS315, Trimble, California, USA). Automated stations were established to collect regular data throughout the winter. Field observations were made between late February 2004 and early June 2004, with a few additional measurements from March 2005. Vegetation and topography data were collected during summer 2004.

The survey grid was used to monitor snow accumulation and ablation rates at each stake. Due to the inability to instrument each and every patch, instruments were deployed to take measurements in a snow and snow-free patch. Secondary small-scale measurements of sensible heat flux and albedo were made to characterise the spatial variability associated with small-scale advection and spatially varying surface properties. Incident radiation across the study site was considered uniform. The snow-free patch was chosen as likely to be exposed throughout the winter and the snowbed station as a deep drift likely to last late into the spring.

Due to the inclement winter conditions numerous problems were encountered accessing the field site and keeping equipment powered and running through the dark winter.

Remote sensed snow-cover data were collected to provide detailed information throughout the winter and to help answer the questions about the relationship between patches and heterogeneous melt rates.

Subsequent data modelling was completed using the MOSES model and a simple boundary layer scheme to simulate advection. Ideally all modelling would have been completed with a full boundary layer that simulated heat and moisture fluxes to evolve the boundary layer conditions, and thus fully elucidate the feedbacks between snow-cover and boundary layer properties. Comparing different

representations of snow and snow-free surfaces in MOSES is made more complex as implicit in the model driving data is the effect of heterogeneous snow-cover. However, no suitable numerical model is available and using a boundary layer model would increase the complexities of this investigation. Investigation with a full surface exchange model coupled to a boundary layer model is planned for future research.

The aim of the numerical modelling is to simulate the observed evolution in snow-cover, and heat and moisture fluxes measured at both the patch and landscape scale. A subsequent aim is to develop appropriate parameterisations of patchy snow that can be applied on the global scale.

3.3.1 METEOROLOGICAL INSTRUMENTATION METHODOLOGY

Instrumentation of the study site was completed with a number of differing aims and objectives as part of the broad STEPPS program. Deployment of sensors was necessarily a compromise between individual research requirements, sensor limitations and financial restraints. The instrumental methodology can be separated into three categories (i) standard meteorological measurements taken above the blending height and assumed uniform across the study site at an automatic weather station (AWS), (ii) surface properties measured in a deep snowbed and a predominantly snow-free patch, and (iii) flux measurements made at the landscape (Eddy Correlation Tower) and patch scales (Snow Station). The deployment of the measurements across the study site can be seen in Figure 3-7.

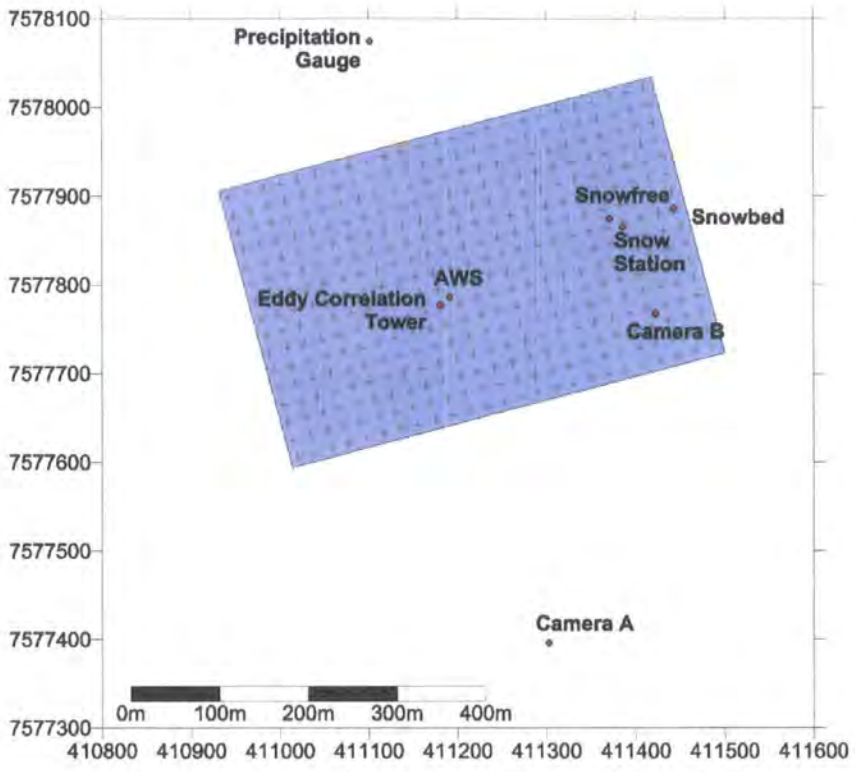

Figure 3-7: Location of meteorological stations and remote digital cameras. The study site is indicated by the shaded polygon. Grey cross-hairs represent snow survey locations.

a) Standard Meteorological Measurements

An automated weather station was used to record standard meteorological variables (Figure 3-8). The weather station was constructed on a Campbell Scientific CR10 data logger (Shepshed, United Kingdom). Half-hour averages were logged and instruments sampled at 0.1 Hz. Relative humidity, air temperature and atmospheric pressure were measured using a capacitive Vaisala HMP45C (Helsinki, Finland) installed at 2 m. The instrument was shielded with a wind aspirated RM Young 12-plate Gill radiation shield (Michigan, USA). Although this type of sensor is prone to riming in cold humid environments (Dery and Stieglitz, 2002; Makkonen and Laakso, 2005), subsequent analysis demonstrated this to be a rare problem. Relative humidity (RH) although easily measured is not a particularly useful quantity, more useful and used to drive the MOSES model are measures of vapour pressure and specific humidity, these are easily estimated from RH, air pressure and temperature (**11.1**). A height of 2 m was chosen as this was considered to be above the blending height. Temperature and moisture measurements are therefore considered to be consistent with a well mixed boundary layer over patchy snow-cover.

Incoming shortwave was measured using a radiometer (Kipp and Zonen CM5, Delft, Netherlands). Incoming longwave radiation was measured with a Kipp and Zonen CG4. Windspeed and direction were measured with an A100R switching anemometer and a W200P Windvane Potentiometer respectively (Vector Instruments, Rhyl, United Kingdom). Both instruments were installed at 2 m. Liquid precipitation was measured with a 0.5 mm tipping bucket precipitation gauge (Rimco, Australia).

Figure 3-8: Automatic Weather Station and Eddy Correlation Tower deployed at the study site.

Measuring solid precipitation is a notoriously difficult process and measured values are usually underestimates (Førland *et al.*, 1996; Foster *et al.*, 1996; Goodison *et al.*, 1981; Goodison *et al.*, 1998). Solid precipitation was measured daily with a SMHI shielded gauge (Sveriges Meteorologiska och Hydrologiska Institut) at Abisko Naturvetenskapliga Station (ANS) situated at 68°21'N, 18°49'E approximately 8 km from the field site and 385 m.a.s.l. Half-hourly data from an automated unshielded heated tipping bucket gauge were also available. However, daily totals are an order of magnitude smaller than the manual gauge either through undercatch or excess evaporation during heating. Subsequent data come from the

manual gauge. The measurements from the manual gauge were corrected for loss of mass by evaporation, undercatch and wetting loss during emptying following the recommendations of Forland *et al.*, (1996) (**11.2**). The correction for undercatch requires knowledge of windspeed at gauge level, windspeed is however routinely measured at 5 m. The local configuration of buildings meant the assumption of a logarithmic wind profile was unsafe. Gauge level windspeed was thus calibrated against the mean SWE across the survey grid up to 27th February 2004 pre-melt, resulting in a gauge windspeed exactly half of the 5 m windspeed. A Nipher Shielded gauge was also installed at the field site, but suffered from a combination of excessive undercatch and overcatch dependent on wind direction and windspeed making any sensible precipitation analysis impossible.

b) Surface Measurements

Surface measurements were made using a combination of three different monitoring stations: snow station, snow-free soil station and snowbed soil station (Figure 3-7). The snowbed and snow-free soil stations recorded soil properties. Each station consisted of a Campbell Scientific CR10X datalogger with instruments sampled at 0.1 Hz and stored as half-hour averages. Soil moisture was measured at 0.1 and 0.3 m depths using Campbell Scientific CS-616 Water Content Reflectometers. Soil temperature was measured at 0.05 m intervals to a depth of 0.4 m using a custom design frost gauge (Lloyd, 1998). The snowbed station was equipped with a Campbell Scientific SR50 ultrasonic depth gauge to automatically record snow depth. An additional snow station was installed in February 2004 to provide additional measurements of surface properties near to the snow-free and snowbed stations. Downward facing Skye Instruments SKS1110 Pyranometers were installed to record surface albedo. Hukseflux (Delft, Netherlands) soil heat flux plates were installed at 0.02 m depth. These unfortunately did not work well in the frozen soils, most likely due to differing thermal conductivities of frozen soil compared to the plate. Exergen IRT/c.10 Type (Watertown, MA, USA) infrared thermometers were installed to monitor surface temperature. IRTs were installed with radiation shields, however the Exergen is known to have a temperature dependent response associated with air temperature and radiative heating (Bugbee *et al.*, 1996). A correction was applied to the observed snow surface temperature to adjust the measurement for reflected radiative heating of the sensor body (**11.3**). A

Campbell Scientific 107 thermistor was installed at the base of the snowpack to monitor pack temperature at depth. Various problems were had with the monitoring stations through the winter due to power problems associated with snow covered solar panels and freezing electrolyte in batteries and also a faulty logger batch. Data recovery from the snow-free soil station was particularly poor.

c) *Flux Measurements*

Standard meteorological measurements give an indication of the state of the boundary layer at a particular point in time; more useful are measures of the rate of change or flux of the boundary layer. In particular, fluxes of sensible and latent heat define the energy and mass balance of the boundary layer. Fluxes can be measured by a number of techniques, including eddy correlation, soil lysimeters, profile measurements, temperature variance and the Bowen ratio method. However, with the exception of eddy correlation and lysimeters for latent heat these techniques all make some approximation of the exchange of mass and heat. Eddy correlation is a direct method of measuring turbulent fluxes in the boundary layer, by correlating vertical velocity (w) against changes in temperature (T) and specific humidity (q) (Shuttleworth *et al.*, 1988):

$$H = \rho c_p \overline{w'T'}$$

Equation 3.1

$$LE = \rho L_f \overline{w'q'}$$

Equation 3.2

The vertical velocity can be correlated against temperature and humidity provided they are concurrent and rapid (i.e. each eddy is measured as it passes through). Eddy correlation towers have a characteristic footprint related to boundary layer stability, wind direction and speed, and the distribution of sources within the footprint (**5.5**). The nature of an eddy correlation tower is that the footprint is relatively large compared to the patch scale experienced in the snow-cover, the measured fluxes are thus representative of the landscape as a whole. The eddy correlation system used was established by C.R.Lloyd on a suitable piece of ground towards the centre of the study site. The system consisted of a Solent sonic anemometer (Gill Instruments, Lymington, UK) and a LI-COR 7500 open path

CO_2 and water vapour analyser (Lincoln, Nebraska, USA) installed at 3 metres. The system was replaced by a more power efficient MK4 Hydra (Centre for Ecology and Hydrology, Wallingford, UK.) in the autumn of 2004. The system was run by a combination of solar panels and wind generators. The new more efficient MK4 Hydra allowed data to be collected through the long dark winter, although riming of sensors led to some data loss. Flux loss and angle of attack corrections were post-processed by C.R.Lloyd and all data presented here includes these corrections.

Measurements at the patch scale are made difficult by the relatively small patch expanse and the low internal boundary layers formed over smooth snow. The temperature variance method was thus employed which has a relatively small footprint and can be installed close to the surface to measure sensible heat fluxes. Under advective conditions flux divergence means that alternative measures generally underestimate sensible heat flux as they integrate across a depth of the boundary layer. If this depth exceeds the height of the internal boundary layer then sensible heat flux will be underestimated.

The temperature method is based on Monin-Obukhov similarity theory which predicts a relationship between the standard deviation of temperature measured at a point and the sensible heat flux. Tillman (1972) showed that for an unstable surface layer the sensible heat flux and momentum flux can be derived from the standard deviation of temperature σ_T, and skewness of temperature S_T derived from experimental data. Following Tillman (1972) the conventional Obukhov (1971) stability parameter can be estimated as:

$$\frac{z-d}{L} = -A\exp(BS_T)$$

Equation 3.3

and subsequently the sensible heat flux:

$$\frac{H}{\rho c_p} = \left[\left(\frac{\sigma_T}{C_1}\right)\left(\frac{kgz}{\overline{T}}\right)\frac{\left[C_2 - \frac{z-d}{L}\right]}{-\frac{z-d}{L}}\right]^{\frac{1}{2}}$$

Equation 3.4

where z is the measurement height, d the displacement height and $\overline{T}$ the mean observed temperature. A, B, C_1 and C_2 are all experimentally derived parameters with values 0.0137, 4.39, 0.95 and 0.05 respectively. The relationship is valid well into the forced convection range. However, the methodology breaks down for stable conditions, which often occur over snow cover. Although not a commonly used technique, this method has been applied elsewhere (e.g. Katul *et al.*, 1995; Lloyd *et al.*, 1991) but not over snow-cover. The method is sensitive to the displacement height, ideally the measurement height would be large relative to d, however d can safely be assumed to be zero over snow-cover.

To accurately determine σ_T and S_T requires rapid measurement of temperature, especially over low roughness snow surfaces where the eddy size will be small. Temperature was thus measured by a fast response fine-wire type E thermocouple (SCXSS-019E-6.75, Omega Manchester, UK), as used on the Mk II Hydra eddy correlation system (Shuttleworth *et al.*, 1988). A type E thermocouple was used as it gives the greatest millivolt response per unit temperature. The thermocouples

were sampled at 9.14 Hz with a CR10X datalogger (Campbell Scientific, Shepshed, UK). Processor and RAM restrictions prevented completion of processing to on-the-fly, raw data were therefore stored and post-processed into thirty minute averages. This restriction meant the system could only be run for four days without attention; measurements were therefore made on a campaign basis. Additional problems were encountered powering the system, which rapidly drained batteries and low-light limited the efficacy of solar panels.

Five fast response thermocouples were deployed during February 2003, three on snow at varying distances from an edge and two on snow-free surfaces at a height of 0.2 m. It was unknown whether such a system would be sensitive enough to differentiate between fluxes at the windward edge versus those at the centre, but this was part of the experiment. Subsequent data analysis shows the temperature variance method measures heat fluxes lower than those modelled for non-advective conditions. This raises the question of whether the measured fluxes are real. This is discussed further in **6.3.1**.

A pair of snow lysimeters were also deployed to measure evaporation from the snowpack. Advection of latent heat was assumed to be a minor process as all surfaces were expected to be a source of evaporation during melt. Lysimeters were thus located in the centre of a snowbed. The lysimeters consisted of plastic boxes approximately 0.5 m cubed carefully filled with blocks of snow cut from the surface and placed level with the surface of the pack. The boxes were weighed regularly with a precise balance (0.1 g), the difference between measurements equating to the evaporated mass and correspondingly latent heat flux. The snow lysimeters proved difficult to run as snow was regularly blown in and out of the boxes affecting the measurement. In addition, the lysimeters regularly increased in weight during the melt period, suggesting condensation despite net evaporation measured by the eddy correlation tower, these measurements were thus discarded as incorrect and the measurements abandoned. However, this appears to have been short-sighted as condensation is a key process driving ablation (Chapter 6).

Latent heat flux over snow-free ground was initially thought less important and is a more complicated process to measure, especially under frozen conditions when installing and running soil lysimeters is near impossible. Latent heat flux from snow-free ground was not measured.

3.3.2 TERRAIN AND VEGETATION MAPPING

Detailed terrain and vegetation spatial data for the study grid are required to develop redistribution parameterisations, to orthorectify the remote camera images and elucidate the processes controlling snow distribution. This study planned to make use of airborne LiDAR (Light Detection and Ranging) data supplied by the NERC Airborne Remote Sensing Facility. LiDAR would provide spatially expansive terrain and vegetation structure data based on first and last laser hits as well as response intensity information to build a map of the terrain overlaid with vegetation at sub 0.15 m resolution in the vertical and horizontal. Unfortunately, due to NERC ARSF technical difficulties these data were unavailable during this study.

In the absence of LiDAR, data for the Digital Terrain Model (DTM) were collected manually using a Differential Global Positioning System (DGPS, Trimble 5800, Trimble, California, USA) which provides high accuracy point elevation data. Data were collected across the survey grid only at approximately 5 m intervals at 0.01 m horizontal and vertical precision. A higher spatial resolution would have been preferred, but manpower restricted the possible resolution as to survey the gridded area at 5 m required a substantial undertaking involving 32 km of surveying. Data were collected by a combination of research assistants and STEPPS co-workers.

After trialling various interpolation algorithms with data subsets it was found that kriging produced the most realistic DTM.

Vegetation data were collected concurrently with the elevation data as part of an undergraduate research project (McCurrach, 2005). Vegetation communities were initially classified into 19 classes as the most abundant community within a 2 m radius. Data were reclassified into the four categories described in **3.2.2**, and mapped onto the 5 m DTM grid by nearest-neighbour analysis.

3.3.3 SNOW SURVEYING AND REMOTE SENSING

Measurements of the spatial and temporal variation in snow lie are critical to understanding the physical processes controlling spatial heterogeneity. A combination of survey SWE measurements and remotely sensed snow-cover data are used to elucidate these processes.

a) SWE Measurements

There are no universally accepted methods of measuring snow depth or density (Pomeroy and Gray, 1995) although there is an International Classification of Seasonal Snow (Colbeck *et al.*, 1990). The large degree of spatial variability and relatively lower variability in density meant that the best method involved point snow depth measurements and relatively fewer snow pits and gravimetric density measurements. Snow surveys were carried out across the survey grid (Figure 3-7), the repeat nature of the method allows direct comparison between surveys. Surveys were extensive (400 measurements) to estimate the bulk snow lie for the study site. A survey interval of 20 m was chosen as representative of the spatial extent of patches and large enough that a sufficient area could be covered in two days surveying. On the third day snow pit data were collected. Snow pits were dug in a typical drift. Snow strata were identified and classified according to the International Classification of Seasonal Snow (Colbeck *et al.*, 1990). An exact 1000 ml scoop was used to cut snow samples at regular 0.1 m intervals through the profile. These samples were then weighed. The bulk snow density is calculated as the average of these densities and the total SWE as the sum of their mass. Profile temperature and wetness were also measured at 0.1 m intervals using a digital thermometer (Fluke 51 Digital Thermometer and 80PK-5A piercing probe, Fluke UK Ltd, Norfolk, UK) and a dielectric moisture meter (Denoth, 1994; Denoth *et al.*, 1984; Frolov and Macheret, 1999).

b) Snow-cover Measurements

Snow distribution is monitored remotely using a combination of oblique automated digital cameras placed at the study site and large-scale satellite data from the MODIS (Moderate Resolution Imaging Spectroradiometer) daily 500 m resolution snow-cover product (Hall *et al.*, 2000).

The camera setup consisted of a pair of RDC365s (Figure 3-9) (MetSupport ApS., Copenhagen, Denmark). The setup consists of a weatherproof enclosure, power supply and Kodak DC3200 digital camera. The CCD resolution of the camera is 1344 by 971 pixels (1.31 Mega pixels). Daily images are stored as 24-bit RBG JPEGS (Kodak, 2000).

Figure 3-9: RDC365 Camera

Two camera positions were chosen to maximise the visible area of the study site (Figure 3-10). Camera A was placed to give an overview of the study site and Camera B was placed perpendicular to counter the bias introduced by snow drifts forming in the lee of the stepped topography. Camera locations were chosen by careful analysis of local topography, using the tools available in ArcInfo (ESRI, Redlands, California, USA), to give the most contiguous visible cover of the study site. Difficulties were encountered due to the complex landscape which meant many areas were shaded from view.

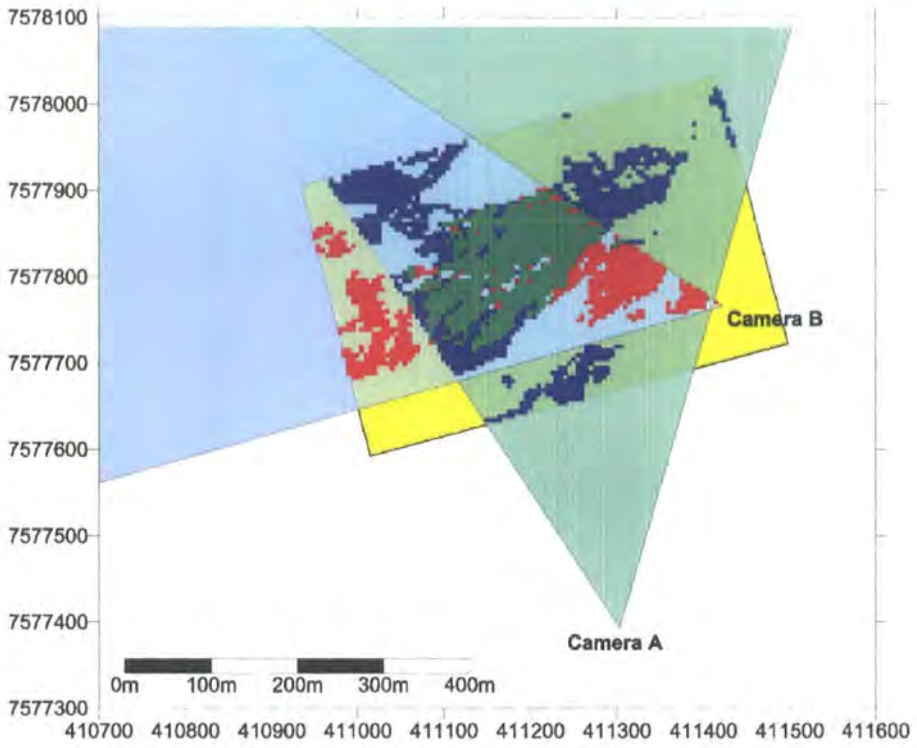

Figure 3-10: Footprint visible from two camera locations. Indicated in green are the areas visible from locations A and B, red is visible from B and blue visible from A. The potential visible area from A and B are marked with green and blue polygons respectively.

Daily images were initially quality controlled to exclude images with low cloud-cover or riming of the camera lens. To map spatial snow distribution orthorectification of the digital images was carried out using the freely available georectifying tool (Corripio, 2004; Corripio *et al.*, 2004) for IDL (Interactive Development Language, RSI, Boulder, Colorado, USA). Orthorectified images are interpolated to 5 m resolution to match the DTM (Figure 3-11b).

Images were manually assessed to check they contain snow before classification into snow and snow-free. Hinkler *et al.* (2002) derived a normalised difference snow index based on the red, blue green values in the image and used a thresholding approach to classify the images. This approach when used for the RDC365 images led to a poor classification in some cases, comparatively simple unsupervised k-means clustering of red, blue and green values proved more satisfactory and was used in subsequent batch processing. The process is outlined in Figure 3-11.

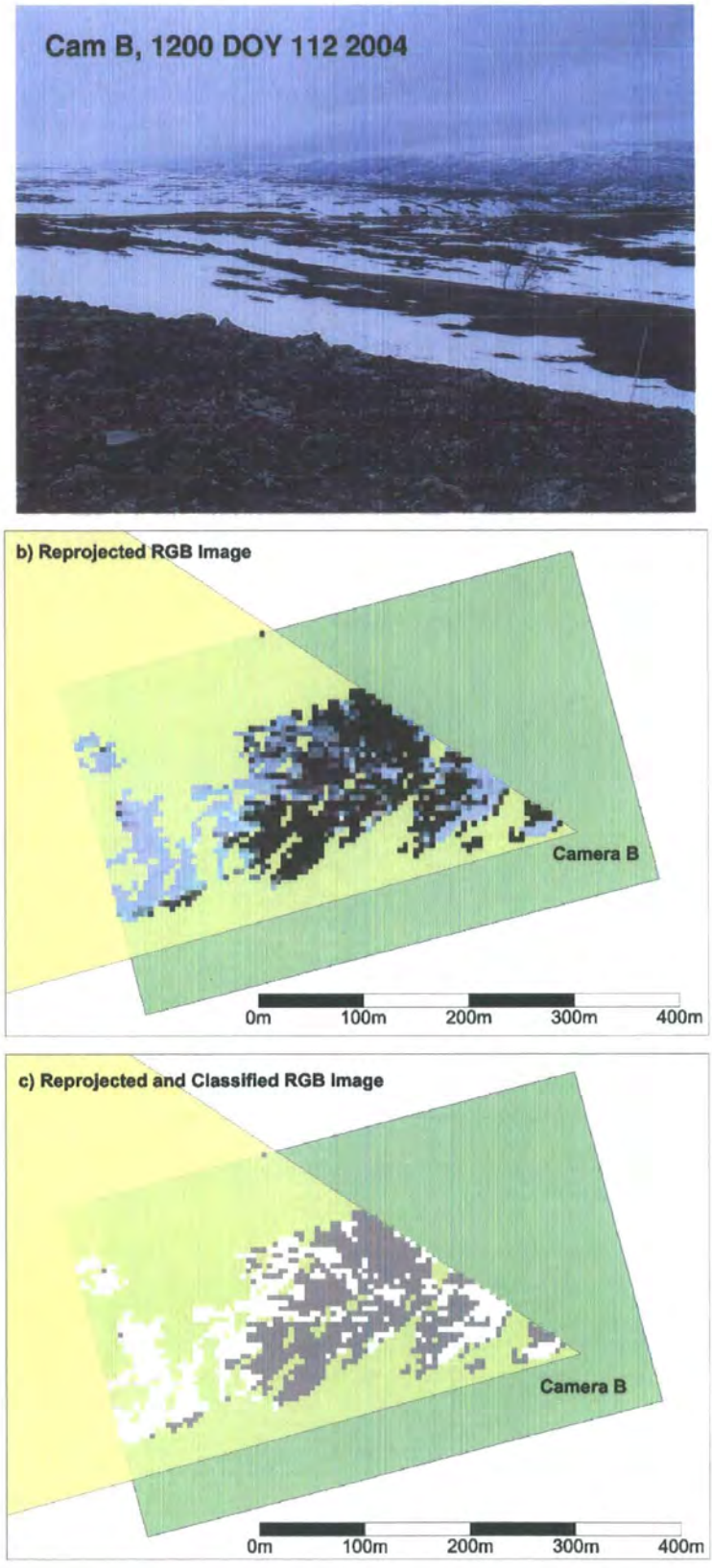

Figure 3-11: Reprojection sequence for an image from Camera B dated 22nd April 2004. a) Original RGB image, b) RGB reprojected image, c) Reprojected and classified RGB image. Snow is shown in white and bareground in grey. The green polygon represents the study site.

The aim was to use the classified maps of snow presence-absence to calculate landscape metrics of snow heterogeneity and compare to observed melt rates, however, the only level of processing that could satisfactorily be completed was to derive snow covered fraction. The DTM used was of too low a spatial resolution (5 m horizontal) to adequately resolve snow patches and the gaps in the viewable arears meant that no patch was fully visible.

One of the major problems in developing hydrological models based on small-scale observations is scaling between the measurement scale and the model scale, which is often substantially larger (Bloschl, 1999; Bloschl and Sivapalan, 1995). In an attempt to analyse the relationship between the camera observations and the larger scale 500 m MODIS daily snow-cover products (Hall *et al.*, 2000) were used to derive snow covered fraction over 10, 50 and 250 km gridboxes (meso-scale, RCM and GCM scale gridboxes) centred over the study site, the larger scale approximating the HadCM3 GCM gridbox at the study site latitude. Figure 3-12 shows the MODIS product for 27th February 2004 corresponding to the first snow survey. The main problem in using the MODIS data is the coverage of cloud experienced during the winter. In calculating snow covered fraction cloud cover was ignored if less than 25% of the box.

Data from these analyses are presented in Figure 4-15.

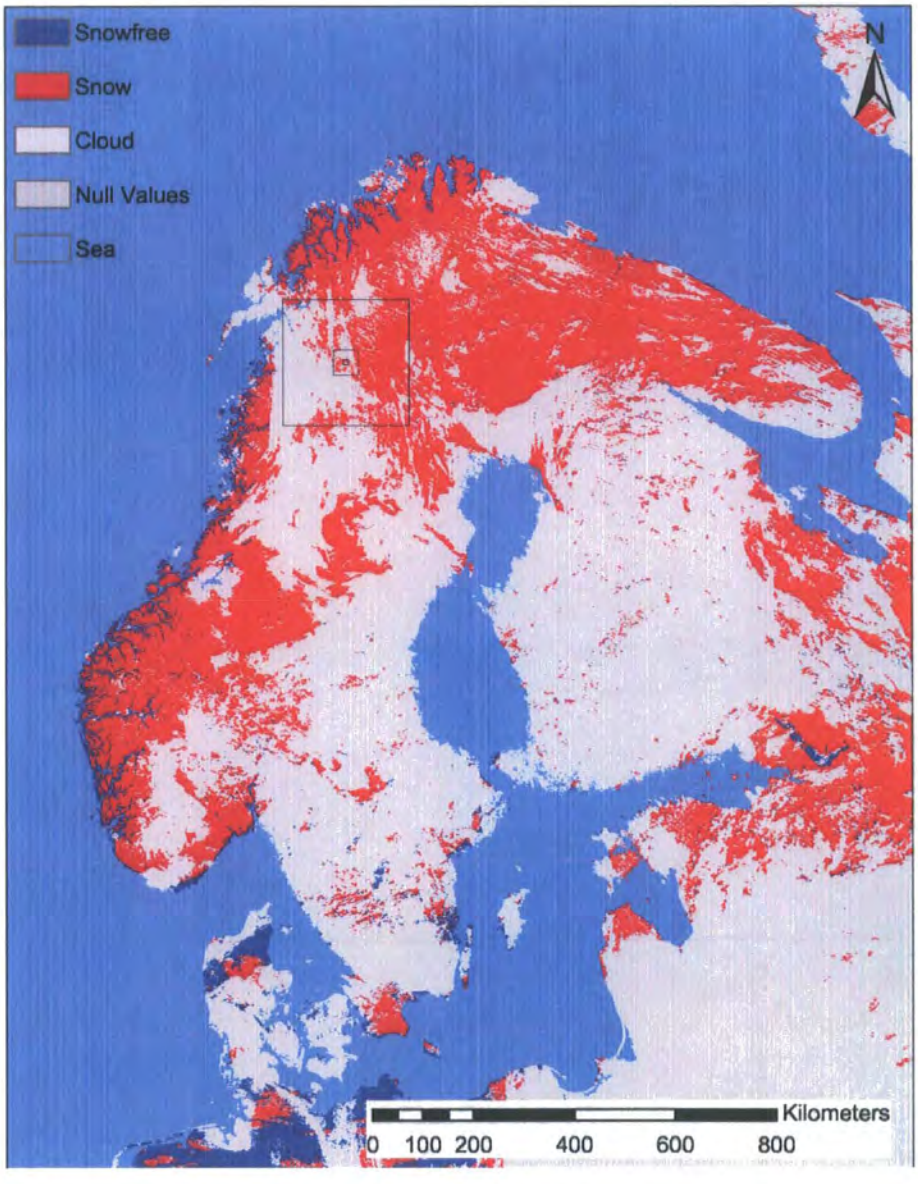

Figure 3-12: MODIS Snow-cover mapped for Scandinavia for 27th February 2004. (Hall *et al.*, 2000). Polygons indicate location of study site and area over which snow covered fraction is derived.

c) *Albedo Measurements*

Albedo measurements were made across the survey grid using a portable albedometer constructed from a pair of collimated SKS1110 pyranometers (Skye Instruments, Powys, UK) connected to a Campbell Scientific CR10 data logger. The albedometer was collimated to a field of view of 30° to give precise local measurements of albedo. Measurements were only taken during complete cloud cover to avoid errors associated with direct radiation in a collimated system.

3.3.4 VALIDATING NUMERICAL SIMULATIONS

An important part of numerical simulation is the use of a robust method for evaluating model performance given the varied modelling aims of this study. The correct choice of performance indicator is dependent on the application and nature of the data and as result is subjective (Davis *et al.*, 2001). For instance given a spatially distributed snow accumulation model, the modelling aim could be threefold: (i) model the location and depth of a snow drift, (ii) model the variation in snow depth across the landscape, and (iii) model the snow covered area, or any combination of the above. The correct choice of performance indicator would be different in each case. In some cases it would be inappropriate to use a measure of model performance due to fundamental differences in the scale of the simulated and validation data (Bloschl, 1999; Bloschl and Sivapalan, 1995).

In this study three performance indicators are used to evaluate continuous data, and a single indicator for classified data.

a) *Continuous Data*

Commonly found in hydrological model applications is the use of linear least-squares regression to evaluate model performance. This approach fails on a number of accounts. Principally the method fits a relationship between the prediction and observations that is not necessarily a 1:1 fit between the model and observations. Secondly the method minimises the error in the model, and assumes the observations are error-free.

A more appropriate method is to use the root of the mean squared error (RMSE) between the model prediction (P) and the observation (O). This is a useful

approach as the units of RMSE are the same as the original data aiding interpretation:

$$RMSE = \left[\frac{1}{N} \sum_{i=1}^{N} (P_i - O_i)^2 \right]^{\frac{1}{2}}$$

Equation 3.5

This method emphasises any large differences between the model prediction and observation.

Alternative approaches include the Nash-Sutcliffe (N-S) index of model efficiency (Nash and Sutcliffe, 1970). This enables the efficiency of a model to be defined as the proportion of the initial variance accounted for by that model. An r^2 value of 1 indicates perfect agreement, a value of 0 indicates the model is no better than using the mean observation, and a negative value suggests the model prediction is worse than assuming the mean of the observation, providing the mean is known:

$$r_{NS}^2 = 1 - \frac{\sum_{i=1}^{N} (O_i - P_i)^2}{\sum_{i=1}^{N} (O_i - \overline{O})^2}$$

Equation 3.6

The Nash-Sutcliffe index was developed to access the ability of hydrological models to predict river discharge where the observation variation can be large, and the aim is for the model to correctly predict the magnitude and timing of a discharge event.

A similar approach is the Willmott index of agreement (*d*) (Willmott, 1981). The index is similar to the N-S in that it relates the variation in the observations with the model predictions, but additionally includes the variation between the model prediction and the observed mean. The Willmott d statistic thus includes an assessment of the potential error in the observation data. An index of 1 indicates complete agreement and 0.0 indicates complete disagreement. The index thus accounts for the ability of the model to simulate the variation in the observed data:

$$d = 1 - \frac{\sum_{i=1}^{N}(P_i - O_i)^2}{\sum_{i=1}^{N}\left[\left(P_i - \overline{O}\right) + \left(O_i - \overline{O}\right)\right]^2}$$

Equation 3.7

The Willmott d statistic will give a higher value of model performance than the N-S index if the model correctly predicts the magnitude of a discharge event, but not the timing.

The value of these performance statistics depends on their ability to aid interpretation. Of the three statistics described the easiest to interpret is the RMSE, which can be interpreted as the absolute error in the model and observational data. The RMSE statistic is most relevant to the model studies in Chapters 6 and 7, which are mainly concerned with the absolute error in model simulations. The Nash-Sutcliffe r^2 and Wilmott d statistics commonly tend towards high values, despite unacceptably large RMSEs. However, the Nash-Sutcliffe r^2 and Wilmott d statistics are given for completeness and aid in the gauging of whether the timing and magnitude of processes is captured in model simulations.

b) Classified Data

Cohen's Kappa statistic (Cohen, 1960) is an index of agreement for classified data. The statistic relates the ability of a model to correctly assign a classification to a data set through the number of correct classifications (C) to the expected occurrence through chance (E). A κ value of 1 indicates perfect agreement between the model and observations, and a value of 0 complete disagreement:

$$\kappa = \frac{C - E}{N - E}$$

Equation 3.8

Chapter 4

Snow Distribution

4 Snow Distribution

4.1 Introduction

Arctic tundra snow-covers are generally shallow and spatially very variable (Pomeroy *et al.*, 1998; Sturm *et al.*, 1995). They are associated with complex topography subject to periglacial processes and a diverse vegetation community. Climate conditions are generally freezing and windy. In an attempt to develop a snow-cover classification, Sturm *et al.*, (1995) describe tundra snow-cover as 'a thin, cold, wind-blown snow,' with a maximum depth of 0.75 m and consisting of a basal layer of depth-hoar overlain by multiple wind slabs.

Observations of snow depth were made across a pre-defined 400 point grid at regular 20 m intervals (**3.3**). Four surveys were made across the period spanning peak accumulation and the onset of melt, from late February to early May in 2004 and late March in 2005. In addition, measurements of the snow profile were made in conjunction with the depth surveys. Additional measurements of surface albedo (ratio of reflected shortwave radiation to incident) and the temperature at the interface between snow and soil were made in 2005.

This chapter outlines the spatial and temporal variability in observed tundra snow-cover across the study domain, in addition to remotely sensed satellite snow-cover products at the resolution of regional and global atmospheric models.

4.2 Snow Surveys

Snow depth proved to be highly variable across the gridded domain, varying from snow-free to drifts up to 2 m in depth. Maps of the variation in snow depth are given in Figure 4-3 and Figure 4-4a, and summary data are presented in Table 4-1. Peak accumulation mean snow depth is of the order of 0.3 m or 120 kg m^{-2} SWE occurring at a certain point between the surveys made on the 28th March and 15th April 2004. The onset of the main ablation period occurs during mid-April and the deep drifts last through to the summer solstice, although it should be noted the winter consists of multiple short melt events. Long term data (1914-2004) from ANS shows a December to February mean snow depth of 0.35 m in the birch

forest. Data from 2004 show mean depths of 0.42 and 0.33 m for February and March 2004 (Kohler *et al.*, 2006). Snow density information is only available at ANS between 1914 and 1929; these data show an increasing density between October and May, with a typical density of 250 kg m^{-3} (Kohler *et al.*, 2006). The accumulated snow-cover during 2004 on the tundra appears to be substantially deeper than that accumulated in the birch forest at a lower altitude.

These snow-covers are highly variable with a coefficient of variation (standard deviation divided by the mean) of the order of 1. As the snow season progresses, snow-cover gradually becomes patchy as the shallowest snow melts out first. Initially, the snow-free patches remain small, but gradually enlarge until they interconnect and the snow forms the patches in the snow-free area. This can be seen in the transition from Figure 4-3a to d and Figure 4-1. This leads to an apparent increase in mean snow depth and decrease in the variation as the shallow snows ablate earlier.

Figure 4-1: Study site viewed from the North with a telescopic lens. Image taken on 13th April 2004 after a short melt period. Image shows distinct patchy nature of snow-cover and the low albedo of the birch forest when viewed from a low zenith angle.

Measurements show the heterogeneity to be higher than the commonly assumed values in large-scale hydrological models. Liston (2005) suggests a coefficient of variation of 0.4 for global applications in tundra regions, and Pomeroy *et al.*, (1998) suggest 0.31 and 0.22 for moderate topography in 'tundra' and 'shrub tundra' regions. However, it must be noted that these suggested values are intended for global application and the classifications of 'tundra' are subjective.

Table 4-1: Descriptive statistics of spatial variation in snow-cover

	Survey 1	Survey 2	Survey 3	Survey 4	Survey 5
Date	27/02/04	28/03/04	15/04/04	29/04/04	28/03/05
Bulk Snow Density (kg m^{-3})	399	399	457.3	457.3	413.1
% Snow-cover	100	100	70	37.5	84
Maximum Snow Depth (m)	1.78	1.53	1.77	1.78	1.92
Mean Snow Depth (m)	0.30	0.26	0.44	0.59	0.39
Standard Deviation Snow Depth (m)	0.34	0.27	0.38	0.36	0.39
Mean SWE (kg m^{-2})	117.8	102.5	201.3	270.5	162
Area Weighted Mean Snow Depth (m)	0.30	0.26	0.3	0.22	0.32
Area Weighted Mean SWE (kg m^{-2})	117.8	103	121	101.7	135.9
Coefficient of Variation	1.12	1.06	0.87	0.6	1.13

The landscape scale variation in snow-cover occurs well before snowmelt begins and is due to wind redistribution of snow. The exact patterning is a function of the interaction between windflow across the topography and surface roughness. Roughness is affected by micro-scale topography and vegetation. Rough surfaces such as tall shrubs collect and retain snow more easily than short vegetation under equal wind stress. The snow-free patches correlate with areas of wind scour due to flow compression, convergence and low roughness. Snow drifts correspond to areas of high roughness, flow divergence and flow separation.

The observed pattern of snow distribution is therefore closely associated with the distribution of roughness elements and the complex topography (**7.2**). Figure 4-2

shows the extent to which thus can be true for complex topography consisiting of ridges and hollows (Figure 3-4). The ridge shown was initially covered with a shallow snow-cover to the windward side and a deep drift on the lee, a short melt event has exposed the dark rock leading to the strong contrast in surface albedo. The vegetation is also closely associated with the variation in topography, with large shrubs (*Betula and Salix spp.*) occurring in the sheltered hollows, and the exposed ridges being largely free of vascular plants. The rest of the domain is dominated by short evergreen shrubs (*Empetrum spp.*) intermixed with woody deciduous shrubs (*Betula nana*) and grass-like sedges (Figure 3-6).

Figure 4-2: The influence of topography on snow distribution. The thin shallow snow that covered the windward side of this ridge has melted earlier than the deep drift on the lee side. Image taken on 12th April 2004.

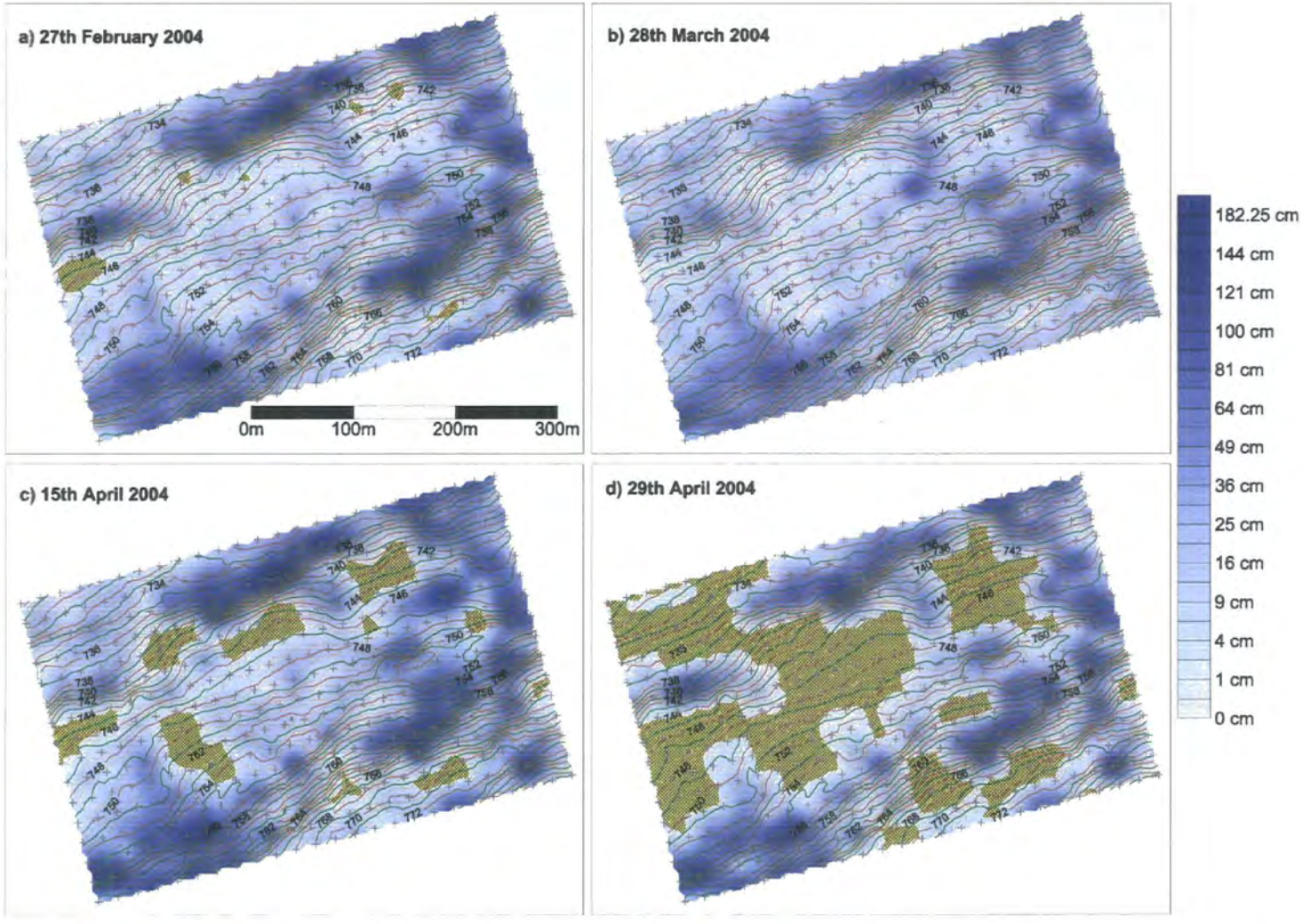

Figure 4-3: Spatial variation in snow depth during 2004. Sample locations are marked with crosshairs. Yellow hatched areas represent krigged snow-free patches. Contours are at 0.5 m intervals.

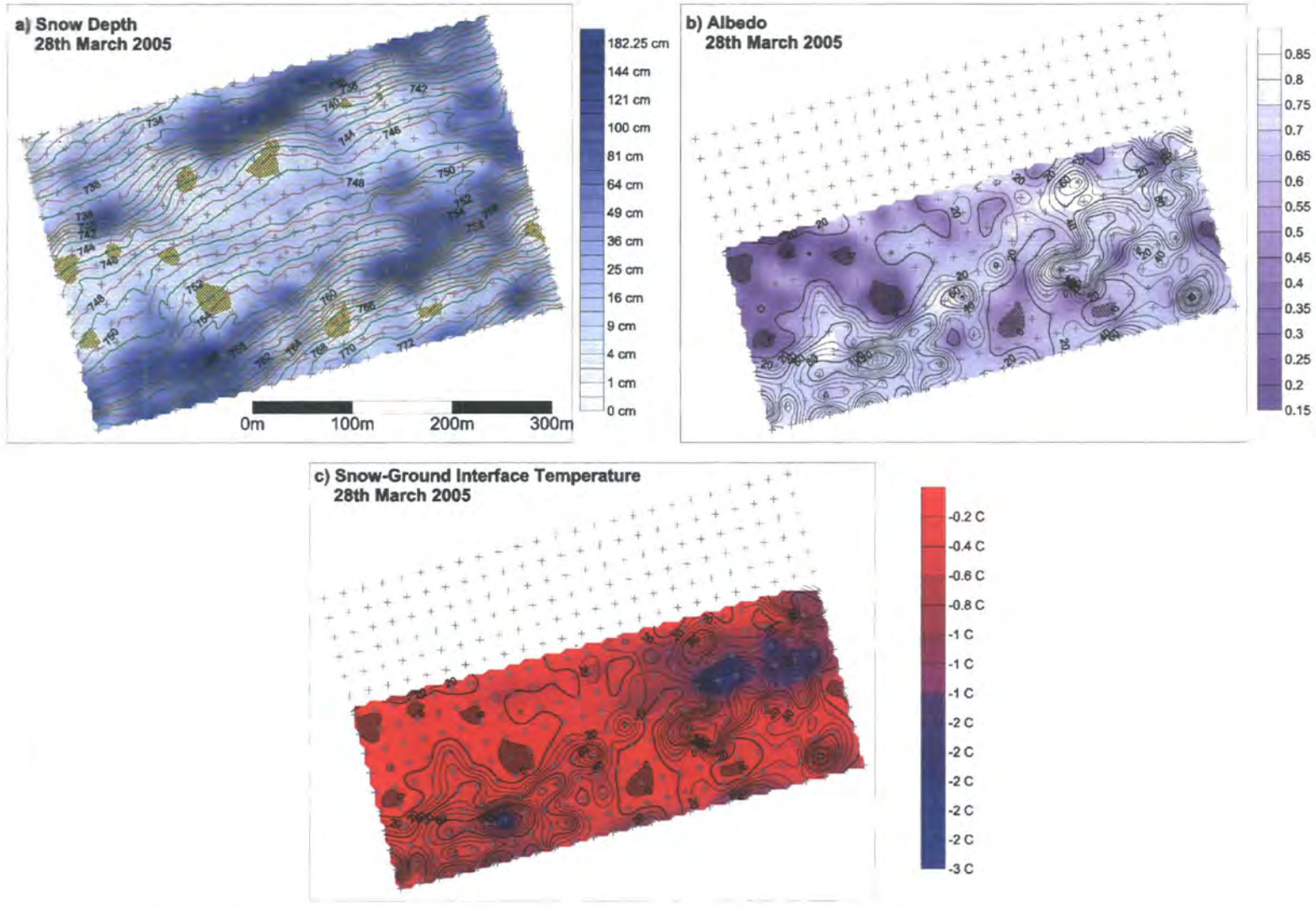

Figure 4-4: Spatial variation in snow depth, albedo and snow-ground interface temperature during 2005. Sample locations are marked with crosshairs. Snow-free patches are represented by hatched patterning. Contours are at 0.5 m intervals in figure a. Figures b and c are contoured with snow depth at 0.1 m intervals.

4.2.1 INTER-SURVEY SPATIAL VARIABILITY

The surveyed snow-cover has been shown to be highly spatially variable, and it has been suggested that the patterning is a function of the interaction of windflow and surface roughness. In which case, it is reasonable to expect a similar pattern of snow distribution within a season and also between seasons.

Correlation analyses of snow depth tied pairs suggest that the inter-survey variability is low (Table 4-2). This is expected to be the case for the surveys completed in a single season. However, the correlation between peak accumulation in 2004 and 2005 (Survey 2 and Survey 5) is also extremely high ($n=305$, $r = 0.893$, $p<0.001$) despite a 15% greater winter snow accumulation in 2005. Although this is just two seasons data, the suggestion is that the processes controlling snow distribution are similar between seasons.

Table 4-2: Correlation Matrix of snow surveys

		Survey 2	Survey 3	Survey 4	Survey 5
	n	362	273	142	329
Survey 1	r	0.935	0.903	0.842	0.929
	p	<0.001	<0.001	<0.001	<0.001
	n		248	118	305
Survey 2	r		0.847	0.737	0.893
	p		<0.001	<0.001	<0.001
	n			140	264
Survey 3	r			0.856	0.867
	p			<0.001	<0.001
	n				142
Survey 4	r				0.778
	p				<0.001

4.2.2 SWE SPATIAL CONTINUITY

Statistically these snow-covers have been shown to be spatially heterogeneous. However, the problem remains of the process length scale of the heterogeneity and whether there is a directional variation in it. This is important should the shape and distribution of snow patches affect their interaction with surrounding snow-free ground. Furthermore, the consistency between the process scale for snow-cover and

elevation potentially provides a way of parameterising snow patchiness from elevation data. The following analysis proves to be invalid for topographic indices without independent observations. The process scale is often estimated as the correlation length of a variogram (Bloschl, 1999). The process scale is therefore a measure of the average distance over which a variable is correlated. Alternative approaches include the use of fractal geometry. Shook and Gray (1996) used the length scale at which snow patches switch from fractal to random behaviour to define process and patch scale.

Experimental variograms were fitted to the SWE data from 28th March 2004, together with an additional 250 data points collected on a 5 m nested grid on 29th March 2004, and the 25,000 DGPS elevation observations. Data pairs were grouped into 10° directional bins and 10 m lag bins and the variance calculated as the mean of all pairs in the lag and directional bins (Isaaks and Srivastava, 1989):

$$\gamma_e(h,\theta) = \frac{1}{2N(h,\theta)} \sum_{(i,j)} \left(SWE_i - SWE_j\right)^2$$

Equation 4.1

Where h is the lag, θ is direction and i and j are the data pairs in the lag bin. The resulting variograms for elevation and SWE are plotted in Figure 4-5 and Figure 4-6 respectively.

The smoothly varying elevation variogram in Figure 4-5 suggests the process scale is very large for elevation. This is not surprising considering the large-scale nature of topography. However, there is no evidence of small-scale discontinuity in elevation, which could be expected to be a function of the distribution of ridges and hollows in the landscape. There is a large degree of anisotropy in the data, suggesting aspect is a strong control on variation. The axis of greatest variation coincides with the hillslope north-westerly aspect (Figure 4-5 and Figure 4-7). SWE shows a great deal of variability, implying a process scale less than 300 m. Particularly evident is the lack of correlation between elevation and SWE, the variability in SWE is thus largely independent of elevation data. There is an indication of co-variation in SWE and elevation with direction, particularly in the direction of aspect and tangential aspect (Figure 4-7). The process scale of SWE

may therefore be independent of elevation, but not necessarily independent of aspect and topography. Similarly, SWE shows no variability associated with prevailing wind direction, and it is appropriate to conclude prevailing wind direction has no effect on the isotropy of SWE or process scale.

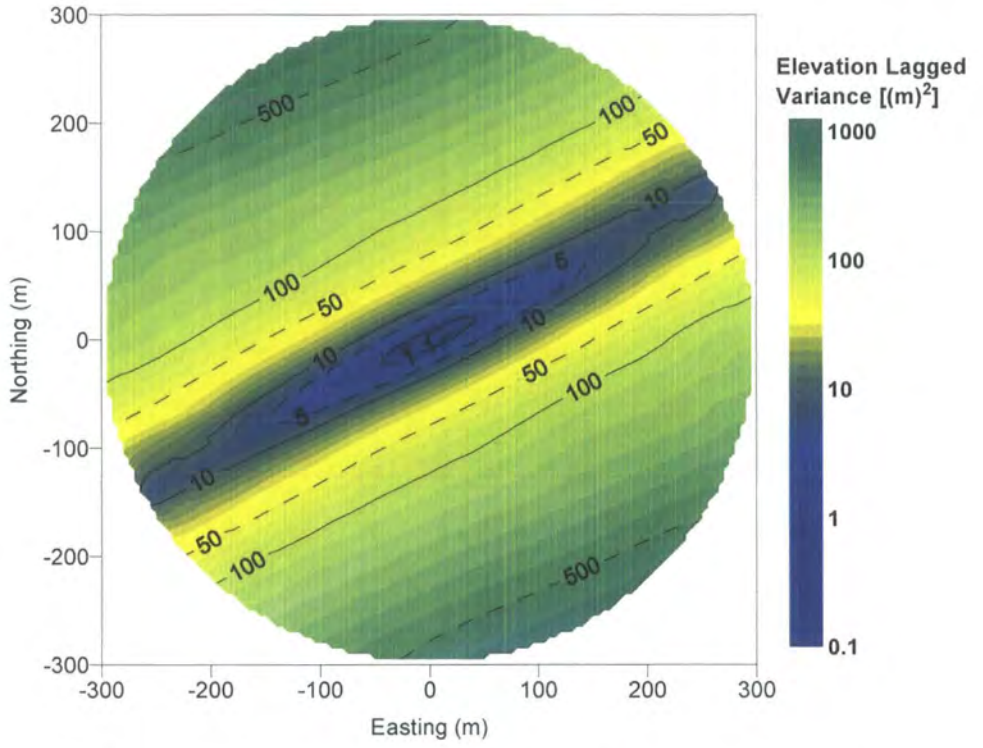

Figure 4-5: Polar plot of lagged elevation variance. Lag Distance is distance from origin and direction is equivalent of compass points.

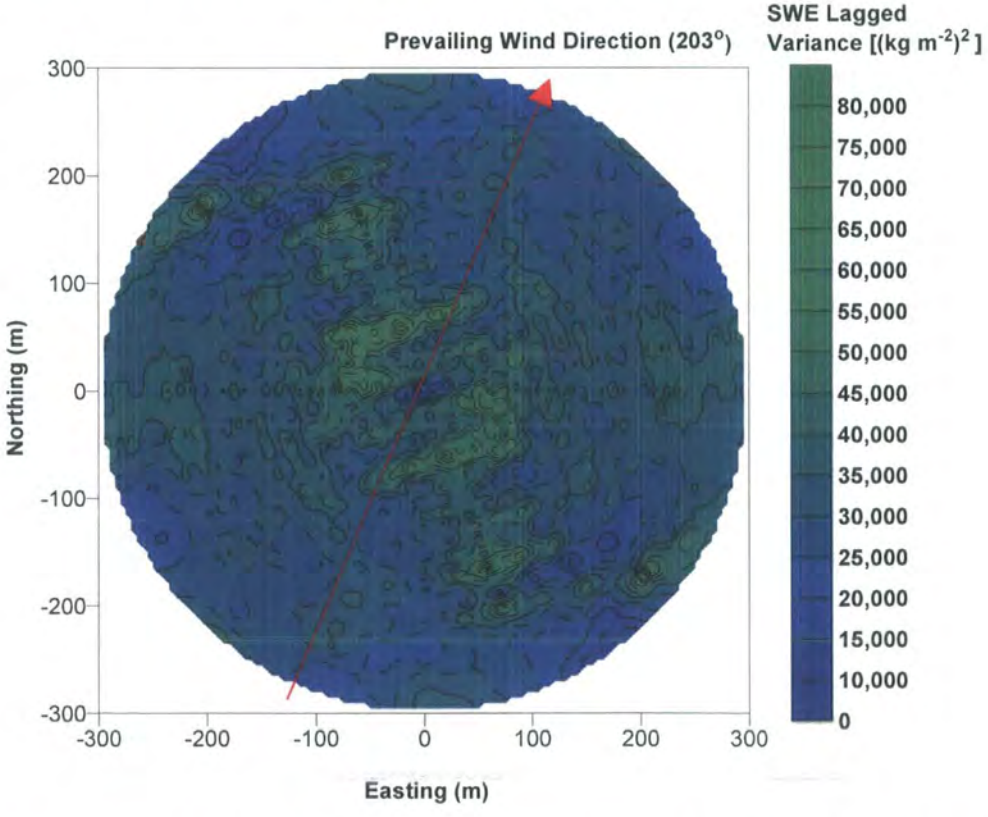

Figure 4-6: Polar plot of lagged SWE variance. Lag Distance is distance from origin and direction is equivalent of compass points.

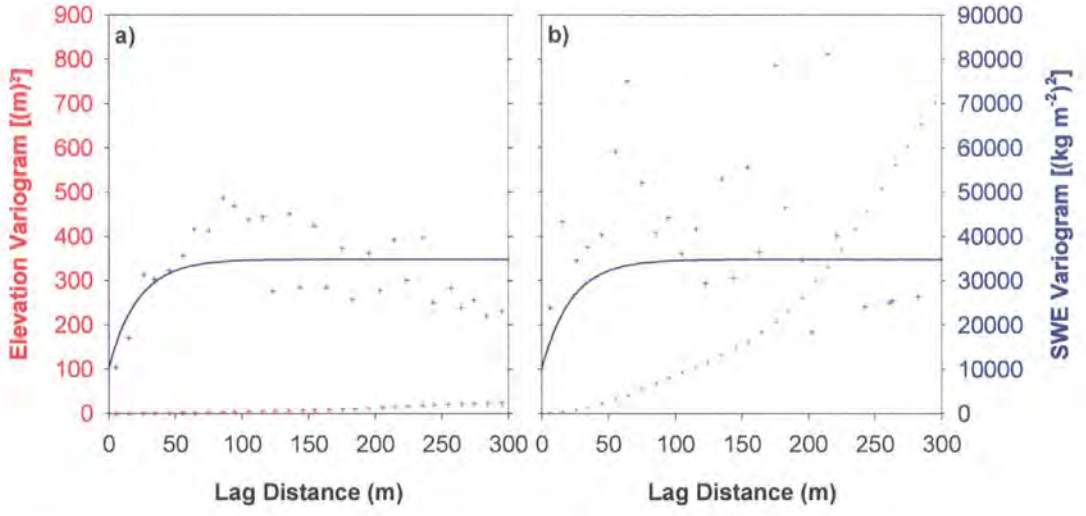

Figure 4-7: Semi-variance of SWE and elevation for (a) 30 and (b) 110 degrees

To infer a process scale affecting SWE requires some simplification. SWE is considered isotropic, and an analytical variogram fitted to SWE, from which population statistics can be drawn (Bloschl, 1999). An exponential variogram is commonly used in hydrological applications (e.g. Petrone *et al.*, 2004; Western *et al.*, 1998a, b) and is appropriate to use here:

$$\gamma_e(h) = \sigma_0^2 + \left(\sigma_\infty^2 - \sigma_0^2\right)\left[1 - \exp\left(\frac{-h}{\lambda}\right)\right]$$

Equation 4.2

where λ is the correlation length, and σ_∞^2 is the spatial variation independent of autocorrelation, and σ_0^2 is sub-lag scale (<10 m) variation or systematic error. The chosen model was numerically fitted to the experimental variogram using an interactive geostatistics package (Surfer 7.0, Golden Software Inc, Colorado, USA).

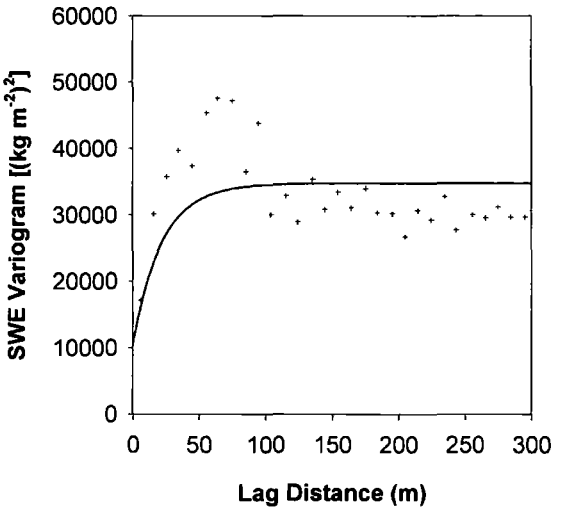

Figure 4-8: Isotropic SWE experimental variogram (cross-hairs) fitted with exponential analytical variogram (solid line).

Figure 4-8 shows the fitted analytical variogram (Equation 4.2), with a process scale of 22.2 m. There are clearly problems in the fit of the analytical variogram, and these are associated with the underlying assumption of a rise in variance associated with the scale of process to a stationary spatial variance. Perhaps more appropriately Figure 4-8 can be interpreted in terms of the patch size, the greatest variation in SWE is at a lag of approximately 62 m, which is the effective patch size. This can be seen in terms of probability; at a lag of 62 m the probability of being in a different patch of snow is at its greatest. This corresponds to the fitted variogram, which gives a length scale of 66.6 m at 95% of the spatial variation. Beyond this length the variogram is stationary; the probability of being in another patch is independent of lag distance. The suggestion is thus of an unorganised distribution of patches, or a random distribution. Shook and Gray (1996) observed a process scale of 20 to 100 m for snow dune (arising out of chaotic behaviour rather than topography) formation in the Canadian prairie. Subsequently, Shook and Gray (1997b) used snow covered area curves, the observed patch scale and observed random behaviour to generate realistic distributed snow-covers. This analysis suggests that a similar approach can be taken for tundra snow-covers.

The suggested sub 10 m standard deviation in SWE from the fitted variogram is 102 kg m^{-2} or the equivalent of 0.22 m of water, the implication here is the existence of significant micro-scale processes that are ignored in the scale of measurement employed in this study.

The spatial standard deviation is 186.5 kg m^{-2} or the equivalent of 0.41 m of water, compared to a sampled standard deviation of 119.3 kg m^{-2} or the equivalent of 0.26 m of water. The mean, however, theoretically remains unchanged, as the extent 400 m is large compared to the patch size (Bloschl and Sivapalan, 1995).

4.3 Snowpack Profiles

Following fresh snow deposition, snow crystals metamorphose rapidly due to vertical vapour transport driven by temperature gradients in the snowpack, and compact due to settling of grains, wind packing and melt-freeze cycles of liquid water (Langham, 1981; Pomeroy and Gray, 1995; Sturm and Benson, 1997; Sturm *et al.*, 1997; Sturm and Johnson, 1992). Typically, this leads to an increased density with time and a stratification of the snow profile. Figure 4-9 shows a typical snow profile during the mid-winter period. Generally, the snow profile consists of two layers; large heavily metamorphosed cup crystals (Figure 4-11) (typically 2 - 3 mm in diameter) at the base of the snowpack, overlain with smaller densely packed wind fragmented particles (typically 0.5 - 1 mm in diameter). They appear on the International Classification of Seasonal Snow on the Ground (ICSSG) as 5a and 5b, and 2b respectively (Colbeck *et al.*, 1990). Often, although not in this example, discontinuous thin layers of ice (typically 5 - 30 mm) are found. These form when advancing liquid water fronts freeze and are spatially discontinuous existing for less than a metre. Later in the season, as the pack begins to melt, large wet crystals form and are classified as ICSSG 6a and 6b.

Observed snow densities are generally high with bulk densities around 400 kg m^{-2}. Depth-hoar layers are on average much less dense than the wind-packed layers with bulk densities of the order of 325-375 kg m^{-3} and 400-450 kg m^{-3} respectively. These correspond well to a theoretical upper limit of 350 kg m^{-3} for heavily

metamorphosed crystals such as depth hoar (Sturm and Johnson, 1992), and an overall suggested value of 380 kg m^{-3} for tundra environments (Sturm *et al.*, 1995).

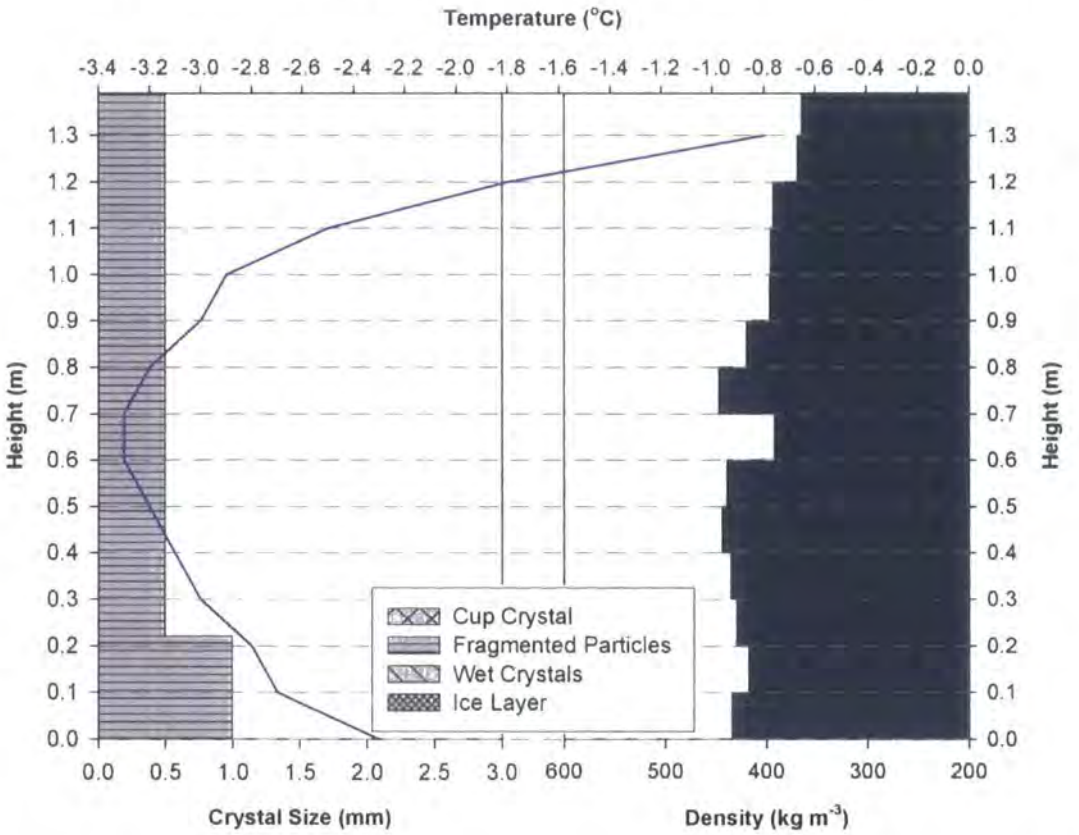

Figure 4-9: Snow Profile 31st March 2005. Ice layers are indicated by a horizontal hatched bar. Crystal size is not given for ice.

Snow crystal metamorphism occurs when water vapour is transported through the snowpack. Crystals can either accumulate mass or ablate, or a combination of both, allowing crystals to grow and completely alter their shape (Sturm and Benson, 1997). This explains the development of the large cup crystals, or depth hoar, seen in virtually all the snow profiles. The overlying crystals are much smaller; having been transported by the wind, they have been shattered by the turbulence and collision during saltation. This explains their fragmented nature.

The observed stratification of snow-cover is comparatively simple compared to observations made in the Alaskan Arctic (e.g. Sturm and Benson, 2004; Sturm and Benson, 1997; Sturm *et al.*, 2001a), which suggest regular layering of depth-hoar and wind shattered crystals. This may be indicative of the influence of wind on the Abisko snow-cover. High winds prevent fresh snow from settling and quickly redistribute the snow to form deep layers of wind packed snow.

The transport of water vapour is driven by temperature gradients between layers in the snow and soil. The temperature gradients are created by radiative cooling of the surface, cool air temperatures, stored heat in the soil and the release of energy during fusion. Observed gradients in the snow profiles tended to be greatest at the interfaces between the snow and soil, and the atmosphere and snow. These gradients are greatest, generally, in seasonal snow-covers due to their predominantly shallow nature.

The temperature gradients can be considerable; values as great as 60°C m^{-1} were commonly measured at the base of drifts (Figure 4-10). The gradients are generally greatest at the snow-soil interface and combined with the fact that deep snow has been buried longer explains the metamorphosis to depth hoar occurring at depth. The mass transported in the form of vapour can also be considerable. Sturm and Benson (1997) reported soil moisture contributing up to 5% of the mass balance and the deposition of isotopically light soil water up to 0.5 m higher in the pack.

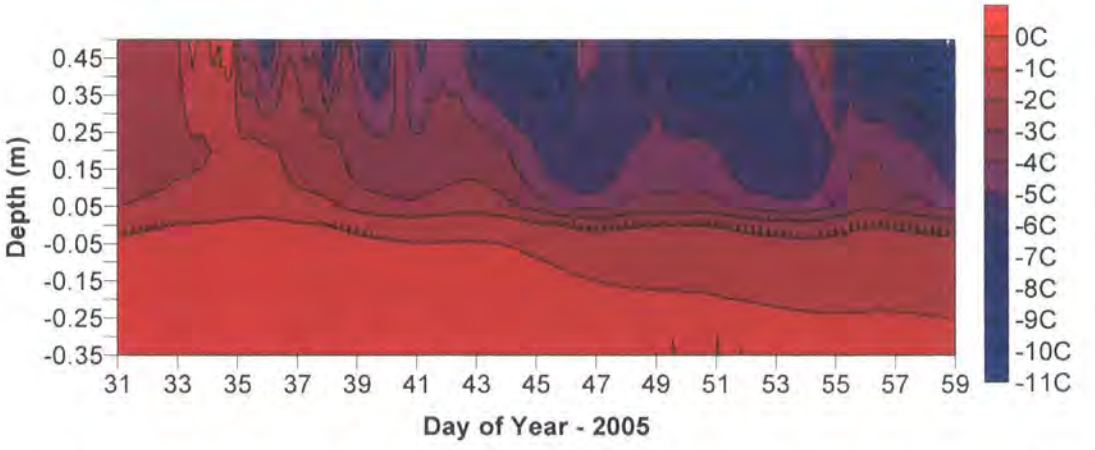

Figure 4-10: Temperature profile across the snow-soil interface. The upper boundary of 0.5 m snow depth represents a minimum depth of snow maintained throughout the charted period.

Crystal structure, size and bonding can all influence the thermal insulation properties of snow-cover (Sturm and Benson, 1997). The formation of large, hollow, poorly bonded, depth hoar crystals (Figure 4-11) can significantly alter the bulk thermal conductivity of snow with time, as depth hoar can be a factor of a half to a quarter less conductive as other snow of a similar density (Sturm and Johnson,

1992). The formation of depth hoar therefore acts to reinforce and maintain temperature gradients.

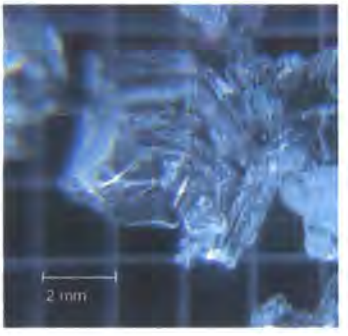

Figure 4-11: Photograph of a large cup crystal – ICSSG class 5a

Depth hoar formation is part of a mechanism suggested by Sturm *et al.* (2001a; 2005) by which deciduous shrubs increase their sub-nivean temperatures by facilitating vapour exchange.

Volumetric liquid water content (VLWC) was also measured in some instances, particularly in the ablation period (Figure 4-12). These measurements showed maximum volumetric liquid water at 8.5% which decreased with depth. This corresponds to a suggested volumetric capacity of 10%. The increase in VLWC above ice-lenses suggest they impede the flow of liquid water through the snowpack.

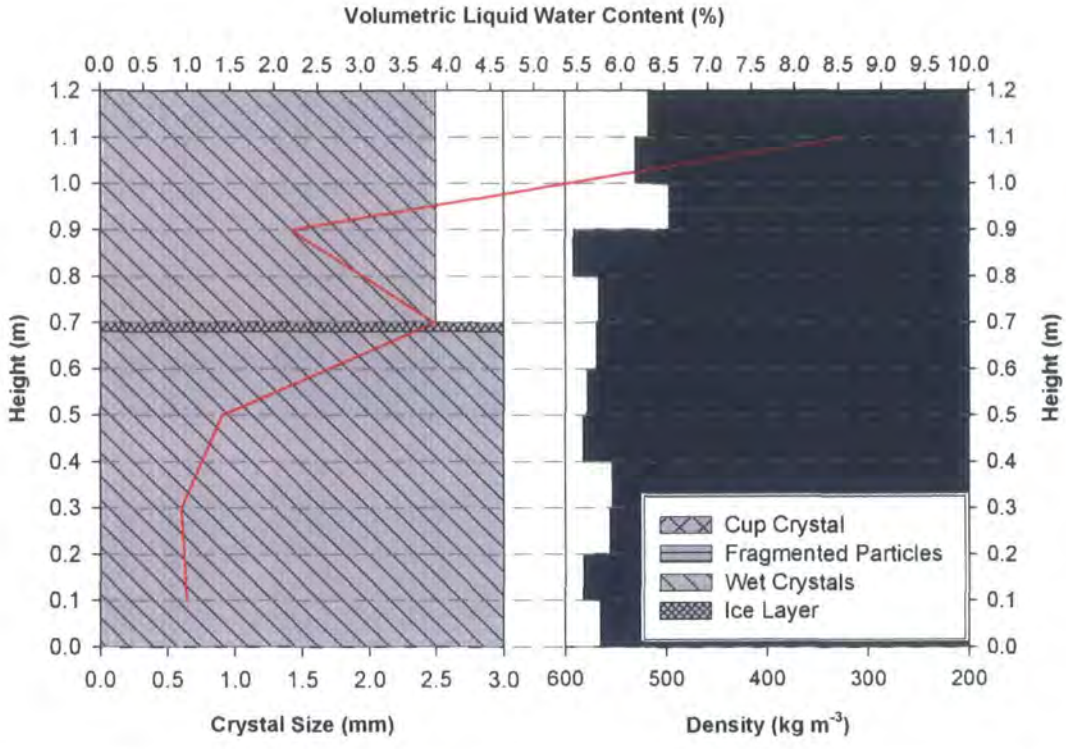

Figure 4-12: Snow Profile 6th May 2004. Ice layers are indicated by a horizontal hatched bar. Crystal size is not given for ice. Volumetric water content is shown in red.

4.3.1 TEMPORAL VARIATION

Observations of the temporal evolution of the snowpack were made over three winter seasons (Figure 4-13). In general, the trend is for the pack to become warmer and denser as it ripens towards the ablation period. Crystal evolution is clearly demonstrated in 2004 when the crystal structure shows dry metamorphism from fragmented particles to depth-hoar and a corresponding increase in density associated with settling and compaction of the snowpack. Wet metamorphism subsequently takes place and the snow pack structure becomes dominated by melt crystals. The large pre-melt increase in SWE (694 kg m^{-2} to 805 kg m^{-2}) is mainly a function of further snowfall settling to form a denser snowpack despite little change in depth (1.74 m to 1.76 m).

Inter-annual variation in density is low, with similar bulk densities at a given point in the season. The ripening of the snowpack appears to occur earlier in 2004 than 2003, indicated by the earlier formation of large wet crystals. The accumulated SWE shows some variability between years, with SWE lower in 2005 despite on average a deeper snowpack of equivalent density.

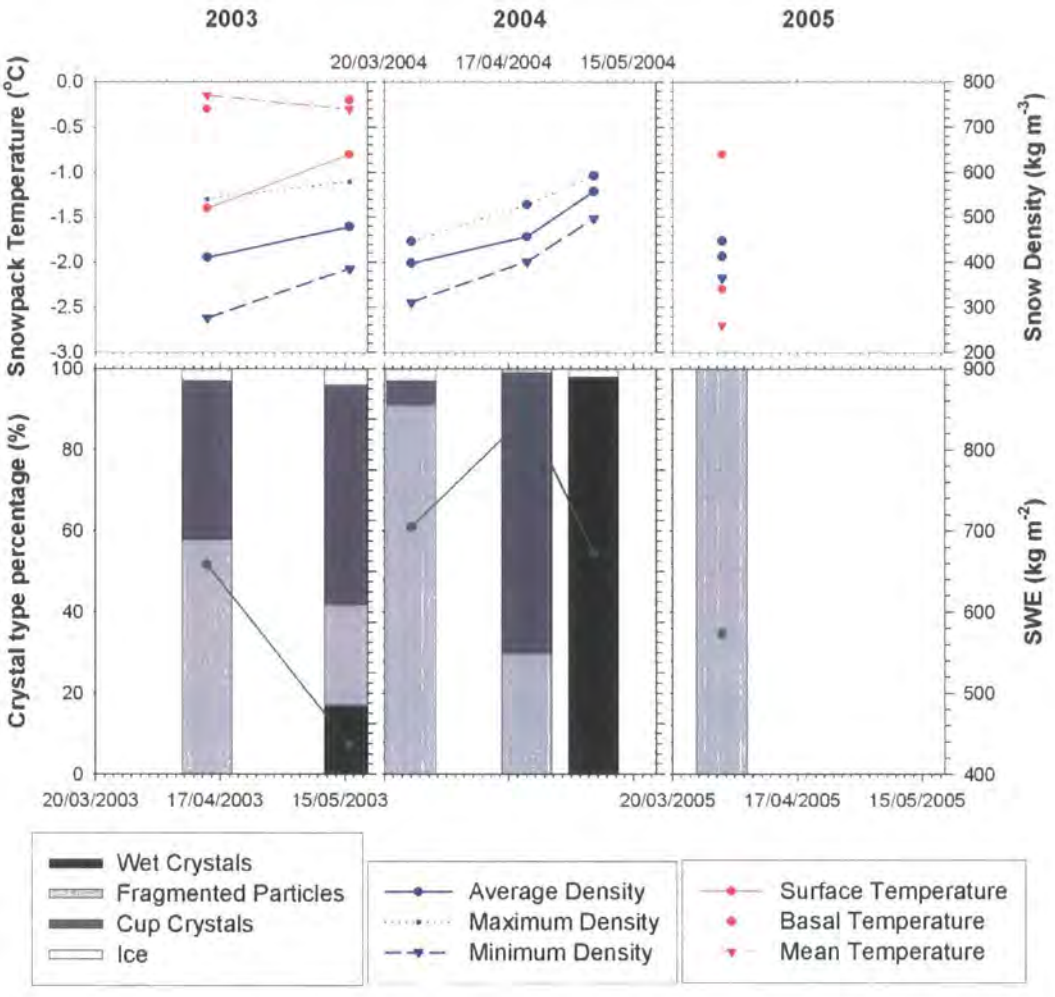

Figure 4-13: Temporal evolution of snowpack properties. Green markers shows total SWE.

4.3.2 SPATIAL VARIATION

In general, it can be assumed that the spatial variation in pack density is low in comparison to variation in depth (Pomeroy and Gray, 1995). To test this assumption three snow pits were dug across a snow depth gradient at approximately peak accumulation in 2003 (Figure 4-14 and summarised in Table 4-3). The profiles revealed some complex but not dissimilar layering. The most obvious difference is the formation of ice layers in the pack, which are variable in their number, depth and extent. The variation in ice layers partly contributes to the small variation in bulk density between profiles. The greatest difference in density (19.3 kg m^{-3}) occurs between the deepest (1.61 m) and shallowest (0.61 m) profiles, the deeper snow being denser. The increased density in the deeper snow can be associated with greater settling of the pack due to the greater overlying mass. In terms of snow water equivalent this leads to an error of less than 4% in assuming a

bulk density from the deep profile. If this is indicative of the spatial variation in density then the basic assumption made in the surveying methodology is safe.

Table 4-3: Summary of spatial variation in snow profile. 21st March 2003

	Profile a	Profile b	Profile c
Snow Depth (m)	1.61	0.96	0.61
SWE (kg m^{-2})	757	441	277
Average Density (kg m^{-3})	407	398	394
Maximum Density (kg m^{-3})	500	422	437
Minimum Density (kg m^{-3})	321	348	311
Average Temperature (°C)	-0.05	-0.24	-0.16
Surface Temperature (°C)	-0.1	-0.3	-0.1
Basal Temperature (°C)	0	-0.3	-0.1
% Cup Crystals	36	27	18
% Fragmented Particles	57	71	77
% Ice	7	2	5

There are distinct differences between the layering in the snowpack. The shallow snow has the smallest proportion of insulating cup crystals seen in three surveys, and similarly the greatest proportion is seen in the deepest profile. Correspondingly the opposite trend is seen in the percentage of fragmented particles. The variation in crystal layering may have important consequences for the bulk thermal conductivity of the snowpack. In an analysis of spatial patterning of snowpack layering in Arctic Alaska, Sturm and Benson (2004) found distinct variation in layering associated with micro-topography and wind flow around topography.

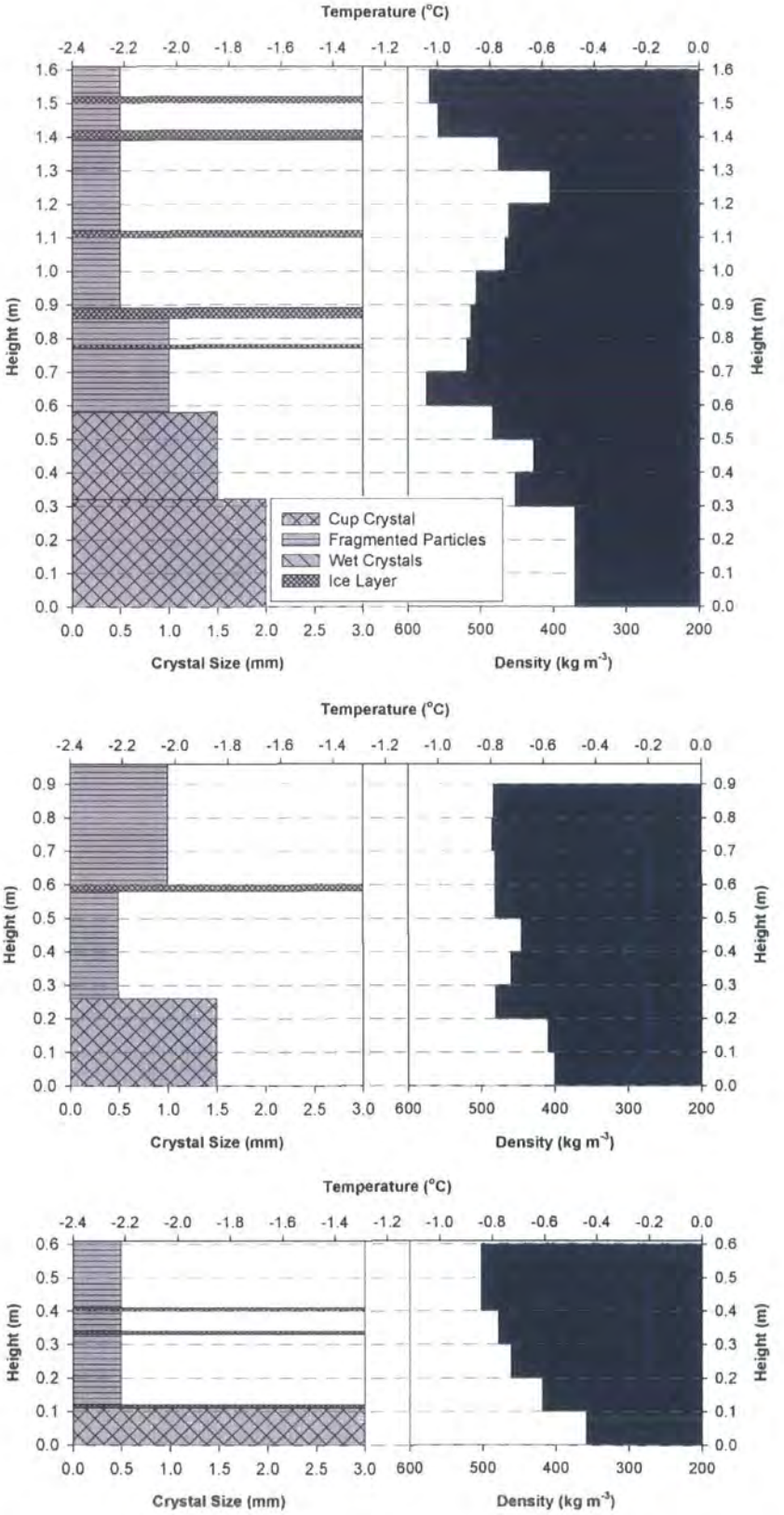

Figure 4-14: Spatial variation in snow profile across varying depths of snow (Profiles a, b and c). Measurements taken on 21st March 2003. Ice layers are indicated by a horizontal hatched bar. Crystal size is not given for ice.

4.4 Snow Covered Area

Remotely sensed data are used to monitor snow-cover throughout the winter of 2003/2004. Two sources of data are available: a pair of automated digital cameras set to collect digital images of snow distribution once daily at solar noon, and daily data from the MODIS (Moderate Resolution Imaging Spectroradiometer) satellite-borne 500 m resolution snow-cover product (Hall *et al.*, 2000). The advantage of the digital cameras is that they provide orthorectified data at 5 m resolution across the study domain, whereas for MODIS data, the study domain will be represented by approximately one pixel (landscape scale). MODIS data are averaged over three scales, representing the meso-scale (10 km), regional circulation models (50 km) and global circulation models (250 km).

Data from these two sources are given in Figure 4-15. Gaps in the data are the result of the typical difficulties of operating a digital camera in these environments: during the period of operation, riming of the camera lens, low cloud cover and power failure resulted in data loss. Similarly, gaps in the MODIS data set are the result of excessively cloudy conditions, commonplace for Abisko, and data retrieval problems.

The agreement between the two cameras is, on the whole, very good, although it should be noted that each camera has a different but overlapping footprint. The differences between the traces increase during the melt phase due to the bias of Camera B to the snow-drifts. Therefore there is no reason for the traces to match perfectly. The fit with the surveyed snow covered area data is poorer. However, this is most likely a factor of the data types involved. The images are area averages compared to the ground truth data, which represent point measurements averaged over the footprint of the image, the fundamental differences in measurement technique means there is no reason for complete agreement (Bloschl, 1999; Bloschl and Sivapalan, 1995). MODIS data, collected over a 10 km^2 area (meso-scale) centred on the field site, suggests an earlier snow-free data than the digital cameras. This is most likely due to the effect of hydrological important small-scale snow-drifts occurring at a smaller scale than MODIS resolution. This effect has been noted elsewhere (Dery *et al.*, 2005). On the basis of a simple comparison between

local data (remote cameras) and large-scale (MODIS) it appears that processes at the study site are broadly comparable to those operating at a larger scale. This is an important result as model parameterisations based on small-scale observation are applicable at much larger scales commonly used in NWP.

The images reveal the variability in snow-cover, especially during the autumn period. Snow-cover during this period is very ephemeral, with snow remaining on the ground for just a few days at a time before ablating. The main snow season begins in early December, which corresponds with the main snowfall of the winter period. The mid-winter period is characterised by highly variable snow-cover, either ablating or redistributed into existing drifts. The main ablation period begins in April and the area becomes largely snow-free by May with the exception of what appears to be spring snowfall events that may be minor in their nature, but sufficient to cover the majority of the camera footprint. These snowfall events do not appear in the snowfall record.

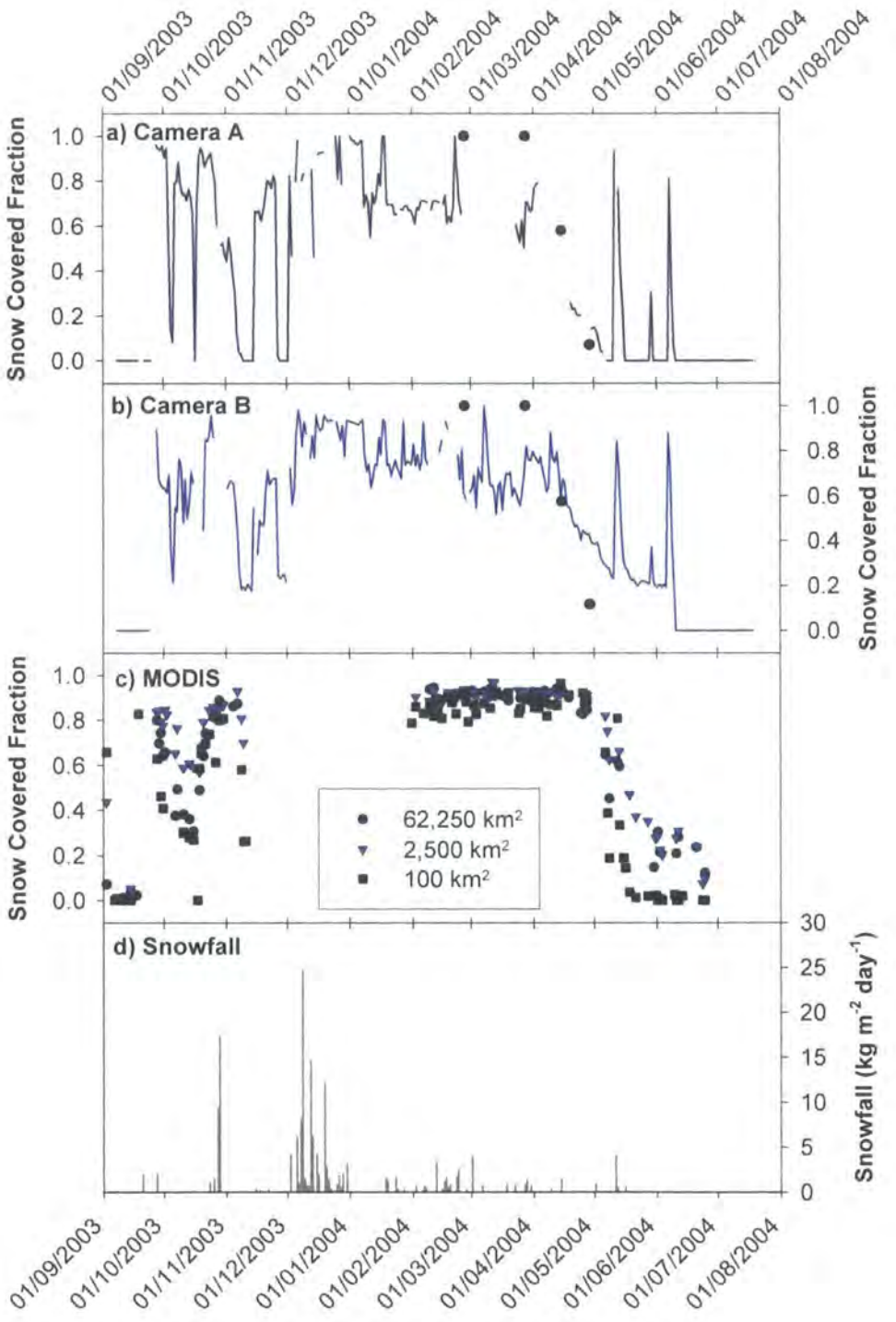

Figure 4-15: Snow covered fraction for the survey domain from remotely sensed data (a and b), and larger regions centred on the study site from MODIS data (c). The three scales given in (c) relate to the meso-scale, and RCM and GCM gridbox size. Black circles (a and b) represent ground truthed data (from snow surveys) weighted for image footprint area. Corrected daily observed snowfall measured at ANS is given in d.

4.5 Snow-cover Ablation

4.5.1 SNOWDRIFT ABLATION

Observations from the remote digital cameras show the main melt phase begins in the first week of April 2004 with the majority of melt over by the start of May. Automated observations of snow depth and manual observations of density indicate the onset of a rapid phase of melt on May 3rd interrupted by snowfall after seven days before becoming snow-free on May 25th (Figure 4-16). Melt rates during this period reached a maximum of 45 kg m^{-2} day^{-1} and averaged 20 kg m^{-2} day^{-1} throughout the period (excluding accumulations). Observations from shrub tundra in Yukon, Canada showed equivalent melt rates of 3 kg m^{-2} day^{-1}, increasing to 7 kg m^{-2} day^{-1} under advective conditions (Pomeroy *et al.*, 2006). Observed melt rates are substantially higher during this phase than those observed in Canada, although they are not directly comparable due to different surface energy-balances. The high rates of melt are generally greater than soil infiltration capacity rates and thus lead to surface runoff with potential consequences for the water balance. Prior to this rapid phase approximately 80 kg m^{-2} of ablation is observed to occur, during which the snow covered area decreases from 80 to the 20-40% observed by the automated cameras. A switch appears to occur in the processes controlling ablation that leads to a rapid change in the rate of ablation. This can only be related to turbulent transfer of energy and/or a changing surface albedo as the seasonal increase in short-wave radiation is comparatively low during this period. This switch in the processes controlling melt appears to be correlated to a change in boundary-layer temperature regime (**5.3**). Although snow covered fraction is focused on here, the degree of interconnection between patches and patch distribution can have significant impacts of the surface energy-balance, particularly under advective conditions. Analysis of the daily images suggests that at the time of onset of rapid melt the patchiness is defined by large isolated snow patches surrounded by interconnected vegetated ground. Attempts at a more rigorous image analysis are limited by the image resolution and image blind spots preventing landscape metrics from being derived.

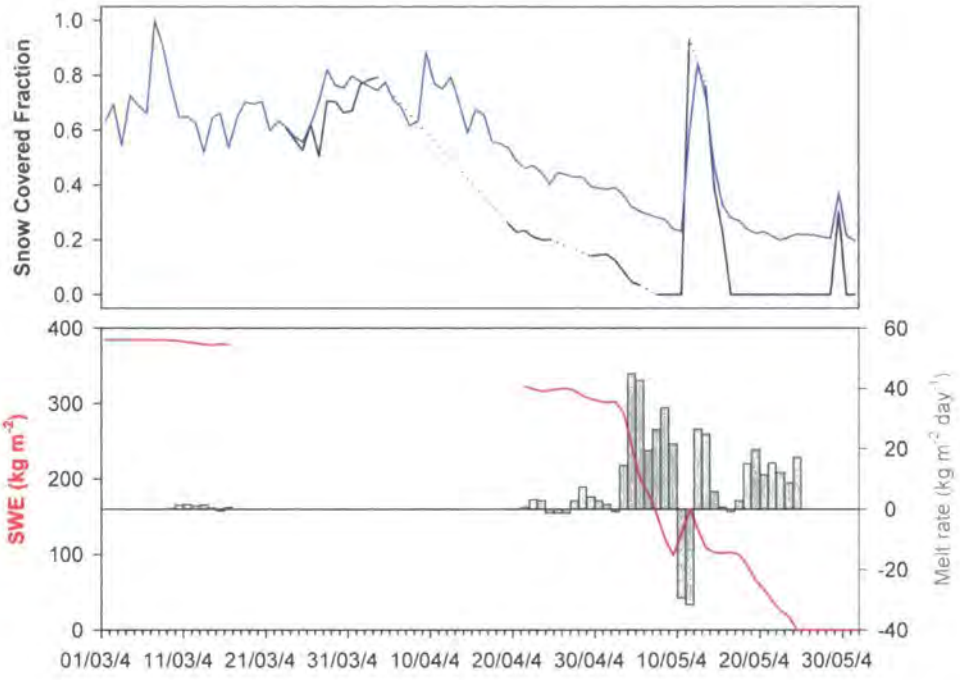

Figure 4-16: Snow covered fraction and ablation during the melt period from remote digital cameras and UDG.

The source of the additional energy for melt may be small-scale advection as suggested in the Canadian observations. Advection processes lead to the greatest melt rate at the edge of snowpacks, an indicator of advection would thus be heterogeneous ablation.

4.5.2 HETEROGENEOUS ABLATION

Heterogeneous snow melt occurs as a result of a spatially variable amount of energy available for melt. The high melt rates demonstrated during the relatively snow-free period are symptomatic of advective processes. There are however a variety of factors that potentially affect the surface energy balance across the domain considered here. These include varying radiation receipt, due to a varying aspect and slope angle, or a varying surface albedo, either through surface dust or radiation penetration of the vegetation surface energising the snowpack from below. Exposed vegetation may also alter the energy balance. Vegetation has a lower albedo than snow, and will generally have a warmer surface temperature than melting snow. Heat energy may be conducted through the stems into the snowpack, radiated through emission of longwave radiation, and through sensible heat flux

into the snow-cover. However, vegetation will also shade the surface, as will any micro-scale variation in the surface, reducing the radiation incident on the surface (Bewley *et al.*, 2005). The effect of exposed vegetation on the magnitude of sub-canopy melt is uncertain but the effect is generally to increase melt rates (Pomeroy *et al.*, 2006).

Figure 4-17: Snow melt around exposed vegetation

Another important process is the advection of sensible heat from relatively warm low albedo surfaces to cold snow surfaces. This leads to an increased melt rate at the edge of the snowpatch.

Each of the processes described above, or a combination, act to create spatially variable melt. It is expected that heterogeneous melt will inversely co-vary with initial SWE as deeper snow will expose less vegetation, require radiation to penetrate further to reach the low albedo surface and is more likely to be in the centre of a drift. Aspect and slope angle are considered to have a minor effect as they are fairly uniform across the surveyed domain.

Figure 4-18 shows net ablation between tied SWE observations made on 15th and 29th April 2004 plotted against initial SWE. Any observations in which the surface became snow-free between these dates are excluded from this analysis.

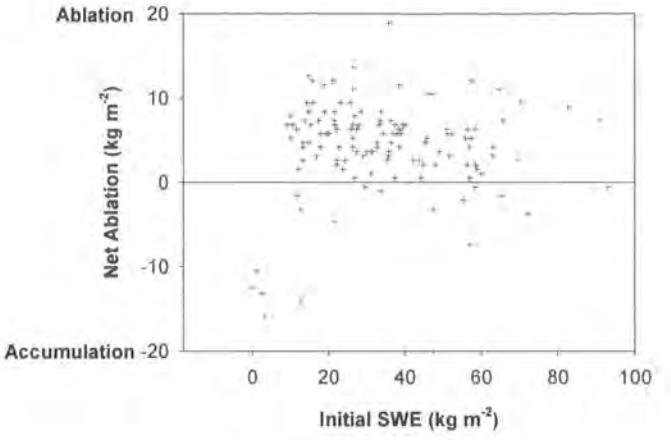

Figure 4-18: Snow ablation between 15th and 29th April 2004 versus initial SWE

Figure 4-18 does not show a statistically significant trend in ablation with initial SWE, implying heterogeneous melt is not a process occurring at the measurement scale. In some cases snow actually accumulated between surveys, which may be related to measurement error or redistribution. Further analysis relating net ablation to distance from the edge along the axis of prevailing wind direction similarly show no correlation. Melt rates thus show a degree of spatial variability probably associated with a combination of the above processes and varying surface albedo. However, there is no evidence to suggest advection is a significant process.

4.6 Snow-cover and Soil Moisture

Soil moisture shows spatial heterogeneity associated with topography, soil depth and soil structure. Figure 4-19 shows the soil moisture mapped across a sub-section of the main survey area for two dates; one post-melt and the second post peak-biomass (Unpublished data courtesy of D.R. Sayer). Soil moisture is highly variable over short distances, with some regions experiencing high degrees of water stress. The implication is for a highly variable partitioning of sensible and latent heat fluxes.

The pattern of soil moisture is clearly fixed in time, and shows a resemblance to the distribution of snow-cover. However, although snowmelt clearly plays an important role in the water budget of the soils the distribution of soil moisture bears a greater resemblance to topography than snow distribution. Winter snow

distribution and post-melt soil moisture are statistically uncorrelated. Lateral flow of melt water is thus clearly important. Snow and soil moisture distributions therefore need to be treated independently in surface exchange schemes. Assuming melt water is uniformly available or only penetrates, the location of snow lie will lead to significant errors in the determination of soil moisture and subsequent turbulent flux for snow-free regions.

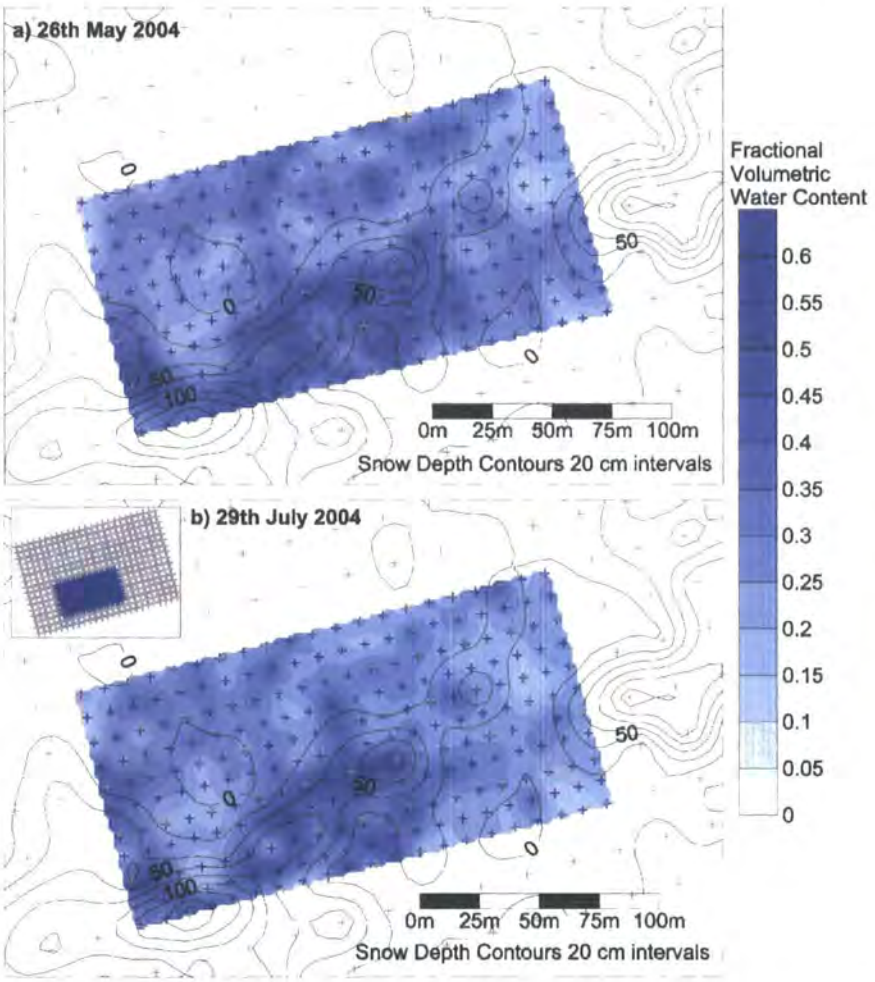

Figure 4-19: Fractional volumetric soil moisture for a sub-section of the survey domain. Sample locations are marked with crosshairs. Snow depth contours are from the 27th February 2004 survey. Data courtesy of David Sayer (unpublished).

4.7 Snow-cover and Sub-Nivean Temperature

The insulating effect of snow-cover exerts a strong influence on sub-nivean temperature, reducing temperature fluctuations within plants and soils. Figure 4-4c shows the spatial variation of sub-nivean temperature with snow distribution. Observed temperatures vary from just below 0°C to -3°C, the colder temperatures

occurring under the deeper snow, although there is no clear correlation between sub-nivean temperature and snow depth. These data provide a snap shot in time after a recent snowfall and during a relatively warm incursion. Sub-nivean temperature is clearly not just a factor of snow depth but also snow pack structure (**4.3**), soil moisture and structure (**4.6**), and date and temperature at time of burial.

4.8 Snow Depth, Elevation and Land Surface Type

Snowfall is known to vary with elevation due to adiabatic cooling of the atmosphere as an air parcel is forced to rise orographically (Langham, 1981). Simultaneously vegetation type changes with elevation, with an elevation determined treeline. These factors combine to affect the distribution of snow-cover by controlling the redistribution of snow across the landscape. Additionally, melt rates are known to vary considerably with altitude due to the lapse in temperature with elevation. The use of elevation tiles in modelling applications has often been proposed (e.g. Essery, 2003; Moore *et al.*, 1999)

A snow course was made at approximately 20 m intervals across an elevation and vegetation gradient, from mountainous terrain above the main research site, through the birch forest, to the valley bottom at 350 m a.s.l. (Figure 4-20). Four basic land-surface types were identified: bare rock, tundra, birch forest and open mire. Elevation was subsequently extracted from a DTM of the region.

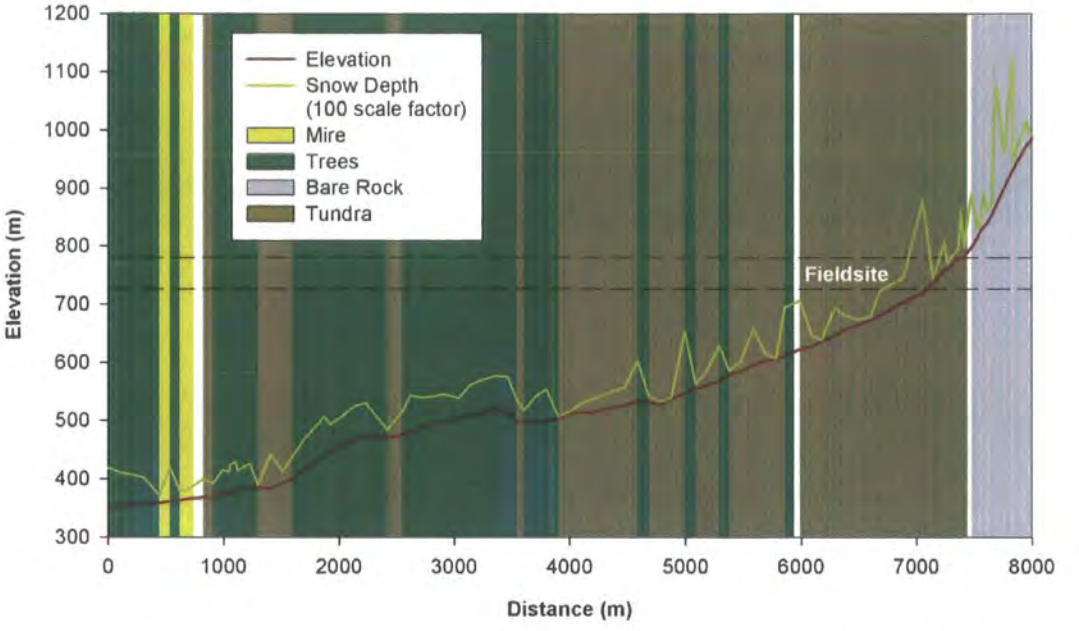

Figure 4-20: Transect of snow depth across an elevation gradient and differing land-surface properties. Snow depth is scaled by a factor of 100 and imposed upon elevation. Survey 29th March 2004.

Over the elevation range of 600 m there is no significant correlation between altitude and snow depth. However, surface type appears to exert a strong control, especially between the dominant surface types of tundra and birch forest (Figure 4-21).

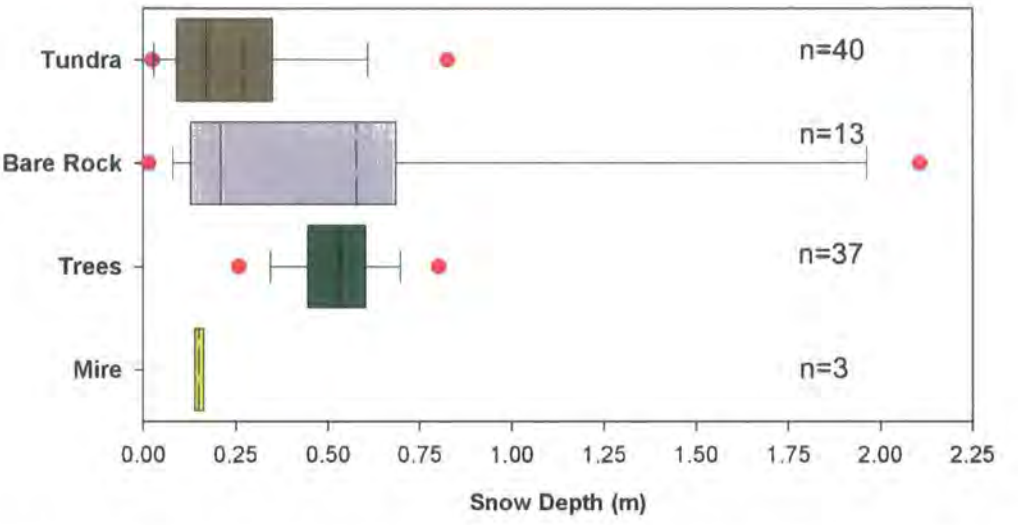

Figure 4-21: Box plot of snow depth classified into land surface type. The mean is shown as a dashed line. The box and whiskers represent the 25th, 75th, 10th and 90th percentiles respectively. Red dots indicate outliers.

Too few data points are available for the surface types of bare rock and mire and are excluded from the following analysis. Mean snow depth in the tundra and forest are 0.27 and 0.5 m, and coefficients of variation 1.1 and 0.3, respectively. Snow depth in the birch forest is therefore nearly twice the depth of tundra and more uniformly distributed. These data take no account of the variation in density, and it is possible that differing rates of metamorphism and densification account for the difference in observed snow depth. Dry snow densities for forested environments reach an approximate maximum of 250 kg m^{-3} (Gray and Prowse, 1993) compared to observed densities in the open tundra which are approximately 400 kg m^{-3}. Measurements taken at a birch site at ANS between 1914 and 1918 show a mean density of 250 kg m^{-3} for this time of year (Kohler *et al.*, 2006). The difference in depth may therefore be partially accounted for by a difference in density, leading to an equivalent SWE. Additional contributory processes are differing rates of sublimation during blowing snow between surface types and the direct transfer of mass from the relative smooth tundra to the high aerodynamic roughness of the forest. Blowing snow occurs when snow crystals are entrained by the wind and either lifted into the air or saltated along the ground (Pomeroy *et al.*, 1993). The greater ventilation of crystals during blowing snow leads to increased rates of

sublimation (Schmidt, 1982). Sublimation during blowing snow can be a significant component of the winter mass balance. Pomeroy *et al.*, (1997) simulated sublimation of 28% of annual snowfall for a tundra catchment in North-West Canada. Sublimation rates may differ between the two land surface types due to the relatively higher wind stress exerted on tundra snow due to the lower aerodynamic roughness, making blowing snow events more probable. Similarly, sublimation is also sensitive to fetch length (Pomeroy *et al.*, 1993). The patchy nature of snow-cover on tundra may limit the full development of blowing snow fetches, limiting sublimation. The more uniform nature of the forest may allow for greater fetches. Further to this, mass may be transferred from the tundra to the forest during blowing snow. Snow crystals are known to travel a great distance before sublimating, for instance Benson (1982) observed transport lengths of 2.5 to 3.5 km for the Alaskan arctic coast.

To fully understand the processes controlling snow distribution across the broader drainage basin requires greater knowledge of processes controlling metamorphism, densification and in particular blowing snow.

4.9 Summary

Tundra snow-covers show a high degree of spatial heterogeneity associated with topography and vegetation. These patterns can be expected to recur annually. Initially, the snow covered fraction is also complete, but as the ablation period begins the snow-cover gradually becomes patchier. The patchiness can be characterised by random distribution and a typical patch size of the order of 60 m. The process scale is 22 m. Typically, the snowpack consists of layers of thermally insulating depth-hoar overlain by layers of heavily fractured compacted wind-blown crystals. The main melt period begins mid-April and the deep drifts last through to mid-summer. Initial melt rates are low whilst the snow-cover is largely complete, but rapidly increase in May when the snow-cover is isolated in patches. However, the change in melt rate is not associated with the arrangement of patches, as the patches are largely formed at this stage. Ablation shows a small degree of spatial variation but appears unrelated to advective processes, thus advective processes do not need to be represented in model schemes. This is discussed in greater detail in Chapter 6.

Evaluation of snow-cover on a much larger scale suggests that the study site is representative of the broader regime. However, there is evidence to suggest that a proportion of the snowfall across the study site is either sublimated during blowing snow or transported to the birch forest at lower elevations.

Chapter 5

Site Micrometeorology and Climatology

5 Site Micrometeorology and Climatology

5.1 Introduction

The climate of the high latitudes is highly seasonal due to the variation in solar energy. Abisko lies in the climatically important zone of seasonal snow-cover. The snow-cover forms during the cold winter and ablates in the spring. This zone has potential feedbacks to global climate due to albedo feedback effects.

This chapter follows on from the previous section to illustrate the climate of the Abisko region, and the relationship between the tundra site and the broader meso-scale meteorology including the relationship between patchy snow and boundary layer properties. The important micrometeorological parameters; aerodynamic resistance and stability, essential to the modelling of energy exchange are also derived. Furthermore, the limits and practicalities of the micrometeorological instrumentation are also investigated. These data and parameters are used in the subsequent energy balance and modelling chapters.

5.2 Climate Measurements

Standard climate measurements of air temperature, precipitation, radiation, atmospheric pressure and specific humidity were made throughout the winter of 2003/2004 (Figure 5-1). Short days and low air temperatures, reaching as low as -20°C during some periods, are characteristic of the deep winter. These low temperatures are generally associated with low wind speeds, related to the low-energy status of the weather systems. Rapid fluctuations in air temperature of 15°C over the course of a 24-hour period normally associated with rapid pressure changes were also experienced. The energy balance during the deep winter is dominated by longwave radiation with fluxes in the order of 250 W m^{-2}, rising slightly in the spring and autumn due to the generally warmer atmosphere and cloudier conditions. Shortwave radiation fluxes increase from the early March onwards with daily averages reaching 300 W m^{-2} in May and June. This in turn correlates with relatively warmer air temperatures. Air temperature also varies with synoptic systems, which can be seen from the atmospheric pressure trace. Relative humidity throughout the winter is generally high with values around 80%, however

due to the low temperatures this corresponds to very low water vapour pressures and very dry air. Changes in humidity are associated with changes in air temperature affecting the saturated vapour pressure and general synoptic conditions.

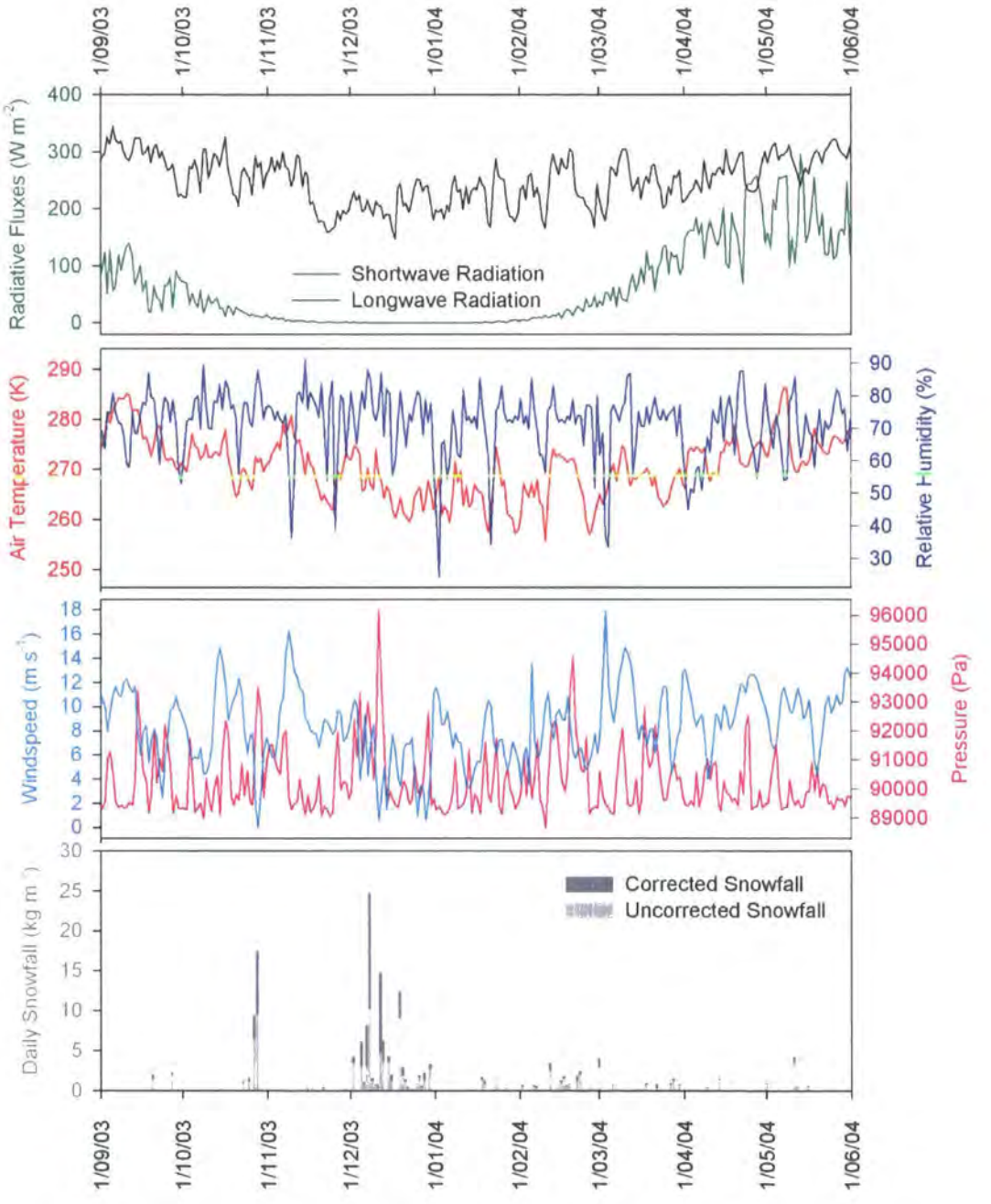

Figure 5-1: Mean daily observed climate variables and daily snowfall total for the 2003-2004 winter period.

Precipitation during the winter is generally very low, with observations totalling 104 kg m^{-2} (equivalent of mm water), and values corrected for undercatch (**11.2**)

totalling 175 kg m^{-2}. Rainfall was occasionally observed during warm periods but no data are available. Total annual precipitation at the research station is approximately 300 kg m^{-2}. Snowfall and consequentially runoff are thus significant components of the annual water balance.

Wind data are plotted in Figure 5-2. Winds are predominantly from the south and west, with the southerlies generally producing the highest observed windspeeds. The average wind vector is 203°.

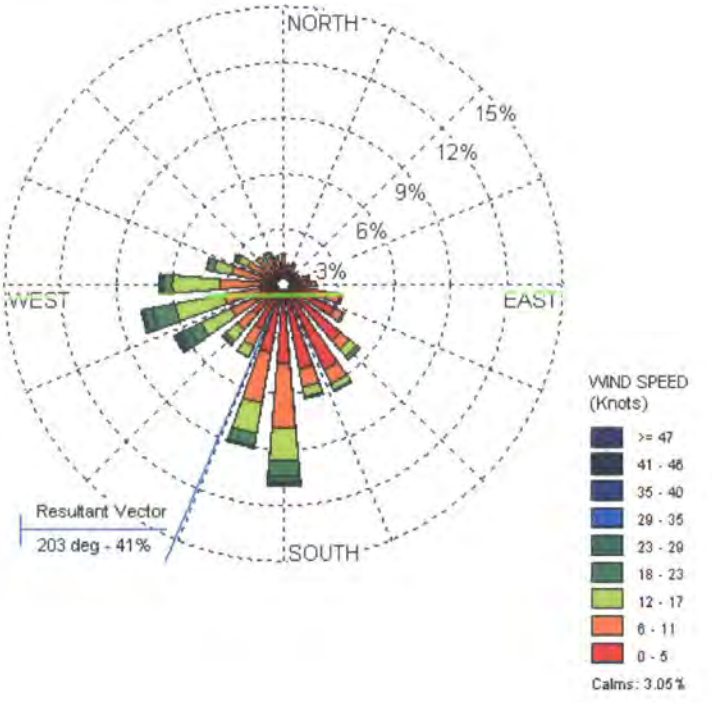

Figure 5-2: Wind-rose of wind direction and wind speed for 1st Sept 2003 to 1st June 2004. Data are clustered into 15 degree bins. The wind-rose expansion relates to the percentage time winds occurred for a given direction.

Soil temperatures are measured at both the snow and snow-free meteorological stations at different heights. Soil moisture is measured at two heights within the soil profile. Unfortunately, data recovery is poor from the snow station due to recurrent logger problems. Snow depth peaked at approximately 1 m depth for the snow station and the snow station remained generally snow-free with the exception of a few short periods which are not reflected in the soil temperature record.

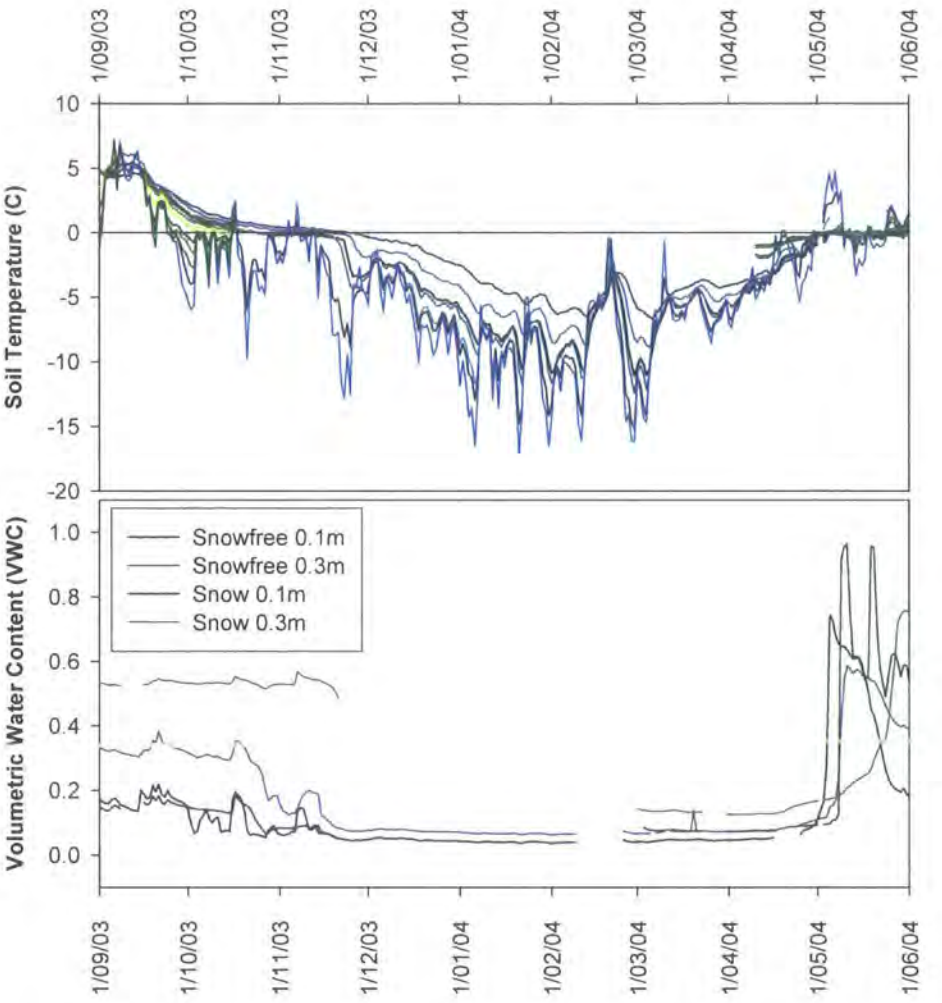

Figure 5-3: Soil Temperature and Volumetric Liquid Water Content (m^3 water m^{-3} soil) for the winter of 2003/2004 for the snow-free and snow station. Plots in green are for the snow station and those in blue for the snow-free station. Soil temperatures are measured at approximately 0.05 m intervals from the surface. Those showing the greatest variation are measured near to the soil surface.

Observed liquid soil moisture during the winter is generally low (0.1 VWC), although the frozen fraction may be higher. Soil moisture rapidly increases in May as a results of an influx of melt water from the snowpack and the thaw of the soil releasing frozen water. The penetration of heat and moisture to the snowbed lags behind the snow-free region as the soil remains frozen for longer due to a prolonged snow-cover. The peak in soil moisture corresponds to saturation of the soils and a period with considerable surface water. The saturation point varies with the soil type, in particular the organic fraction. Gravimetric measurements suggest an average saturation point of 0.62 VWC (David Sayer, unpublished data). Soil

freeze-thaw cycles are highly dependent on soil moisture content and are thus difficult to model (Hall *et al.*, 2003). This has important implications on modelled surface resistance and thus turbulent energy and carbon fluxes modelled for tundra regions.

5.3 Air Temperature

The observed 2 m air temperature would be expected to relate to both sensible heat fluxes and large-scale synoptic weather systems. The observed 2 m air temperature shows a large diurnal range, particularly during the period of patchy snow-cover. Diurnal temperature ranges of up to 10 K are common during periods of patchy snow-cover and cloud-free conditions. This is indicative of sensible heat fluxes having a strong influence on air temperature. This is further complicated by the presence of snow-cover, which, due to a constrained surface temperature, acts to draw energy out of a warm air mass, whilst a nearby snow-free patch may act to warm the overlying air mass. Ellis and Leathers (1998) modelled a 1-4 K difference in air temperature between a snow-free area and a snow patch under high solar radiation. The processes controlling air temperature are therefore not clear during patchy snow-cover conditions and for heterogeneous terrain.

To investigate these processes in detail requires a boundary layer model. However, an understanding can be gained by correlating eddy correlation measured sensible heat fluxes with air temperature and incoming radiation measurements. For a large uniform surface it would be expected that the diurnal ranges in shortwave, sensible heat and air temperature would all be correlated. However, where the surface is heterogeneous, or where the air temperature is responding to large-scale processes, this expectation may no longer hold true. By combining measurements of incoming radiation, representing the energy available to warm the surface, and eddy correlation sensible heat flux, representing the response of the surface for a small area, it is possible to elucidate the response of the air temperature to processes at local to landscape scales.

Figure 5-4 shows the relationship between the diurnal range in air temperature, the diurnal range in shortwave radiation receipt and the diurnal range in sensible heat flux, for two periods: (*i*) largely complete snow-cover and (*ii*) patchy snow-cover,

relating to the early season and the melt period. These periods were defined by classifying air temperature and flux data according to the snow lie conditions derived from the automated camera images.

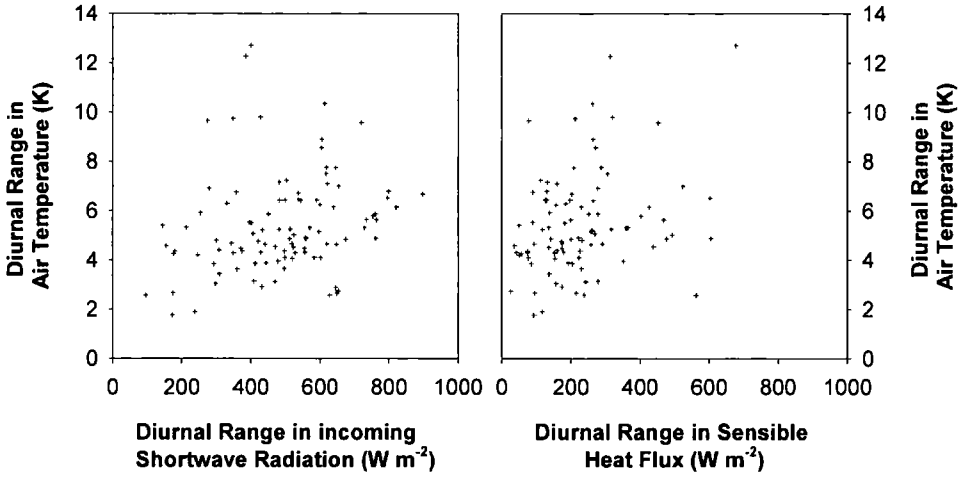

Figure 5-4: Relationship between the 2 m temperature of the surface boundary layer and the surface sensible heat flux as measured by Solent Eddy Correlation system during the (*i*) snow covered period (black) and (*ii*) patchy snow-cover period (red).

During the period of patchy snow-cover, air temperature is correlated to the observed shortwave radiation ($r=0.437$, $p=0.006$, $n=38$), but not to the sensible heat flux ($r=0.111$, $p=0.507$, $n=38$). However, during the snow covered period the reverse is true; air temperature is correlated with sensible heat flux ($r=0.431$, $p=0.001$, $n=54$), but not to the incoming shortwave radiation ($r=0.072$, $p=0.592$, $n=54$). During the period of patchy snow-cover a decoupling appears to occur between the air temperature and locally observed sensible heat flux. The implication is that the air temperature is controlled by processes on a scale larger than the footprint of the eddy correlation system (**5.5**) and thus responding to the shortwave radiation. The snow patches are draining heat out of the overlying air mass driven by a landscape positive heat flux. The energy available for melt is thus coming from the landscape as a whole rather than the local patches. This is evidence of the formation of a deep convective boundary layer which is the assumption made in large scale atmospheric models. These models ignore the distribution and patchiness of surface heterogeneity and assume that each contributes to form a uniform boundary layer.

During the pre-melt period the reverse situation occurs. The air temperature is responding to sensible heat fluxes but is uncorrelated to shortwave radiation. During this period the snow covered area is 70-100% complete and air and surface temperatures are generally below freezing. The cold snow surface and the relatively warm overlying air mass create a stable boundary layer, thus reducing the efficiency of turbulent exchange. The high surface albedo results in a reduced response to incoming shortwave radiation. The combined effect of stability and high albedo is to loosen the coupling between incoming radiation and sensible heat flux. However, the air temperature is still responding to the sensible heat flux across the flux footprint and possibly at larger scales as well.

Clearly, the varying snow-cover conditions affect the processes controlling the surface air temperature. The change from nearly complete snow-cover to patchy snow-cover leads to a change in process as the air becomes warmer, and a greater differential exists between snow and snow-free areas in terms of the sensible heat flux. Potentially, this switch has significant importance in determining a boundary layer temperature in an atmospheric model, which correspondingly has important feedbacks to the correct determination of the contribution of sensible heat flux to melt.

5.4 Snow Breezes

The above discussion shows that the air temperature is responding to heat fluxes at varying scales from the local to the landscape. A differing surface temperature can lead to thermally induced flows between surfaces.

Snow breezes form in the lower atmosphere as a result of strong temperature gradients between components of the land surface (Segal *et al.*, 1991a; Segal *et al.*, 1991b; Taylor *et al.*, 1998). Temperature differences are common when one of the surfaces is snow covered, and the corresponding surface snow-free. The snow acts to constrain the surface temperature to the melting point, while the snow-free surface can respond to the diurnal cycle in energy availability. Temperature gradients lead to pressure differences, which in turn lead to gentle breezes providing synoptic scale winds are low (Segal *et al.*, 1991a; Segal *et al.*, 1991b;

Taylor *et al.*, 1998). The diurnal cycle in temperature difference leads to a diurnal cycle in snow breeze.

Figure 5-5 and Figure 5-6 show the diurnal wind and air temperature data collected for the months of September 2003 and May 2004. Air temperatures are generally higher during the daylight hours, peaking shortly after midday, associated with sensible heat flux as described in **5.3**. This is correlated with a northerly wind during the daylight hours. The wind flows upslope from the birch forest during daylight, as would be expected from normal anabatic flow conditions, and correspondingly down-slope during the hours of darkness (katabatic flow). However, during the month of May the upslope flow during daylight conditions appears to be more exaggerated. Although there is no air temperature information from the birch forest this increase in windspeed is thought to be the result of snow-cover influenced temperature differences creating a snow breeze. During September the birch forest is largely devoid of foliage and the landscape as a whole is snow-free. The surfaces are therefore expected to have a similar energy-balance and subsequently surface temperature, the resulting windflow being a function of topography-defined drainage.

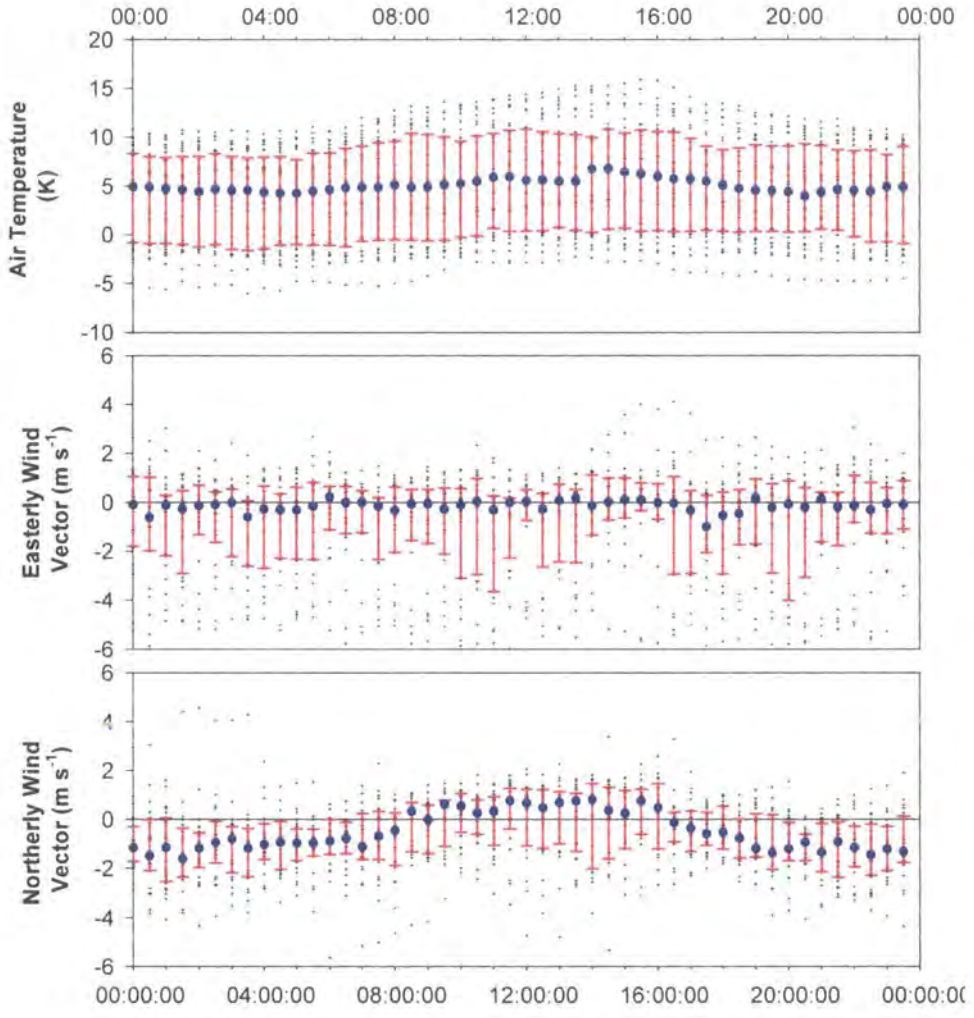

Figure 5-5: Diurnal variation in observed air temperature and windspeed during September 2004. Blue diamonds indicate the median, red bars interquartile range.

During May 2004 the birch forest was snow covered and the tundra site covered in patchy snow. The birch forest retains more snow due to a greater initial snow accumulation (**4.8**) and a different energy-balance. It is therefore likely that the tundra will be relatively warmer than the birch, implying the windflow to be southerly, contrary to the observations. It may however be that the due to the relatively lower albedo of the birch forest the surface temperature is warmer than the tundra and thus a leads to a northerly wind.

Due to the lack of meteorological data this process, although evident, warrants further investigation.

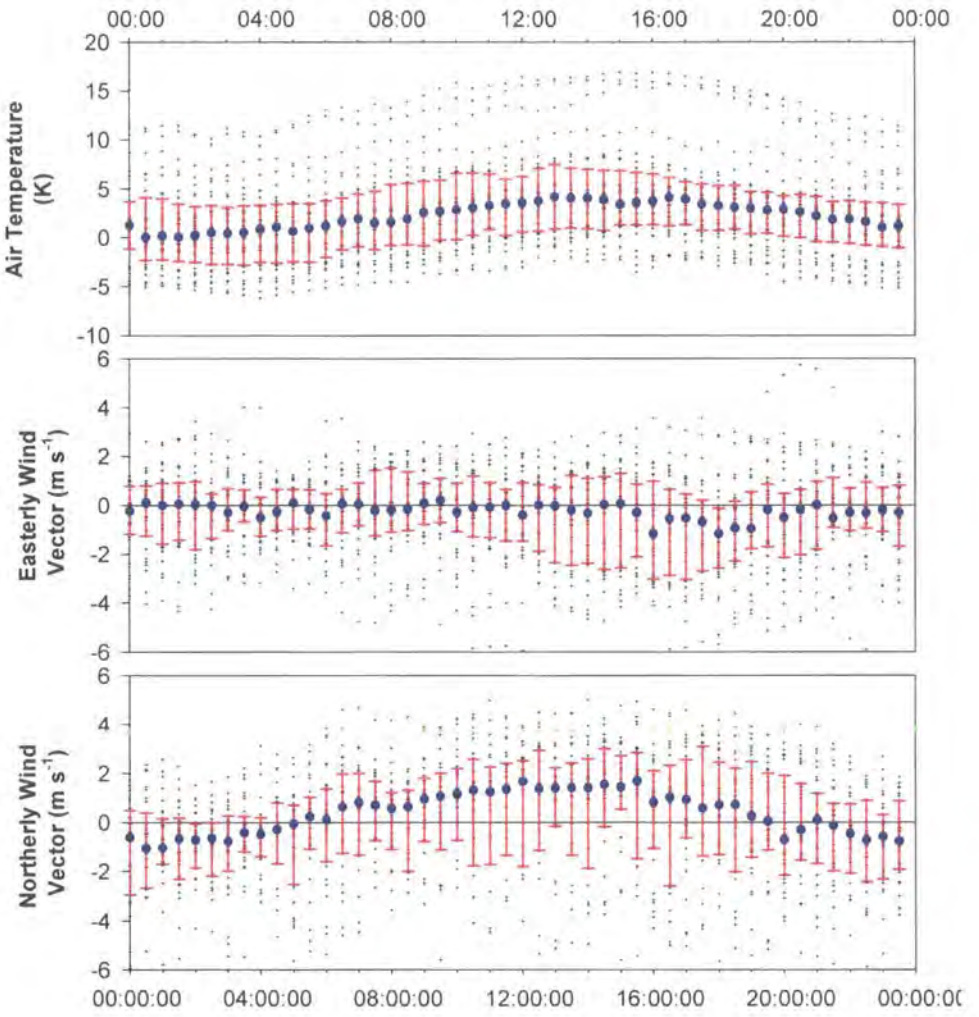

Figure 5-6: Diurnal variation in observed air temperature and windspeed during May 2004. Blue diamonds indicate the median, red bars interquartile range.

5.5 *Flux Measurements over Heterogeneous Surfaces*

Micrometeorological measurements have a characteristic footprint associated with them. Measurements can thus be seen as a spatial average of the footprint. Over inhomogeneous surfaces the measured value is dependent on the patches with the strongest influence and their location within the footprint. The measurement is both a function of the source-area (location) and also the source-strength of the flux being measured. For instance, the source-area of an eddy correlation system is a function of the atmospheric stability and the wind-direction and variability. The source-area of a surface facing radiometer is dependent on the diffuse and direct components of the radiation and the azimuthal and zenith angle of the sun. The footprint is more complex if there is a significant contribution of direct radiation as

the position of the sun and the surface aspect and angle will contribute to the measured radiation. The footprint under direct radiation will thus vary throughout the day with sun location. Diffuse radiation can be assumed to be uniformly distributed and thus the measured radiation will be dependent on the visible surface. The source-strength may also vary according to heterogeneous surface albedo and the strength of the incoming radiation.

The sensible and latent fluxes, although made with the same instrument, may have different sources and sinks within the footprint of the Eddy Correlation tower. The use of varying sensors to characterise surface energetics over inhomogeneous surfaces is one of constant debate within the micrometeorological literature (see Schmid, 1997). Closing the energy-balance using the standard approach of eddy correlation derived turbulent fluxes and radiometer measured radiation fluxes combined with soil heat flux observations is thus problematic over heterogeneous terrain due to the differing measurement footprints. Observations of diffusive scalars (e.g. air temperature and specific humidity) are more complex, as they are responding to changes in the atmospheric layer, which occurs at a timescale an order of magnitude faster than the data are averaged. Models of the footprint of diffuse scalars are thus defined by atmospheric properties averaged over a measurement period. Conceptually, over a single measurement period, the average distribution of sources and sinks within the flux footprint may not relate directly to the observed flux. However, over longer time scales, consisting of multiple measurement periods, the observed flux should bear a closer resemblance to the distribution of sources and sinks. A 'footprint climate composite' is thus derived which is defined as the footprint integrated over all the measurement periods within the winter/spring of 2004. Analysis of subsets of measurements taken during the winter period show little variation compared to the averaged source-area.

To evaluate the effect of differing source-areas between sensors, two simple source-area models for the CM5 radiometer and Eddy correlation tower were used (Appendix B: Footprint Models). The momentum source-area model used is based on Lloyd's (1995) version of the 2D model of Schuepp *et al.* (1990), distributed by assuming the wind to be a Gaussian distribution about the mean wind direction.

The radiometer footprint ignores direct radiation and assumes uniformly distributed diffuse radiation only. The model is based on a DTM-derived topographic aspect and slope. The source-areas for the radiometer and momentum flux from the Eddy Correlation tower are shown in Figure 5-7 and Figure 5-8 respectively.

Assuming that the source-area is the same for sensible and latent heat fluxes as it is for momentum, then on average 60% of the source-area comes from within the study domain, compared to 97% for the downward looking radiometer.

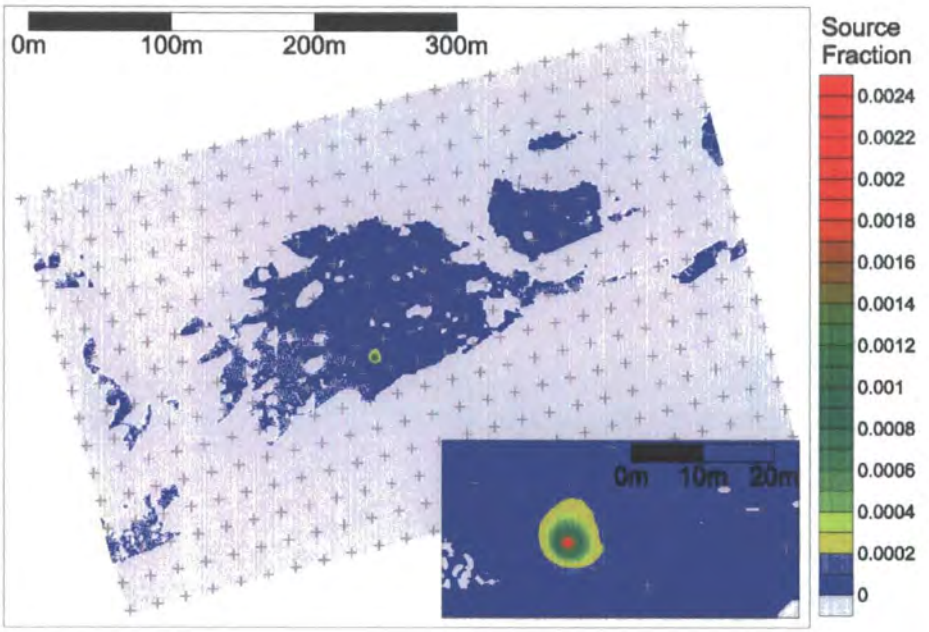

Figure 5-7: Reflected radiometer source-area. Grey indicates areas hidden by topography from radiometer.

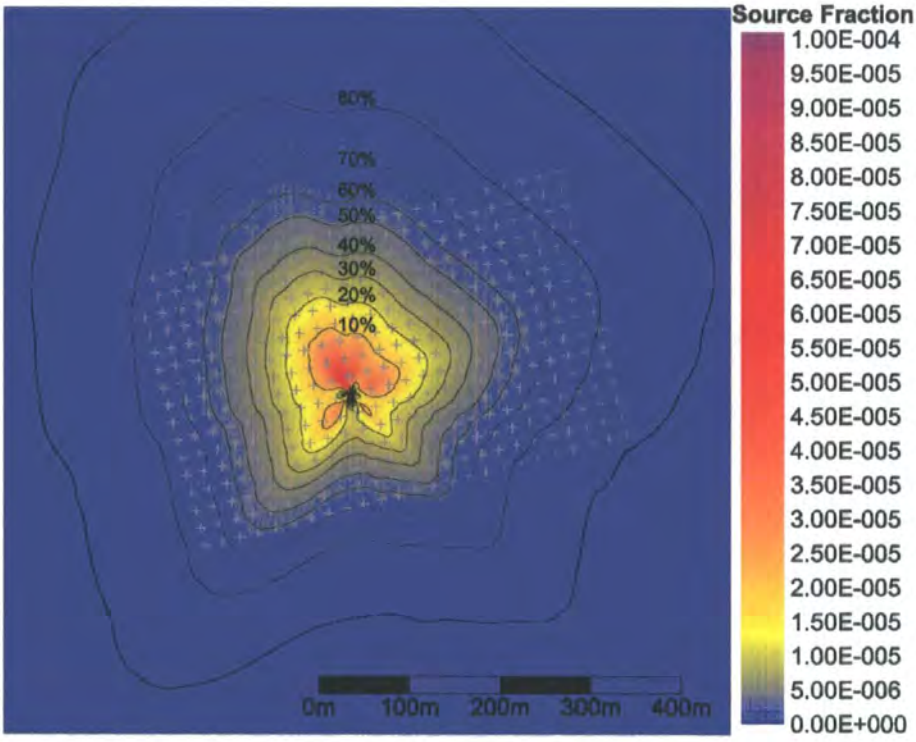

Figure 5-8: Eddy correlation tower composite source area.

5.6 *Aerodynamic Exchange Parameters*

The magnitude of turbulent fluxes from the surface is partly dependent on the efficiency of mixing within the boundary layer. As discussed in **2.3,** this is a function of the aerodynamic resistance to momentum, heat and vapour transport, as well as the surface resistance to vapour exchange. A major component of the aerodynamic resistance is stability within the boundary layer. These are all difficult to measure, but can be derived from eddy correlation and are used to parameterise MOSES. The data presented here are for the winter of 2004/2005 including the spring melt period.

Measurements presented in this section are from the MK4 Hydra (winter 2004/2005) and Solent/Licor (spring 2004) eddy correlation systems. The observations can be considered as averages over a footprint (**5.5**), and variation between individual measurements is partly a function of a changing footprint.

5.6.1 ATMOSPHERIC STABILITY

Under low wind conditions mechanical mixing of the boundary layer is low, especially over aerodynamically smooth surfaces such as snow. Under these conditions temperature profiles can be established within the boundary layer. A parcel of air therefore has stability relative to the temperature profile. A decrease in temperature with height leads to high buoyancy and thus unstable conditions, and correspondingly a relatively efficient transfer of turbulent energy. A reverse profile, where the temperature increases with height leads to stable conditions and a relatively inefficient turbulent exchange. The stability of the boundary layer therefore affects the turbulent exchange between the surface and the atmosphere.

Stability can be expressed by any of several quantities but the easiest to derive from eddy correlation is the Obukhov stability parameter (see section **2.3** for a detailed definition). This parameter has a value of zero during neutral conditions, positive during stable conditions and negative during unstable conditions.

Stable conditions are commonly associated with snow-cover due to the constrained surface temperature of 0°C. For unconstrained surfaces such as vegetation, stable

conditions are relatively less common, especially during daylight hours when incoming shortwave radiation warms the surface. Atmospheric stability thus shows seasonality associated with the arrival of snow-cover and seasonal variation in available radiation. This is illustrated by measurements from the Mk4 Hydra (Figure 5-9), which clearly shows stable conditions during the majority of the winter, and unstable conditions developing as radiation receipt increases and snow melts revealing relatively low albedo vegetation and an unconstrained surface temperature.

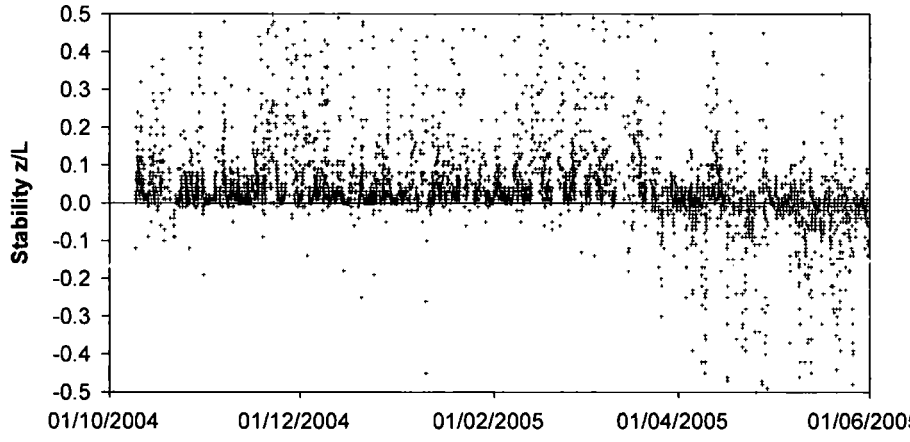

Figure 5-9: Boundary Layer Stability measured by the Mk4 Hydra. Negative values indicate unstable conditions and positive values stable conditions.

Also evident in Figure 5-9 is a diurnal pattern in the boundary layer stability. This is shown for cloudy and cloud-free conditions in Figure 5-10 derived from measurements taken with the Solent. Stability tends to be neutral to slightly stable during the hours of darkness and unstable during daylight hours. The magnitude of the diurnal variation is dependent on the diurnal variation in available energy. Figure 5-10a is for cloud-free conditions and shows stability during the hours of darkness as the surface radiatively cools, creating stable stratification in the boundary layer. High shortwave radiation during daylight hours warms the surface, creating turbulence and unstable conditions. Conversely, during cloudy conditions the surface remains relatively warm and coupled to the overlying air mass due to turbulent exchange leading to neutral conditions throughout the day (Figure 5-10b).

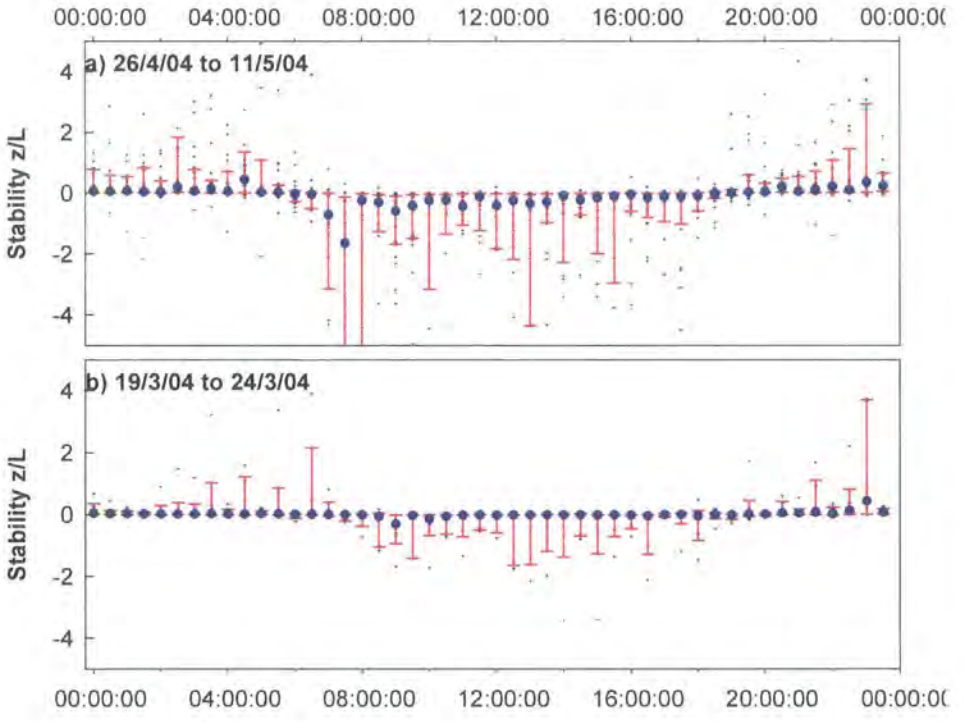

Figure 5-10: Diurnal development of the boundary layer under a) cloud free conditions, and b) cloudy conditions. Blue diamonds indicate the median, red bars the interquartile range.

Determination of turbulent fluxes over snow during stable conditions is uncertain (Martin and Lejeune, 1998), partly as they are associated with low wind speed conditions, which are difficult to measure due to inertia and stalling of cup anemometers. Stable conditions are also uncommon, with the exception of snow and ice covered surfaces, and have therefore received little attention. Underestimation of night-time turbulent fluxes may lead to an underestimation of surface temperature, as downward turbulent fluxes balance radiative cooling. This in turn leads to a dampening of daytime melt fluxes (Martin and Lejeune, 1998).

5.6.2 AERODYNAMIC RESISTANCE TO MOMENTUM

The aerodynamic surface roughness determines the efficiency of turbulent transport in the boundary layer. The aerodynamic resistance to momentum is defined as:

$$r_{a_m} = \frac{u}{u_*}$$

Equation 5.1

where u is the windspeed at a reference height, and u_* is the friction velocity, both of which are observed by eddy correlation. The aerodynamic resistance for the winter period of 2004/2005 is shown in Figure 5-11.

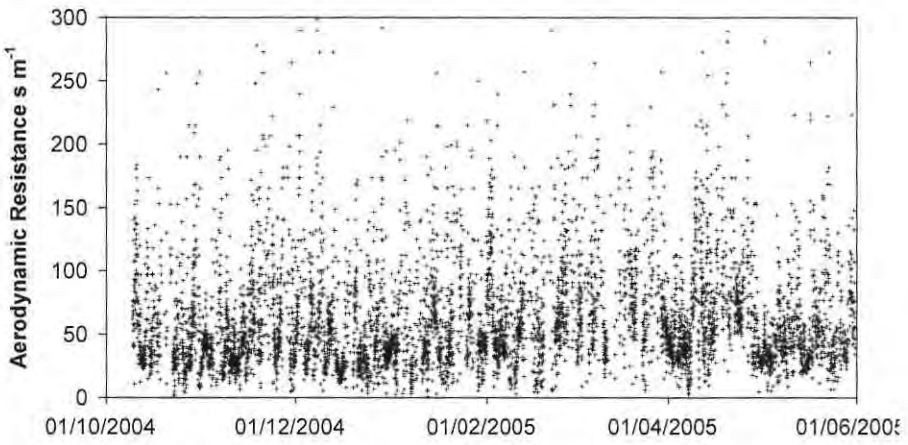

Figure 5-11: Aerodynamic resistance measured by the MK4 Hydra for the winter period October 2004 to June 2005.

The variation in aerodynamic resistance is a function of a changing footprint, an evolving surface aerodynamic roughness, changing atmospheric stability and windspeed. On average the aerodynamic resistance is of the order of 50 s m^{-1} and is fairly stable over the transition from snow to snow-free conditions, which indicates a similar roughness length between surfaces.

The length z_0 is a measure of the aerodynamic roughness of the surface and is an important parameter in surface exchange schemes. It is related to, but not equal to, the height of the roughness elements. It is also a function of the shape and density distribution of the elements (Oke, 1987). Commonly, it is approximated as a tenth of the vegetation height. Roughness lengths for snow and snow-free surfaces can derived separately by individual description of roughness elements (Lettau, 1969). Alternatively, z_0 can be estimated from eddy correlation measurements of wind velocity and the friction velocity following Lloyd *et al.* (1992). As the measurements of wind velocity and friction velocity are characteristic of a heterogeneous footprint, data are pooled according to surface snow-cover conditions to provide separate estimates of the roughness length for snow and snow-free surfaces.

Under neutral atmospheric stability the wind profile can be described using the following well known logarithmic equation:

$$u = \frac{u_*}{k} \ln\left\{\frac{z-d}{z_0}\right\}$$

Equation 5.2

Where u is the windspeed at height z, d is the zero plane displacement height, z_0 is the surface roughness length, u_* is the friction velocity and k is the von Kármán constant. The zero plane displacement height takes into account the height of the roughness elements, such that the distribution of shearing stress is equivalent to the imposition of the entire stress at height d. Wind velocity is theoretically zero at a height equal to z_0 plus d. The displacement height is commonly approximated as two-thirds of the vegetation height. Over snow covered ground it can be assumed to be zero. Equation 5.2 can be rearranged for the aerodynamic roughness length (Lloyd *et al.*, 1992):

$$z_0 = \frac{z-d}{e^{\frac{ku}{u_*}}}$$

Equation 5.3

By taking the mean ratio of u and u_*, and assuming a value of d, a value of z_0 can be gained. Lloyd *et al.* (1992) used sonic anemometers at two heights to gain an independent measure of d. However, as long as d is small compared to z, z_0 remains insensitive to d. This is the case for the short tundra heath vegetation found in the footprint.

Eddy correlation data pooled from the MK4 Hydra and Solent setups between 1st December and 1st April for the winters of 2002-2003, 2003-2004 and 2004-2005 are used to represent winter conditions when the flux footprint is known to be snow covered. Data between 1st May and 1st October for 2003, 2004, and 2005 are used to represent snow-free conditions. The data used in this analysis are restricted to near neutral conditions due to the assumption of a logarithmic wind profile. Neutral conditions are defined by the following range:

$$-0.01 < z/L < 0.01$$

where z/L is the scaled Monin-Obukhov stability length (Obukhov, 1971) measured by eddy correlation. In addition u_* and u values less than 0.1 m s^{-1} and 1 m s^{-1} respectively are excluded to account for inaccuracies in measurements during low windspeed conditions. After imposition of these conditions there are 472 half-hour observations of u and u_* during the defined snow covered period and 1015 during the snow-free period (Figure 5-12).

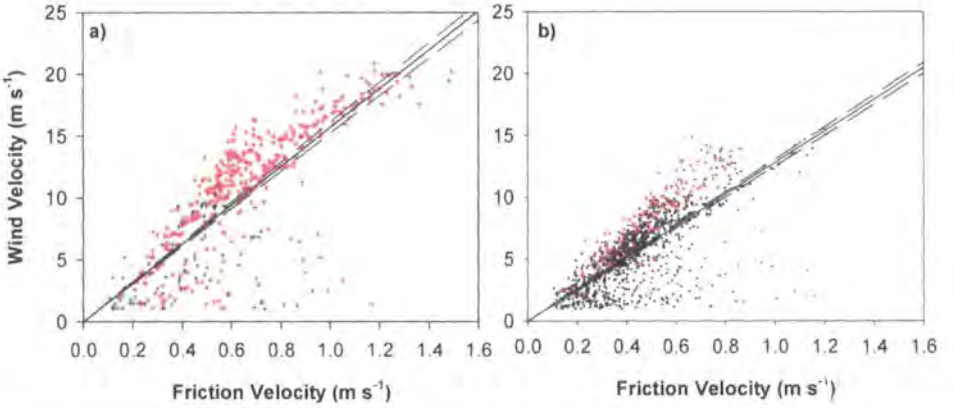

Figure 5-12: Scatter plot of wind velocity against friction velocity. Plot a represents winter observations (1st December – 1st April) and plot b summer observations (1st May – 1st October). Plotted in black are observations from the Solent, and in red are observations from the Mk4 Hydra. The black line shows a fitted line and the blue dashed lines represent the 95% confidence intervals.

Vegetation height across the eddy flux footprint is approximately 0.05 metres, d is therefore assumed equal to 0.66 during snow-free periods and zero under snow covered conditions. Solving Equation 5.3 reveals a roughness length of 0.00481 m for snow and 0.0154 m for snow-free conditions. The value of surface roughness for snow covered surfaces is comparable to ranges of 0.1 to 6.8 mm and potentially up to 20 mm for 'weak friable snow,' as denoted in Morris (1989) and Moore (1983). Assuming a displacement height equal to zero under snow-free conditions reveals a roughness length of 0.0156 metres, emphasising the relative insensitivity to d where vegetation is short and z is large. The variability shown in Figure 5-12 is associated with a varying footprint with wind direction and windspeed. The aerodynamic properties vary slightly with topography and vegetation height. Evidence of a secondary trend in Figure 5-12 can also be seen, in which, relative to the main trend, high friction velocities are observed for low wind velocities. This appears to be associated with boundary layer stability tending towards the stable

side of neutral. This is evidence of a reduction in turbulent mixing and laminar flow decoupling the friction velocity and wind velocity.

The derivation of aerodynamic resistance to momentum is critical to simulating fluxes in surface exchange schemes. There is however a great deal of debate on the use of a constant relationship between the roughness lengths for momentum and heat and vapour transfer as is currently used in numerical simulations (e.g. Blyth, 1994; Verhoef, 1994). This is examined in greater detail in section **6.3.1a),** and the basis behind the roughness length in section **2.3**.

5.6.3 SURFACE RESISTANCE

Surface resistance describes the ease with which evaporation from the soil and vegetation can take place (see **2.3**). The surface resistance consequently has important implications for the turbulent fluxes, the Bowen ratio, and the surface temperature. The surface resistance is largely a function of soil moisture content, for vegetation free surfaces and a function of stomatal resistance for vegetation. It would be expected that the surface resistance is high during the frozen period and rapidly decreases during the thaw period due to the abundance of surface water from snowmelt.

Surface resistance can be calculated from eddy correlation data, by replacing the available energy term in the Penman-Monteith equation (Equation 2.17) with the measured turbulent flux, and inverting for the surface resistance (Lloyd, 2001). However, doing this with the Solent/Licor data suggests a high degree of variability in the surface resistance associated with a varying source area and consequently snow covered fraction. It appears the assumption of the sum of the latent and sensible heat fluxes equalling the available energy is invalid during periods of patchy snow-cover. This is because the sources and sinks of the turbulent fluxes may not necessarily correspond. The snow patches act as sinks for sensible heat, and snow-free areas as a source, whilst both surfaces act as a source of latent heat. Consequently surface resistance is assumed to be zero for snow covered surfaces and is modelled (Cox *et al.*, 1998) for snow-free regions and used as a driving variable in the subsequent modelling chapter.

5.7 *Albedo*

Surface albedo is crucial to modelling energetics at the land-surface, particularly for snow-cover as a result of its strong feedback properties. Albedo is defined as the ratio of reflected to incident radiation. Consequently, the albedo plays an important role in melt energetics. Albedo has a spectral signature, but is greatest for the shortwave radiations with wavelengths between 0.15 and 3.0 μm. The albedo referred to in the present study corresponds to the spectral albedo integrated over the shortwave radiation window (**2.3**).

The albedo of snow is a function of snow depth, grain size, liquid water and solar incident angle with the surface (Oke, 1987; Wiscombe and Warren, 1980). Contamination with plant material, soot and dust are also important to snow albedo (e.g. Hansen and Nazarenko, 2004; Warren and Wiscombe, 1980). The albedo of fresh uncontaminated snow can be as high as 0.95, and as a low as 0.4 for old metamorphosed crystals (Oke, 1987).

Observations (**3.3.1b**) made with a collimated albedometer indicate a fresh snow albedo of 0.85, slightly higher than the default value used in MOSES 2, but as would be expected for relatively clean arctic snow. However, observed albedos showed a great deal of spatial variability associated with vegetation above and just below the snow surface, especially for shallow snowpacks. The observed albedo is thus a composite of the snow and vegetation albedo. Separating the albedo effect in a numerical model requires a dual-source canopy model, alternatively an effective albedo parameterisation formulation can be used. Exposed vegetation may have a significant effect on the surface energy balance and consequently melt rates, as an exposed canopy may be several degrees warmer then the underlying snow surface (Bewley *et al.*, 2005; Pomeroy *et al.*, 2006).

In the standard MOSES configuration, the effective albedo is parameterised as a function of the snow depth required to cover the vegetation (where vegetation height is approximated as ten times the roughness length). The fraction of the vegetation covered by snow is given as:

$$f_{snow-veg} = \frac{S}{S + k\rho_{snow} z_{0snowfree}}$$

Equation 5.4

where S is the water equivalent of lying snow, $z_{0_{snowfree}}$ the snow-free surface roughness length and k, an adjustable parameter assumed equal to 10 (thus $kz_{0snowfree}$ is equal to the vegetation depth). The fraction of the vegetation covered by snow is used to calculate an effective albedo as:

$$\alpha_{effective} = \alpha_{snowfree}(1 - f_{snow-veg}) + f_{snow-veg}\alpha_{snow}$$

Equation 5.5

where α is the surface albedo.

Snow albedo models generally fall into two categories: temperature-dependent and prognostic. In an intercomparison study, Pedersen and Winther (2005) found a better performance by prognostic models, but a sensitivity to the snowfall required to reset the albedo to that of fresh snow. The snow albedo model used in MOSES is a simplification of the Marshall (1989) parameterisation of the prognostic Wiscombe and Warren (1980) spectral snow albedo model (Essery *et al.*, 2001) and is defined in detail in **12.1.3.**

During 2005, measurements of albedo and snow-depth were made across the domain (Figure 4-4b) using a collimated albedometer (**3.3.1b**). The relationship between depth and collimated albedo is shown in Figure 5-13.

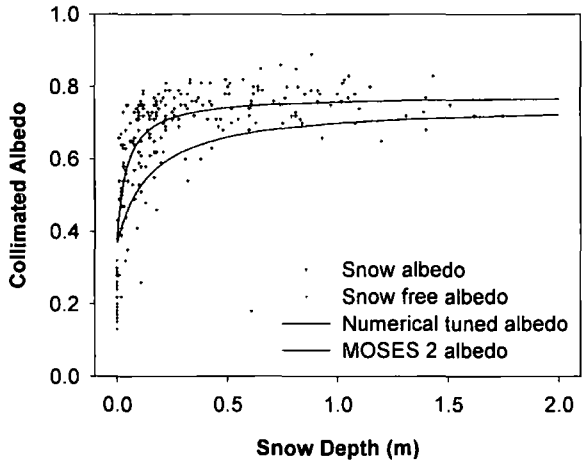

Figure 5-13: Variation of collimated snow albedo with snow depth.

Using the standard MOSES formulation for effective albedo generally underestimated measured values. A much better fit was acquired by setting the coefficient of the roughness length, k, in Equation 5.4 to a value of 2.9 (n=400, r^2=0.42). The coefficient is a function of the density of exposed vegetation canopy above the snowpack.

Long-term average *in-situ* measurements of snow-free albedo indicate an albedo of 0.19 which varies slightly with phenological phase. This falls within a suggested albedo range of 0.18 to 0.25 for tundra (Oke, 1987). The evolution of snow-cover albedo is a function of both snowpack metamorphism and the gradual exposure of vegetation during snowmelt. Observations of effective albedo and snow depth made in a late-lying snow drift are shown in Figure 5-14.

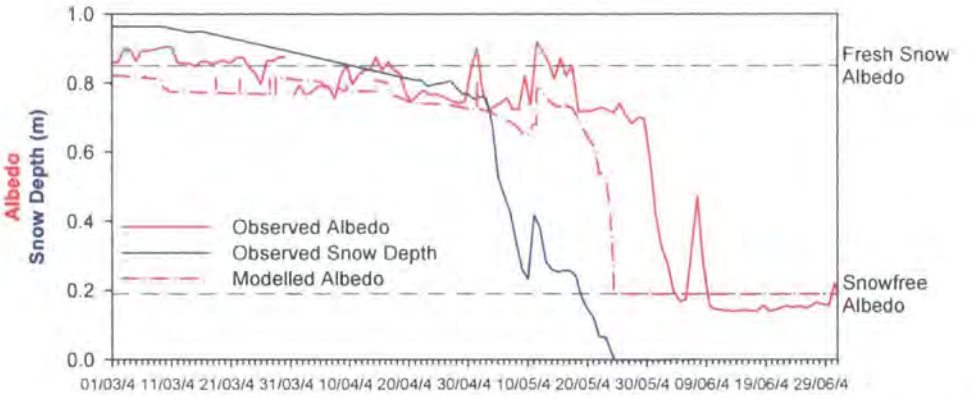

Figure 5-14: Observed and modelled albedo in a late-lying snow drift. Snow depths are a composite of manual and automated UDG measurements. Observed albedo values are for solar noon for March to June 2004.

Immediately obvious from Figure 5-14 is the approximate 10-day difference in timing between the snow-free date from the snow-depth and albedo sensors. This is due to the slightly different siting of the snow-depth and radiation sensors and the different depth of snow at each location. Observed albedo shows a gradual decline from the start of March with spikes most likely associated with snowfall and drifting. The greatest change in albedo occurs at the start of June when the snow depth is less than 0.1 m. At this point the albedo rapidly drops as more vegetation becomes exposed. Also shown in Figure 5-14 is the modelled albedo using the prognostic albedo model, combined with the effective albedo parameterisation. The model, although offset by 10 days, generally simulates the initial decline in snow albedo well, but fails to model the spikes in albedo as the effect of drifting snow is ignored in the model. There are also potential errors in the snowfall data, as well as poor parameterisation of the snow depth required to reset the albedo. More importantly the model accurately represents the rapid decline in albedo during snowmelt. It should be noted that the model would not be significantly degraded by using a simple switch between a snow and snow-free albedo, as the melt occurs over a short period of time and is controlled by turbulent rather than radiative energy exchange (Chapter 6). As noted by Essery *et al.* (2005) the Gray and Landine (1987) model, consisting of a simple three stage model; an initial decline of albedo with age, a rapid decline during melt and final albedo for snow-free conditions, would be as effective as the prognostic model.

5.8 Surface Emissivity

The surface emissivity is the ratio of the radiation emitted by a surface to the radiation emitted by a black-body radiator. Surface emissivity is not explicitly dealt with in this study and is assumed equal to unity for both snow and tundra surfaces. Oke (1987) suggests values of 0.82 to 0.99 for old and fresh snow respectively, and 0.9 to 0.99 for tundra. A change in emissivity of 0.1 corresponds to an approximate error in the estimated outgoing longwave radiation of 30 W m^{-2} for a melting snow surface. The model therefore shows a degree of sensitivity to this parameter, but for want of a better value, unity is used throughout this study.

5.9 Summary

The presence of snow clearly influences the local meteorology and boundary properties and the influence changes as the snow melts and becomes patchy. Observations of wind direction and windspeed imply that windflow is not simply a result of the interaction between large-scale circulation and topography but that mesoscale circulation has an important effect when the tundra is largely snow-free and while the birch forest retains snow, leading to the formation of northerly breezes blowing upslope from the forest to the tundra. The most significant conclusion from this chapter is that the boundary layer temperature appears to be responding to landscape scale heat fluxes, supporting the use of tiling schemes in large scale atmospheric models. The lack of any evidence for advection driven heterogeneous melt shown in **4.5.2** implies that the use of separate energy balances for snow and snow-free surfaces combined with a effective parameterisation of snow covered fraction will adequately simulate the boundary later response to surface fluxes and also the melt of patchy snow. This is investigated in greater detail in the following chapter.

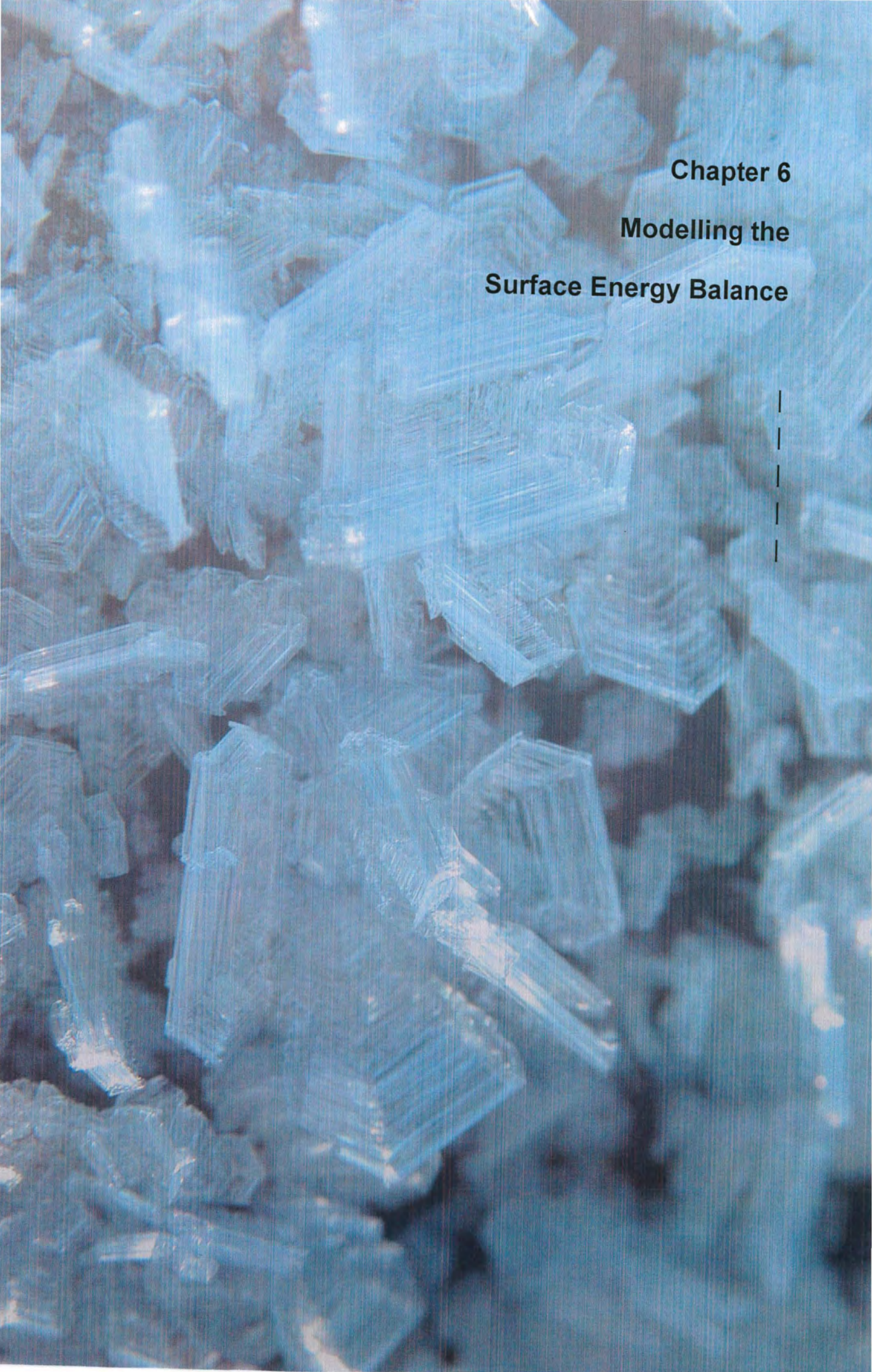

Chapter 6

Modelling the Surface Energy Balance

6 Modelling the Surface Energy Balance

6.1 Introduction

The energy balance of a patchy snow-cover is complex due to the interaction between the surface and overlying air mass (**5.3**), the potential for small-scale advection and the rapid variation in snow covered area. These processes are particularly important during the melt period when available energy is greater than any prior period through the winter.

The core question of this thesis centres on how to represent complex snow-covers in regional and global models in order to accurately simulate the contribution of the land-surface to the heat and water balance of the overlying atmosphere, critical to numerical weather prediction. Previous chapters have presented evidence that the spatial variation in melt is small and uncorrelated to advective processes, and that the boundary layer air temperature is responding to the landscape as a whole. This chapter presents data and model results of the energy-balance of snow and snow-free patches to test whether the conclusions made in the previous chapters hold true in numerical simulations.

Critical to successful modelling of the energy balance is the accurate simulation of snowmelt, as this effectively defines the fractional coverage of each surface type given a snow-cover distribution. Processes relating to the energy-balance of snow-free surfaces remain extremely important in determining boundary layer heat and moisture particularly processes pertaining to soil moisture and soil freeze-thaw. However, these processes are beyond the scope of this thesis and are the subject of ongoing research within the STEPPS project. Processes relating to boundary-layer mixing are not dealt with here, and the boundary layer state is represented by tower measurements at 2 m. This chapter concludes that patchy snow-covers can be represented using separate energy balances for snow and snow-free surfaces and an appropriate parameterisation of the distribution of snow-cover which in turn defines the snow covered fraction.

6.2 *Melt Period Observations*

6.2.1 AVAILABLE ENERGY

The available energy in the Arctic has a strong seasonality associated with day length and solar intensity. During the deep winter day lengths are short and shortwave radiation is low, as the season progresses day length increases concomitantly with solar shortwave radiation. Longwave radiation is principally a function of atmospheric temperature and shows a relatively small seasonal variation. The increasing energy availability that allows snowmelt to take place is incoming shortwave radiation. The increase in solar insolation leads to a doubling, from 20 to 40 MJ day^{-1} m^{-2}, of available energy during the March to June period, totalling 3400 MJ m^{-2} over the entire period (Figure 12-1). However, much of these energies are either reflected or re-radiated leading to a net available radiation of 150 MJ m^{-2} for a snow covered surface; this increases to 550 MJ m^{-2} for a low-albedo snow-free surface. Snow surveys indicate that an average of 40 MJ m^{-2} of energy (latent heat of fusion) is required to melt the observed snow-cover for the study site. However, when the distribution of snow-cover is included it becomes evident that net radiation is insufficient to account for the observed melt. The deepest drifts, equate to a minimum of 240 MJ m^{-2} of melt energy (value calculated assumes only melt with no evaporation and is thus based on the latent heat of fusion) compared to a radiation receipt of 150 MJ m^{-2} for snow-cover. The remaining energy for melt must come from turbulent flux, implying snowmelt is principally controlled by sensible and, to a lesser extent, latent heat flux. The source of this energy may be synoptic scale advections of warm dry air or local fluxes from snow-free surfaces, leading to small-scale advection or the development of a warm, moist well-mixed boundary-layer as suggested in **5.3**. The magnitude of the differences in net available radiation between snow and snow-free surfaces show that local processes must be important to the landscape energy balance.

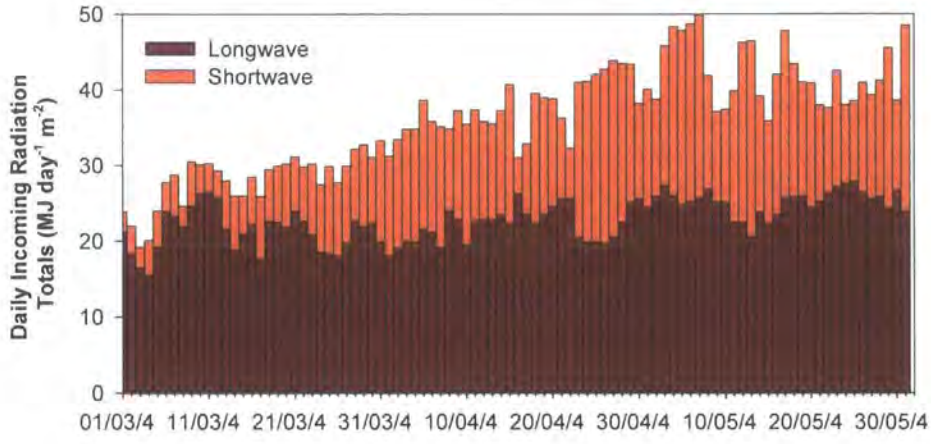

Figure 6-1: Daily incoming radiation between March and June 2004.

6.2.2 SURFACE OBSERVATIONS

Observations of typical patches of snow and snow-free ground were made during the March-June period of 2004 (Figure 6-2). The 'snow-free' sensors were free of snow throughout the period with the exception of a 5-day period beginning 11th May 2004, when a late snowfall covered the site. Sensors were located so as to remain either as free of snow, or as covered by snow as possible to maximise data receipt. The snow sensors were located in a deep drift and the snow-free sensors on a ridge top that is likely to remain snow-free throughout the period.

Observations made included automatic measurements of albedo (**5.7**), surface temperature, snowpack temperature and snow depth. Observations of sensible heat flux were also attempted using the temperature variance method, however a number of difficulties were experienced with the method, as discussed below.

The snowpack became isothermal in late March, and a rapid period of melt began five days later. Prior to this, observations of surface temperature suggest melt occurs at the surface during the midday hours.

Surface temperature data show the strong difference between snow and snow-free surfaces from mid-March onwards. This corresponds to thawing of the surface soil layer and increasing daily insolation levels. Surface temperatures measured for the snow-free patch indicate a maximum temperature of 30°C under high radiation

conditions whilst the melting snow-surface is constrained to 0°C. Under these conditions there is a large potential for advection of sensible heat.

Also shown in Figure 6-2 are measurements of windspeed, specific humidity and air temperature, corresponding to boundary layer properties. From these measurements it is possible to model turbulent flux using the bulk aerodynamic formula. Evident during the period of rapid melt are high air temperatures, high windspeeds and high water vapour levels, all of which indicate sizeable turbulent transfer of energy into the snowpack. The short warm periods (above 0°C) observed throughout the spring melt phase are typical of the meteorological conditions during this period for the Abisko region. Similar periods can be found throughout the long-term meteorological data available from ANS.

The question arises of why the temperature variation method failed to work. The basis behind the method is that a flux of sensible heat will lead to an observed skewness in the distribution of temperatures measured at a point within the boundary layer. The skewness or variation of the temperature will directly relate to the sensible heat flux. The method is only suitable for the unstable range and the failure may be associated with the formation of stable conditions, which are expected when warm air overlays a cold snowpack. However, turbulence is high and the suggestion from eddy correlation is prevailing unstable conditions during the daylight hours during snowmelt. Although the exact reasons behind the failure of the method are unknown, it is hypothesised that the boundary layer condition over patchy snow are highly variable with internal boundary layers forming and high energy turbulent eddies breaking the structures up. The formations of internal boundary layers are thus unstable. These processes will all act to change the temperature measured at a point and change the characteristics of a temperature distribution, leading to an underestimation of the observed heat flux. . It is thought that the method failure is associated with a constant change in boundary layer properties associated with the patchiness of the landscape.

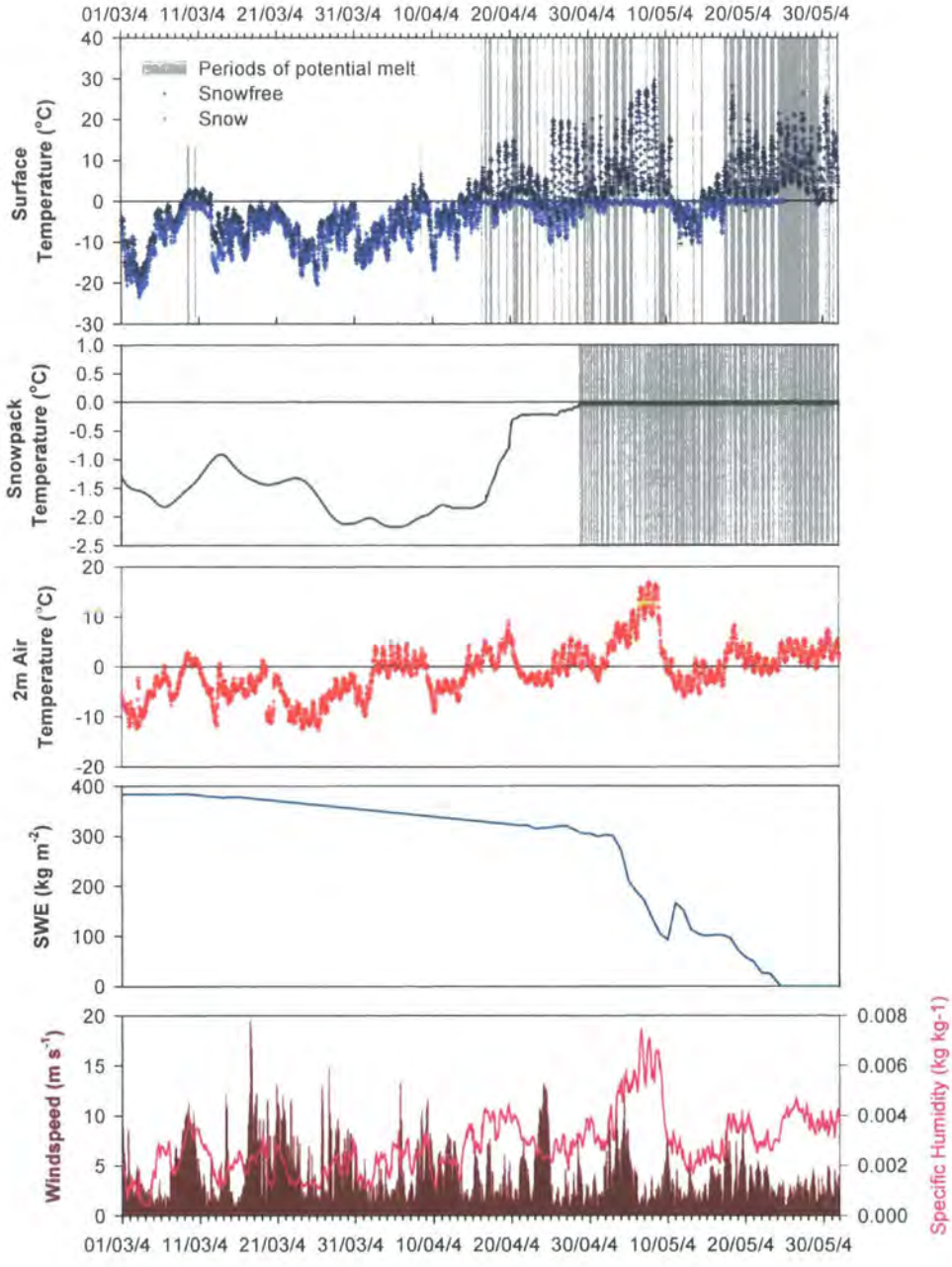

Figure 6-2: Surface properties during the spring melt phase of 2004. Grey sections indicate potential melt periods when the temperature is at the melting point. Air temperature, windspeed and specific humidity are measured at the main AWS.

6.3 *Surface Energy Balance*

The results presented here are modelled fluxes from the MOSES model validated against surface temperature and SWE. The models are configured to run as point simulations in this section. The spatial averaging of snow albedo is thus switched off. Measurements of turbulent flux made at the patch scale would provide better validation data but are unavailable. Landscape-scale heat fluxes are measured by eddy correlation.

6.3.1 SNOW SURFACES

The energy balance of snow covered surfaces is complicated by surface melt. The rate of melt is defined by initially solving the energy-balance, assuming no melt, for the surface temperature. If the surface is melting then the solved surface temperature will be above the melting point. In this case, the energy balance is solved for a second time, this time with the surface temperature set to the melting point, and solving for the melt heat flux. The energy balance of a snowdrift is modelled here with the MOSES snow model, but with the effective albedo parameterisation switched off. The effective albedo is a parameterisation of the amount of snow-covered fraction in gridbox simulations.

Model validation is complicated by the model layer configuration. In the current configuration the surface soil and snow layers are coupled to make an effective surface layer, this means that modelled surface layer temperature and heat fluxes are not strictly comparable to measurements. The best validation data for a melting snow-cover is SWE. Surface temperature is also useful as it is directly related to surface melt, turbulent exchange and surface heat flux.

The model is initialised with observed data. Volumetric soil moisture is set at 0.2 $m^3 m^{-3}$, and soil temperature and surface temperature are set as -10°C. Sensitivity analysis suggests the model is insensitive to the choice of these values. Model parameters are set based on observations, standard MOSES values, or from calibrated values (Table 6-1).

Table 6-1: Parameters used in the point MOSES snow model. Parameters shaded in grey are derived from field measurements, other parameters are standard parameters used in MOSES. Calibrated parameters are tuned values used to fit the model to validation data.

Parameter	Variable
Fresh snow albedo	0.85
Albedo reset snowfall water equivalent	10 kg day^{-1}
Maximum grain size	2 mm
Snow Density	400 kg m^{-3}
Snow Heat Conductivity	0.265 W m^{-2} s^{-1}
Aerodynamic Roughness Length (calibrated)	0.001 m

Model calibration was completed by tuning aerodynamic roughness length to observed SWE for the rapid period of melt shown in the UDG trace. Changing the roughness length for momentum from an eddy correlation derived value of 0.00481 m to 0.001 m resulted in a 15 day shift in the snow-free date. The higher roughness length led to an increased turbulent flux into the snowpack and premature melting. A roughness length of 0.001 m is more in keeping with values suggested in the literature (Moore, 1983; Morris, 1989). The relationship between the roughness lengths for momentum and heat has been a matter of some debate in the literature and is discussed further in **6.3.1a)**. Snowpack observations (Chapter 4) show that melt-refreeze within the snowpack is a common process, but is not represented in the MOSES snow model. To investigate further a simple representation of snowpack hydrology is tested in **6.3.1b)**.

Simulation results are shown in Figure 6-3 and Figure 6-4. Simulated surface temperature RMSE is 2 K (estimated instrument error 1.5 K) and model efficiency tests are good (NS r^2=1, d=1). Statistics are not calculated for SWE as only daily measurements are available, however model fit is generally close, with the model overestimating the snow-free date by two days. The model fails to simulate the

magnitude of an observed peak in SWE on 12th June, which most likely correlates with a drifting event, but does simulate a slight increase in SWE associated with a small snowfall.

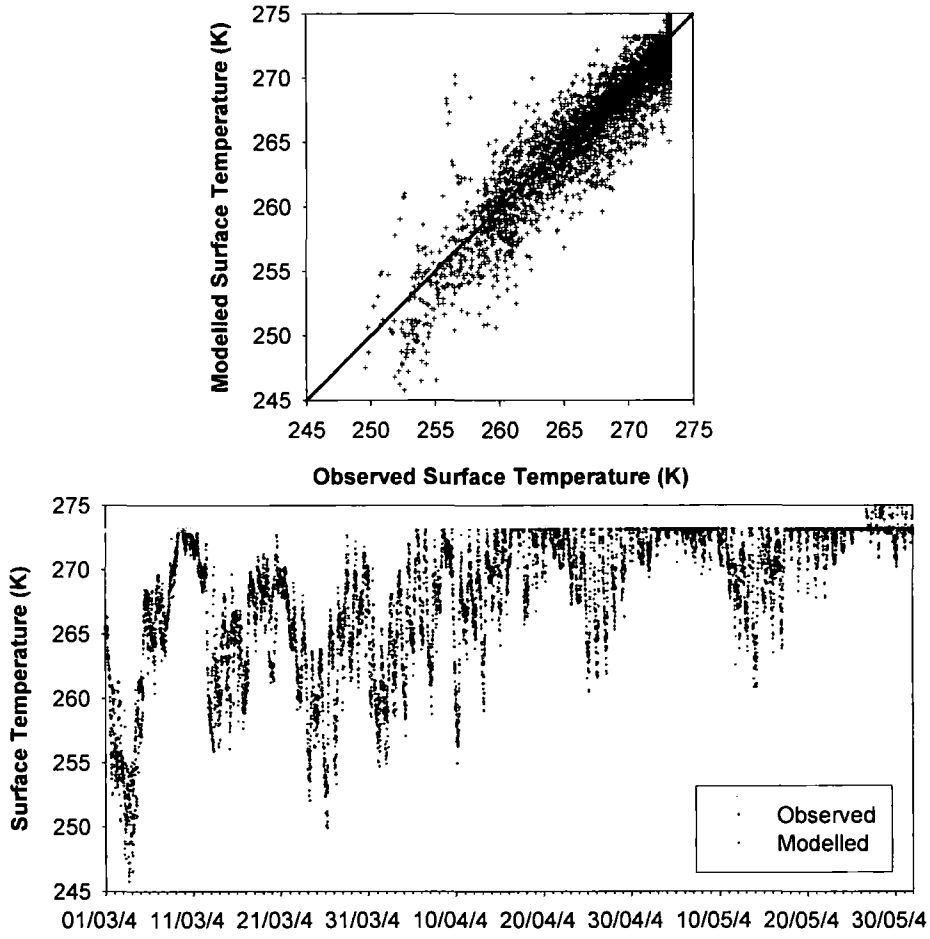

Figure 6-3: Observed and simulated surface temperature. Data are from the automated snow station or are point MOSES simulations for a snowdrift. The upper plot shows a 1:1 plot (blue line) and the lower plot shows a time series.

Over the three month simulation period, the equivalent of 400 kg m^{-2} of ablation takes place. Of the energy required for ablation 350 MJ m^{-2} comes from shortwave radiation, 250 MJ m^{-2} is re-radiated as longwave radiation, 75 MJ m^{-2} evaporates, 120 MJ m^{-2} is transferred as sensible heat flux and 20 MJ m^{-2} is conducted into and through the snowpack. Of the original snowpack 374 kg m^{-2} melts and 26 kg m^{-2} evaporates. At first glance it would appear that melt is controlled by shortwave radiation, however during the majority of the 3 months the snowpack is not melting, but is warming by a few degrees. The majority of the melt occurred

rapidly in a few days, which was followed by a 7 day quiescent phase, when there was a snowfall covering the majority of the site and air temperatures and humidity fall. The pack finally melted on 24th May.

The majority of the melt occurred in an 8 day period between 2nd and 10th May. During this period 228 kg m^{-2} of melt occurred, equating to an energy requirement of 76.3 MJ m^{-2}, a further 1 MJ m^{-2} was conducted through the pack and 8.7 MJ m^{-2} was radiated in the form of longwave radiation. Simulations suggest nearly 43% of the energy required for melt was from solar radiation (36.9 MJ m^{-2}), a further 33% from sensible heat flux (28.4 MJ m^{-2}) and 24% from latent heat flux (20.5 MJ m^{-2}). Latent heat fluxes during this period change from generally being away from the surface to being strongly into the pack. This corresponds with a strong temperature gradient driving sensible heat fluxes (10 to 15 K differences between surface and screen-level temperature) and a moisture-laden air (0.006 kg kg^{-1} specific humidity). The air has a dew point of 6 K when cooled adiabatically. This corresponds to a strong humidity gradient towards the surface, rather than a gradient away from the surface; leading to condensation and frosting of the snow surface which releases significant amounts of latent heat. The efficiency by which the latent heat of condensation relates to the latent heat of fusion was close to an order of magnitude. Therefore condensation of the surface of 7 kg m^{-2} leads to an energy release of 20.5 MJ m^{-2}, which in turn can melt 61 kg m^{-2} of snow. Condensation in warm humid environments was thus a highly efficient method to melt snow. Peak rates of condensation can be close to 1 kg m^{-2} per hour, but on average were a tenth of this rate. The 8 day period was also generally breezy with windspeeds of 5-10 m s^{-1}, creating efficient turbulent exchange and increasing these sizeable heat fluxes into the surface. Observations in the literature suggest that sensible heat into a melting snowpack can reach twice the net radiation during warm, windy conditions (Morris, 1989), often contributing around 50% of the energy balance (Pohl and Marsh, 2005; Pohl *et al.*, 2006a). However, in this Abisko case equivalent levels are reached under clear sky conditions; the warming of the snowpack and subsequent melt is thus driven by a combination of high radiative and turbulent fluxes.

The onset of melt is therefore rapid and is related to the increasing specific humidity, air temperature and windspeed during the period. The melt is correspondingly driven by the sensible and latent heat fluxes set against a background increase in shortwave radiation. It is indicative that during the previous 8 days the snowpack received slightly more shortwave radiation (42 MJ m^{-2}), but associated melt was just 50 kg m^{-2}, a fifth of that observed during the following 8 day rapid melt period. The quality of the model fit suggests that local advection processes are comparably unimportant, however it must be noted that advection processes increase melt at the edge and the model fits are for measurements made in the centre of a snow patch, where the energy delivered by advection is comparably smaller. The fact that the evolution of SWE at a point can be modelled excluding local advection in the model physics does not necessarily preclude advection as an important process on the larger scale.

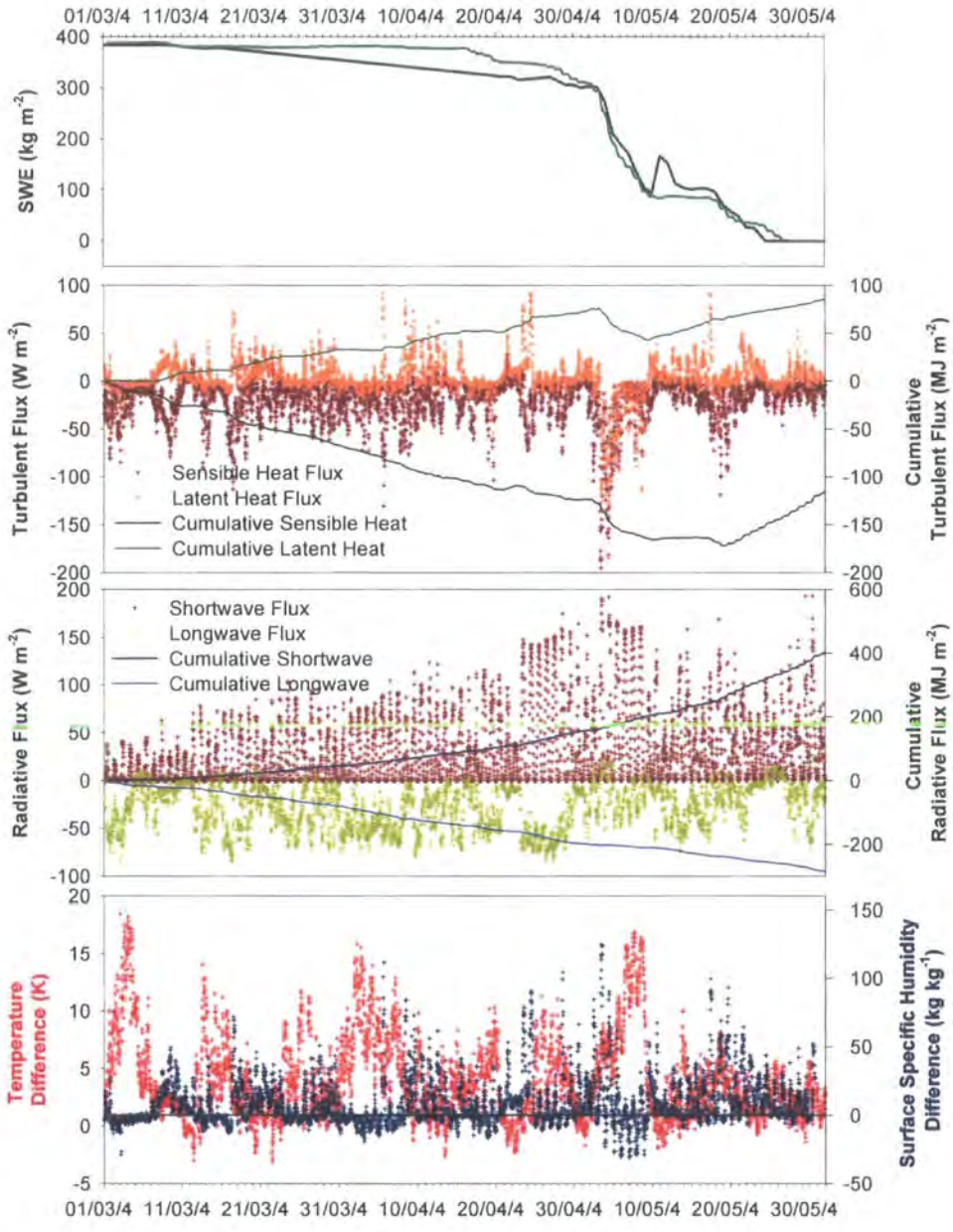

Figure 6-4: Modelled SWE, heat fluxes and surface-screen level differences in temperature and specific humidity for a point MOSES simulation for a snow drift. Observational data are from the automated snow station.

a) *Aerodynamic Roughness Length for Momentum, Sensible Heat and Water Vapour*

The aerodynamic roughness length for various scalars, including momentum, sensible heat and water vapour are defined as the height above the displacement height at which the scalar assume their surface value (Brutsaert, 1975). In the case of momentum, this is the theoretical height at which windspeed equals zero. For sensible heat and water vapour these are the heights at which the air temperature and vapour pressure are equal to those at the surface. The difference between roughness lengths for different scalars lies in the process of exchange across the surface; heat and water vapour are transferred by molecular diffusion, whereas momentum involves additional pressure forces (Brutsaert, 1975; Garatt, 1992). From a theoretical perspective the roughness length for momentum is expected to be greater than those for heat and water vapour, furthermore the roughness lengths for heat and water vapour are likely to be of similar magnitude due to the similarity in mechanism. In practice the aerodynamic roughness lengths for heat and water vapour are difficult to measure under controlled conditions, and even harder under field conditions. Accordingly, numerical models are normally parameterised in terms of the roughness length for momentum, which is more easily quantified from eddy correlation measurements (**5.6.2**) or roughness element description (Lettau, 1969). The roughness length for heat and water vapour are related to the roughness length for momentum by:

$$z_{0v} = z_{0h} = z_{0m} \exp\left(-kB^{-1}\right)$$

Equation 6.1

where k is the von Kármán constant, and B a dimensionless constant derived from wind-tunnel experiments. Early work by Thom (1972) and Garatt and Hicks (1973) found that kB^{-1} has a constant value of approximately 2 for vegetation, the roughness length for momentum is correspondingly an order of magnitude greater than the roughness lengths for heat and water vapour. There is some debate in the micrometeorological literature about the extent to which the assumption of a fixed ratio holds true. The crux of the debate lies in whether a surface acts a 'bluff' or 'permeable' body, and at what point a transition occurs between the two. Over a rock strewn grassy surface, representing a partial 'bluff' surface, the value of kB^{-1}

varies with the Reynolds number (degree of turbulence), in which case the value of kB^{-1} does not remain constant (Kohsiek *et al.*, 1993). Similarly, observations for a homogeneous diffuse grassland also show strong variation in kB^{-1} (Duynkerke, 1992), whereas for a diffuse surface a constant value is expected. Model simulations have also shown a dependence of kB^{-1} on the parameterisation of surface temperature; a dual source model producing a different value of kB^{-1} to a single source (Blyth and Dolman, 1995). The conclusion from the literature is that there is no unanimity over a single value for kB^{-1} whether a surface is acting as a bluff or permeable body.

Tuning the MOSES point snow model aerodynamic roughness length for heat and water vapour z_{0h} suggests a value of 0.0001 m for snow-cover, whereas derived values from the eddy correlation tower suggest an aerodynamic roughness length for momentum z_{0m} of 0.00481 m. The combination of modelled and observed roughness lengths used here suggests the ratio to be closer to 50. The reason for the differences in this ratio lies in the poor understanding of the expected relationship and also the differing measurement techniques for deriving the roughness length. The first is an average over a flux tower footprint; approximately 300 m in extent (see **5.5**), the second is derived from a numerical model at a point. There is undoubtedly a difference between snow acting as a permeable body at a point and over an approximate 300 m fetch of variable topography, however there is no clear unanimity within the literature over the type of behaviour expected.

The conclusion is thus that an aerodynamic roughness length for heat and water vapour of 0.0001 m provides a better simulation of SWE and falls within values found in the literature. However the relationship between the roughness length for heat and momentum over a patchy snow-cover remains inconclusive. The use of a fixed value of kB^{-1} in surface exchange schemes is a matter of some concern, however no suitable solution is available. The common use of a fixed ratio thus persists and is a fixed parameter in GCMs.

b) Water Retention

A significant difference in model formulation and snowpack observations is the retention of liquid water within the crystal matrix. The assumption made within the standard model is that melt either infiltrates the soil or runs off if the infiltration capacity is reached. This retained liquid water can refreeze, especially as the surface temperature falls overnight (Figure 6-2) leading to an overestimation of runoff and premature snowmelt in the standard model. Laboratory observations suggest that the irreducible volumetric liquid water fraction of a wet snowpack is 0.065 to 0.085 (Coléou and Lesaffre, 1998), and observations suggest a volumetric water retention fraction of approximately 0.1 (**4.3**).

A simple water retention model was thus tested, in which up to 10% of the snow volume can be retained as liquid water. Should the surface layer temperature fall below zero, the mass of snow could refreeze, releasing latent energy. The fraction of the pool to refreeze was limited by the energy that would raise the layer temperature to the melting point. This simple parameterisation is complicated due to the use of an effective surface snow/soil layer. The layer temperature is thus not strictly the simulated bulk snowpack temperature.

Model runs found the parameterisation significantly increased the duration of snow lie and failed to further increase model fit. This process is thus left out of the current model formulation. Although this process is undoubtedly important the failure to improve model performance lies in the model formulation. A layered snow-model with hydrologic and heat conductivity between layers would be a much better parameterisation of process. A layered snow model is intended for future MOSES/JULES releases.

6.3.2 SNOW-FREE SURFACES

The dynamics of a thawing snow-free surface play an important role in the landscape energy-balance. The relatively lower albedo (0.19) means the surface responds more readily to seasonal changes in radiation levels. The dynamics of a thawing snow-free surface are complex due to the partitioning of energy between thawing frozen water and soil temperature. This has consequences for the surface temperature, which in turn effects the turbulent exchange. This is further

complicated by the lack of liquid water which puts plants under a great deal of moisture stress. The thaw releases liquid water and thus affects the surface resistance feeding back on the partitioning of the turbulent flux. Thus, accurate modelling of moisture and thermal properties of arctic soils are essential to accurate simulation of surface fluxes, however the theoretical basis for this is incomplete at present (Hall *et al.*, 2003).

Included here are simulation results from MOSES run with the C3 grass surface resistance to moisture. Table 6-2 gives the site specific parameters, and the soil parameters are from Hall *et al.*, (2003) and Lloyd *et al.*, (1999). Moisture input to the soil is from the surface runoff modelled in **6.3.1**. Excluding this moisture input leads to unrealistic dry soil and moisture stressed plants. A great deal of surface standing water was observed at this time, and this assumption is more valid than assuming no water input and concurs with the aim of a single soil layer used in subsequent tiling schemes. The model is initialised with surface and soil temperatures set at -10°C, and a volumetric soil moisture content of 0.2 $m^3 m^{-3}$ based on measurements. The model was spun-up with data from the previous 4 weeks to separate the frozen and unfrozen soil moisture fractions. Both phenology and canopy heat capacity are switched off in the current configuration.

Table 6-2: Parameters used in point snow-free model. Parameters are derived from field observation.

Parameter	Variable
Surface Albedo	0.19
Aerodynamic Roughness Length (Observed)	0.0481 m
Rooting Depth	0.2 m
Leaf Area Index	0.8

Results from the simulation are shown in Figure 6-5. The model has a tendency to underestimate surface temperatures during the midday hours, with an overall RMSE of 4.4 K. However measures of model efficiency imply the model does a

good job at representing the variation (NS r^2=1.0, d=1.0). The diurnal range in the error can partially be explained by the diurnal error in the IRT observations (**11.3**).

During the three months of the simulation, 534 MJ m^{-2} of energy is available from radiative sources; of this, 320 MJ m^{-2} warms the overlying air, 173 MJ m^{-2} is used in evaporation and 40 MJ m^{-2} is conducted through the soil. Over the simulation period this equates to 69 kg m^{-2} of liquid water. During the first three weeks of the simulation, soils are frozen and vegetation is highly water-stressed. Any evaporation from this period comes from surface water made available from snowmelt. This is illustrated in the Bowen ratio (ratio of sensible to latent heat flux), which shows a great deal of variation and rapid change of sign. During this period the sensible heat flux is generally into the surface and is used to warm the soil and thaw frozen water. During the start of April the soil warms to the melting point (although a significant proportion of water remains frozen and the plants can access a limited amount of water) leading to latent heat fluxes up to 200 W m^{-2} from surface and soil water. From this period on, the soils thaw and the plants are available to transpire fully resulting in strong evaporation and a rapid increase in the surface conductance.

The turbulent fluxes during the rapid period of melt described above are generally upwards during the daylight hours and strong. Sensible heat fluxes of 400 W m^{-2} are simulated during midday conditions and corresponding latent fluxes of 200 W m^{-2}, evaporating up to 0.2 kg of water per hour, mainly from surface water.

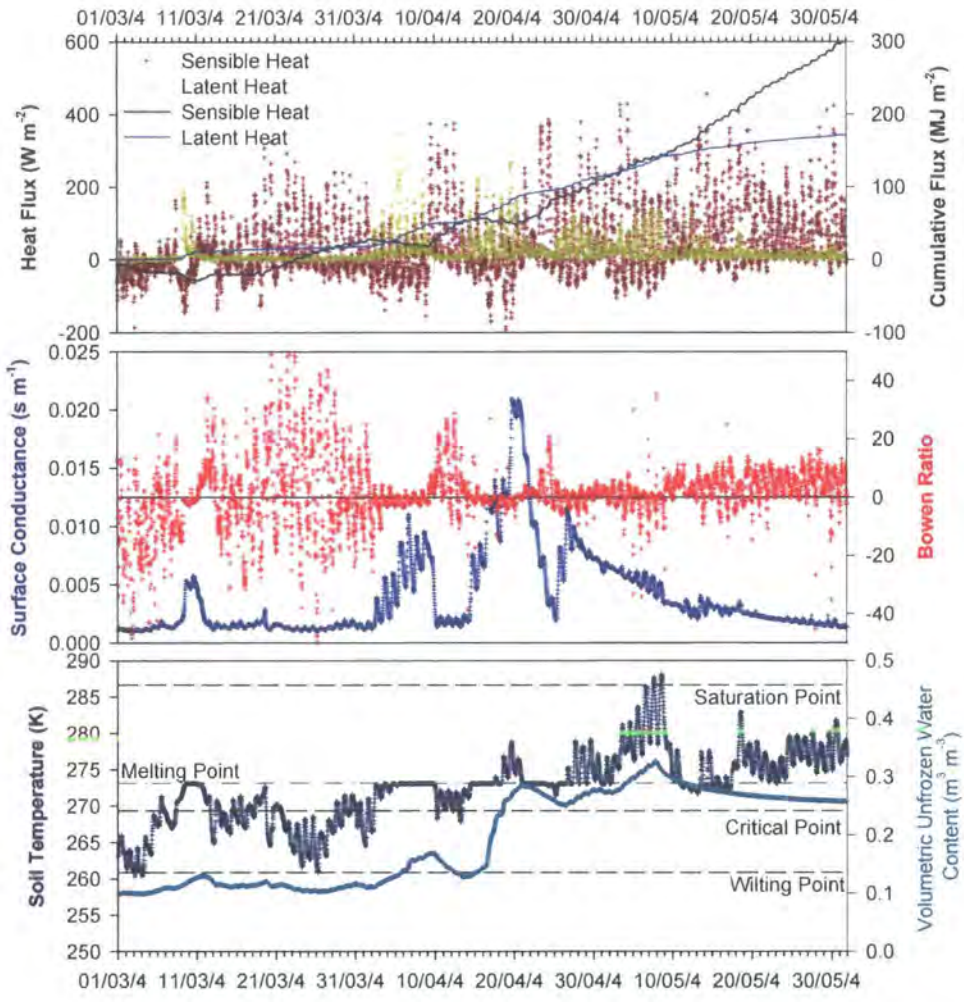

Figure 6-5: Modelled turbulent fluxes, surface conductance, soil temperature and soil moisture for the snow-free sensor site. Soil temperature and moisture are from the surface 0.1 m of soil.

a) Sensitivity to Soil Freeze-thaw

The Bowen ratio is strongly controlled by the availability of liquid water either at the surface, or within the soil matrix. The volume of liquid water is dependent on the fraction of frozen to unfrozen water in the soil, and thus the freeze-thaw conditions of the soil. The modelling of freeze-thaw processes is an area of concern in the current MOSES model configuration (Hall *et al.*, 2003), and is an area of current research (David Sayer, personal communication).

The turbulent fluxes from the snow-free surfaces are of importance to the energy-balance of the landscape and, potentially, may be a key driving factor in the energy

available for melt. A simple way to illustrate the sensitivity of the Bowen ratio to water availability is to modify the wilting and critical volumetric liquid water content points. Rather than adjust the actual volume of liquid water, this simple experiment allows the vegetation to access water at varying volumetric concentrations. Both the wilting and critical points are varied from 0 to 0.6 in 0.01 intervals, and the cumulative flux over the simulation period is summed. In theory, the wilting point cannot exceed the critical point, however when it does so in the simulation, the wilting point takes precedence. The results from this experiment are shown in Figure 6-6.

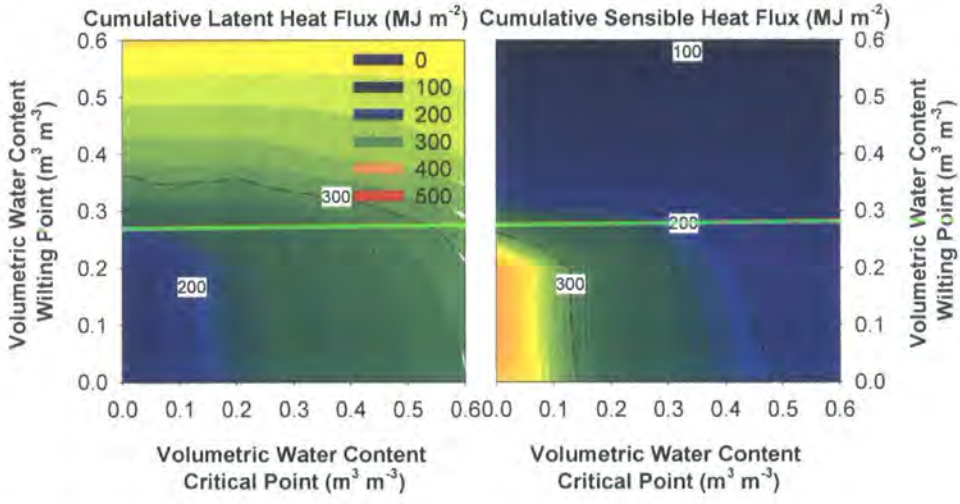

Figure 6-6: Sensitivity of modelled heat fluxes to the wilting and critical points.

Sensitivity analyses show that the cumulative sensible and latent heat ranges from 145-386 MJ m^{-2} and 43-383 MJ m^{-2}. Generally, modifying the water use points affects the Bowen ratio rather than the total turbulent flux. The sensitivities shown are a function of the step change in soil moisture shown in Figure 6-5. Simulations correspondingly show a sensitivity to the wilting point around 0.25 m^3 m^{-3}, as this is the post-thaw volumetric soil water content. Sensitivity to the critical point is lower as it is the point at which plants start to become stressed and control water use, rather than stop transpiring, which occurs at the wilting point.

Although this experiment does not explicitly vary the soil thaw physics it is an indicator of the sensitivity of the turbulent flux in simulation of soil freeze-thaw patterns. Clearly, to simulate correctly the landscape energy-balance during freeze-thaw conditions requires suitable parameterisations of this process.

6.3.3 LANDSCAPE SCALE ENERGY BALANCE

Simulations so far have concentrated on the energy-balance of individual points centred in a snow and snow-free patch. The fluxes at the landscape scale are complicated by the fraction of snow-cover, the distribution of snow, soil moisture and soil freezing and the interaction between patches.

The landscape-scale heat fluxes are measured using the Solent-Licor eddy correlation system. The observed fluxes are a composite of the fluxes taking place within the footprint of the system. The footprint varies with wind direction, and stability within each measurement period. However on average the footprint climatology is an appropriate representation of the research domain (**5.5**). The bias towards snow and snow-free patches varies as the snow patches melt, and in general there is a bias towards the snow-free patches, as the tower was intentionally located on a relatively flat piece of ground. Thus, eddy correlation fluxes cannot be seen as true landscape averages. The observations made during the melt period are shown in Figure 6-7.

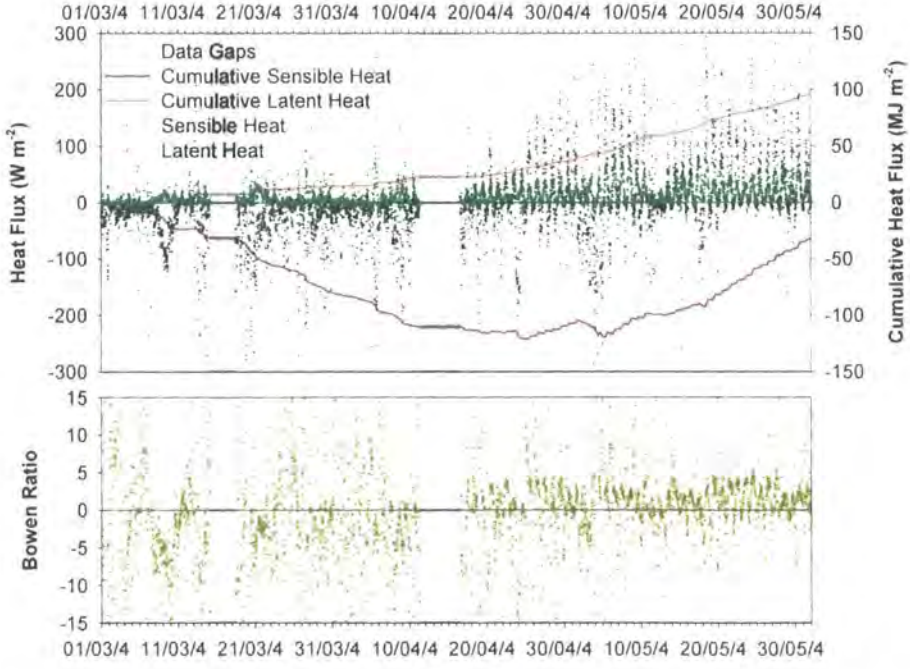

Figure 6-7: Landscape average turbulent fluxes and Bowen ratio as measured by Eddy Correlation during the melt period.

Generally, over the measurement period sensible heat fluxes are directed towards the surface, and the latent heat fluxes into the atmosphere, when the snow-cover is largely complete. However, a change occurs during the observed period of rapid melt in which sensible heat fluxes are directed away from the surface. This is echoed in the Bowen ratio, which is highly variable early in the period, when fluxes are low due to a largely snow covered footprint and a high albedo. Later, as the snow-cover recedes, the fluxes increase in size and the energy-balance is dominated by upward heat fluxes. During the period of rapid melt, the observed sensible heat fluxes are strongly downward, implying the snow patches are drawing energy from the warm atmosphere, whereas the latent fluxes are positive during this period implying a general trend of evaporation, but slightly lower than in previous and subsequent days. Model simulations suggest that during this period the sensible and latent fluxes are behaving similarly, however this is not reflected in the eddy correlation data. This may be because the sources and sinks of latent and sensible heat do not necessarily coincide within the footprint, alternatively the model may be over-predicting the latent fluxes. Observed fluxes are generally smaller than those modelled for snow and snow-free patches, supporting the idea of snow-free patches warming the atmosphere and providing a source of evaporation, whilst heat fluxes are downward into the snow patches. Cumulated latent and sensible heat fluxes are lower than those simulated for snow-free ground and greater than those for snow-cover. The changing direction of sensible heat and more positive latent heat fluxes all fit with the pattern of a decreasing snow covered fraction of the eddy correlation source area (Figure 6-8). After the rapid period of melt a quiescent phase of low turbulent flux was observed associated with a snowfall largely covering 90% of the site (Figure 6-8). The quiescent phase may result from changing synoptic conditions or the rapid increase in snow covered area diminishing the fluxes from bare ground, and thus providing a greater sink for energy, leading to a colder drier boundary layer, which in turn leads to small fluxes across the eddy correlation source area.

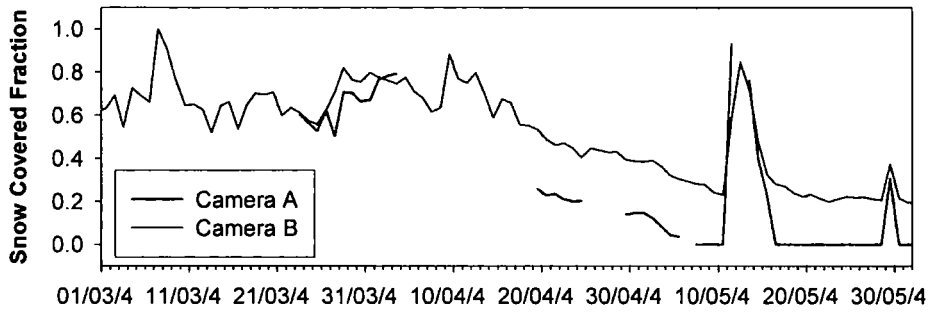

Figure 6-8: Snow covered fraction derived from camera locations for the melt period.

When examining a combination of modelling and measurements, a picture emerges of a landscape energy-balance as a composite of snow and snow-free surfaces controlled by the changing snow covered fraction. The melt is being principally driven by heat and water from the low-albedo snow-free surfaces warming and moistening a well-mixed boundary layer, whilst the snow patches act as a sink for this energy. It appears that the changing boundary layer is closely related to the changing patchiness of the surface, rather than large scale synoptic conditions, hence, the quiescent phase when a snowfall covers the flux footprint. Observations made at similar latitudes over more complete snow-covers on the Alaskan North Slope suggest that melt is controlled by radiation (Zhang *et al.*, 2001), the suggestion here is that melt is more complex, with radiation as the source of energy interacting with the surface and boundary-layer leading to an efficient transfer of energy into the snowpack.

The evidence of a well-mixed boundary layer and heat fluxes from snow-free sources driving the melt, does not necessarily provide support for advection in the light of observations from snow surveys that do not provide any evidence of greater melt at the edge of patches, as would be expected with advective processes (**4.5.2**). In addition, modelling and observational efforts of advective processes within the literature have concentrated on sensible heat fluxes, however evidence here suggests advection of latent heat may also be an important process. The role of advection is investigated in **6.3.4**.

6.3.4 THE IMPORTANCE OF SMALL-SCALE HEAT ADVECTION

Evidence presented so far suggests a complicated interaction between the boundary layer and snow and snow-free surfaces. As the turbulent fluxes are in opposite directions over the two surfaces the potential for advection is large. However, evidence from observations and model simulations suggests that melt is near homogeneous and the energy-balance at the centre of patches can be adequately simulated with no representation of advection. However, the contribution of advection would vary with the patch size and distribution and thus may vary in importance as the patches evolve. This section aims to examine the theoretical energy contribution of advection to the energy-balance through numerical simulation of patch dynamics in comparison to the well-mixed boundary layer approach.

Advection leads to a spatially variable energy-balance that is related to the snow-free to snow transition. As advection supplies energy to the edge of snow patches it is a very efficient process of increasing the snow-free fraction, which as shown above has important effects on the landscape energy-balance. The process of small-scale advection centres on the formation of internal boundary layers, at which there is a change in direction of flux associated with upward fluxes from warm snow-free surfaces and downward fluxes into the cold snow-cover (**2.3.1**). At the edge of snow patches the internal boundary layer is at its closest to the surface, hence advection is at its most efficient at the point of transition in the surface. The alternative process suggested here is of a well-mixed boundary layer in which there is an instantaneous change in direction of flux. The result is a uniform energy-balance across each snow and snow-free surface This is much easier to parameterise in large-scale models. The instantaneous change of flux direction is a less efficient process of heat transfer at the edge of patches, and thus leads to slower rates of melt at patch edges.

To investigate the change in energy-balance of a snow patch associated with advection, a set of experiments was carried out using a boundary layer model (Essery *et al.*, 2006). The advantage of this model is that it is 2-D and can deal with partial snow-cover. The first experiment models sensible heat advection under

typical conditions during the rapid period of melt. The second investigates the degree to which the sensible heat balance of a whole snow-patch will be underestimated if the well-mixed boundary layer hypothesis is true. Although, latent energy may be advected as well, the analysis here concentrates on sensible heat as this is the greater contributor of energy to the snowpack and is the generally focussed on in the literature.

a) Model Description

The model used here is a simple two dimensional boundary layer developed by Essery (2006). The model makes an important simplification by assuming the roughness is the same throughout the domain and that windflow is uniform. The model has a partially snow covered domain, with known surface temperatures, a known air temperature at the top domain boundary at a height approximately equal to the blending height, and a fixed windspeed at the top boundary. The model simulates sensible heat flux over a fine grid of 0.1 m and 0.02 m in the horizontal and vertical respectively. The model is spun-up until equilibrium is reached. The basic assumption with the modelling approach is that the observed air temperature at 2 m is at or above the blending height and thus the horizontal variation in the 2 m air temperature is low. A full model description can be found in Essery *et al.* (2006).

b) Model Simulations

Figure 6-9 shows the results for a typical midday period with a windspeed of 2 m s^{-1}, a surface temperature of 15°C and 0°C for snow-free and snow surfaces and an air temperature of 10°C measured at 2 m. The domain is 120 m and is half-covered with snow, consistent with the snow-covers described in Chapter 4. Clearly shown is the formation of internal boundary layers where there is a reversal in the direction of heat flux. The internal boundary layer is at its lowest at the transition in surface types. Correspondingly sensible heat fluxes are greatest at the edge of patches, and melt would consequently be expected to occur at a greater rate at the edge. During advective conditions, snowpacks would thus melt from the edge. For the conditions simulated here, the sensible heat energy available for melt varies from a maximum of 300 W m^{-2} at the windward edge of the snowpatch to 100 W m^{-2} at the lee edge of a 60 m patch.

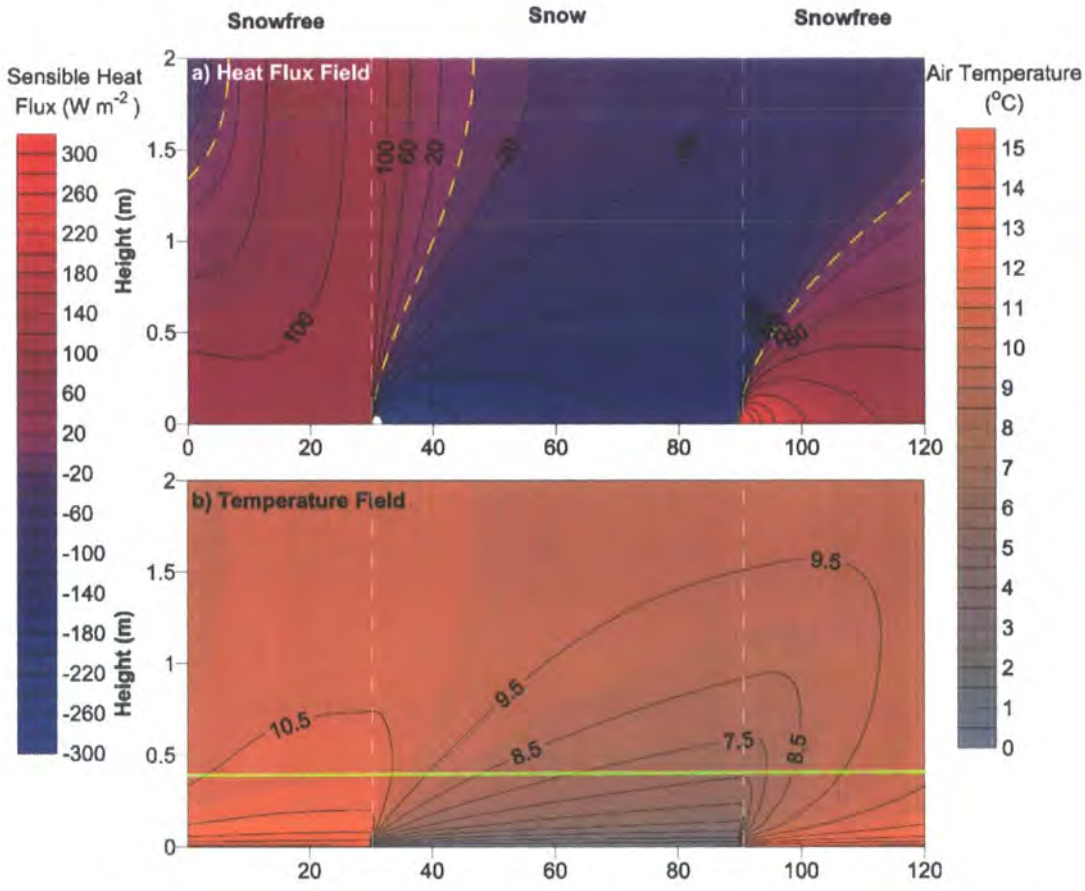

Figure 6-9: Simulated temperature and heat flux fields over a 120 m domain with a contiguous snow-cover fraction of 0.5. Model parameters: 2 m air temperature of 10°C, 2m wind speed of 2 ms^{-1}, snow-free surface temperature of 15°C, snow surface temperature of 0°C. Yellow dashed lines represent the formation of internal boundary layers.

Clearly, advection may significantly increase the energy available for melt at patch edges, especially if advection of latent energy is included. The effect of advection will be twofold, firstly to increase the rate of melt of snowpacks and secondly to increase the snow-free fraction, and therefore the efficiency of advection. A tiled model would significantly underestimate the amount of melt, and potentially the snow covered fraction if homogeneous ablation is assumed. To quantify the potential error in modelled sensible heat flux, a simple advection efficiency is derived for varying conditions including patch and domain size, surface temperature, air temperature and windspeed.

Advection efficiency is defined as the increase in sensible heat flux into snow patch over that estimated by a tiled model:

$$E_{Advected} = \frac{\overline{H}^{Snow}_{Advected} - H^{Snow}_{Tiled}}{H^{Snow}_{Tiled}}$$

Equation 6.2

where $\overline{H}^{Snow}_{Advected}$ is the average sensible heat flux into the snow patch and H^{Snow}_{Tiled} is the sensible heat flux simulated for a complete snow-cover. The derived efficiency thus ignores the spatial variation in sensible heat flux shown in Figure 6-9, but focuses on the error associated with the assumption of a constant flux layer assumed in a tiled model.

Figure 6-10 shows the advection efficiency under varying conditions. The error associated in assuming a constant flux may reach an order of magnitude where the horizontal variation in surface temperature is high and the snow covered fraction low. The magnitude of the advected sensible heat is most sensitive to the horizontal variation in surface temperature which shows a great deal of diurnal variation associated with shortwave radiation. Observed temperature differences reached 30°C at solar noon on calm clear days. The sensitivity to windspeed is much lower except when windspeeds are particularly low. The efficiency of advection is at its greatest where patches of snow are isolated in an expanse of snow-free ground. The role of advection in the initial formation of snow-free patches is minimal as when the snow covered extent is large compared to the snow-free extent the additional energy made available is small.

Clearly the relationship between snow covered fraction and advection efficiency is non-linear, and the efficiency of advection is highly sensitive to patch size, extent and degree of lacunarity. Including advective effects into land surface models for complex snow-covers that are randomly distributed and of varying size (**4.2.2**) is thus highly challenging.

Numerical simulation with a boundary layer scheme implies that small-scale advection is important, however there is no evidence of heterogeneous melt associated with patches and the energy balance at the centre of a patch is well simulated, with no representation of internal boundary layers. The following section outlines a simple numerical experiment to see if the standard model can represent the evolution of snow-cover over the melt period and accurately simulate the landscape energy-balance.

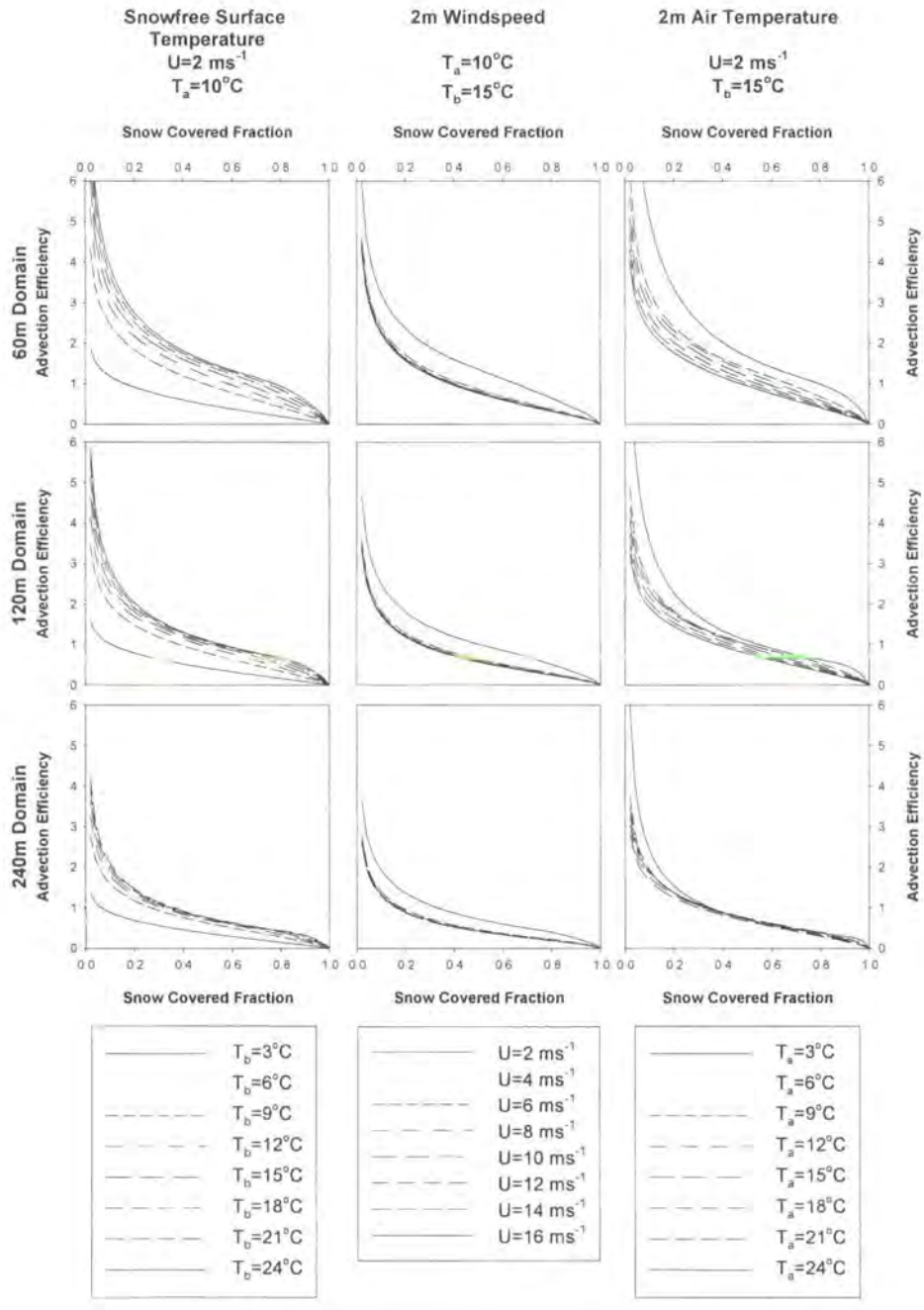

Figure 6-10: The efficiency of advection over various domain size and contiguous snow covered fractions under varying wind speed (U) , air temperature (T_a) and snow-free surface temperature (T_b) for a melting snow-cover. Specifically, advection efficiency is defined as the ratio between the total sensible heat fluxes to a snow patch under advective conditions over the simulated heat flux for an infinitely expansive snow-cover.

6.4 Modelling Heterogeneous Snow-covers

The mosaic of snow and snow-free surfaces interacts through horizontal energy exchange either through small-scale advection or a well-mixed boundary layer. The difference in mechanism is that small-scale advection leads to heterogeneous ablation rates whilst the well-mixed boundary layer hypothesis implies that the energy-balance can be considered uniform across a patch and there is an instantaneous change in flux at the transition a snow patch to a snow-free patch.

The point snow simulation implies that the MOSES model physics are correct and no advection takes place. However, as discussed in **6.3.1,** this experiment is limited as the sensors are located in the centre of a large patch where the effect of advection is felt least. Further to this, the assumption that the screen level temperature is greater than the blending height is also limiting. The blending height will vary with the magnitude and extent of the fluxes of momentum, heat and water vapour. The screen-level temperature measurement is made over a snow-free patch, which may implicitly include an advective term. It is therefore difficult to exclude small-scale advection as an important process as the effect will be implicit within the driving data. However, what is clear with small-scale advection is the efficiency by which the process melts snow patches from the edge. A simple of way of testing the well-mixed boundary layer hypothesis is to relate turbulent fluxes from individual patches to the flux at the landscape scale. The landscape consists of snow and snow-free patches. The patch scale fluxes are represented by distributed point MOSES simulations and the landscape scale fluxes with eddy correlation measurements.

A close simulation of the landscape flux during a period of snowmelt and changing snow covered fraction implies the model physics and assumptions are appropriate. It should be noted that this is not to say that advection is not important, but rather that an accurate simulation can be achieved whilst excluding advection.

The assumption made here is that the driving data for the distributed point MOSES runs is uniform across the flux tower footprint. As already discussed point screen-level measurements may not be appropriate in an advective environment.

Furthermore, the receipt of radiation is affected by topographic shading, sky-view, aspect and slope angle relative to the solar azimuth and solar elevation. Research into topographic effects on radiation research have generally been undertaken in areas of high relief, however small-scale features such as the hollows associated with complex topography, considered in this study may also affect radiation receipt. Research undertaken at Trail Valley Creek, Northwest Territories, Canada with similar topographic features to the Abisko study site, suggest basin-wide variation in modelled radiation receipts of up to 10% of incoming shortwave radiation, with the effect more pronounced during cloud-free conditions (Pohl *et al.*, 2006b). The sheltered hollows receive less radiation than surrounding areas due to the effect of shading. Similarly, the effect of windflow around topography may also affect turbulent flux. Pohl *et al.*, (2006a) found variation of up to 39% in windflow and consequential spatial variation in turbulent flux of up to 20%. Although these processes are undoubtedly important on a basin scale, the effects here are thought neglible due to the small domain size and the model is distributed only in terms of initial SWE.

6.4.1 SCALING FLUXES FROM PATCH TO LANDSCAPE

To scale modelled heat fluxes with eddy correlation measurements requires a representation of the distribution of surface types and their source-fraction within the flux footprint. To accomplish this, a distributed version of MOSES was run across the survey grid from 15th April 2004 to 1st June 2006. The distributed model has 400 nodes of 400 m^2 corresponding to each observation at 20 m spacing. Each node has a separate energy and mass balance regime and is either snow covered or snow-free. No representation of sub 20 m processes are included. Runoff from snowmelt is first routed into the soil, and any excess above the infiltration capacity is allowed to runoff. No explicit runoff routing is included in the model. Runoff is instead assumed to infiltrate the soil anywhere in the domain, up to the point of the infiltration capacity. Any excess is assumed to leave the model domain. MOSES is initially distributed using the observed SWE.

During the simulation period the snow covered fraction decreases from 0.7 to less than 0.1. Spatial variation in albedo, surface roughness, windspeed and shortwave radiation receipt are not included. Snowfall is assumed to fall uniformly across the

domain. This is thought valid as during the melt period very little redistribution of snow took place due to prevailing warm conditions. Snowfall corresponds to a small fraction of the mass balance during the model period, but has a significant effect on the snow covered area (Figure 6-8).

Comparing the distributed model with the flux tower measurements is not a simple matter of averaging across the model domain due to the characteristic source-area of the flux tower (**5.5**). Individual flux measurements may, or may not, be representative of the landscape scale fluxes at any moment in time; but averaged over time the measurements are representative of a characteristic footprint. The average fluxes across the domain are correspondingly weighted by the source fraction integrated over the area of the model node (Figure 5-8). The extent of the model domain corresponds to approximately 87% of the source fraction. The additional 13% is treated as an average of the model domain.

The results from the scaled distributed model are shown in Figure 6-11. There is a good fit between the model and the observations when the cumulative curves are parallel. Cumulative curves generally provide a better estimate of model performance than individual time-steps. The model performs well at simulating the sensible heat fluxes, but overestimates the latent fluxes. The observed sensible heat fluxes are quite variable and are influenced by short periods of high magnitude fluxes, as might occur when the footprint is centred over a largely snow-free area. However, the rapid period of melt is well simulated with good agreement between the model simulation and observation. There are periods of divergence between the simulated and observed fluxes, where the model predicts large fluxes which are not observed. Again this may result from a varying source-area. However the trend with time implies the problem is more systematic and may be a result of spatial variation in surface moisture. The simple representation of spatial hydrology does not account for the effect of topography and simulates soil moistures above the wilting and critical points. However, survey evidence (Figure 4-19) shows that within the top 0.05 m of soil significant areas are water stressed. Moreover, point simulations in **6.3.2a)** show the importance of accurate simulation of soil freeze-

thaw to get the heat balance correct. These are almost certainly simulated inaccurately.

Also evident within the simulation is the close relation between the flux footprint source area and the area-average flux. Cumulative measurements from the flux tower can thus be considered to representative of the landscape rather than just the footprint, which greatly extends the usefulness of eddy correlation flux data.

An accurate simulation of the landscape heat and water fluxes can be achieved using a distributed model which represents the transition between snow and snow-free surfaces. The distributed model does not include any parameterisation of advection and assumes a well mixed boundary layer that is effectively defined by the 2 m air, humidity and windspeed data used to drive the model. The conclusion has to be that an accurate simulation of snow ablation and the fluxes of sensible and latent can be achieved without including advective processes.

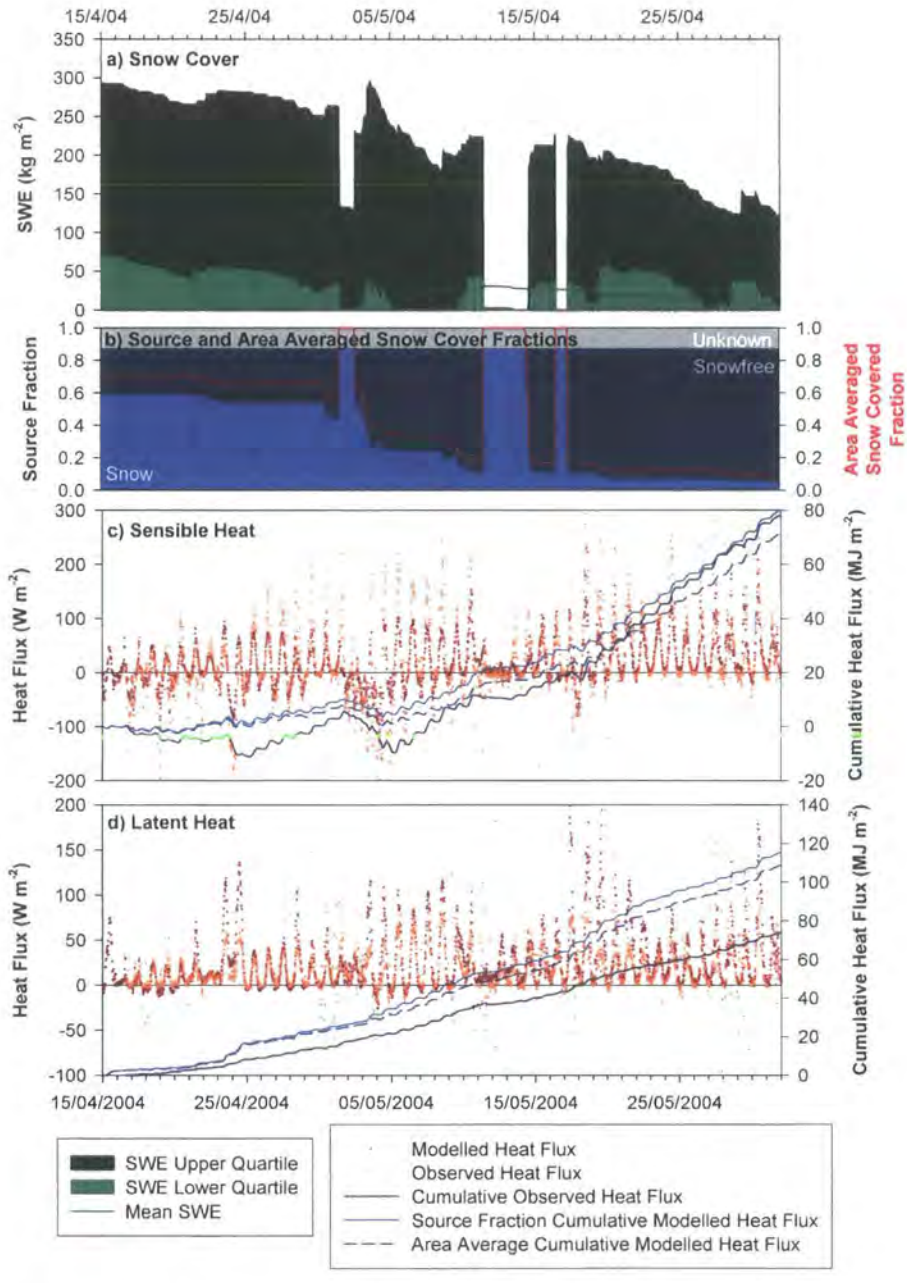

Figure 6-11: Average and source-area weighted heat fluxes from distributed MOSES and observations from the eddy correlation tower for a 27 day period during the melt. Figure a) shows the range in simulated SWE across the domain, b) the source fraction of snow and snow-free surfaces. The unknown section represents the source fraction from outside of the model domain (approximately 13%), c and d show the observed and modelled heat fluxes for the domain weighted for the source fraction (solid) and averaged over the domain (dashed).

6.4.2 MODEL TILING SCHEMES

The scaling of the distributed model to the landscape provides a good simulation of the fluxes at the larger scale and is confirmation of the model physics and the need to represent heterogeneous complex snow-covers. However, what are required are parameterisations that are appropriate to regional and global scale models rather than computational and 'data-expensive' distributed simulations. One of the hypotheses explored in this study is that appropriate parameterisation can be achieved through separate energy-balances for snow and snow-free surfaces in a tiling scheme.

The aim of a parameterisation of snow heterogeneity is to produce landscape average fluxes comparable to the landscape fluxes indicated by the distributed model. In this way, the distributed model is acting as the 'truth'. Before exploring a tiling scheme it is worth exploring the performance of the standard MOSES model. Snow-cover heterogeneity is represented by a snow-cover fraction which is used to weight the albedo (**2.2.1** and **12.1.3**). The results are shown in Figure 6-12. Standard MOSES melts snow-cover 30 days earlier than simulated in the distributed model by assuming the snow is uniformly distributed across the domain until the snowdepth is equivalent of the vegetation height (0.05 m). When the snowdepth is less than this the snow covered fraction rapidly declines, decreasing the albedo and melting the remaining shallow snow rapidly. This parameterisation helps prevent the model from the documented tendency to retain shallow snow-covers (Slater *et al.*, 2001). The model simulates a sensible heat flux in the opposite direction to the domain average and a lack of evaporation. Post snow-melt, the sensible heat fluxes exceed those simulated by the distributed model associated with dry moisture stressed soils. This occurs as rates of snowmelt exceed soil infiltration capacity and a significant proportion of snowmelt runs off (Figure 6-14). Model performance would be further degraded if coupled to a boundary layer model, as the driving data includes the complex effects of patchy snow-cover on boundary layer heat and moisture content. The post-melt effect on sensible heat fluxes is a documented tendency in the current HadCM3 GCM and a possible contribution to the observed warm bias in these models in the high latitudes (Martin Best, personal communication).

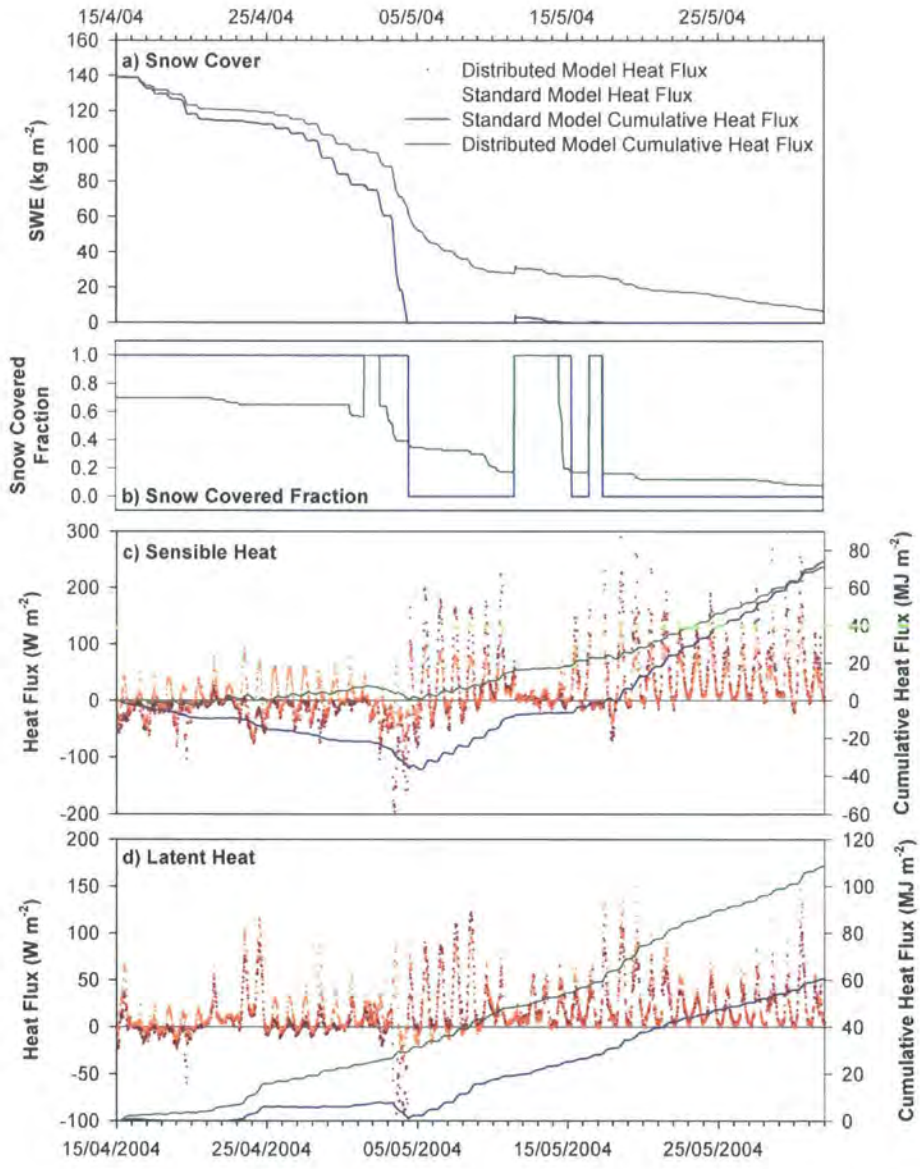

Figure 6-12: Snow-cover (a,b) and landscape average heat fluxes (c,d) from the distributed version of MOSES (green and brown)against a calibrated version assuming a homogenous snow surface (blue and orange).

Clearly what is required is the calculation of separate energy-balances for snow and snow-free surfaces. This can be seen in Figure 6-13 which shows the variation between snow and snow-free surfaces in the distributed model. The cumulative sensible heat fluxes between the surfaces are in opposite directions and the latent heat fluxes are an order of magnitude different. The variation within each surface type is also low, in the order of 2-10 MJ m^{-2}, due to the effect of a spatially varying snow depth, plus spatially varying soil moisture and temperature associated with varying snow-free date. The low spatial variation is thus implicit within the methodology behind model distribution. However, what is important is the difference between the surfaces. The two surfaces can be represented by using a tiling scheme by which separate energy balances are calculated for each surface, and a parameterisation of snow distribution included. The parameterisation of snow distribution is important as it defines the snow covered fraction and the depth of lying snow. The derivation of an appropriate parameterisation remains a challenge and is discussed further in Chapter 7. As a proof of concept, the tiled model here is driven by the snow covered fraction from the distributed model and snow mass-balance calculated interactively, as such the mean snow tile SWE initially increases as the shallow snow melts and the snow covered fraction decreases. Only the surface energy-balance is tiled. The underlying soil model remains one layer and the heat and moisture fluxes into the soil are calculated as the gridbox average. The gridbox is defined as the study site in this instance.

The results from the tiled model are shown in Figure 6-13. The tiled model, when driven by snow covered fraction, closely reproduces the different energy balances of the snow and snow-free surfaces as well as the gridbox average heat fluxes. The tiled model has a slight tendency to underestimate the sensible heat flux and overestimate the latent heat flux. This is associated with the spatial variation in surface soil moisture, which is not represented in the tiled model.

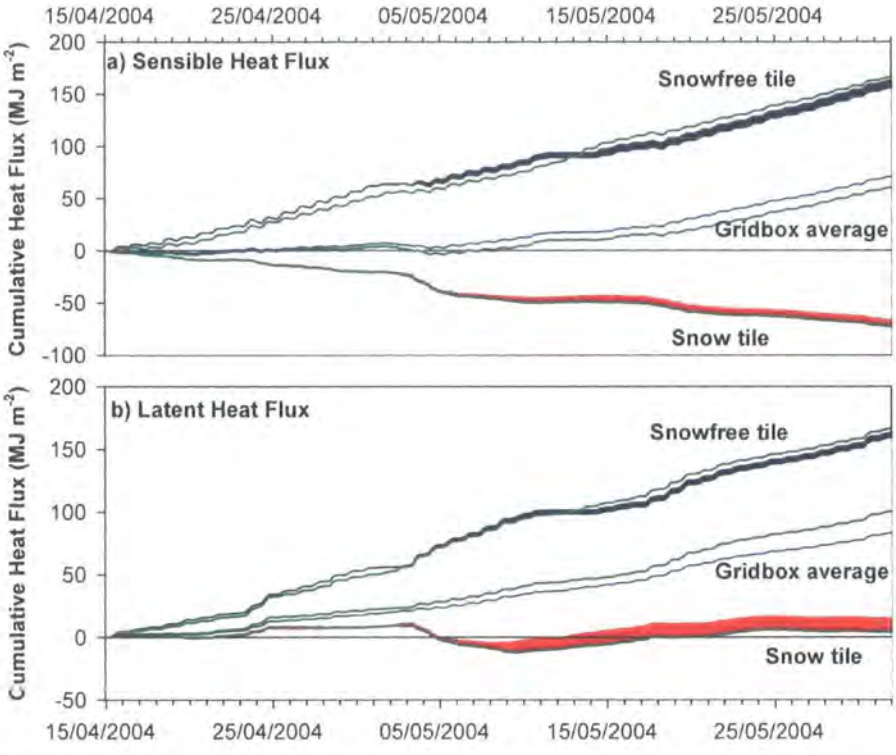

Figure 6-13: Cumulative sensible (a) and latent heat (b) fluxes averaged over the snow and snow-free surfaces and gridbox average in the distributed model and tiled model. The width of the red band indicates the interquartile range of the distributed model. Green lines represent fluxes modelled by the tiled model and blue the average heat flux from the distributed model.

Another important consideration with model design is the effect on the water balance. Figure 6-14 shows the daily surface runoff simulated by the different configurations. Surface runoff is assumed to occur if the infiltration capacity is exceeded. In the standard model runoff comes from the entire gridbox whilst for the distributed and tiled models snowmelt only comes from the snow covered fraction and excess runoff is routed in the distributed model to the snow-free nodes. In the tiled model the soil moisture accounting is completed for the gridbox, however as melt only comes from a fraction of the gridbox the infiltration rate is rarely exceeded.

The runoff simulated by the standard model peaks at over 47 kg m^{-2} of water, enough to generate substantial flooding in a catchment, whilst the parameterised models have peaks of 10-20 kg m^{-2}.

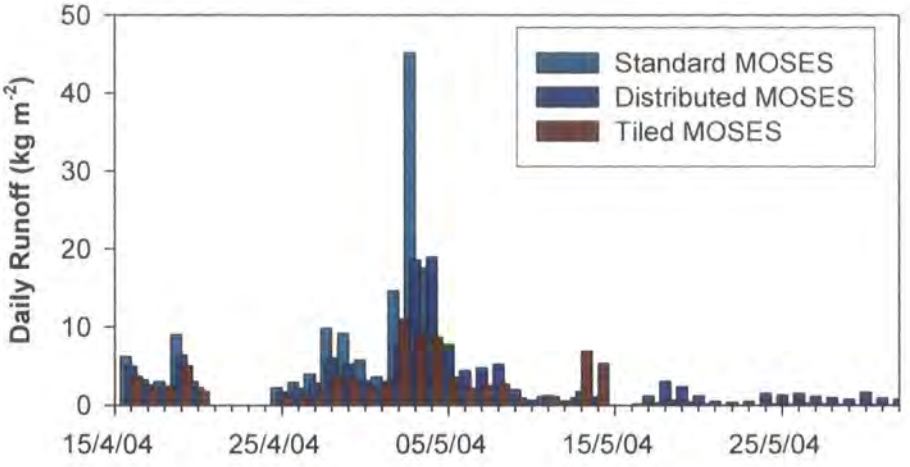

Figure 6-14: Daily surface runoff for the melt period as predicted by standard, distributed and tiled MOSES.

6.4.3 EFFECTIVE PARAMETERISATIONS

Effective parameterisations are the ideal way of including spatial heterogeneity in land surface models, providing they work. Effective parameterisations average the surface albedo, aerodynamic and surface resistances according to the fractional coverage of each surface. This simplifies a tiled model into a single call to a surface exchange scheme and is thus the easiest way to parameterise surface heterogeneity in land-surface models. However, there is considerable difficulty in deriving effective parameterisations. Work by Mason (1988) found that momentum exchange is dominated by the rougher elements in the domain, whilst subsequent work demonstrated heat fluxes are dominated by the smoother elements (Wood and Mason, 1991). Appropriate parameterisations therefore lie somewhere between the two, and Blyth (1994) suggested using an average of the two as the best guess. Blyth (1994) showed that effective parameterisations can be used when the variation is small, but when variation is large, average parameters do not predict average heat fluxes. Although the variation is relatively small during cold frozen conditions, this is certainly not the case during periods of melt. The fact that the turbulent fluxes are generally in opposite directions during melt means that effective parameterisations will generally lead to an underestimation of the energy exchange for a snow-free surface and vice versa for snow-cover. This in turn leads

to excessive melt rates. This error occurs within the standard MOSES model which includes an effective parameterisation of albedo (**6.4.2**).

Consequently, appropriate effective parameters are very difficult to deal with, and are generally inappropriate to use where there are strong contrasts in surface such as heterogeneous snow-covers. This leaves only the tiled and distributed approach as valid methods of modelling spatial heterogeneous snow-covers in large-scale modelling applications.

6.5 Summary

The landscape scale surface energy balance is a composite of snow and snow-free surfaces interacting with the boundary layer. The direction of turbulent flux at the time of peak melt are generally in opposite directions over snow and snow-free surfaces. The snow-free patches warming and moistening the boundary layer and the snow patches cooling and drying the boundary-layer. This leads to a complex interaction in which turbulent energy from the snow-free ground melts the snow patches. Initially, a picture emerges of advective conditions between snow-free and snow patches. However, the evidence here suggests that although mixing within the boundary layer is clearly important, the heterogeneous effect on melt rates is not. This is not to say that advection is not taking place, but rather that there are not enough data to understand these complex processes, particularly as the screen-level temperature and humidity data implicitly include an advective term. To further understand these processes requires a full boundary-layer model with a surface energy-balance that can be driven by measured incoming short and long-wave radiation.

Scaling experiments suggest that the heat fluxes can be scaled successfully from the patch to the landscape if the distribution of snow-cover is known. Ignoring heterogeneous snow-covers leads to significant errors in heat fluxes and surface runoff. Moreover, spatial heterogeneity can be represented by aggregating snow and snow-free patches into two surfaces with separate energy-balances. The landscape flux is correspondingly a fraction of their relative proportions. The spatial variation in soil moisture and soil freeze-thaw is important to correctly simulating heat fluxes and is worthy of further research.

Accurate simulations of heat and water fluxes over patchy snow-cover can be achieved with a tiled model using separate energy-balances for the snow and snow-free surfaces. The distribution and patchiness of the snow and snow-free surfaces does not need to be represented. To correctly scale the fluxes requires a parameterisation of the snow distribution. This is the subject of the following chapter.

Chapter 7

Modelling Snow Distribution

7 Modelling Snow Distribution

7.1 Introduction

Snow is well recognised to play a key role in defining the energy and moisture balances of the high latitudes. It is also apparent that snow-covers are generally non-uniform and spatially variable, particularly in the case of exposed tundra snow-covers (Chapter 4). The patchiness of snow leads to significant differences in energy and moisture fluxes between snow covered and snow-free surfaces (Chapter 6). The non-uniformity of snow-cover correspondingly influences weather and climate on a local, regional and global scale. The last decade has seen a concerted effort to develop more complex and physically realistic representations of the land surface in atmospheric models, with several model intercomparison studies focusing purely on the representation of snow processes (e.g. Essery *et al.*, 1999b; Etchevers *et al.*, 2004, Henderson-Sellers *et al.*, 1995; Slater *et al.*, 2001). However, the main direction of change has been to develop more complex 1-D models and largely ignore sub-grid scale snow distribution. This is partly due to the complexity of these processes. Consequently, snow-cover is generally considered uniform in large-scale atmospheric models. However, as shown in Chapter 6, the assumption of uniformity can lead to substantial errors in both the energy and water balances. Developing appropriate parameterisations of snow distribution remains a challenge. The aims of a sub-grid scale parameterisation of snow-cover for large scale atmospheric models are threefold: to (i) model inhomogeneous snow accumulation, (ii) model snow ablation, and (iii) represent heat and moisture fluxes over patchy snow (Liston, 2004).

There are two ways heterogeneous snow can be included into hydrological models; (i) implicitly through probability distribution functions, e.g. log-normal distributions (Donald *et al.*, 1995), or (ii) explicitly through distributed models simulating redistribution processes e.g. (Essery *et al.*, 1999a; Liston and Sturm, 1998; Pomeroy *et al.*, 1997). Fully distributed, explicit, blowing snow models are computationally very expensive and require a great deal of information. However, the distributed blowing snow models generally rely on a parameterisation of the spatial distribution of sources of sinks of snow or a simplified representation of

windflow around topography. The Distributed Blowing Snow Model (Pomeroy *et al.*, 1997) uses a classified Landsat image to define sources and sinks for blowing snow, and SnowTran-3D (Liston and Sturm, 1998) uses slope and curvature derived from a DTM to modify the windspeed with topography. This chapter outlines two distinct approaches to the problem, the first uses spatially distributed terrain parameters to develop simple physically based models, and the second approach uses a probability distribution function to predict a snow-cover distribution. These differing approaches are scale-dependent, the first is appropriate to the meso-scale where high resolution DTMs are available, the second is more appropriate to large-scale atmospheric models where high resolution topographic data are unavailable. The models are coupled to the 1D tiled MOSES model described in Chapter 6 and driven with meteorological observations, and are validated against snow survey data. Simulations show the importance of snow-cover to the timing and magnitude of surface runoff as well as the heat balance.

7.2 Snow distribution and Terrain Indices

Terrain indices derived from analysis of DTMs provide readily available, spatially explicit, data sources that can be used as surrogates for the physical processes controlling snow distribution. Snow distribution at the landscape scale is well documented to be a function of windflow around topography and surface roughness. The first step in developing a terrain-based snow redistribution model is to evaluate the ability of terrain indices to act as surrogates for snow distribution. The indices used here include the commonly derived indices of elevation, slope, aspect and curvature e.g. (Copland, 1998; Elder *et al.*, 1991; Elder *et al.*, 1989), in addition to the indices of topographic similarity (Beven and Kirkby, 1979) and the topographic shelter (Winstral *et al.*, 2002). It is hypothesised that each of these indices inform us about the way wind flows around topography. Vegetation height is included as a proxy for surface roughness.

7.2.1 TERRAIN INDICES

a) Terrain Elevation, Slope, Aspect and Curvature

Indices of slope, aspect and curvature are derived from the DTM using the method of Zevenbergen and Thorne (1987) as outlined in Appendix A. Elevation data are

taken directly from the DTM (Figure 3-4). The sine and cosine of aspect is derived to give measures of east-west and north-south aspect respectively (Figure 3-5c and d). Furthermore, curvature is calculated in the direction of slope, to give profile curvature, and perpendicular to the slope to give transverse curvature (Figure 3-5a and b). To take account of the prevailing wind direction, slope gradient and curvature are calculated in line with the prevailing wind direction (Figure 7-1a and b).

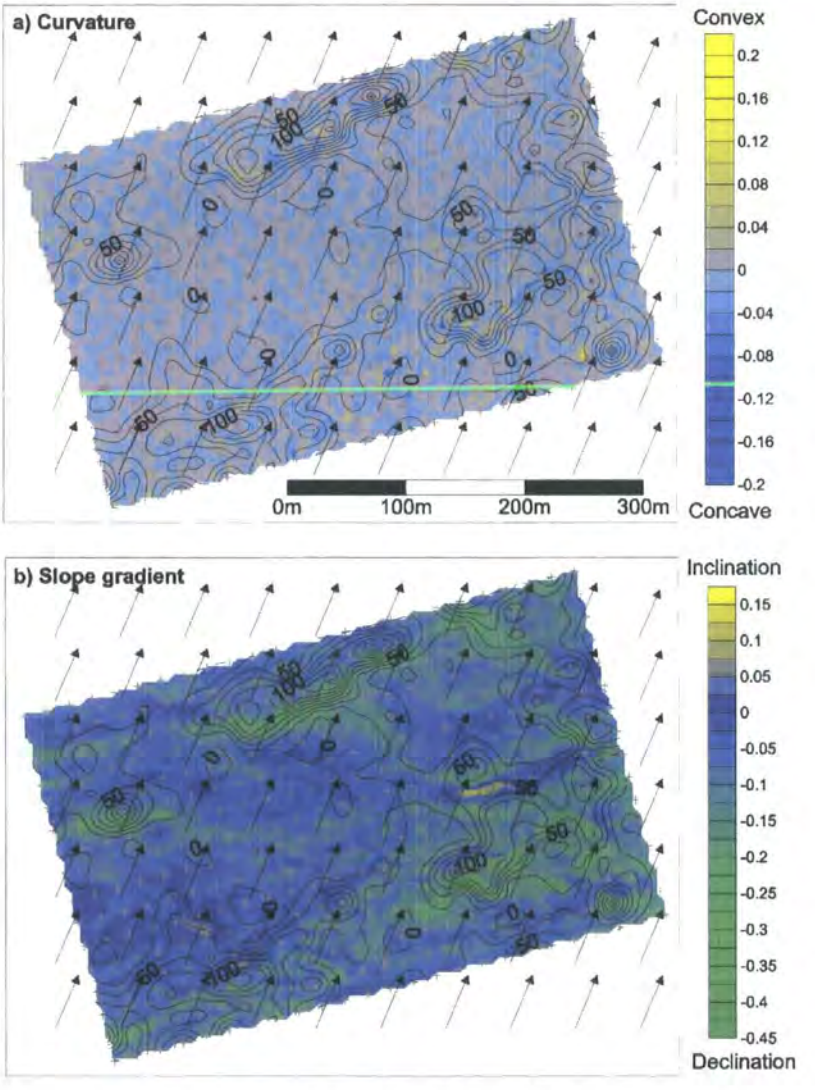

Figure 7-1: Terrain indices. a) Terrain curvature in line with prevailing wind direction, and b) Slope gradient in line with prevailing wind direction. Sample locations are marked with crosshairs. Snow depth contours are from the 27th February 2004 survey. Prevailing wind direction is indicated.

b) Topographic Similarity Index (TSI)

The topographic similarity index was introduced by Beven and Kirkby (1979) as a measure of the likelihood of an elevation cell retaining liquid water. The index relates the upslope drained area to the slope angle and therefore the likelihood of water accumulating to the likelihood of run-off occurring. The fundamental underpinning assumption is that the topographic and hydraulic gradients are similar i.e. the flow of water will follow topography. High *TSI* values are gained where water is likely to pool and form lakes, medium values in valleys and riverbeds and low values on ridges. Hartman *et al.* (1999) surmised that transport flows of snow follow a similar pattern to the flow of water, i.e. the transport of snow will follow the hydrologic gradient.

The 'similarity' in the index indicates that every point with the same value will behave functionally the same. The TSI is currently implemented as a probability distribution of soil moisture in some versions of MOSES (Blyth *et al.*, 2004). The advantage of using the TSI to distribute snow-cover is that it allows the spatial variation of snow, surface runoff and soil moisture components of MOSES to be coupled.

The relationship between TSI and snow-cover is shown in Figure 7-2. The derivation of TSI is given in Appendix A.

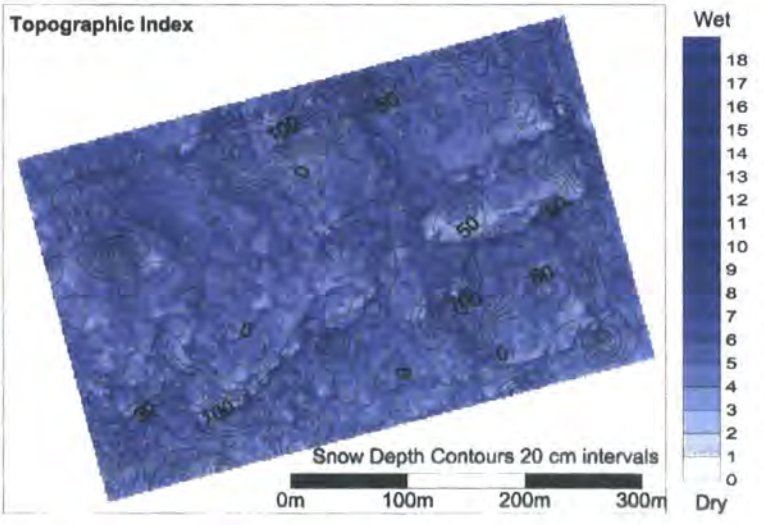

Figure 7-2: Topographic similarity index. Sample locations are marked with crosshairs. Snow depth contours are from the 27th February 2004 survey.

c) Topographic Shelter Index

The topographic shelter index (SX) is based upon the index produced by Winstral *et al.* (2002). The index represents the degree of shelter given to a particular cell by the upwind topography and thus the likelihood of accumulating snow (Figure 7-3) for a given wind direction. Three versions of the index are derived based upon three hypotheses of the controls on snow distribution: (i) snow distribution is controlled by the prevailing wind direction of 203° (Prevailing Wind Shelter Index Figure 7-3a), (ii) snow distribution is independent of the direction of wind and windspeed, as all winds independent of occurrence affect snow distribution (Global Shelter Index Figure 7-3a), and (iii) snow distribution is a function of both wind direction and windspeed (Global Weighted Shelter Index Figure 7-3c).

The global index is derived by calculating the shelter index for all directions and finding the minimum. The global weighted index is derived by calculating the shelter index for all directions and weighting for the occurrence and wind velocity for each direction. The derivation of the index is given in Appendix A.

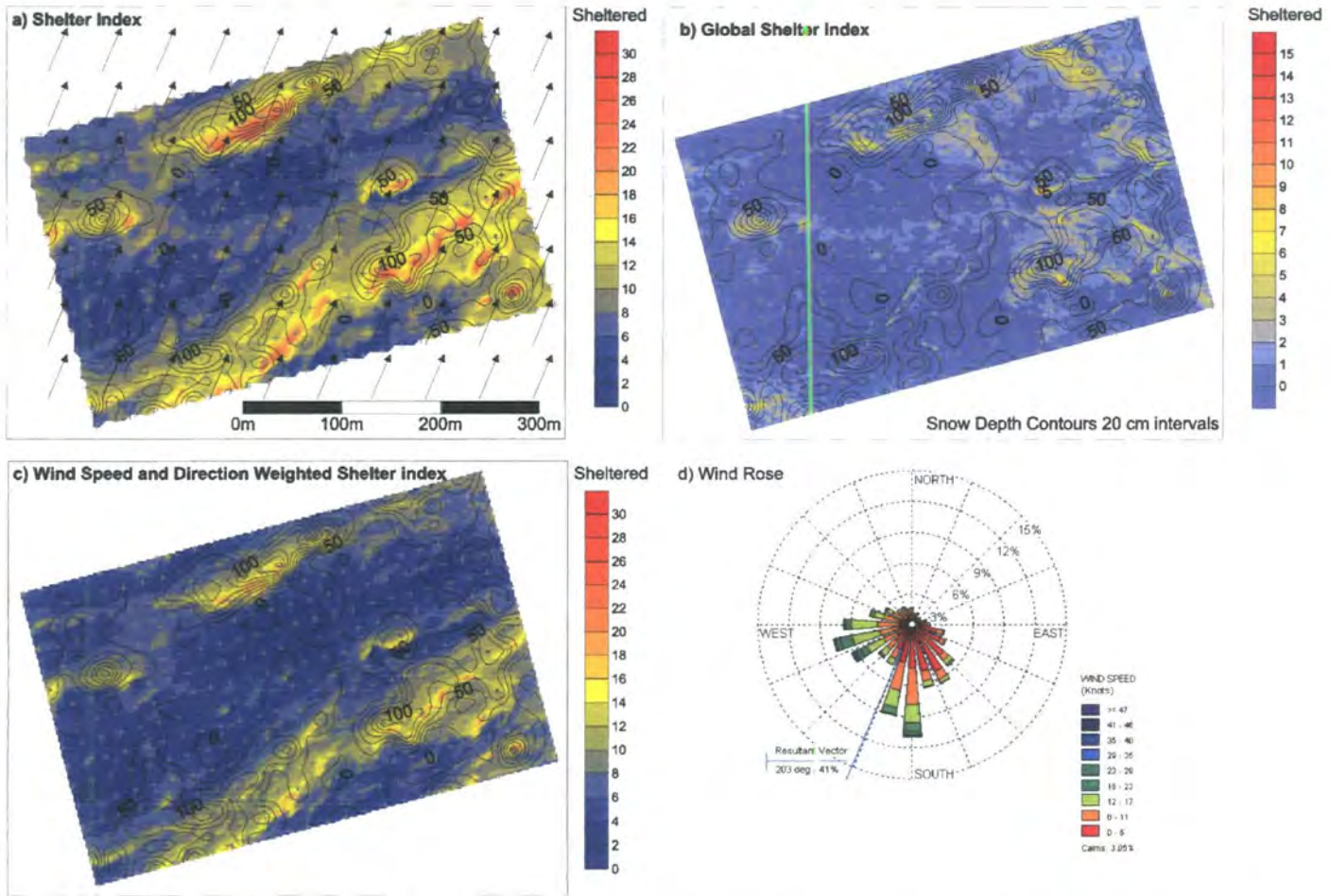

Figure 7-3: Topographic shelter indices. a) Topographic shelter index in line with prevailing wind direction, b) Global topographic exposure index, c) Global weighted topographic shelter index, and d) wind rose indicating prevailing wind direction and velocity for 2003 to 2005. Sample locations are marked with crosshairs. Snow depth contours are from the 27th February 2004 survey. Prevailing wind direction indicated by arrows on appropriate figures.

d) Vegetation Height

Vegetation structure and height act to affect the surface roughness and thus the windflow. Deep, dense, vegetation slows windflow and retains and accumulates snow. Vegetation height has the greatest effect on surface roughness and is measured across part of the survey grid (Figure 3-6).

7.2.2 SIMULATING SNOW DISTRIBUTION WITH TERRAIN INDICES

There are a number of ways terrain indices can be incorporated into snow distribution models, but the easiest method to evaluate the suggested terrain indices is to use observational data to derive simple two-parameter statistical models using least-squares regression. This method allows each index to be evaluated according to predictive ability.

The snow survey data are regressed against the derived terrain indices and vegetation height data (Table 7-1). All snow-free values are removed from this analysis to avoid non-linearity in the observational data. Data entered into the regression analyses are therefore only for survey locations where snow was present. For the snow surveys completed during the accumulation phase (SWE 1, SWE 2, SWE 5), vegetation height, prevailing wind shelter index and global weighted shelter index are consistently the best predictors and are used in the subsequent analysis.

Table 7-1: Univariate linear regression matrix of terrain indices predicting SWE. Tabulated values are r^2. Asterisks represent insignificant fits at the 95% confidence limit. Shaded surveys indicate data collected during the ablation phase.

	SWE 1	SWE 2	SWE 3	SWE 4	SWE 5
Vegetation Height	0.46	0.38	0.29	0.12	0.44
Prevailing Wind Shelter Index	0.39	0.28	0.33	0.25	0.37
Global Shelter Index	0.21	0.21	0.10	0.09	0.12
Weighted Shelter Index	0.39	0.27	0.32	0.25	0.36
Prevailing Wind Slope Angle	0.08	0.05	0.06	0.17	0.05
Slope Angle	0.10	0.06	0.09	0.17	0.07
Prevailing Wind Curvature	0.05	0.05	0.03	*	0.03
Profile Curvature	0.05	0.08	0.05	*	0.05
Transverse Curvature	0.04	0.05	0.02	*	0.01
Topographic Index	0.01	0.02	*	*	*
Easterly Aspect	*	*	*	*	*
Northerly Aspect	*	*	*	*	*
Elevation	*	*	*	*	*

There is a large degree of co-linearity in these indices, especially between the indices of shelter, and also between the indices of shelter and vegetation height. This is to be expected as taller shrubs are found in more sheltered areas.

To investigate the predictive power of shelter and vegetation height, the indices are fed into a stepwise multiple linear regression analysis. As 'prevailing wind shelter' and 'globally weighted shelter' are highly co-linear, the weighted version is excluded from the subsequent analysis. The prevailing wind index is preferred as it is the simplest. Furthermore, as vegetation height is partly dependent on the degree of shelter, the shelter index is entered into the regression first (Table 7-2).

Table 7-2: Stepwise multiple linear regression of snow-covers against terrain indices. Shelter index entered into the regression first. Tabulated values are r^2. Shaded surveys indicate data collected during the ablation phase. Vegetation height data is only available for a subset of the study site. Data fed into the stepwise regression analysis are thus a subset of the available data due to the requirement of tied observations. Thus r^2 values for Prevailing Wind Shelter Index differ from those in Table 7-1. The data subset is shown graphically in Figure 7-4.

	Prevailing Wind Shelter Index	Vegetation Height
SWE 1	0.29	0.62
SWE 2	0.20	0.50
SWE 3	0.25	0.50
SWE 4	0.16	0.39
SWE 5	0.25	0.59

The regression analyses clearly show the importance of both vegetation height and terrain shelter on understanding snow distribution. However, it must be noted that the multivariate regressions are for a smaller region of the study site than the more expansive shelter index. The model fits are consistently better for snow surveys undertaken in the accumulation period.

Thus far, we have two regression models of snow distribution, the first is the univariate model using prevailing wind shelter index and the second is the multivariate model using shelter index and vegetation height. The model fits and residuals are plotted in Figure 7-4.

Large differences in the snow-cover predicted by the two models are clearly shown in Figure 7-4a and c. The shelter index model consistently underestimates the snow-cover forming in the shrub-beds, and overestimates in more exposed areas. The multivariate model generally performs much better, with the exception of a couple of sample sites, which correspond to gaps in the shrub cover. This can be seen particularly in the south-west corner of the survey domain where the shelter index is low, and the vegetation height high. This appears to be a region where the

shrubs are accumulating snow-cover independent of terrain. This is an important process by which shrub-bed expansion may significantly alter snow distribution under environmental change.

Terrain derived indices of shelter and vegetation height and clearly suitable for modelling snow distribution. However, they are hugely limited as they are calibrated for a particular observed snow-cover and are therefore not suitable for use in predictive models. Further to this, the more accurate multivariate model makes use of difficult to acquire vegetation height data.

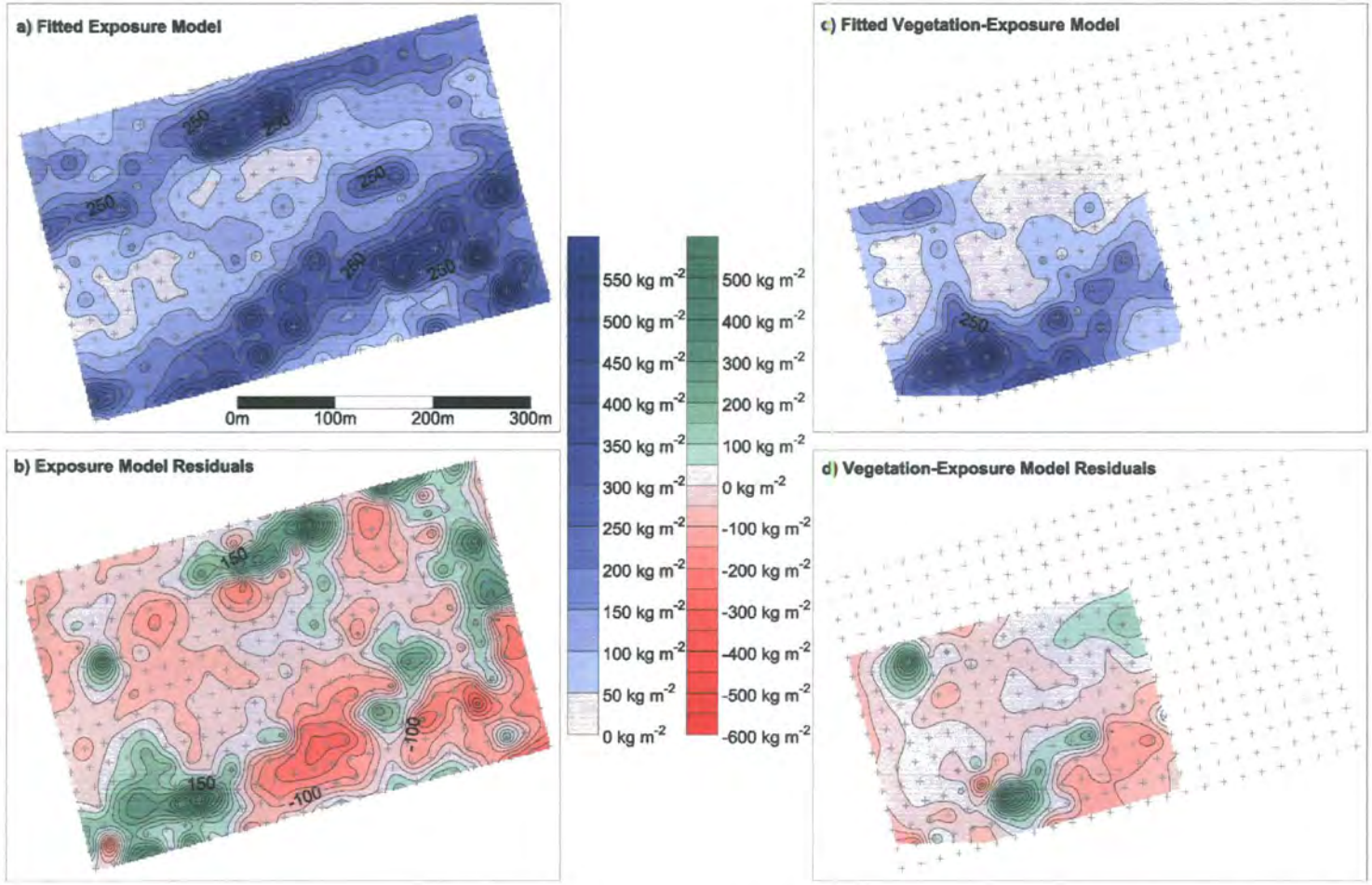

Figure 7-4: Predicted snow distribution using two forms of the regression model, both including the shelter index (a and b) and one with vegetation height. (c and d). The models are fitted to snow survey data collected on 27th February 2004 (SWE 1). Residuals are plotted in b and d. Negative values imply the model is overestimating. Cross-hairs indicate survey locations.

7.3 Process Based Models

The simple linear models of snow distribution, shown above, clearly demonstrate that indices of terrain and surface roughness can be used to model snow-cover given observational data. However, these models assume a linear relationship between surface and snow redistribution, and have to be calibrated with observational data.

The challenge is to develop a method by which snow distribution can be related to terrain, without assuming linearity or resorting to a statistical model fitting procedure. In physical terms the model has to simulate the degree of redistribution of snowfall. Ideally such a model would conceptually have a representation of windflow around topography and surface roughness. However, although spatially explicit data on topography is readily available from DTMs, data of vegetation structure and height generally relies on surveyed data. Although vegetation structure was found to be a significant control on snow distribution, it is excluded from the subsequent model development due to the lack of readily available data. Models are thus built upon the prevailing wind shelter index.

The difficulty in developing a physical model of snow redistribution is determining the degree of redistribution and the route that snow is transported over. The two models described here make critical assumptions about this process. The first and most simplistic assumes that snow is always redistributed to fill the hollows first to make for a topographically smooth surface. The second model uses the shelter index to derive hydrological units between which snow is transported. These units can then be mapped back onto the terrain.

7.3.1 EQUILIBRIUM MODEL

The simplest approach to modelling snow redistribution is to assume that there is enough time and high enough winds for the snow distribution to reach equilibrium with the landscape. Snow is therefore scoured from exposed areas and transported into sheltered zones. The end result is a topographically smooth land surface as defined by the prevailing wind shelter index (Figure 7-3a). Snowfall is thus

assumed to be instantaneously redistributed. This approach is termed the equilibrium model.

The model assumes snowfall initially falls uniformly across the study domain, the wind then acts to redistribute the exposed snow to less exposed sites. The process is iterated until eventually the snow fills the sheltered regions effectively making the topographic surface, as described by the index, as smooth as possible. The equilibrium model therefore deals with snow depth rather than SWE. This process of iteratively redistributing snow is shown schematically in Figure 7-5.

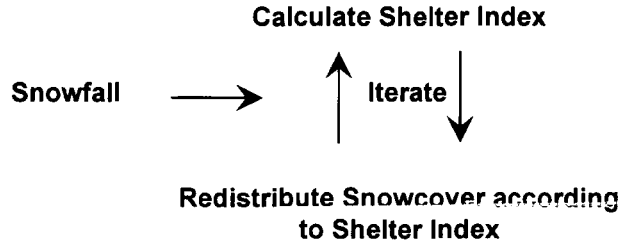

Figure 7-5: Schematic diagram of equilibrium model

A mass-balance is retained within the model domain; no snow is assumed to leave the domain. Snow is able to travel as far as is required to satisfy the shelter index, and no sublimation takes place during transport. The advantage of this model is it's simplicity and that it allows SWE to be mapped at the resolution of the shelter index. The main disadvantage is that there are no parameters to be tuned – snow must always lay in equilibrium with the prevailing wind shelter index. Figure 7-6 shows the distribution of snow given different accumulations of snow. The tendency under this model is to overestimate the degree of redistribution and for the vast majority of snow to fill the snow beds. However, the model does pick out the effect of small-scale topography on retaining shallow snow-covers. Figure 7-7 shows the snow covered fraction for a given mean snow depth that is used to drive the tiled energy-balance model. During melt the mean snow depth is updated and the snow covered fraction is adjusted to suit. The crucial assumption in the coupling is that although melt may be homogenous, redistribution will instantaneously take place so the snow-cover is always in equilibrium with the terrain.

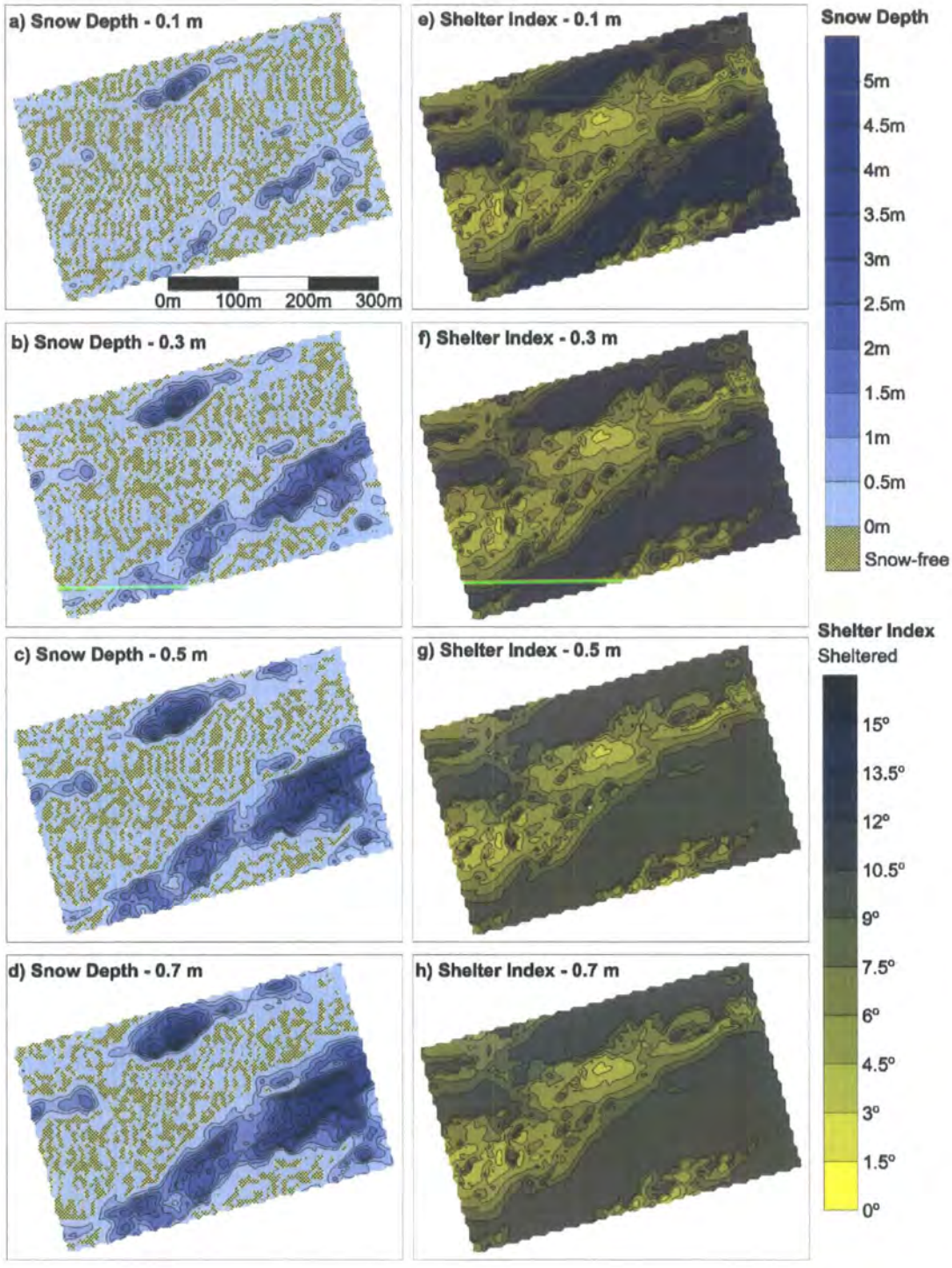

Figure 7-6: Snow distribution (a-d), and shelter index (e-h) as predicted by the equilibrium model under varying depths of snow.

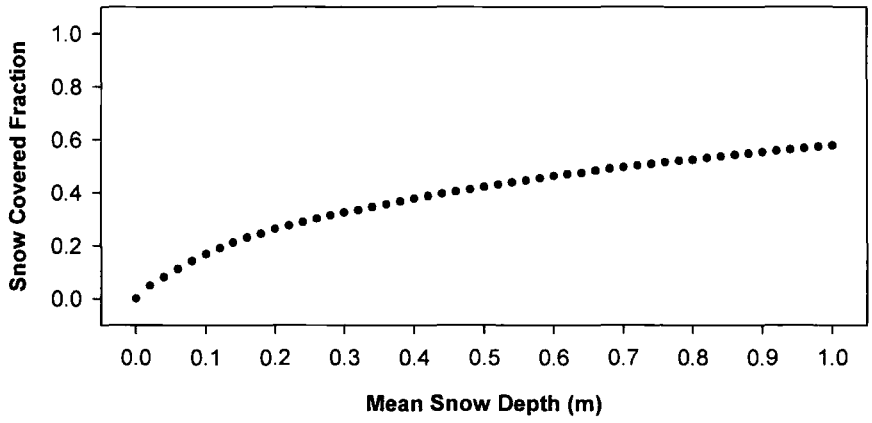

Figure 7-7: Snow covered fraction (SCF) derived assuming snow-cover in equilibrium with shelter index.

The equilibrium model allows snow-cover to be mapped onto the terrain from knowledge of the mean snow depth. Results from the simulation of observed snow-covers are shown in Table 7-3 and Table 7-4. In general, the model over redistributes snow leading to overly deep drifts and too low a snow covered fraction, to the extent that assuming a uniform snow-cover produces a better result. Despite this, however, the model goes some way to representing the spatial variation in snow depth. Clearly, a more complex representation of the degree of redistribution is required. This can be achieved with a parameterised rate and direction of redistribution as shown in the following section.

Table 7-3: Model efficiency of fitted equilibrium model versus a uniform snow-cover.

	RMSE		Nash-Sutcliffe Model Efficiency (Nash and Sutcliffe, 1970)		Willmott Index of Agreement (Willmott, 1981)	
	Model	**Uniform**	**Model**	**Uniform**	**Model**	**Uniform**
Survey 1	0.44	0.337	-1.21	0	0.69	0
Survey 2	0.37	0.27	-1.30	0	0.65	0
Survey 5	0.50	0.38	-0.73	0	0.725	0

Table 7-4: Kappa scores of observed and modelled snow covered fraction

	Snow covered Area (%)		Cohen's Kappa
	Model	Observations	
Survey 1	34	100	0.34
Survey 2	29	100	0.29
Survey 5	35	84	0.42

7.3.2 DISCRETIZED HYDROLOGICAL UNIT MODEL

The Discretized Hydrological Unit Model uses the prevailing wind shelter index to define hydrological units that have similar snow-cover characteristics. A simple redistribution model is used to transport snow between units, dependent on windspeed. The definition of a hydrologically similar unit is based on the distribution of the terrain-derived shelter index. Four units are used in this application, each of a different areal extent (Figure 7-3). Snow is assumed to move from less sheltered to more sheltered units on this basis (Figure 7-9). A more physical approach would replace the simple redistribution-parameter model with a blowing snow model as applied by Pomeroy *et al.* (1997) to the Canadian Arctic.

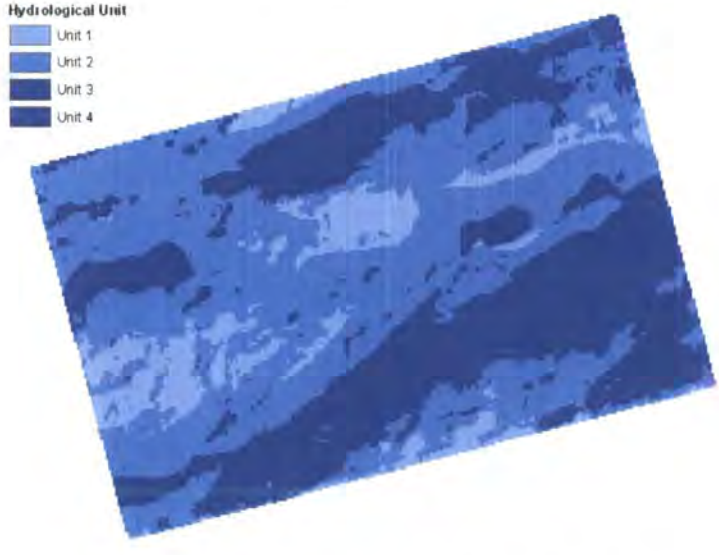

Figure 7-8: Hydrological unit modelled snow distribution mapped onto the study site.

At the heart of the model is a mass balance equation for each of the hydrological units of the following form:

$$Q_S = P + \frac{Q_{Tin} A_0}{A_{in}} - Q_{Tout}$$

Equation 7.1

qhere Q_S is the instantaneous flux to the bin, ***P*** is snowfall, A_0 and A_{in} are the areas of the receiving and contributing units respectively and Q_T is the transported flux of snow, given a snow covered surface. Snow is assumed to accumulate only in the 'sink' unit and be redistributed from the 'source' unit (Figure 7-9). Other units are allowed to be both 'source and sink'. Due to the different areal extents of each bin, redistribution flux can either converge or diverge (Table 7-5).

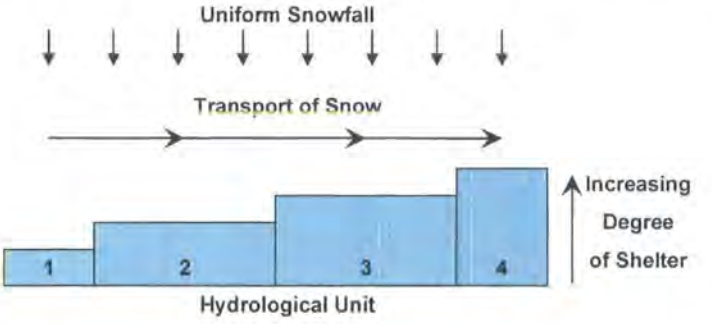

Figure 7-9: Schematic diagram of hydrologic unit snow redistribution model.

The transport flux is parameterised as the fourth power of the wind velocity, following Pomeroy *et al.* (1997):

$$Q_T = ku^4$$

Equation 7.2

where k is an adjustable parameter determined by model calibration representing drift factor. The model thus assumes that, providing snow is present and the wind velocity is above zero, transport will take place. Furthermore, sublimation during transport is ignored. A further model development could include a snow entrainment model to determine when snow is loosely bound and available for entrainment. Such a model would require a more complex representation of snowpack metamorphism than is currently included.

Table 7-5: Hydrological unit model setup and results

Hydrological Unit	Shelter Index Classification (Degrees)	Area (m^2)	Survey 1 SWE ($kg\ m^{-2}$)	Modelled SWE ($kg\ m^{-2}$)
1	$0 < SX \leq 5$	17025	36	38.2
2	$5 < SX \leq 10$	81950	67	50.5
3	$10 < SX \leq 15$	47750	165.5	149.6
4	$SX > 15$	13425	342	341.5

The hydrological unit model was calibrated against snow survey data collected on 27th February 2004. The model was initialised on Sept 1st 2003 and run through to the survey date. The redistribution parameter (k) was tuned to minimise the Chi-squared statistic between the modelled bins and observations. A significant fit is achieved with a redistribution parameter equal to 3.14E-6 ($\chi^2 = 2.33$, df = 2, p = 0.525).

Figure 7-10 shows the modelled binned SWE against the observed SWE for different degrees of shelter. The model clearly performs well at simulating the mean distribution, however there is a great deal of variation within each bin that is not represented in the model.

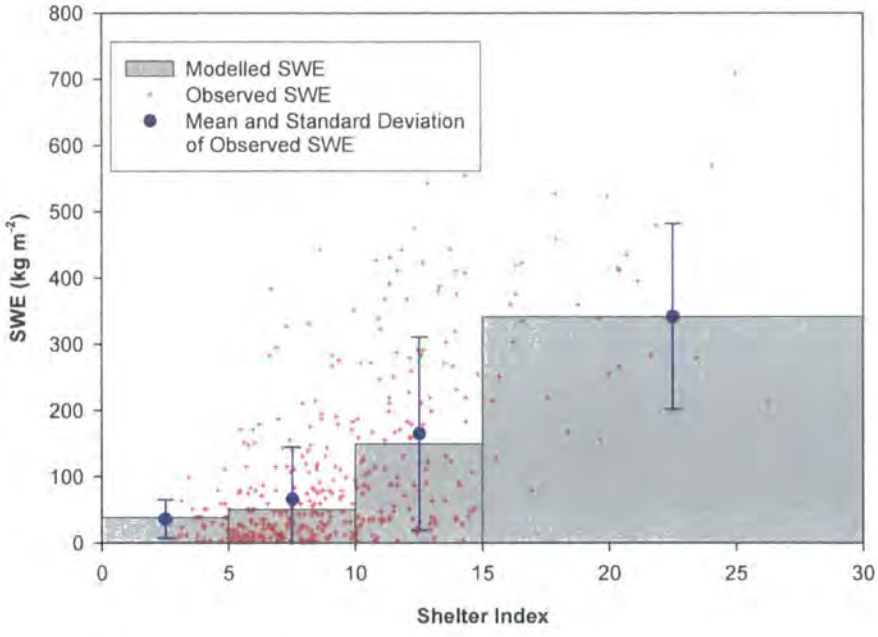

Figure 7-10: Modelled SWE as a function of hydrological unit.

7.4 Probability Distribution Models

Probability distribution models (PDM) represent heterogeneous snow-cover as a mathematical function with a characteristic form. The spatial distribution is thus modelled implicitly, and cannot be mapped back to the terrain. Several probability distributions have been used to represent heterogeneous snow-cover including beta distributions, gamma distributions (e.g. Alfnes *et al.*, 2004; Skaugen *et al.*, 2004) and log-normal distributions (Donald *et al.*, 1995). Once the initial distribution has been defined subsequent distributions can be derived assuming a homogenous melt. Work by Luce and Tarboton suggest that the choice of distribution is less important that the choice of coefficient of variation (Luce and Tarboton, 2004).

a) Model Description

Donald *et al.* (1995) suggested that spatially variable snow-covers can be expressed by two parameter log-normal probability distributions of the following form (Liston, 2004):

$$p(S)=\frac{1}{S\zeta\sqrt{2\pi}}\exp\left[-\frac{1}{2}\left[\frac{(\ln(S)-\lambda)^2}{\zeta}\right]^2\right]$$

Equation 7.3

where S is the lying snow mass; λ and ζ describe the shape of the distribution. ζ is given as:

$$\zeta^2=\ln\left(1+C_s^2\right)$$

Equation 7.4

With:

$$\lambda=\ln(S_0)-\frac{1}{2}\zeta^2$$

Equation 7.5

where C_S is the coefficient of variation, and S_0 is the initial mean snow mass. This formulation thus assumes that snow-cover is 100% during accumulation and that a drift can be infinitely deep, but correspondingly infinitely unlikely. The shallowest snow is correspondingly infinitely shallow.

Integrating $p(S)$ allows the fractional snow covered area to be derived for a given initial SWE S_0, coefficient of variation C_S and an accumulated homogenous change in SWE S_Δ:

$$f_{snow}=\int_{S_\Delta}^{\infty}p(S)dS$$

Equation 7.6

Correspondingly the fractional snow-free area can be given as:

$$f_{snowfree} = \int_0^{S_\Delta} p(S)dS$$

Equation 7.7

Expanding f_{snow} gives:

$$f_{snow} = \frac{1}{2} erfc\left[\frac{z}{\sqrt{2}}\right]$$

Equation 7.8

where:

$$z = \frac{\ln(S_\Delta) - \lambda}{\zeta}$$

Equation 7.9

The mean mass of lying snow is simply the distribution of snow minus the melt rate.

$$\overline{S} = \int_M^{\infty} (S - M)p(S)dS$$

Equation 7.10

$$\overline{S} = \frac{1}{2}\exp\left(\lambda + \frac{\zeta^2}{2}\right) erfc\left(\frac{z-\zeta}{\sqrt{2}}\right) - S_\Delta f_{snow}$$

Equation 7.11

Incorporating Equation 7.8 and Equation 7.11 into a numerical model requires the complementary error function (erfc). This can be approximated as (Essery and Pomeroy 2004):

$$erfc(x) = \frac{2}{1 + \exp(2.4x)} + e$$

Equation 7.12

with $|e| < 0.02$ for all x.

As noted by Essery and Pomeroy (2004) a more serious problem is that both f_{snow} and $\overline{S}$ have the parametric form, and require the storage of pre-melt SWE S_0 and the accumulated change in SWE S_Δ. This is straight forward if an accumulation period was followed by ablation, however as commonly occurs snowfall can interrupt melt. To incorporate this, snowfall during the melt period is used to decrease S_Δ, shifting the snow covered fraction back towards 100% and correspondingly increasing mean SWE.

The pre-melt SWE is derived from the accumulation pre-melt, and correspondingly the snow covered fraction is 100%. Should accumulated snowfall exceed accumulated ablation during a melt phase then S_Δ is set to zero and S_0 is increased to maintain mass-balance.

As $p(S)$ is a continuous distribution the snow covered fraction and SWE never reaches zero, it is thus assumed to be snow-free when post-melt SWE is less than 1 kg m^{-2}, S_0 and S_Δ are correspondingly reset to zero. The distribution is thus reset for another accumulation-ablation phase. The coefficient of variation is set as a parameter of the model.

b) Log-Normal Distributions

Log-normal distributions fitted to the observed distributions of snow-cover are shown in Figure 7-11. Using only paired values of SWE gives a slightly lower estimate of the coefficient of variation (C_s) of 1.12 for 27th February 2004 survey (SWE 1, Figure 7-11a) than when all the data is taken into account. A C_s of 1.13 is used for the 28th March 2005 survey (SWE 5, Figure 7-11e). Subsequent surveys in 2004 are derived using the mean change in SWE (S_Δ) between paired observations. Between the 27th February 2004 survey and the subsequent two surveys no net change in SWE occurred, despite a changing distribution of snow-cover. The same distribution is thus assumed to fit. However, between the first and final surveys, a net decrease of 35 kg m^{-2} is observed.

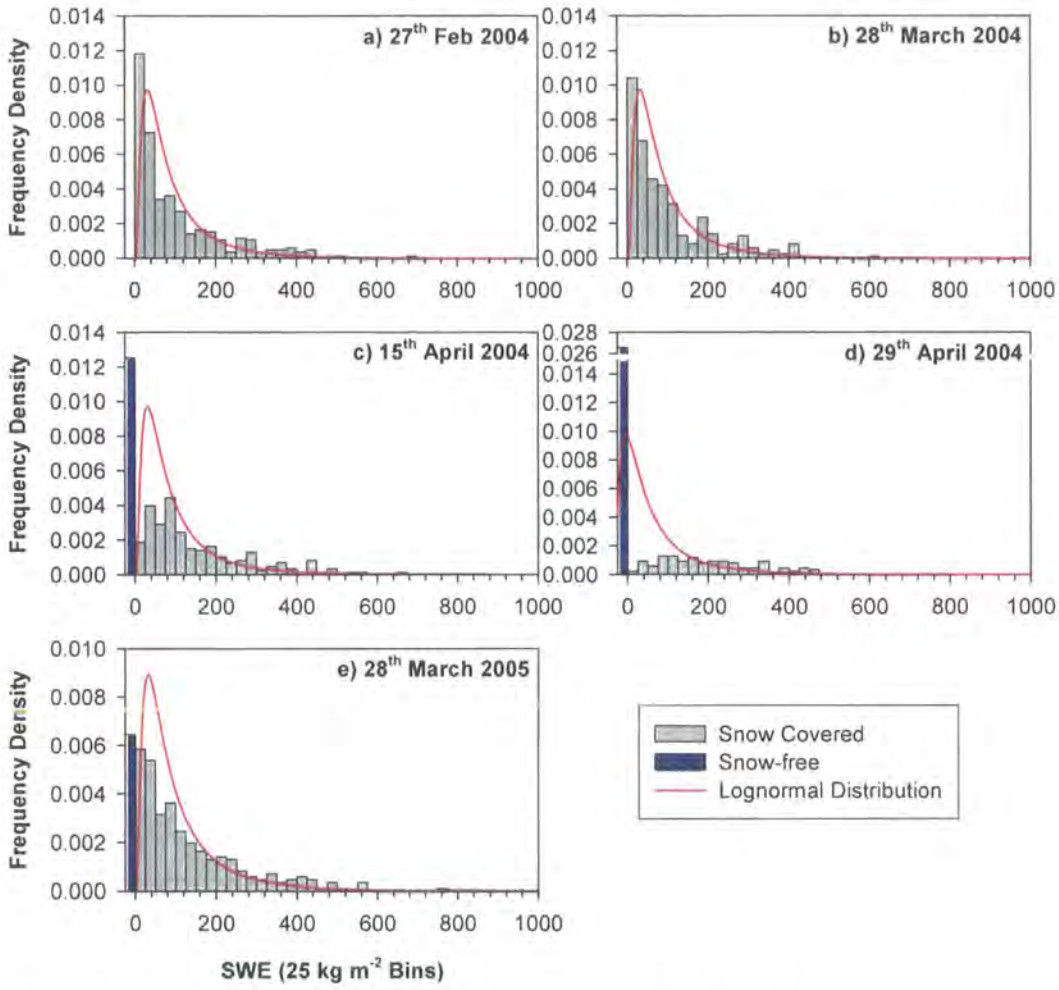

Figure 7-11: Snow distribution histograms with fitted log-normal distributions from 337 paired observations of SWE. Grey bars indicate snow-cover and blues bars snow-free areas, the integral of the bars sums to 1. A coefficient of variation of 1.12 is used in a-d, and 1.13 in e based on field observations. The lognormal distribution in c-d is the same as a, but shifted to the left according to the degree of ablation taking place between the survey and figure a.

The general fit of the log-normal distribution is reasonable, however, when formally tested using a Chi-squared goodness of fit test the assumption of a log-normal distribution is not statistically significant for all five surveys (Table 7-6). In particular, the greatest error is found when simulating melting snow-cover.

Table 7-6: Chi-Squared goodness of fit tests for log-normal distributions

	Chi-squared ($kg\ m^{-2}$)	Degrees of freedom	P-value
SWE 1	117.4	13	P<0.01
SWE 2	97.3	13	P<0.01
SWE 3	91.0	13	P<0.01
SWE 4	444.6	14	P<0.01
SWE 5	42.0	13	P<0.01

Although, the ability to simulate a distribution of SWE at a given point in time is poor, the efficacy of simulating snow covered fraction under homogenous melt conditions is substantially improved upon (Figure 7-12). However, assuming a coefficient of variation of 0.4 as suggested for a global value for tundra (Liston, 2005) would substantially underestimate the snow-free area for a given melt. The choice of coefficient of variation is thus critical.

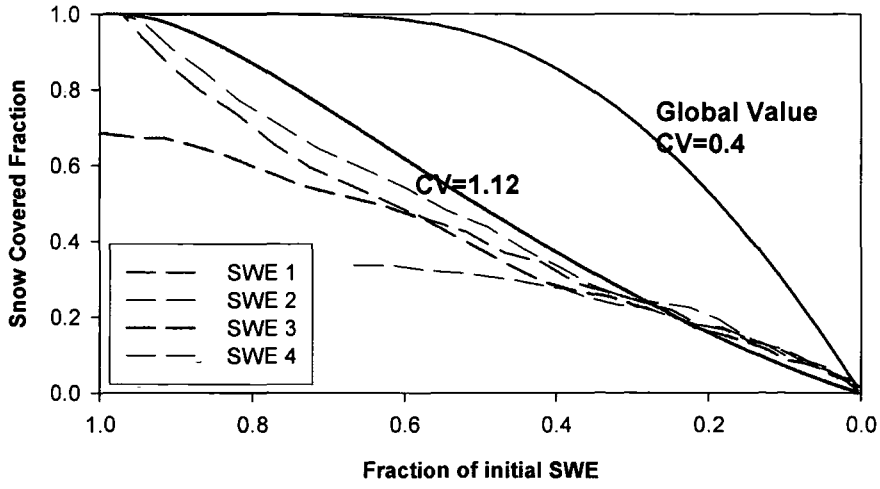

Figure 7-12: Snow-cover depletion curves from observations (dashed lines) and predicted according to a log-normal distribution (solid line). Light green shows a suggested global tundra fit (Liston, 2005), and dark green a distribution based on observations.

7.5 Simulating Snow Distribution

Simulations of snow-cover for the 2003/2004 winter season were completed using the snow distribution models coupled to the tiled version of MOSES. In general, the three models described are better at predicting broad scales than individual cell snow mass typical of snow distribution models (Bruland *et al.*, 2004; Prasad *et al.*, 2001). Further to this, there is strictly no reason why the distributed models should predict individual cell snow mass due to the difference in the extent and support of the measurement and model (Bloschl, 1999; Bloschl and Sivapalan, 1995). The snow distribution parameterised models are compared with the standard uniform version of MOSES and to the daily snow covered fraction observations.

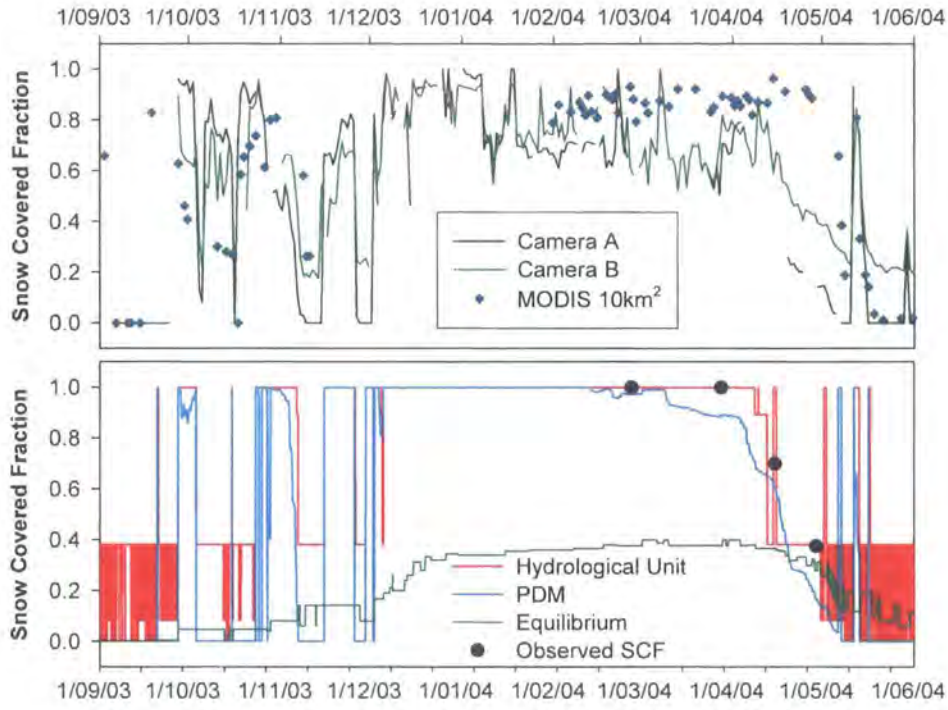

Figure 7-13: Modelled and Observed Snow covered Fraction for the winter of 2003-2004.

Stimulated snow covered fraction and SWE are shown in Figure 7-13 and Figure 7-14. The equilibrium model over-redistributes snow leading to excessively deep snow drifts in the lee of topography and a low snow covered fraction. As snowfall is instantaneously redistributed, the snow covered fraction never exceeds 40%. The result is snow patches that last late into the summer. Both the PDM model and the hydrological unit model perform similarly, modelling a near 100% snow-cover for the majority of the winter before melt begins. The hydrological unit model predicts the deepest drifts to average 350 kg m^{-2}, and the shallowest, most exposed, unit to average 50 kg m^{-2}, similar to what observations suggest. The ability of the HU model to redistribute snow at a given rate allows simulation of snowfall events that correspond well to observations, particularly early in the season when snow-cover is highly variable. Similarly the formulation of the log-normal curve also simulates early season complete snowfalls. Both models extend the snow covered period to 3rd May 2005; extending the period by 15 days compared to the standard model. Both models, predict unrealistically complete snow-covers for the winter which observations suggest are only 70% complete.

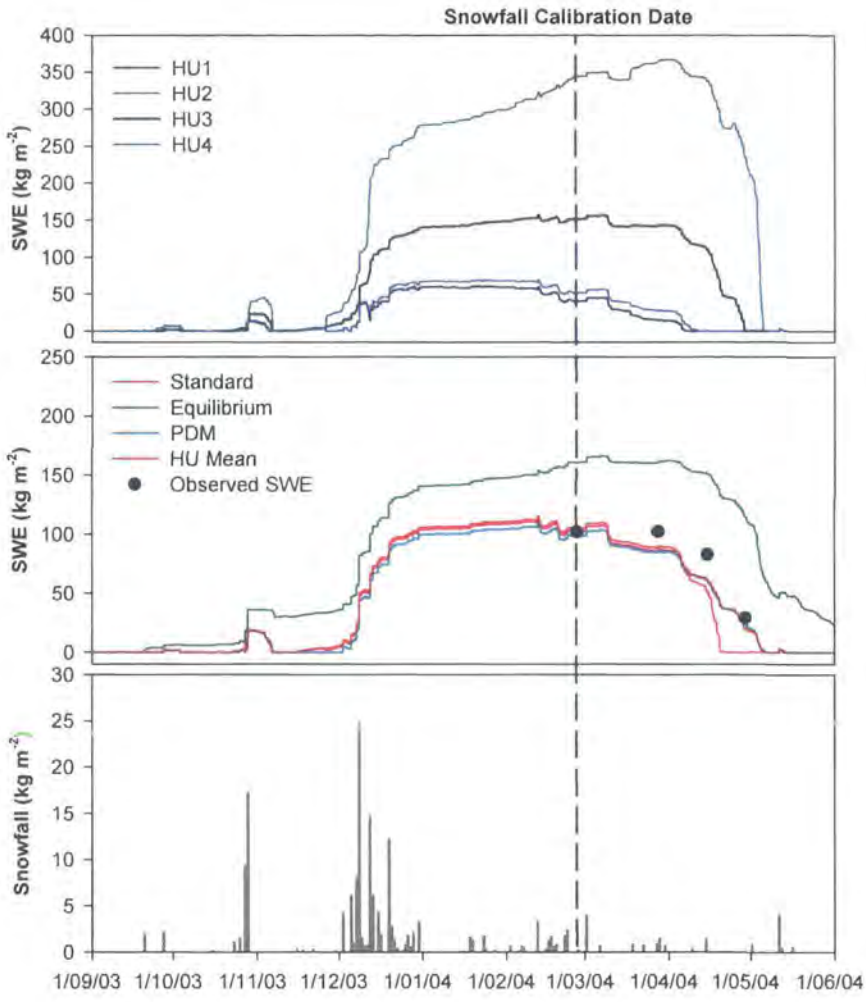

Figure 7-14: Modelled and Observed Snow Water Equivalent for the winter of 2003-2004.

As shown in Chapter 6, the fluxes of heat and water vapour are very sensitive to the snow covered fraction in a tiled model. Figure 7-15 shows a comparison of the predicted fluxes from the PDM tiled version of MOSES and the standard model. Modelled turbulent fluxes during the mid-winter are very similar, due to the almost complete snow-cover simulated by the snow distribution parameterisation. However, the modelled latent heat flux is clearly sensitive to changes in the soil moisture associated with early season melt events. The standard model predicts a more complete melt event and thus a greater flux of moisture into the soil, which can be seen in the simulated runoff. The greatest differences are during the rapid melt phase when the difference between the PDM and standard simulated snow covered fraction are at their greatest. The greatest difference however is in the simulated surface runoff and post-melt soil moisture. The PDM model simulates a

total of 50 kg m^{-2} of surface runoff, compared to 105 kg m^{-2} from the standard model. This is because the relative contributing area of melt is smaller in the PDM model and the melt period lasts longer allowing the soils to thaw earlier and increasing the infiltration capacity.

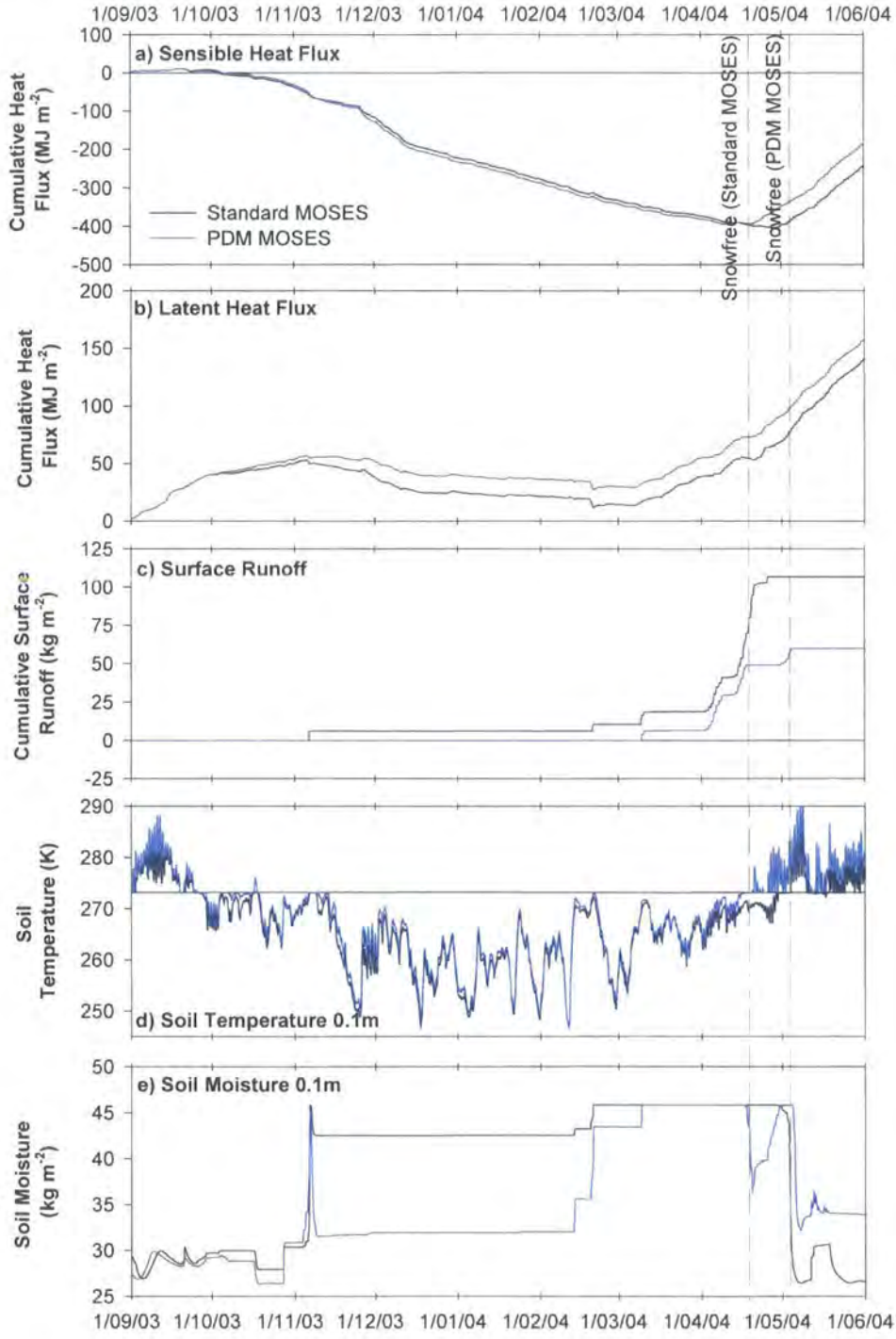

Figure 7-15: Modelled heat fluxes and soil parameters simulated with the tiled PDM and standard MOSES models. Blue and black lines show results from the standard and probability distribution MOSES versions respectively.

7.6 Summary

The assumption of a uniform snow-cover has important consequences for the simulated heat and water fluxes in the MOSES model. Simple models of snow distribution can be developed using terrain-derived indices. In particular the topographic shelter index can be used to generate hydrologically similar units, which can be coupled with a simple snow redistribution algorithm or a more complex blowing snow model. The advantages of using terrain derived parameters are that they are spatially explicit and allow snow-cover to be mapped back onto the terrain. Model performance, however, was as good when using a log-normal probability distribution with a prescribed coefficient of variance. This approach avoids the need for a DTM and extra processing and is more appropriate for use with a large scale atmospheric model (RCM/GCM). This method is, however, very sensitive to the choice of coefficient of variance (Luce and Tarboton, 2004). The advantage to using 'hydrological unit area' models is that they can be defined for a number of different surface types, for instance a development on the model used here could be to have units which are highly sheltered but north or south facing.

Chapter 8

Discussion

8 Discussion

Arctic tundra snow-cover is heterogeneous on length-scales too small to be reproduced in large-scale atmospheric models. The scale of this sub-grid heterogeneity varies from the scale of mountain ranges affecting accumulation and ablation to complex topography on the 50 m scale. However, what is known is that GCMs show a great deal of sensitivity to snow-cover, principally through the snow-albedo feedback mechanism. Many GCMs assume a uniform snow-cover, and maybe an effective albedo to account for exposed vegetation, nominally intended for use with large-tree canopies rather than shrub-tundra. The challenge has been to develop some form of parameterisation of sub-grid scale heterogeneity appropriate for use in numerical weather prediction and global climate simulations. This thesis presents the results of an intensive study at the patch scale in northern Sweden. The aim was to use a multi-scale approach to link processes at the patch scale to the landscape and develop parameterisations suitable for use in large-scale models.

Practical restraints restricted this field study to a small area of tundra in Northern Sweden. However, many of the processes and snow-cover patterns are thought to be representative of Pan-Arctic snow-covers in general. Some care however must be taken when extrapolating the numerical methods used in this thesis to large-scale global models. The pattern and evolution of a patchy arctic tundra snow-cover were successfully monitored for a small study site in northern Sweden during the winter of 2003-2004. The snow-cover showed heterogeneity on the 1-100 m scale, associated with complex topography and the distribution of shrub-beds. During a large part of the winter substantial areas remain snow-free, particularly exposed ridge-tops, whilst sheltered snow-beds accumulate deep drifts that may last through until mid-summer. Analysis of drift formation suggests that the typical process-scale controlling drift formation is of the order of 20 m, with an overall drift size of approximately 60 m. . The locations of the patches were maintained between the 2003-2004 and 2004-2005 winters, as was the prevailing wind direction. This suggests that the drifts are regular formations. The location of drift formation appears to be a function of both topography and deep shrub-beds. Topographic data analysis shows that, in certain locations, deeper snow-beds form

than the topography offers shelter for. In these locations, tall, dense shrubs are found. Simple analysis of the depth of drifts formed against topographic shelter suggests that, should winter snowfall increase, this snowfall will most likely lead to deeper drifts, rather than a uniform increase in depth, or be transported away from the tundra entirely most likely to the birch forest. The presence of snow clearly has an effect on plant productivity, by controlling the growing season length and soil temperatures during the winter, both of which are strong controls on the carbon balance and plant performance of tundra ecosystems (e.g. Cook, 2005; Wookey, 2002). Snow-vegetation feedbacks may well have potential climate implications, especially with the observed shrub expansion in the pan-Arctic (Sturm *et al.*, 2001b; Tape *et al.*, 2006). This is part of a feedback mechanism suggested by Sturm *et al.* (2001a; 2005) by which shrub expansion may occur. The increased size, density and extent of shrubs would act to retain more snow by reducing transport and sublimation (sublimation commonly occurs during transport) and thus feedback to soil temperatures and shrub productivity. However, there appears to be a limit to this feedback as where snow drifts are particularly deep and last late into the growing season the dominant *Betula* spp. and *Salix* spp. tend to be replaced by a herb-rich flora. The mechanism behind this is unknown, but speculatively it may be related to nutrient availability and growing season length. There is a case for greater research in this field. Traditional snow manipulation experiments (e.g. Cook, 2005; Jones *et al.*, 1998; Wahren *et al.*, 2005; Welker *et al.*, 2000) have generally concentrated on snow augmentation across the shallow vegetation under the hypothesis that predicted increased winter precipitation in the Arctic will lead to an uniform increase in snow depth. Results from these snow augmentation experiments have shown an increase in plant performance with a tendency towards larger morphologies under deeper drifts, however this vegetative response is highly species and community dependent (Cook, 2005; Wahren *et al.*, 2005). The effect of pro-longed snow-cover on the CO_2 balance is less clear, with some experiments showing little difference in annual carbon balances (Cook, 2005), and others significant reduction in carbon efflux (Jones *et al.*, 1998; Welker *et al.*, 2000). In some cases, the effect of snow augmentation is to switch tundra systems from a net source to a sink of carbon, although these responses are highly seasonally dependent. The inclusion of heterogeneous snow into a land-surface model should

in theory affect the simulated carbon-balance for tundra regions and may therefore have substantial feedbacks to global climate.

The combined presence of snow and snow-free surfaces over relatively small extents exerts a strong effect on the surface energy-balance and local air temperature, humidity, windspeed and direction. Evidence presented here suggests that the atmosphere is responding to surface conditions generated by the patchy tundra and also meso-scale circulations associated with the low albedo birch forest. This interaction has strong implications for the energy available for melt. The timing of melt is associated with seasonally increasing shortwave radiative fluxes, with the snowpack gradually ripening through April. The volume and rate of melt is however controlled by both sensible and latent heat fluxes, with turbulent fluxes contributing nearly double the energy (64%) to melt than net radiation (36%). The contribution of latent heat (24%) is surprising since a melting snow surface is a freely evaporating surface. The warm, wet boundary layer state, however, leads to a reversal in the vapour pressure gradient, leading to condensation onto the snow surface. Condensation releases a great deal of energy, which is used to melt snow. The ratio of condensation to melt is nearly 1:10; condensation is thus a very efficient way of melting snow.

Snow ablation is strongly controlled by the formation of a relatively warm, humid and windy atmosphere overlying the snowpack. These atmospheric conditions appear to be responding to strong positive sensible heat and evaporation from the snow-free surfaces. The interaction between the snow and snow-free surfaces is therefore key to accurately simulating melt rates. However, none of the evidence presented here suggests that small-scale advection is leading to heterogeneous melt: observed melt shows no correlation to distance from patch edge, numerical simulations of advection suggest much greater heat fluxes than fit the observed melt rates, and accurately up-scaling fluxes from the patch to the landscape needs no parameterisation of advection. The mechanism by which these patches interact is through a well-mixed boundary layer. Thus evaporation and sensible heat from snow-free patches warms and moistens the overlying air, and the snowpack dries and cools the air. This process occurs through mixing in the boundary layer, rather

than advection. This is supported through numerical simulations that suggest that the energy-balance of the snowpack is a function of a well mixed boundary layer, with heat fluxes controlled by blending height temperature and humidity.This is a very important result in developing a sub-grid parameterisation of heterogeneous snow-covers. The implication is that separate surface-energy balances are required for snow and snow-free surfaces, rather than a complex representation of advection and correspondingly the size, shape and distribution of snowpatches, which evolve in response to heterogeneous melt. Rather, snow patches can all be lumped together into a single tile with a parameterisation relating the fraction of snow-cover to surface characteristics and snow depth. A major limitation of this study is the use of observed air temperature and humidity to drive the models used in this study. These driving variables implicitly include the effect of the two surfaces on the atmosphere, this assumption holds fine when the measurements are made at the local blending height. This assumption most likely holds true for the majority of the time, however during periods of high instability and sizeable positive turbulent fluxes this assumption may be invalid. There is clearly some difficulty in proving small-scale advection is either a process that is occurring and is important or that it is a process that is not occurring. Studies published in the literature have shown that accurate simulations of snow-cover evolution cannot be achieved without some form of extra energy in the form of advection (Neumann and Marsh, 1998; Pohl and Marsh, 2005), more recent work has been able to show the formation of internal boundary layers thus actually showing advection(Granger *et al.*, 2006). In the case of Abisko no definite answer can be given without employing a method such as Granger *et al.* (2006). However, the important result is that it doesn't need to be modelled explicitly, as long as the effects of the two surfaces are represented at the blending height. Within HadAM3 the lower boundary layer height is approximately 20 m (actually a hybrid function of atmospheric pressure). This level is above the blending height for patchy snow. It is difficult to test the sensitivity of the turbulent fluxes, surface runoff and snowmelt to model engineering of the snow-covered fraction without a full boundary-layer model, which is beyond the scope of this thesis.

Having shown that separate energy-balances are an appropriate form of model engineering, the next step is to provide a parameterisation of snow covered fraction. Three methods were trialled here; the first relied purely on a shelter index to define a rough surface that snow would attempt to fill. The problem here was that redistribution was assumed instantaneous and generated deep snow drifts and low snow covered fractions. The second approach classified the shelter index to generate 'hydrological units' between which redistribution took place. The third approach used assumed a probability distribution function to represent snow distribution, the function used was a log-normal distribution, as suggested by Donald *et al.* (1995), and implemented following the recommendations of Liston (2004). Both the hydrological unit model (HUM) and probability distribution model (PDM) produced more realistic snow distributions than assuming a uniform snow distribution. However, the resemblance to observed snow-cover on a cell by cell basis was poorer. Using these fractions in the tiled version of MOSES 2 led to an extension of the snow lie period by nearly a month over the uniform model and a reduced peak surface runoff from 105 kg m^{-2} to 50 kg m^{-2} and exerted a small effect on the simulated turbulent flux. The reduction in surface runoff leads to substantially greater soil moisture stores, which last through the summer months and may help reduce the warm bias generally seen in GCMs for the high latitudes. The actual magnitude of the effect of model engineering on runoff and surface fluxes is affected by the use of observed driving data. This is particularly the case for the turbulent fluxes. The sensitivity to model engineering will be substantially greater if a full boundary layer scheme is included. The representation of heterogeneous snow-covers will therefore affect the GCM simulated feedback to global climate through the snow-albedo mechanism. The expected warming in the high latitudes is predicted to lead to a large change in the hydrological cycle for snow covered basins (Barnett *et al.*, 2005). Model engineering of heterogeneous snow-covers will undoubtedly have an impact on simulated hydrological cycles. For instance, spring snow melt contributes as much as 80% of the yearly discharge of the Kuparuk river basin, Alaska (McNamara *et al.*, 1998). Model engineering will therefore affect the simulated freshwater balance of the Arctic Ocean, and consequently, through a second feedback mechanism to the global climate.

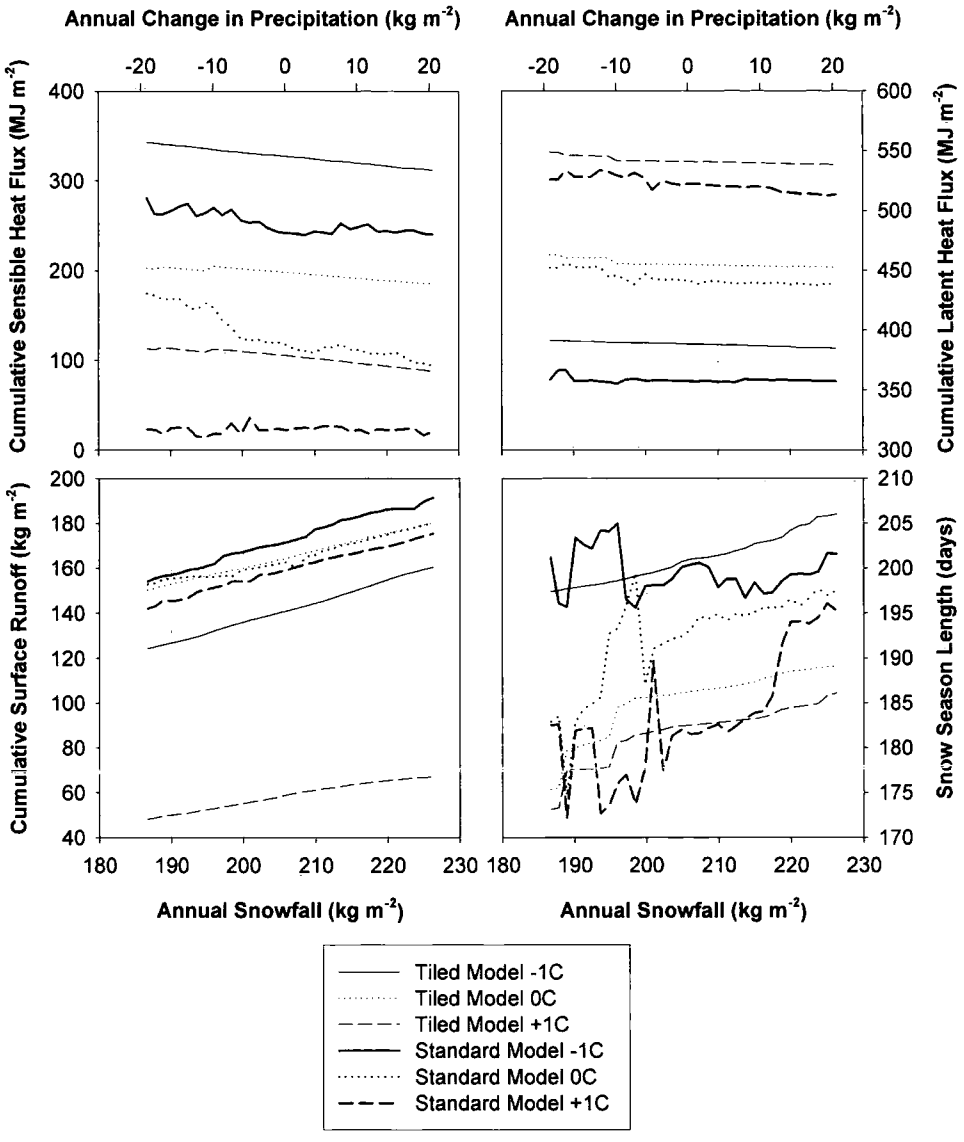

Figure 8-1: Model Engineering Sensitivity to changing annual solid precipitation and air temperature in equilibrium model runs.

An example of the sensitivity of land surface models to model engineering is shown in Figure 8-1. The figure shows model sensitivity to changing air temperature (plus and minus 1°C applied annually) and solid precipitation (plus and minus 20 kg m^{-2} applied at times of observed snowfall) for the standard model with uniform snow-cover and the tiled model with the log-normal distribution of snow-cover. The models are equilibrium simulations and are spun up for 100 years for soil moisture and temperature to reach equilibrium. The aim of this figure is not to show the effect of climate change, but rather to show the model sensitivity to climate perturbations for different parameterisations of snow-cover. The greatest sensitivity is to annual air temperature, however for the reasons discussed earlier

this is to be expected when using observed driving data as air temperature directly impacts upon the turbulent fluxes, the affect of snowfall is to change the surface conditions and is thus much more subtle. However, clearly the sensitivity to solid precipitation is much greater for the standard model than for the tiled model which moderates the effects, particularly for snow season length. It is difficult to elucidate the feedbacks to climate based on the experiments in Figure 8-1 as the climate response is largely dependent on the feedback to air temperature and humidity (which are used as driving data in these offline simulations), which almost certainly will affect cloud formation in online simulations. Cloud formation in NWP and GCMs is of considerable uncertainty and may therefore moderate or exacerbate any feedbacks to climate. It is therefore difficult to say whether feedbacks will be positive, negative or insignificant to climate. Furthermore, the parameterisation of snow-cover potentially will affect simulated carbon exchange in tundra regions. However, surface runoff appears to be much less sensitive to climate change in the tiled model compared to the standard model. The effect of climate change on Arctic hydrology may therefore be less than currently predicted.

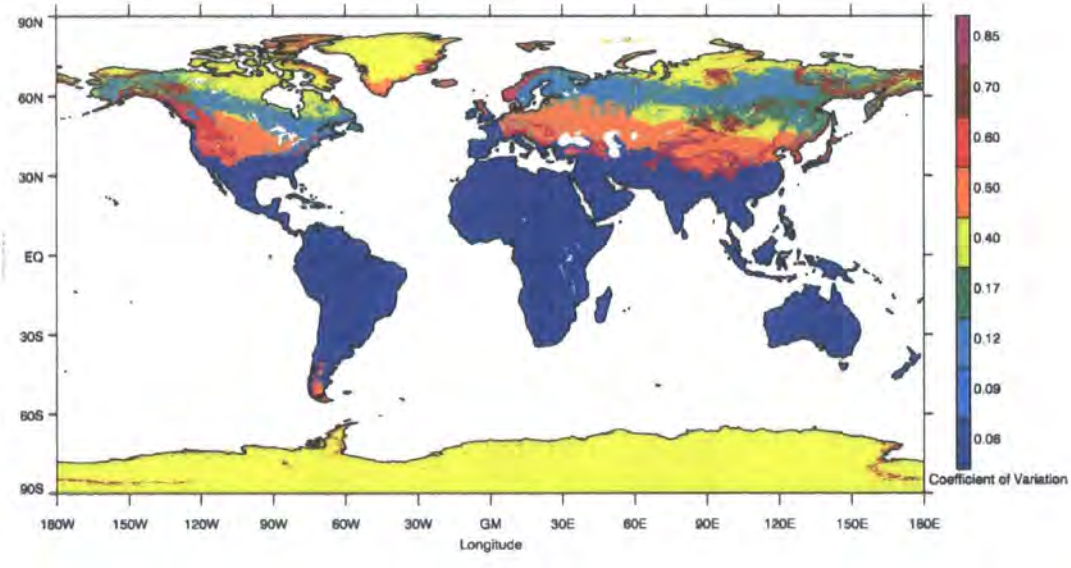

Figure 8-2: Global distribution of snow coefficient of variation. Data are plotted at 2.5 arc-minute and are classified according to global distributions of air temperature, topography and windspeed (Liston, 2005).

This study has provided a method by which heterogeneous snow-covers can be included in large-scale models based on observations for a relatively small patch of tundra in Northern Sweden. A major difficulty in developing sub-grid scale

parameterisations is that 'the scale at which conceptualisation is formulated then becomes critically important and the transfer of information across scales becomes very difficult' (Bloschl, 1999). Parameterisations developed at the landscape scale are therefore not necessarily appropriate at the GCM gridbox scale. The challenge remains as to how to parameterise the snow covered fraction to the surface properties (i.e. forest, tundra, etc.) and snow depth on the gridbox scale. Added to this are complications with sub-grid scale orography, which influences snowfall and temperature and humidity lapse rates. One suggestion put forward by Liston (2005) is a global distribution of the coefficient of variance for snow distribution, from which log-normal snow-cover distributions can be generated (Figure 8-2). Alternative methods may include 'hydrological unit' models or different formulations of snow probability distributions. This research is being continued through the National Environmental Research Council: Climate and Land Surface Systems Interaction Centre (CLASSIC). Plans for future work based on this research involve developing the parameterisation for snow-covered fraction using MODIS remote sensed data to validate snow-covered fractions in 1° offline simulations with JULES (successor to MOSES). The aim is to develop separate parameterisations for high and low vegetation, this has been implemented successfully in the ECMWF TESSEL model (van den Hurk *et al.*, 2000). In addition, tiles of elevation, aspect and slope are being investigated. These are being derived from global elevation data sets, available at 90 m resolution (Shuttle Radar Topography Mission data) for the low latitudes and at 1 km for the high latitudes (Global Topography, United States Geological Survey). However, even at these resolutions topography is often poorly represented. The use of high-resolution remotely sensed products (e.g. MODIS snow presence/absence - 500 m resolution, SRTM, GTOPO) allow the fundamental differences in scale between landscape scale observations of physical processes and parameterisations in large-scale models to be reconciled. A new multi-layer snow model is also under development, with improved thermal and hydrologic physics. Through the CLASSIC consortium these model developments are scheduled to be part of the 2010 HadGEM2 (Global Earth System Model 2), which will contribute to the IPCC (Intergovernmental Panel on Climate Change) 5th assessment. More rapid implementation of these developments is planned for the models used in numerical weather prediction. An

improved parameterisation of heterogeneous melt is planned to be implemented before the spring melt in 2007.

Of critical importance is an assessment of GCM sensitivity in online and offline roles of turbulent fluxes and surface runoff to the parameterisation of snow distribution. Online sensitivity analysis with the HadAM3 model suggest that surface runoff is highly sensitive to the spatial distribution of soil moisture (Gedney and Cox, 2003). The implication is that GCMs will show similar levels of sensitivity to snow distribution. The inclusion of sub-grid heterogeneity will also help with specific failures of the Unified Model associated with excessive surface runoff, plus potentially reduce the warm bias generally seen in most GCM simulations. The inclusion of new snow physics and parameterisations will most likely have a significant impact on the simulated climate in the high latitudes.

References

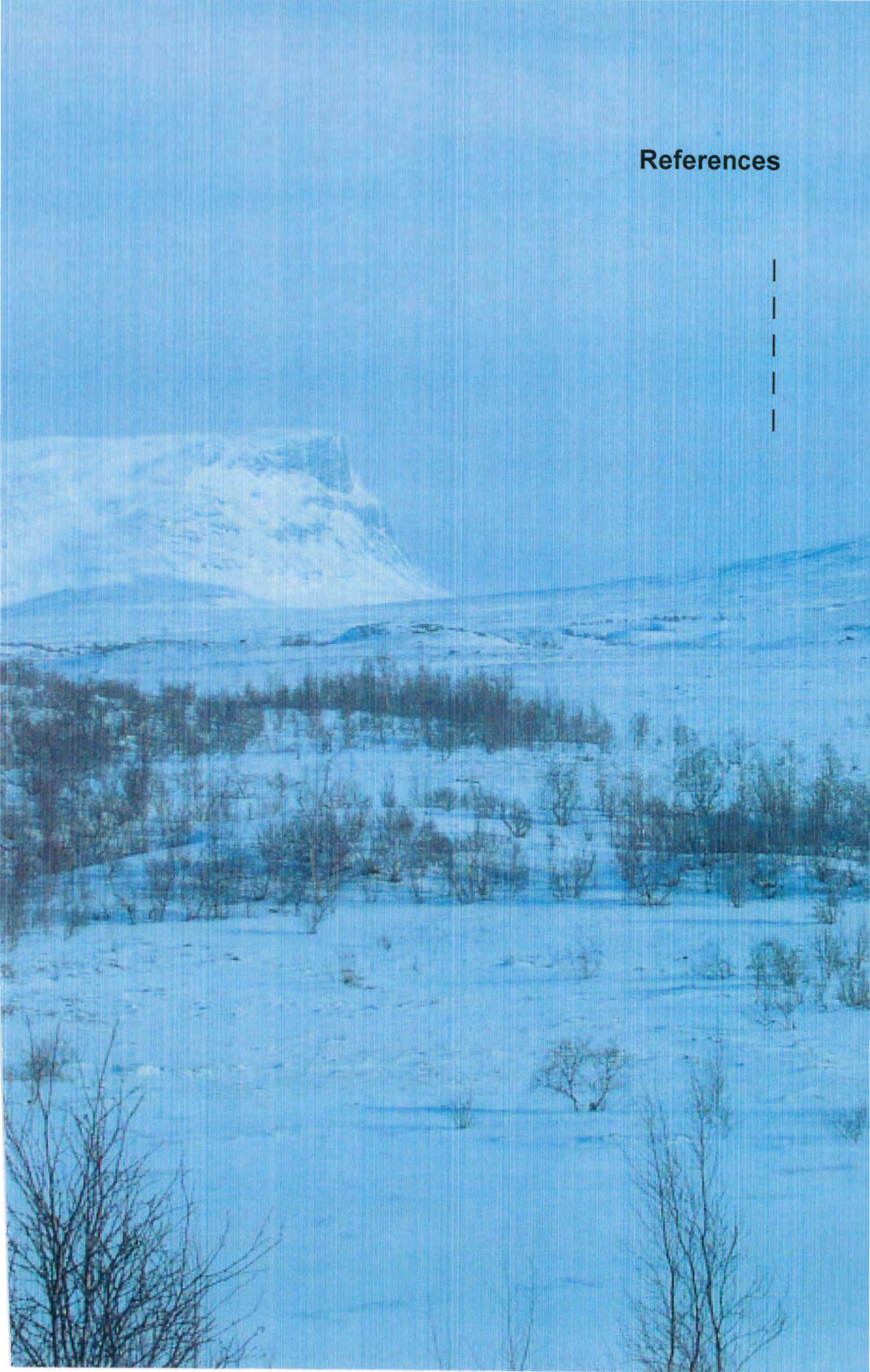

References

Alfnes, E., Andreassen, L.M., Engeset, R.V., Skaugen, T. and Udnaes, H.C., 2004. Temporal variability in snow distribution, Annals of Glaciology, Vol 38, 2004. Annals of Glaciology, pp. 101-105.

Avissar, R. and Pielke, R.A., 1989. A Parameterization of Heterogeneous Land Surfaces for Atmospheric Numerical-Models and Its Impact on Regional Meteorology. Monthly Weather Review, 117(10): 2113-2136.

Barnett, T.P., Adams, J.C. and Lettenmaier, D.P., 2005. Potential impacts of a warming climate on water availability in snow-dominated regions. Nature, 438(17): 303-309.

Benson, C.S., 1982. Reassessment of winter precipitation on Alaska's North Slope and measurements on the flux of wind-blown snow, University of Alaska, Fairbanks, Geophysical Institute Report UAG R-288.

Beven, K.J. and Kirkby, M.J., 1979. A physically based, variable contribution area model of basin hydrology. Hydrological Scientific Bulletins, 24(1): 43-69.

Bewley, D., Pomeroy, J.W. and Essery, R.L.H., 2005. Processes of solar radiation transfer through a sub-arctic shrub canopy. In prep.

Billings, W.D. and Bliss, L.C., 1959. An alpine snowbank environment and its effects on vegetation, plant development, and productivity. Ecology, 40(3): 388-397.

Bliss, L.C. and Matveyeva, N.V., 1992. Circumpolar Arctic Vegetation. In: Chapin Iii, F.S., Jefferies, R.L., Reynolds, J.F., Shaver, G.R., Svoboda, J. and Chu, E.W. (Editors), Arctic Ecosystems in a Changing Climate: An Ecophysiological Perspective. Academic Press, pp. 11-34.

Bloschl, G., 1999. Scaling issues in snow hydrology. Hydrological Processes, 13(14-15): 2149-2175.

Bloschl, G. and Sivapalan, M., 1995. Scale Issues in Hydrological Modeling - a Review. Hydrological Processes, 9(3-4): 251-290.

Blyth, E., Finch, J.W., Robinson, M. and Rosier, P., 2004. Can soil moisture be mapped onto the terrain? Hydrology and Earth System Sciences, 8(5): 923-930.

Blyth, E.M., 1994. The effect of small scale heterogeneity on surface heat and moisture fluxes. PhD Thesis, University of Reading.

Blyth, E.M. and Dolman, A.J., 1995. The Roughness Length for Heat of Sparse Vegetation. Journal of Applied Meteorology, 34(2): 583-585.

Boone, A. and Etchevers, P., 2001. An intercomparison of three snow schemes of varying complexity coupled to the same land surface model: Local-scale evaluation at an Alpine site. Journal of Hydrometeorology, 2(4): 374-394.

Bowling, L.C., Lettenmaier, D.P., Nijssen, B., Graham, L.P., Clark, D.B., El Maayar, M., Essery, R., Goers, S., Gusev, Y.M., Habets, F., Van Den Hurk, B., Jin, J.M., Kahan, D., Lohmann, D., Ma, X.Y., Mahanama, S., Mocko, D., Nasonova, O., Niu, G.Y., Samuelsson, P., Shmakin, A.B., Takata, K., Verseghy, D., Viterbo, P., Xia, Y.L., Xue, Y.K. and Yang, Z.L., 2003. Simulation of high-latitude hydrological processes in the Torne-Kalix basin: PILPS phase 2(e) - 1: Experiment description and summary intercomparisons. Global and Planetary Change, 38(1-2): 1-30.

Bruland, O., Liston, G.E., Vonk, J., Sand, K. and Killingtveit, A., 2004. Modelling the snow distribution at two high arctic sites at Svalbard, Norway and at an alpine site in central Norway. Nordic Hydrology, 35(3): 191-208.

Brun, E., David, P., Sudul, M. and Brunot, G., 1992. A Numerical-Model to Simulate Snow-Cover Stratigraphy for Operational Avalanche Forecasting. Journal of Glaciology, 38(128): 13-22.

Brun, E., Martin, E., Simon, V., Gendre, C. and Coleou, C., 1989. An Energy and Mass Model of Snow Cover Suitable for Operational Avalanche Forecasting. Journal of Glaciology, 35(121): 333-342.

Brutsaert, W., 1975. The Roughness Length for Water Vapor, Sensible Heat, and Other Scalars. Journal of the Atmospheric Sciences, 32: 2028-2031.

Bugbee, B., Monje, O. and Tanner, B., 1996. Quantifying Energy and Mass Transfer in Crop Canopies: Sensors for Measurement of Temperature and Velocity. Advances in Space Research, 18(4-5): 149-156.

Campbell Scientific, I., 2005. IRTS-P Precision Infrared Temperature Sensor (3/05).

Carson, D.J., 1982. Current parameterisations of land-surface processes in atmospheric general circulation models. In: Eagleston, P.S. (Editor), Land surface processes in atmospheric circulation models. Cambridge University Press, Cambridge, UK.

Casiniere, D.L., 1974. Heat exchange over a melting snow surface. Journal of Glaciology, 13(64): 55-72.

Cess, R.D., Potter, G.L., Zhang, M.H., Blanchet, J.P., Chalita, S., Colman, R., Dazlich, D.A., Delgenio, A.D., Dymnikov, V., Galin, V., Jerrett, D., Keup, E., Lacis, A.A., Letreut, H., Liang, X.Z., Mahfouf, J.F., Mcavaney, B.J., Meleshko, V.P., Mitchell, J.F.B., Morcrette, J.J., Norris, P.M., Randall, D.A., Rikus, L., Roeckner, E., Royer, J.F., Schlese, U., Sheinin, D.A., Slingo, J.M., Sokolov, A.P., Taylor, K.E., Washington, W.M., Wetherald, R.T. and Yagai, I., 1991. Interpretation of Snow-Climate Feedback as Produced by 17 General-Circulation Models. Science, 253(5022): 888-892.

Claussen, M., 1991. Estimation of Areally-Averaged Surface Fluxes. Boundary-Layer Meteorology, 54(4): 387-410.

Cohen, J., 1960. A Coefficient of Agreement for Nominal Scales. Educational and Psychological Measurement, 20(1): 37-46.

Cohen, J. and Rind, D., 1991. The Effect of Snow Cover on the Climate. Journal of Climate, 4(7): 689-706.

Colbeck, S., Akitaya, E., Armstrong, R., Gubler, H., Lafeuille, J., Lied, K., Mcclung, D. and Morris, E.M., 1990. The International Classification for Seasonal Snow on the Ground, The International Commission on Snow and Ice of the International Association of Scientific Hydrology and the International Glaciological Society.

Coléou, C. and Lesaffre, B., 1998. Irreducible water saturation in snow: experimental results in a cold laboratory. Annals of Glaciology, 26: 64-68.

Cook, J.G., 2005. A Study of the ecological significance of snow distribution in the low arctic plant communities of northern Fennoscandia. PhD Thesis, University of Durham, Durham, UK, 207 pp.

Copland, L., 1998. The use of terrain analysis in the evaluation of snow cover over an alpine glacier. In: Lane, S.N., Chandler, J.H. And Richards K.S. (Editor), Landform Monitoring, Modelling and Analysis. Wiley, Chichester.

Corripio, J.G., 2004. Snow surface albedo estimation using terrestrial photography. International Journal of Remote Sensing, 25(24): 5705-5729.

Corripio, J.G., Durand, Y., Guyomarc'h, G., Merindol, L., Lecorps, D. and Pugliese, P., 2004. Land-based remote sensing of snow for the validation of a snow transport model. Cold Regions Science and Technology, 39: 93-104.

Cox, P.M., Betts, R.A., Bunton, C.B., Essery, R.L.H., Rowntree, P.R. and Smith, J., 1999. The impact of new land surface physics on the GCM simulation of climate and climate sensitivity. Climate Dynamics, 15: 183-203.

Cox, P.M., Huntingford, C. and Harding, R.J., 1998. A canopy conductance and photosynthesis model for use in a GCM land surface scheme. Journal of Hydrology, 213(1-4): 79-94.

Davis, R.E., Jordan, R., Daly, S. and Koenig, G., 2001. Validation of Snow Models. In: Anderson, M.G. and Bates, P.D. (Editors), Model Validation: Perspectives in Hydrological Science. John Wiley and Sons Ltd., Chichester, UK, pp. 261-292.

De Bruin, H.A.R. and Hartogensis, O.K., 2005. Variance method to determine turbulent fluxes of momentum and sensible heat in the stable atmospheric surface layer. Boundary-Layer Meteorology, 116(2): 385-392.

Dean, A.M., 2003. Vegetation, Topography and Snow-melt at the Forest-Tundra Ecotone in Arctic Europe: A study using Synthetic Aperture Radar. PhD Thesis, University Of Durham.

Denoth, A., 1994. An electronic device for long-term snow wetness recording. Annals of Glaciology, 19: 104-106.

Denoth, A., Foglar, A., Weiland, P., Mätzler, C., Aebischer, H., Tiuri, M. and Sihvola, A., 1984. A comparative study of instruments for measuring the liquid water content of snow. Journal of Applied Physics, 56(7): 2154-2159.

Déry, S.J., Crow, W.T., Stieglitz, M. and Wood, E.F., 2004. Modeling snow-cover heterogeneity over complex terrain for regional and global climate models. Journal of Hydrometeorology, 5: 33-48.

Dery, S.J., Salomonson, V.V., Stieglitz, M., Hall, D.K. and Appel, I., 2005. An approach to using snow areal depletion curves inferred from MODIS and its application to land surface modelling in Alaska. Hydrological Processes, 19(14): 2755-2774.

Dery, S.J. and Stieglitz, M., 2002. A note on surface humidity measurements in the cold Canadian environment. Boundary-Layer Meteorology, 102(3): 491-497.

Donald, J.R., Soulis, E.D., Kouwen, N. and Pietroniro, A., 1995. A land cover-based snow cover representation for distributed hydrologic models. Water Resources Research, 31(4): 995-1009.

Duynkerke, P.G., 1992. The Roughness Length for Heat and Other Vegetation Parameters for a Surface of Short Grass. Journal of Applied Meteorology, 31(6): 579-586.

Dyer, A.J., 1974. A review of flux profile relationships. Boundary-Layer Meteorology, 7: 363-372.

Elder, K., Dozier, J. and Michaelsen, J., 1991. Snow Accumulation and Distribution in an Alpine Watershed. Water Resources Research, 27(7): 1541-1552.

Elder, K., Dozier, J. and Michaelson, J., 1989. Spatial and temporal variation of net snow accumulation in a small alpine watershed, Emerald Lake basin, Sierra Nevada, California, U.S.A. Annals of Glaciology, 13: 56-53.

Ellis, A.W. and Leathers, D.J., 1998. The effects of a discontinuous snow cover on lower atmospheric temperature and energy flux patterns. Geophysical Research Letters, 25(12): 2161-2164.

Essery, R., 1997. Modelling fluxes of momentum, sensible heat and latent heat over heterogeneous snow cover. Quarterly Journal of the Royal Meteorological Society, 123(543): 1867-1883.

Essery, R., 2003. Aggregated and distributed modelling of snow cover for a high-latitude basin. Global and Planetary Change, 38: 115-120.

Essery, R., Best, M. and Cox, P., 2001. MOSES 2.2 Technical Documentation, Hadley Centre, Met Office, UK.

Essery, R., Blyth, E., Harding, R. and Lloyd, C., 2005. Modelling albedo and distributed snowmelt across a low hill in Svalbard. Nordic Hydrology, 36(3): 207-218.

Essery, R., Granger, R. and Pomeroy, J., 2006. Boundary-layer growth and advection of heat over snow and soil patches: modelling and parameterization. Hydrological Processes, 20(4): 953-967.

Essery, R., Li, L. and Pomeroy, J., 1999a. A distributed model of blowing snow over complex terrain. Hydrological Processes, 13(14-15): 2423-2438.

Essery, R., Martin, E., Douville, H., Fernandez, A. and Brun, E., 1999b. A comparison of four snow models using observations from an alpine site. Climate Dynamics, 15(8): 583-593.

Essery, R. and Pomeroy , J.W., 2004. Implications of spatial distributions of snow mass and melt rate for snow-cover depletion: theoretical considerations. Annals of Glaciology, 38: 261-265.

Etchevers, P., Martin, E., Brown, R., Fierz, C., Lejeune, Y., Bazile, E., Boone, A., Dai, Y.J., Essery, R., Fernandez, A., Gusev, Y.M., Jordan, R., Koren, V., Kowalczyk, E.A., Nasonova, O., Pyles, D., Schlosser, C.A., Shmakin, A.B., Smirnova, T.G., Strasser, U., Verseghy, D., Yamazaki, T. and Yang, Z.L., 2004. Validation of the energy budget of an alpine snowpack simulated by several snow models (SnowMIP project). Annals of Glaciology, 38: 150-158.

Fahnestock, J.T., Povirk, K.L. and Welker, J.M., 2000. Ecological significance of litter redistribution by wind and snow in arctic landscapes. Ecography, 23: 623-631.

Faria, D.A., Pomeroy, J.W. and Essery, R.L.H., 2000. Effect of covariance between ablation and snow water equivalent on depletion of snow-covered area in a forest. Hydrological Processes, 14(15): 2683-2695.

Førland, E.J., Allerup, P., Dahlström, B., Elomaa, E., Jónsson, T., Madesn, H., Perälä, J., Rissanen, P., Vedin, H. and Vejen, F., 1996. Manual for operation of correction of Nordic precipitation. 24/96, Norwegian Meteorological Institute.

Foster, J., Liston, G., Koster, R., Essery, R., Behr, H., Dumenil, L., Verseghy, D., Thompson, S., Pollard, D. and Cohen, J., 1996. Snow cover and snow mass intercomparisons of general circulation models and remotely sensed datasets. Journal of Climate, 9(2): 409-426.

Frolov, A.D. and Macheret, Y.Y., 1999. On dieletric properties of dry and wet snow. Hydrological Processes, 13: 1755-1760.

Garatt, J.R., 1992. The atmospheric boundary layer. Cambridge Atmospheric and Space Science Series. Cambridge University Press, Cambridge, UK.

Garatt, J.R. and Hicks, B.B., 1973. Momentum, heat and water vapour transfer to and from natural and artificial surfaces. Quarterly Journal of the Royal Meteorological Society, 99: 680-687.

Gedney, N. and Cox, P.M., 2003. The sensitivity of global climate model simulations to the representation of soil moisture heterogeneity. Journal of Hydrometeorology, 4(6): 1265-1275.

Goodison, B.E., Ferguson, H.L. and Mckay, G.A., 1981. Measurement and Data Analysis. In: Gray, D.M. and Male, D.H. (Editors), The Handbook of Snow. Pergamon, Toronto.

Goodison, B.E., Louie, P.Y.T. and Yang, D., 1998. WMO Solid Precipitation Measurement Intercomparison Final Report, World Meteorological Organisation.

Gordon, C., Cooper, C., Senior, C.A., Banks, H., Gregory, J.M., Johns, T.C., Mitchell, J.F.B. and Wood, R.A., 2000. The simulation of SST, sea ice extents and ocean heat transports in a version of the Hadley Centre coupled model without flux adjustments. Climate Dynamics, 16(2-3): 147-168.

Granger, R.J., Essery, R. and Pomeroy, J.W., 2006. Boundary-layer growth over snow and soil patches: field observations. Hydrological Processes, 20(4): 943-951.

Gray, D.M. and Landine, P.G., 1987. Albedo Model for Shallow Prairie Snow Covers. Canadian Journal of Earth Sciences, 24(9): 1760-1768.

Gray, D.M. and Male, D.H., 1981. Handbook of snow : principles, processes, management & use. Pergamon Press, New York, xx, 776 pp.

Gray, D.M. and Prowse, T.D., 1993. Snow and floating ice. In: Maidment, D.R. (Editor), Handbook of Hydrology. McGraw-Hill, New York, pp. 7.1-7.58.

Groisman, P. and Davies, T.D., 1999. Snow Cover and the Climate System. In: Jones, H.G., Pomeroy , J.W., Walker, D.A. and Hoham, R.W. (Editors), Snow Ecology: an interdisciplinary examination of snow covered ecosystems. Cambridge University Press, Cambridge, pp. 1-44.

Groisman, P.Y., Karl, T.R. and Knight, R.W., 1994a. Observed Impact of Snow Cover on the Heat-Balance and the Rise of Continental Spring Temperatures. Science, 263(5144): 198-200.

Groisman, P.Y., Karl, T.R., Knight, R.W. and Stenchikov, G.L., 1994b. Changes of Snow Cover, Temperature, and Radiative Heat-Balance over the Northern-Hemisphere. Journal of Climate, 7(11): 1633-1656.

Halberstam, I. and Schieldge, J.P., 1981. Anomalous Behaviour of the Atmospheric Surface-Layer over a Melting Snowpack. Journal of Applied Meteorology, 20(3): 255-265.

Hall, A., 2004. The role of surface albedo feedback in climate. Journal of Climate, 17(7): 1550-1568.

Hall, D.K., 1988. Assessment of polar climate change using satellite technology. Reviews of Geophysics, 26: 26-39.

Hall, D.K., Riggs, G.A. and Salomonson, V.V., 2000. MODIS/Terra Snow Cover Daily L3 Global 500m Grid V004, September 2003 to July 2004. Updated Daily. National Snow and Ice Data Center, Boulder, Colarado, USA.

Hall, R.L., Huntingford, C., Harding, R.J., Lloyd, C.R. and Cox, P.M., 2003. An improved description of soil hydraulic and thermal properties of arctic peatland for use in a GCM. Hydrological Processes, 17: 2611-2628.

Hansen, J. and Nazarenko, L., 2004. Soot climate forcing via snow and ice albedos. Proceedings of the National Academy of Sciences of the United States of America, 101(2): 423-428.

Hartman, M.D., Baron, J.S., Lammers, R.B., Cline, D.W., Band, L.E., Liston, G.E. and Tague, C., 1999. Simulations of snow distribution and hydrology in a mountain basin. Water Resources Research, 35: 1587-1603.

Heegaard, E., 2002. A model of alpine species distribution in relation to snowmelt time and altitude. Journal of Vegetation Science, 13: 493-504.

Henderson-Sellers, A., Pitman, A.J., Love, K., Irannejad, P. and Chen, T.H., 1995. The Project for Intercomparison of Land Surface Parameterization Schemes (PILPS): Phases 2 and 3. Bulletins of the American Meteorological Society, 76: 489-503.

Hinkler, J., Pedersen, S.B., Rasch, M. and Hansen, B.U., 2002. Automatic snow cover monitoring at high temporal and spatial resolution using images taken by a standard digital camera. International Journal of Remote Sensing, 23(21): 4669-4682.

Ipcc, 1990. Climate Change: The Intergovernmental Panel on Climate Change (IPCC) Scientific Assessment., Cambridge University Press, Cambridge.

Ipcc, 1996. Climate Change 1995: The Science of Climate Change. Contribution of Working Group I to the Second Assessment Report of the Intergovernmental Panel on Climate Change (IPCC). Cambridge University Press, Cambridge.

Ipcc, 2001. Climate Change 2001: The Scientific Basis. Contribution of Working Group I to the Third Assessment Report of the Intergovernmental Panel on Climate Change (IPCC), Cambridge University Press, Cambridge.

Isaaks, E.H. and Srivastava, R.M., 1989. An introduction to applied geostatistics. Oxford University Press, Oxford.

Jia, G.J., Epstein, H.E. and Walker, D.A., 2003. Greening of arctic Alaska, 1981-2001. Geophysical Research Letters, 30(20): HLS 3-1, HLS 3-4.

Jones, M.H., Fahnestock, J.T., Walker, D.A., Walker, M.D. and Welker, J.M., 1998. Carbon dioxide fluxes in moist and dry arctic tundra during season: Responses to increases in summer temperature and winter snow accumulation. Arctic and Alpine Research, 30(4): 373-380.

Jordan, R., 1991. A one-dimensional temperature model for a snow cover. Special report 91-16, US Army Corps of Engineers, Cold Regions Research and Engineering Laboratory.

Katul, G., Goltz, S.M., Hsieh, C.I., Cheng, Y., Mowry, F. and Sigmon, J., 1995. Estimation of Surface Heat and Momentum Fluxes Using the Flux-Variance Method above Uniform and Nonuniform Terrain. Boundary-Layer Meteorology, 74(3): 237-260.

King, L., 1986. Zonation and ecology of high mountain permafrost in Scandinavia. Geografiska Annaler A, 68(3): 131-139.

Kodak, 2000. Kodak DC3200 Digital Camera User's Guide. Eastman Kodak Company, New York, USA.

Kohler, J., Brandt, O., Johansson, M. and Callaghan, T.V., 2006. A long-term Arctic snow depth record from Abisko, northern Sweden, 1913–2004. Polar Research, 25(2): 91-113.

Kohsiek, W., Debruin, H.A.R., The, H. and Vandenhurk, B., 1993. Estimation of the Sensible Heat-Flux of a Semiarid Area Using Surface Radiative Temperature-Measurements. Boundary-Layer Meteorology, 63(3): 213-230.

Kullman, L., 2002. Rapid recent range-margin rise of tree and shrub species in the Swedish Scandes. Journal of Ecology, 90: 68-77.

Lachenbruch, A.H. and Marshall, B.V., 1986. Changing Climate - Geothermal Evidence from Permafrost in the Alaskan Arctic. Science, 234(4777): 689-696.

Langham, E.J., 1981. Physics and properties of snowcover. In: Gray, D.M. and Male, D.H. (Editors), Handbook of snow : principles, processes, management & use. Pergamon Press, New York, pp. xx, 776.

Lettau, H., 1969. Note on aerodynamic roughness parameter estimation on the basis of roughness element description. Journal of Applied Meteorology, 8(828-832).

Ling, F. and Zhang, T.J., 2005. Modeling the effect of variations in snowpack-disappearance date on surface-energy balance on the Alaskan North Slope. Arctic Antarctic and Alpine Research, 37(4): 483-489.

Liston, G.E., 1995. Local Advection of Momentum, Heat, and Moisture During the Melt of Patchy Snow Covers. Journal of Applied Meteorology, 34(7): 1705-1715.

Liston, G.E., 2004. Representing Subgrid Snow Cover Heterogeneities in Regional and Global Models. Journal of Climate, 17: 1381-1397.

Liston, G.E., 2005. Global Snow-Water Equivalent Depth Coefficient-of-Variation Classification. National Snow and Ice Data Centre.

Liston, G.E., Mcfadden, J.P., Sturm, M. and Pielke, R.A., Sr, 2002. Modelled changes in arctic tundra snow, energy and moisture fluxes due to increased shrubs. Global Change Biology, 8: 17-32.

Liston, G.E. and Sturm, M., 1998. A snow-transport model for complex terrain. Journal of Glaciology, 44(148): 498-516.

Lloyd, C.R., 1995. The effect of heterogeneous terrain on micrometeorological flux measurements: a case study from HAPEX-SAHEL. Agricultural and Forest Meteorology, 73: 209-216.

Lloyd, C.R., 1998. The application of an instrument for non-destructive measurements of soil temperature and resistance profiles at a high Arctic field site. Hydrology and Earth System Sciences, 2(1): 121-128.

Lloyd, C.R., 2001. The Micrometeorology of a High Arctic Site. PhD Thesis, The University of Edinburgh, Edinburgh, UK.

Lloyd, C.R., Aurela, M., Bruland, O., Friborg, T., Fowler, D., Hall, R.L., Hansen, B.U., Harding, R.J., Hargreaves, K.J., Laurila, T., Merchal, D., Nordstroem, C., Sand, K., Soegaard, H., Tuovinen, J.P. and Vehvilainen, B., 1999. Final Report LAPP: Land Arctic Physical Processes., Institute of Hydrology, Wallingford.

Lloyd, C.R., Culf, A.D., Dolman, A.J. and Gash, J.G.C., 1991. Estimates of sensible heat flux from observations of temperature fluctuations. Boundary-Layer Meteorology, 57: 311-322.

Lloyd, C.R., Gash, J.H.C. and Sivakumar, M.V.K., 1992. Derivation of the aerodynamic roughness parameters for a sahelian savannah site using the eddy correlation technique. Boundary-Layer Meteorology, 58(261-271).

Louis, J.F., 1979. Parametric Model of Vertical Eddy Fluxes in the Atmosphere. Boundary-Layer Meteorology, 17(2): 187-202.

Lowe, P.R., 1977. An approximating polynomial for the computation of saturation vapor pressure. Journal of Applied Meteorology, 16: 100-103.

Luce, C.H. and Tarboton, D.G., 2004. The application of depletion curves for parameterization of subgrid variability of snow. Hydrological Processes, 18: 1409-1422.

Magnuson, J.J., Robertson, D.M., Benson, B.J., Wynne, R.H., Livingstone, D.M., Arai, T., Assel, R.A., Barry, R.G., Card, V., Kuusisto, E., Granin, N.G., Prowse, T.D., Stewart, K.M. and Vuglinski, V.S., 2000. Historical trends in lake and river ice cover in the Northern Hemisphere. Science, 289(5485): 1743-1746.

Makkonen, L. and Laakso, T., 2005. Humidity measurements in cold and humid environments. Boundary-Layer Meteorology, 116(1): 131-147.

Marsh, P., Neumann, N.N., Essery, R. and Pomeroy , J.W., 1999. Model estimates of local advection of sensible heat over a patchy snow cover. In: Tranter, M., Armstrong, R., Brun, E., Jones, G., Sharp, M.J. and Williams, M. (Editors), Interactions Between the Cryosphere, Climate and Greenhouse Gases. International Association of Hydrological Sciences Publication No.256.

Marsh, P. and Pomeroy , J.W., 1996. Meltwater fluxes at an Arctic forest-tundra site. Hydrological Processes, 10: 1383-1400.

Marshall, S.E., 1989. A physical parameterization of snow albedo for use in climate models., National Centre for Atmospheric Research, Boulder, CO.

Martin, E. and Lejeune, Y., 1998. Turbulent fluxes above the snow surface. Annals of Glaciology, 26: 179-183.

Mason, P.J., 1988. The Formation of Areally-Averaged Roughness Lengths. Quarterly Journal of the Royal Meteorological Society, 114(480): 399-420.

Mccurrach, N., 2005. Arctic Tundra Plant Community Distribution. B.Sc Thesis, University of Durham.

Mcnamara, J.P., Kane, D.L. and Hinzman, L.D., 1998. An analysis of streamflow hydrology in the Kuparuk River basin, Arctic Alaska: A nested watershed approach. Journal of Hydrology, 206(1-2): 39-57.

Monteith, J.L., 1981. Evaporation and Surface-Temperature. Quarterly Journal of the Royal Meteorological Society, 107(451): 1-27.

Monteith, J.L. and Unsworth, M., 1990. Principles of Environmental Physics. Butterworth Heinemann.

Moore, R.D., 1983. On the Use of Bulk Aerodynamic Formulas over Melting Snow. Nordic Hydrology, 14(4): 193-206.

Moore, R.J., Bell, V.A., Austin, R.M. and Harding, R.J., 1999. Methods for snowmelt forecasting in upland Britain. Hydrology and Earth System Sciences, 3(2): 233-246.

Morris, E.M., 1989. Turbulent Transfer over Snow and Ice. Journal of Hydrology, 105(3-4): 205-223.

Nash, J.E. and Sutcliffe, J.V., 1970. River Flow Forecasting Through Conceptual Models Part I - A Discussion of Principles. Journal of Hydrology, 10: 282-290.

Neumann, N. and Marsh, P., 1998. Local advection of sensible heat in the snowmelt landscape of Arctic tundra. Hydrological Processes, 12: 1547-1560.

Nyberg, R. and Lindh, L., 1990. Geomorphic features as indicators of climatic fluctuations in a periglacial environment, northern sweden. Geografiska Annaler A, 72: 203-210.

Obukhov, 1971. Turbulence in an atmosphere with a non-uniform temperature. Boundary-Layer Meteorology, 2(1): 7-29.

Oechel, W.C., Hastings, S.J., Vourlitis, G., Jenkins, M., Riechers, G. and Grulke, N., 1993. Recent change of arctic tundra ecosystems from a net carbon dioxide sink to a source. Nature, 361: 520-523.

Oechel, W.C., Vourlitis, G.L., Hastings, S.J., Zulueta, R.C., Hinzman, L. and Kane, D., 2000. Acclimation of ecosystem CO2 exchange in the Alaskan Arctic in response to decadal climate warming. Nature, 406(6799): 978-981.

Oke, T.R., 1987. Boundary Layer Climates. Routledge, London, 435 pp.

Pedersen, C.A. and Winther, J.G., 2005. Intercomparison and validation of snow albedo parameterization schemes in climate models. Climate Dynamics, 25(4): 351-362.

Penman, H.L., 1948. Natural Evaporation from Open Water, Bare Soil and Grass. Proceedings of the Royal Society of London Series a-Mathematical and Physical Sciences, 193(1032): 120-&.

Petrone, R.M., Price, J.S., Carey, S.K. and Waddington, J.M., 2004. Statistical characterization of the spatial variability of soil moisture in a cutover peatland. Hydrological Processes, 18(1): 41-52.

Philip, J.R., 1959. The Theory of Local Advection .1. Journal of Meteorology, 16(5): 535-547.

Pohl, S. and Marsh, P., 2005. Modelling the spatial-temporal variability of spring snowmelt in an arctic catchment. Hydrological Processes, 20(8): 1773-1792.

Pohl, S., Marsh, P. and Liston, G.E., 2006a. Spatial-temporal variability in turbulent fluxes during spring snowmelt. Arctic Antarctic and Alpine Research, 38(1): 136-146.

Pohl, S., Marsh, P. and Pietroniro, A., 2006b. Spatial-temporal variability in solar radiation during spring snowmelt. Nordic Hydrology, 37: 1-19.

Pomeroy, J.W., Bewley, D.S., Essery, R.L.H., Hedstrom, N.R., Link, T., Granger, R.J., Sicart, J.E., Ellis, C.R. and Janowicz, J.R., 2006. Shrub tundra snowmelt. Hydrological Processes, 20(4): 923-941.

Pomeroy, J.W. and Gray, D.M., 1995. Snowcover. Accumulation, Relocation and Management. National Hydrology Research Institute Science Report No.7.

Pomeroy, J.W., Gray, D.M. and Landine, P.G., 1993. The Prarie Blowing Snow Model: characteristics, validation, operation. Journal of Hydrology, 144: 165-192.

Pomeroy, J.W., Gray, D.M., Shook, K.R., Toth, B., Essery, R.L.H., Pietroniro, A. and Hedstrom, N., 1998. An evaluation of snow accumulation and ablation processes for land surface modelling. Hydrological Processes, 12(15): 2339-2367.

Pomeroy, J.W., Marsh, P. and Gray, D.M., 1997. Application of a distributed blowing snow model to the arctic. Hydrological Processes, 11(11): 1451-1464.

Pope, V.D., Gallani, M.L., Rowntree, P.R. and Stratton, R.A., 2000. The impact of new physical parameterisations in the Hadley Centre climate model: HadAM3. Climate Dynamics, 16: 123-146.

Prasad, R., Tarboton, D.G., Liston, G.E., Luce, C.H. and Seyfield, M.S., 2001. Testing a blowing snow model against distributed snow measurements at Upper Sheep Creek, Idaho, United States of America. Water Resources Research, 37(5): 1341-1350.

Ramsay, B.H., 1998. The interactive multisensor snow and ice mapping system. Hydrological Processes, 12(10-11): 1537-1546.

Randall, D.A., Cess, R.D., Blanchet, J.P., Chalita, S., Colman, R., Dazlich, D.A., Delgenio, A.D., Keup, E., Lacis, A., Letreut, H., Liang, X.Z., Mcavaney, B.J., Mahfouf, J.F., Meleshko, V.P., Morcrette, J.J., Norris, P.M., Potter, G.L., Rikus, L., Roeckner, E., Royer, J.F., Schlese, U., Sheinin, D.A., Sokolov, A.P., Taylor, K.E., Wetherald, R.T., Yagai, I. and Zhang, M.H., 1994. Analysis of Snow Feedbacks in 14 General-Circulation Models. Journal of Geophysical Research-Atmospheres, 99(D10): 20757-20771.

Robinson, D.A., 1993. Hemispheric snow cover from satellites. Annals of Glaciology, 17: 367-371.

Roesch, A., Wild, M., Gilgen, H. and Ohmura, A., 2001. A new snow cover fraction parametrization for the ECHAM4 GCM. Climate Dynamics, 17(12): 933-946.

Schmid, H.P., 1997. Experimental design for flux measurements: matching scales of observations and fluxes. Agricultural and Forest Meteorology, 87: 179-200.

Schmid, H.P. and Oke, T.R., 1990. A model to estimate the source area contributing to turbulent exchange in the surface layer over patchy terrain. Quarterly Journal of the Royal Meteorological Society, 116(965-988).

Schmidt, R.A., 1982. Vertical Profiles of Wind-Speed, Snow Concentration, and Humidity in Blowing Snow. Boundary-Layer Meteorology, 23(2): 223-246.

Schuepp, P.H., Leclerc, M.Y., Macpherson, J.I. and Desjardins, R.L., 1990. Footprint prediction of scalar fluxes from analytical solutions of the diffusion equation. Boundary-Layer Meteorology, 50: 355-373.

Segal, M., Cramer, J.H., Pielke, R.A., Garratt, J.R. and Hildebrand, P., 1991a. Observational Evaluation of the Snow Breeze. Monthly Weather Review, 119(2): 412-424.

Segal, M., Garratt, J.R., Pielke, R.A. and Ye, Z., 1991b. Scaling and Numerical-Model Evaluation of Snow-Cover Effects on the Generation and Modification of Daytime Mesoscale Circulations. Journal of the Atmospheric Sciences, 48(8): 1024-1042.

Serreze, M.C., Walsh, J.E., Chapin, F.S., Osterkamp, T., Dyurgerov, M., Romanovsky, V., Oechel, W.C., Morison, J., Zhang, T. and Barry, R.G., 2000. Observational evidence of recent change in the northern high-latitude environment. Climatic Change, 46: 159-207.

Shook, K. and Gray, D.M., 1996. Small-Scale Spatial Structure of Shallow Snowcovers. Hydrological Processes, 10: 1283-1292.

Shook, K. and Gray, D.M., 1997a. Snowmelt resulting from advection. Hydrological Processes, 11: 1725-1736.

Shook, K. and Gray, D.M., 1997b. Synthesizing shallow seasonal snow covers. Water Resources Research, 33(3): 419-426.

Shuttleworth, W.T., Gash, J.G.C., Lloyd, C.R., Mcneil, D.D., Moore, C.J. and Wallace, J.S., 1988. An integrated micrometeorological system for evaporation measurement. Agricultural and Forest Meteorology, 43(295): 317.

Skaugen, T., Alfnes, E., Langsholt, E.G. and Udnaes, H.C., 2004. Time-variant snow distribution for use in hydrological models, Annals of Glaciology, Vol 38, 2004. Annals of Glaciology, pp. 180-186.

Slater, A.G., Pitman, A.J. and Desborough, C.E., 1998. The validation of a snow parameterisation designed for use in general circulation models. International Journal of Climatology, 18: 595-617.

Slater, A.G., Schlosser, C.A., Desborough, C.E., Pitman, A.J., Henderson-Sellers, A., Robock, A., Vinnikov, K.Y., Mitchell, K., Boone, A., Braden, H., Chen, F., Cox, P.M., De Rosnay, P., Dickinson, R.E., Dai, Y.J., Duan, Q., Entin, J., Etchevers, P., Gedney, N., Gusev, Y.M., Habets, F., Kim, J., Koren, V., Kowalczyk, E.A., Nasonova, O.N., Noilhan, J., Schaake, S., Shmakin, A.B., Smirnova, T.G., Verseghy, D., Wetzel, P., Yue, X., Yang, Z.L. and Zeng, Q., 2001. The representation of snow in land surface schemes: Results from PILPS 2(d). Journal of Hydrometeorology, 2(1): 7-25.

Stainforth, D.A., Aina, T., Christensen, C., Collins, M., Faull, N., Frame, D.J., Kettleborough, J.A., Knight, S., Martin, A., Murphy, J.M., Piani, C., Sexton, D., Smith, L.A., Spicer, R.A., Thorpe, A.J. and Allen, M.R., 2005. Uncertainty in predictions of the climate response to rising levels of greenhouse gases. Nature, 433(7024): 403-406.

Sturm, M. and Benson, C., 2004. Scales of spatial heterogeneity for perennial and seasonal snow layers, Annals of Glaciology, Vol 38 2004. Annals of Glaciology, pp. 253-260.

Sturm, M. and Benson, C.S., 1997. Vapor transport, grain growth and depth-hoar development in the subarctic snow. Journal of Glaciology, 43(143): 42-59.

Sturm, M., Holmgren, J., Konig, M. and Morris, K., 1997. The thermal conductivity of seasonal snow. Journal of Glaciology, 43(143): 26-41.

Sturm, M., Holmgren, J. and Liston, G.E., 1995. A Seasonal Snow Classification System for Local Global Application. Journal of Climate, 8(5(2)): 1261-1283.

Sturm, M. and Johnson, J.B., 1992. Thermal-Conductivity Measurements of Depth Hoar. Journal of Geophysical Research-Solid Earth, 97(B2): 2129-2139.

Sturm, M., Mcfadden, J.P., Liston, G.E., Chapin, F.S., Racine, C.H. and Holmgren, J., 2001a. Snow-shrub interactions in Arctic tundra: A hypothesis with climatic implications. Journal of Climate, 14(3): 336-344.

Sturm, M., Racine, C. and Tape, K., 2001b. Climate change - Increasing shrub abundance in the Arctic. Nature, 411(6837): 546-547.

Sturm, M., Schimel, J., Michaelson, G., Welker, J.M., Oberbauer, S.F., Liston, G.E., Fahnestock, J. and Romanovsky, V.E., 2005. Winter biological processes could help convert arctic tundra to shrubland. Bioscience, 55(1): 17-26.

Tape, K., Sturm, M. and Racine, C., 2006. The evidence for shrub expansion in Northern Alaska and the Pan-Arctic. Global Change Biology, 12(4): 686-702.

Taylor, C.M., Harding, R.J., Pielke, R.A., Vidale, P.L., Walko, R.L. and Pomeroy, J.W., 1998. Snow breezes in the boreal forest. Journal of Geophysical Research-Atmospheres, 103(D18): 23087-23101.

Thom, A.S., 1972. Momentum, mass and heat exchange of vegetation. Quarterly Journal of the Royal Meteorological Society, 98: 124-134.

Tillman, J.E., 1972. The indirect determination of stability, heat and momentum fluxes in the Atmospheric Boundary Layer from simple scalar variables during dry unstable conditions. Journal of Applied Meteorology, 11: 783-792.

Van Den Hurk, B.J.J.M., Viterbo, P., Beljaars, A.C.M. and Betts, A.K., 2000. Offline validation of the ERA40 surface scheme. Tecbical Memorandum 295, European Centre for Medium-Range Weather Forecasts.

Verhoef, A., 1994. Surface energy balance of shrub vegetation in the Sahel, Agricultural University, Wageningen.

Verseghy, D.L., 1991. Class - a Canadian Land Surface Scheme for Gcms .1. Soil Model. International Journal of Climatology, 11(2): 111-133.

Verseghy, D.L., Mcfarlane, N.A. and Lazare, M., 1993. Class - a Canadian Land-Surface Scheme for Gcms .2. Vegetation Model and Coupled Runs. International Journal of Climatology, 13(4): 347-370.

Vinnikov, K.Y., Robock, A., Stouffer, R.J., Walsh, J.E., Parkinson, C.L., Cavalieri, D.J., Mitchell, J.F.B., Garrett, D. and Zakharov, V.F., 1999. Global warming and Northern Hemisphere sea ice extent. Science, 286(5446): 1934-1937.

Wahren, C.H.A., Walker, M.D. and Bret-Harte, M.S., 2005. Vegetation responses in Alaskan arctic tundra after 8 years of a summer warming and winter snow manipulation experiment. Global Change Biology, 11(4): 537-552.

Walker, D.A., 2000. Hierarchical subdivision of Arctic tundra based on vegetation response to climate, parent material and topography. Global Change Biology, 6(Supplement 1): 19-34.

Walsh, J.E., Anisimov, O., Hagen, J.O.M., Jakobsson, T., Oerlemans, J., Prowse, T.D., Romanovsky, V., Savelieva, N., Serreze, S., Shiklomanov, A., Shiklomanov, I. and Solomon, S., 2005. Cryosphere and Hydrology, Arctic Climate Impact Assessment (ACIA). Cambridge University Press, Cambridge, pp. 1042.

Warren, S.G. and Wiscombe, W.J., 1980. A Model for the Spectral Albedo of Snow .2. Snow Containing Atmospheric Aerosols. Journal of the Atmospheric Sciences, 37(12): 2734-2745.

Warrilow, D.A. and Buckley, E., 1989. The Impact of Land Surface Processes on the Moisture Budget of a Climate Model. Annales Geophysicae-Atmospheres Hydrospheres and Space Sciences, 7(5): 439-449.

Welker, J.M., Fahnestock, J.T. and Jones, M.H., 2000. Annual CO2 flux in dry and moist arctic tundra: Field responses to increases in summer temperatures and winter snow depth. Climatic Change, 44(1-2): 139-150.

Western, A.W., Bloschl, G. and Grayson, R.B., 1998a. Geostatistical characterisation of soil moisture patterns in the Tarrawarra a catchment. Journal of Hydrology, 205(1-2): 20-37.

Western, A.W., Bloschl, G. and Grayson, R.B., 1998b. How well do indicator variograms capture the spatial connectivity of soil moisture? Hydrological Processes, 12(12): 1851-1868.

Willmott, C.J., 1981. On the evaluation of model performance in physical geography. In: Gaile, G.L. and Willmott, C.J. (Editors), Spatial statistics and models, Reidel, Dordrecht, pp. 443-460.

Winstral, A., Elder, K. and Davis, R.E., 2002. Spatial snow modeling of wind-redistributed snow using terrain based parameters. Journal of Hydrometeorology, 3(5): 524-538.

Wiscombe, W.J. and Warren, S.G., 1980. A Model for the Spectral Albedo of Snow .1. Pure Snow. Journal of the Atmospheric Sciences, 37(12): 2712-2733.

Wood, N. and Mason, P., 1991. The Influence of Static Stability on the Effective Roughness Lengths for Momentum and Heat-Transfer. Quarterly Journal of the Royal Meteorological Society, 117(501): 1025-1056.

Wookey, P.A., 2002. Tundra. In: Mooney, H.A. and Canadell, J.G. (Editors), Encyclopaedia of Global Environmental Change. John Wiley & Sons, Ltd, Chichester, pp. 593-602.

Yang, Z.L., Dickinson, R.E., Robock, A. and Vinnikov, K.Y., 1997. Validation of the snow submodel of the biosphere-atmosphere transfer scheme with Russian snow cover and meteorological observational data. Journal of Climate, 10(2): 353-373.

Zevenbergen, L.W. and Thorne, C.R., 1987. Quantitative analysis of land surface topography. Earth Surface Processes and Landforms, 12: 47-56.

Zhang, T., Stamnes, K. and Bowling, S.A., 2001. Impact of the atmospheric thickness on the atmospheric downwelling longwave radiation and snowmelt under clear-sky conditions in the Arctic and Subarctic. Journal of Climate, 14(5): 920-939.

Appendices

9 Appendix A: Terrain- Derived Topographic Indices

Topographic indices are calculated from raster elevation data.

9.1 Terrain Curvature, Aspect and Slope

Values of slope, aspect and curvature are calculated from the DEM using the equations given by Zevenbergen and Thorne (1987).

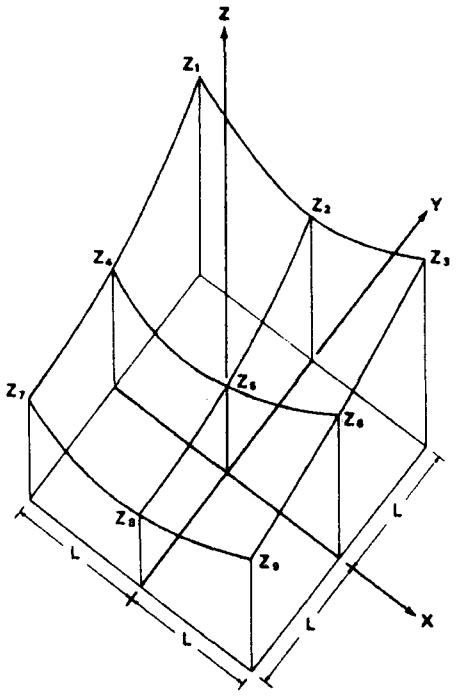

Figure 9-1: 3 by 3 cell submatrix used in calculation of terrain indices (Zevenbergen and Thorne, 1987). Z_5 represents the cell for which the terrain index will be calculated.

The topographic indices are quantitatively derived by passing a 3 by 3 cell matrix over the DTM. Zevenbergen and Thorne (1987) defined a surface (Figure 9-1) that passes exactly through the submatrix of the partial quartic form:

$$Z = Ax^2y^2 + Bx^2 + Cxy^2 + Dx^2 + Ey^2 + Fxy + Gx + Hy + I$$

Equation 9.1

where:

$$A = \left[\frac{(Z_1 + Z_3 + Z_7 + Z_9)}{4} - \frac{(Z_2 + Z_4 + Z_6 + Z_8)}{2} + Z_5\right] / L^4$$ **Equation 9.2**

$$B = \left[\frac{(Z_1 + Z_3 - Z_7 - Z_9)}{4} - \frac{(Z_2 - Z_8)}{2} + Z_5\right] / L^3$$ **Equation 9.3**

$$C = \left[\frac{(-Z_1 + Z_3 - Z_7 + Z_9)}{4} - \frac{(Z_4 - Z_6)}{2} + Z_5\right] / L^3$$ **Equation 9.4**

$$D = \left[\frac{(Z_4 + Z_6)}{2} - Z_5\right] / L^2$$ **Equation 9.5**

$$E = \left[\frac{(Z_2 + Z_8)}{2} - Z_5\right] / L^2$$ **Equation 9.6**

$$F = \left[\frac{(-Z_1 + Z_3 + Z_7 - Z_9)}{4L^2}\right]$$ **Equation 9.7**

$$G = \left[\frac{(-Z_4 + Z_6)}{2L}\right]$$ **Equation 9.8**

$$H = \left[\frac{(Z_2 - Z_8)}{2L}\right]$$ **Equation 9.9**

$$I = Z_5$$ **Equation 9.10**

Z_1 to Z_9 are the 9 submatrix vertices shown in Figure 9-1. The DTM gridcell size corresponds to length L. Slope, aspect and curvature are calculated for each cell based on the surrounding 8 cells.

Topographic indices are found by differentiating Equation 9.1 and solving for Z_5.

9.1.1 SLOPE AND ASPECT

The slope gradient is the rate of change in elevation with distance. Slope gradient is thus the first derivative of Z with respect to the distance S, at an angle θ:

$$SLOPE(\theta) = \frac{\partial Z}{\partial S} = G\cos\theta + H\sin\theta$$

Equation 9.11

Aspect is defined as the direction of steepest slope, and can be found by differentiating Equation 9.11 to find the minimum (where derivative is equal to zero):

$$ASPECT = \frac{\partial SLOPE}{\partial \theta} = -G\sin\theta + H\cos\theta = 0$$

Equation 9.12

or:

$$ASPECT = \arctan\left(\frac{H}{G}\right)$$

Equation 9.13

9.1.2 CURVATURE

Curvature is the second order derivative of Z with respect to the distance S, at an angle θ:

$$CURVATURE = \frac{\partial^2 Z}{\partial^2 S} = 2\left(D\cos^2\theta + E\cos^2\theta + F\cos\theta\sin\theta\right)$$

Equation 9.14

The two most useful derivatives of curvature are in the line of steepest slope $(\theta = ASPECT)$, giving profile curvature:

$$PROFC = -2D\left(D\cos^2\theta + E\sin^2\theta + F\cos\theta\sin\theta\right)$$

Equation 9.15

$$PROFC = \frac{-2\left(DG^2 + EH^2 + FGH\right)}{\left(G^2 + H^2\right)}$$

Equation 9.16

and transverse to the slope $\left(\theta = ASPECT + \frac{\pi}{2}\right)$, giving transverse curvature:

$$TRANC = -2D\left(D\sin^2\theta + E\cos^2\theta + F\cos\theta\sin\theta\right)$$

Equation 9.17

$$TRANC = \frac{-2\left(DH^2 + EG^2 + FGH\right)}{\left(G^2 + H^2\right)}$$

Equation 9.18

9.2 Topographic Similarity Index

The topographic similarity index was introduced by Beven and Kirkby (1979) as a measure of the likelihood of an elevation cell retaining water. It is given as:

$$TSI = \ln\left(\frac{A}{\tan\beta}\right)$$

Equation 9.19

where A is the upslope drained area, and β is the angle of slope. β is calculated using the methods outlined in Equation 9.11. A is derived using algorithms that route flow in the direction of aspect, where aspect is calculated using Equation 9.13. Where a cell drains to two or more cells the flow is assumed to diverge according to the aspect.

9.3 Topographic Shelter Index

The shelter index is a measure of the shelter given to a gridcell from surrounding cells. If the upwind cells have a greater elevation for a given azimuth, then the cell is considered sheltered. The degree of shelter is calculated as the zenith angle. The algorithm used is from Winstral *et al.* (2002):

Following Winstral *et al.* (2002) the index is calculated for a given cell, (x_i, y_i), along a vector, v, as:

$$SX_{\theta,d}(x_i, y_i) = \max\left[\tan\left(\frac{ELEV(x_v, y_v) - ELEV(x_i, y_i)}{\sqrt{(x_v - x_i)^2 + (y_v - y_i)^2}}\right)\right]$$

Equation 9.20

where (x_v, y_v) is the shelter-defining cell. The vector, v, is defined by the azimuth, θ, and length d.

To account for variation in wind direction, and the problems associated with using vectors with raster data, an average over a range of azimuths is used:

$$\overline{SX}_{\theta,d,A}(x_i, y_i) = \frac{1}{n}\sum_{\theta-A}^{\theta+A} SX_{A,d}(x_i, y_i)$$

Equation 9.21

where 2A is the range of azimuths over which the index will be calculated.

Equation 9.21 therefore allows an exposure index to be derived for a given wind direction and search length. Sensitivity analyses for domain topography revealed the index to be relatively insensitive to search length for lengths greater than 30 m. The algorithm also proved sensitive to azimuth range, when the range is greater than 45°. Consequently, a search length of 50 m, and an azimuth range of 30 $(A = 15°)$ was chosen.

Equation 9.21 only provides the facility to calculate the exposure for a given wind vector. This may be appropriate to use to derive a shelter index for short periods when wind direction is reasonably static, but over long periods of time wind direction can reasonably be expected to vary. An index of shelter from all wind directions is thus required. For instance a bowl-shaped hollow will be sheltered from every wind direction, but a north-facing slope will only be sheltered from 180°.

A global value of shelter can be derived using the minimum of the above equation calculated over 0 to 2π radians, at an interval equal to $2A$:

$$\overline{SX}_{global,d}(x_i, y_i) = \min_{\theta=0}^{2\pi}\left[\overline{SX}_{\theta,d,A}(x_i, y_i)\right]$$

Equation 9.22

10 Appendix B: Footprint Models

Micrometeorological instruments have characteristic source footprints, for both radiation and turbulent fluxes.

The measurement taken at the sensor is a product of the source area of the footprint and the source strength. Described here are two simple approaches to modelling the source area for turbulent measurements taken by eddy correlation and radiation measurements taken by standard radiometers.

10.1 Eddy Correlation Source Area Footprint Model

The footprint model used here is one initially proposed by Schuepp *et al.* (1990) and modified by Lloyd (1995) to include Scheupp *et al.*'s proposed changes for stability. The nature of eddy correlation means that the method breaks down under stable conditions, which by definition are not turbulent. The model is thus only applicable under neutral to unstable conditions.

The following two-dimensional model is taken from Lloyd (1995) (note sign error in original paper):

$$\frac{1}{Q_0}\frac{dQ}{dx} = \frac{2x_{\max}}{x^2}\phi_m \exp\left[\frac{-2x_{\max}}{x}\phi_m\right]$$

Equation 10.1

where the left-hand side represents the relative contribution of flux at sensor height (z), where Q_0 is the unit area flux density (assumed to be 1 in subsequent model), $x_{\max}$ is the upwind distance at which the source strength is at its greatest (Equation 10.3), and ϕ_m is the stability correction for momentum assumed equal to that for heat and moisture. Following Dyer (1974), ϕ_m is given as:

$$\phi_m = \left[1 - 16\frac{(z-d)}{L}\right]^{\frac{-1}{4}}$$

Equation 10.2

where d is the displacement height and L the Obukhov stability length. x_{max} is expressed following Schmid and Oke (1990). Note that measurement height z is now z_s following the nomenclature of Schmid and Oke:

$$X_{\max} \approx \frac{1.7 z_s^{1.03}\left[\ln\left(\frac{z_s}{z_0}\right) - \psi\left(\frac{z_s}{L}\right)\right]}{\left(1 - \frac{z_s}{L}\right)^{\frac{1}{2}}}$$

Equation 10.3

and:

$$\psi\left(\frac{z_s}{L}\right) = \left(1 - \frac{76 z_s}{L}\right)^{\frac{-1}{4}} - 1$$

Equation 10.4

The two-dimensional footprint model is solely dependent on measurement height, roughness length and boundary-layer stability. This approach assumes a boundary layer of constant flux, no advection and sources are all at ground level on a flat plain.

To turn the two-dimensional model into a three-dimensional model requires the use of a method of incorporating the variation in wind direction. The approach used here is to assume the variation in wind-direction follows a Gaussian distribution:

$$P(y) = \frac{1}{\sigma\sqrt{2\pi}} \exp\left[\frac{-(y-\mu)^2}{2\sigma^2}\right]$$

Equation 10.5

where y is the wind direction and μ and σ are the mean and standard deviation of the wind. A limit of using a Gaussian distribution is that wind direction is assumed infinite, whereas y is bounded to 360°. Thus, for large values of σ substantial errors can be introduced. However, σ is generally small.

The flux density can thus be expressed in polar co-ordinates as:

$$Flux(x,y) = Q(x).p(y)$$

Equation 10.6

Flux footprint climates can be calculated by averaging flux footprints over time.

10.2 Radiometer Source Area Footprint Model

The footprint model described here is a simple representation of reflected diffuse radiation from the surface. The reflected diffuse radiation towards the radiometer sensor is a function of both slope angle and incident angle with the radiometer. This approach ignores the direct fraction of reflected radiation. The model is shown schematically in Figure 10-1.

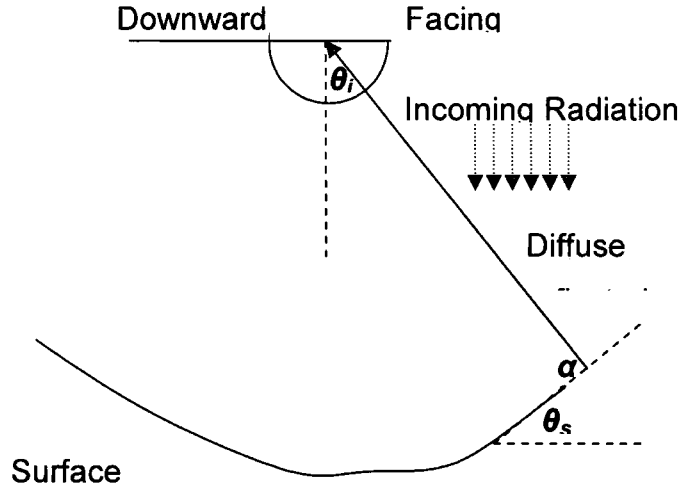

Figure 10-1: Schematic diagram of radiometer source area model

The radiation fraction directed towards the radiometer is thus:

$$q = \cos(\alpha) = \cos(\theta_i - \theta_s)$$

Equation 10.7

Where θ_i and θ_s are the angles of incidence and slope respectively. In this case the angle of slope is in the direction of the radiometer. Slope angle is derived from a DTM using the formulations given in **9.1.1**.

Since, the radiometer has a cosine response, the area contribution is:

$$Flux = \cos(\theta_i)[\cos(\theta_i - \theta_s)]$$

Equation 10.8

11 Appendix C: Micrometeorological Calculations

11.1 Specific Humidity

Specific humidity (q) was calculated from relative humidity, air temperature and atmospheric pressure using the following approximating algorithm (Monteith and Unsworth, 1990):

$$q \approx \frac{\varepsilon e}{P}$$

Equation 11.1

where ε is the ratio of the molecular weights of water and air, P is the atmospheric pressure and the vapour pressure (e) is derived as:

$$e = e_s h$$

Equation 11.2

where h is the measured relative humidity expressed as a fraction of the vapour pressure (e) over the saturated vapour pressure (e_s). The saturated vapour pressure is calculated from empirically-derived functions of the vapour pressure over ice and water for a given temperature, modified from Lowe (1977) into SI units. The equation given here is simplified to 3 significant figures and a third order polynomial:

$$e_s \approx \begin{cases} 0.01\left[6.107 + 4.43E-1(T) + 1.42E-2(T^2) + 2.65E-4(T^3)\right] & T \geq 0 \\ 0.01\left[6.109 + 5.03E-1(T) + 1.89E-2(T^2) + 4.18E-4(T^3)\right] & T < 0 \end{cases}$$

Equation 11.3

where T is the air temperature expressed in degrees centigrade. It is assumed that at the freezing point water remains liquid. Only at temperatures below the freezing point is the vapour pressure over ice used.

11.2 Solid Precipitation Correction

The measurements from the manual gauge were corrected for loss of mass by evaporation, undercatch and a wetting loss during emptying following the

recommendations of Førland *et al.* (1996). The corrected precipitation (P_c) as determined by the dynamic correction model for a SMHI gauge is:

$$P_c = k(P_m + \Delta P_w + \Delta P_e)$$

Equation 11.4

where P_m is the measured precipitation, ΔP_w is the wetting loss during emptying of the gauge, taken as 0.02 mm per measurement, and ΔP_e is the rate of evaporation (Table 11-1). The coefficient, k, is a correction for gauge undercatch, where:

$$k = \exp\left[\beta_0 + V_g\beta_1 + \beta_2 T + \beta_3 V_g T\right]$$

Equation 11.5

where β is an experimentally defined coefficient (Table 11-2), T is the air temperature in degrees centigrade and V_g is the windspeed at gauge height.

Table 11-1: Precipitation gauge daily evaporation rates by month (Førland *et al.*, 1996)

Month	Evaporation Loss (mm day^{-1})
January	0.02
February	0.03
March	0.04
April	0.12
May	0.1
June	0.15
July	0.15
August	0.1
September	0.05
October	0.03
November	0.03
December	0.02

Table 11-2: Gauge undercatch correction coefficients (Førland *et al.*, 1996)

Coefficient	Value
β_0	-0.08871
β_1	0.16146
β_2	0.0011276
β_3	-0.00877

11.3 Infra-Red Thermometer Correction

The Exergen IRT/c.10's used were found to have a slight temperature response associated with a varying body temperature - a warmer body being more likely to lead to an underestimation of surface temperature. The installation of the sensors included an upward facing radiation shield, however both sensors were found to have a bias associated with heating by reflected radiation. This effect was negligible over the snow-free ground, but much more significant over snow. Figure 11-1 shows the diurnal temperature bias with the diurnal range in measured reflected shortwave radiation. The bias is derived as the observed temperature minus the melting point, as a melting snow surface has to be at the melting point. The bias is clearly greatest under high insolation levels.

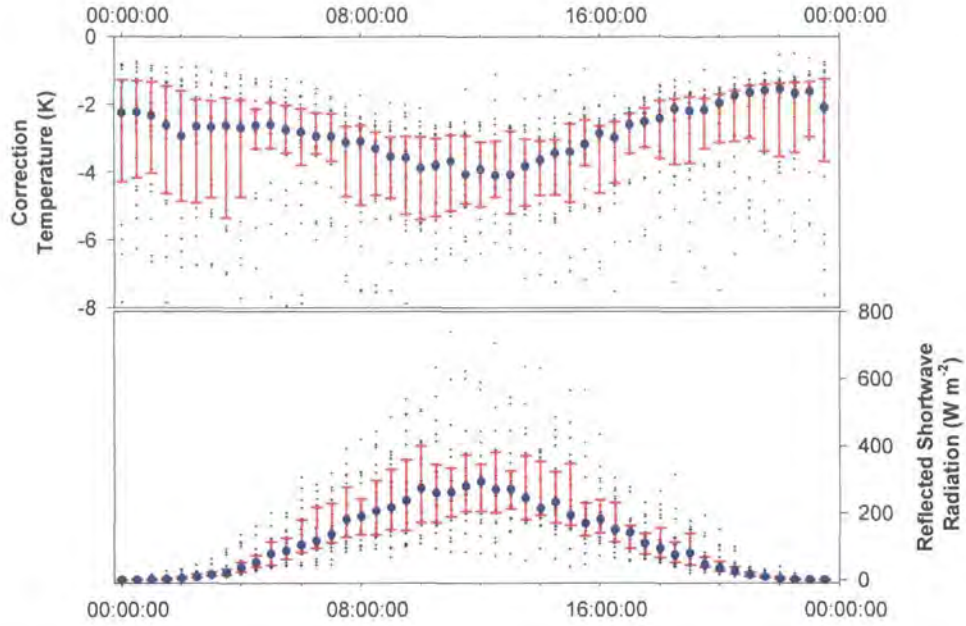

Figure 11-1: Diurnal pattern in IRT bias with diurnal pattern in shortwave radiation. Blue diamonds indicate the mean, red bars the interquartile range, and black crosses the individual half-hourly observations.

A simple correction was applied to the observed surface temperatures by regressing the temperature bias against shortwave radiation (r^2=0.41), with an offset of -1.9°C and a radiation response of -0.01 K W m^{-2}.

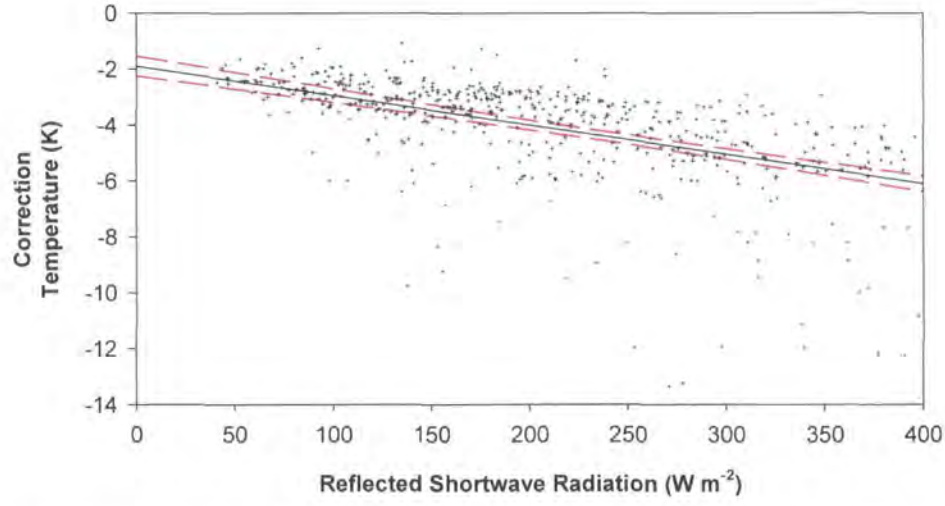

Figure 11-2: Temperature bias correction curve. Red lines indicate the 95% confidence intervals, the black line the fitted regression and black crosses the individual half-hourly data.

To counter this problem Apogee Instruments (Logan, Utah, USA), have recently released an IRT with an internal thermocouple to measure body temperature

directly. An empirically-derived polynomial is then used to correct observed temperature in a similar method to that used here (Bugbee *et al.*, 1996; Campbell Scientific, 2005).

12 Appendix D: MOSES Snow Model Description

12.1 Introduction

The MOSES snow model is based on the principle of mass and energy conservation. The model therefore solves the energy balance (Equation 12.1) and mass balance equations (Equation 12.23). These two equations are closely linked, as the energy-balance equation determines the energy advected by snowmelt, and the evaporation flux density. Correspondingly the mass balance determines the depth of lying snow and thus the heat flux conducted into the snowpack. The mass balance includes snowfall, but ignores the processes controlling spatial redistribution of snow, and the internal redistribution of mass. Rainfall ($\mathbf{P_r}$) is assumed to have a negligible effect during the winter period and is therefore ignored in this version of the model. Snow-cover is thus assumed to lie uniformly across the gridbox.

The model structure is fairly simple (Figure 12-1). The snow-cover is treated as an extension of the surface soil layer rather than a layer in its own right. To do this requires aggregation of the thermal conductivity of the lying snow and soil layer (Equation 12.9). The lying snow is treated as homogenous with a prognostic grain size and a temperature/age dependent albedo (**12.1.3**). Snow density is a prescribed parameter, as is snow thermal conductivity. The surface energy balance is used to calculate surface exchanges and update the lying snow (S) with the melt flux density (**M**) (**12.1.4**). Snow melt is allowed to infiltrate the soil layer and run-off. No liquid water is allowed to reside in the snowpack.

The energy balance is solved by linearizing the equations about the skin temperature (T_*). The skin temperature is defined as the effective temperature of the boundary between the atmosphere and the land surface. If T_* is greater than the melt point (T_m) and there is lying snow, then T_* is reset to T_m and the excess energy used to calculate **M**. The calculated fluxes are thus highly dependent on T_*, making T_* a good diagnostic of model performance.

Turbulent fluxes are calculated using the bulk aerodynamic method. In particular the latent heat flux density (**LE**) is dependent on the surface resistance factor (ψ) which is set to zero for lying snow. Turbulent fluxes are adjusted for aerodynamic stability by use of a heat exchange coefficient (C_H). This is formulated by way of the Richardson number (Ri) (Louis, 1979). The Richardson number is a dimensionless measure of atmospheric stability.

Spatial variability in snow-cover is not modelled explicitly, but parameterised by a snow covered area curve (f_{snow}). This is used to create an effective albedo parameterisation by averaging the snow albedo (α_{snow}) with the snow-free albedo (α_0).

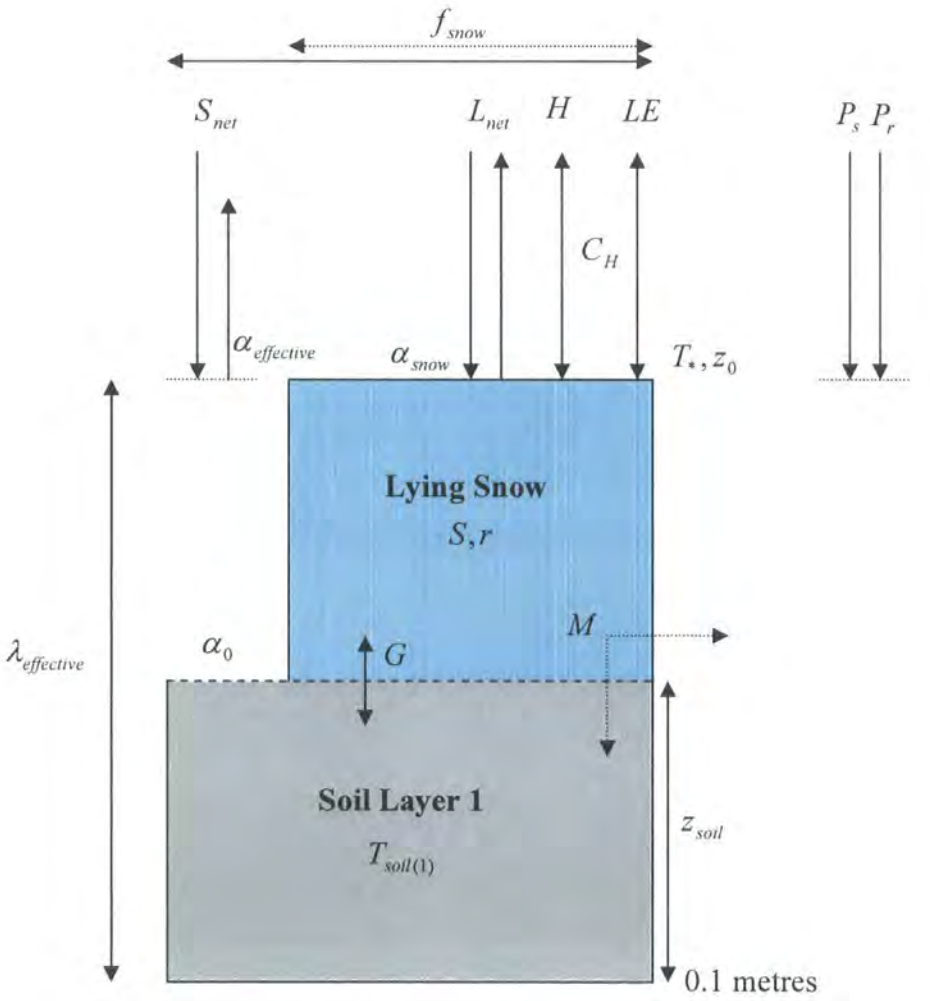

Figure 12-1: Schematic MOSES Snow Model

The data used to drive the model are basic meteorological measurements. These data would be simulated by the atmospheric model in a coupled GCM. Required data consists of snowfall (P_s), horizontal wind velocity (u), specific humidity (q), air temperature (T) and incident short ($S_{incident}$) and longwave ($L_{incident}$) radiation. Rainfall is ignored in this version of the model. Driving data are provided contiguously to the model at a 30 minute (1800 seconds) timestep (Δt).

12.1.1 SURFACE ENERGY BALANCE

The basis of the MOSES snow model is solutions of the surface energy balance:

$$H_{sm} = S_{net} + L_{net} - LE - H - G$$

Equation 12.1

where $\mathbf{H_{sm}}$ is the advected heat flux density due to snowmelt, **H** is the sensible heat flux density into the atmosphere, **G** is the heat conducted into the ground, **E** is the rate of evaporation/sublimation, **L** is the latent heat of evaporation/sublimation, $\mathbf{S_{net}}$ and $\mathbf{L_{net}}$ are the net short- and longwave radiative components.

If no lying snow is present then $\mathbf{H_{sm}}$ is set to zero, and the other fluxes are adjusted appropriately according to T_*. An additional photosynthetic term can be included in the energy-balance, however, this is generally very small and is ignored in the model.

a) Radiative flux densities

The radiative flux densities are net short- ($\mathbf{S_{net}}$) and net longwave ($\mathbf{L_{net}}$). Net $\mathbf{S_{net}}$ is calculated as:

$$S_{net} = S_{incident}(1 - \alpha_{effective})$$

Equation 12.2

where $\mathbf{S_{incident}}$ is a measured input variable and $\alpha_{effective}$ is a weighted surface albedo, given as:

$$\alpha_{effective} = f_{snow}\alpha_{snow} + (1 - f_{snow})\alpha_0$$

Equation 12.3

where f_{snow} is the snow covered fraction derived from (**12.1.3b)**), and α_0 is a prescribed snow-free albedo.

Net $\mathbf{L_{net}}$ is calculated as:

$$L_{net} = L_{incident} - 4\varepsilon\sigma T_*^4$$

Equation 12.4

where $\mathbf{L_{incident}}$ is a measured input variable. Emitted longwave radiation is calculated from the skin temperature T_*, assuming the surface acts as a black body radiator, where ε is the surface emissivity and is assumed equal to unity, and σ is the Stefan-Boltzmann constant.

b) Turbulent flux densities

The turbulent fluxes are calculated by the bulk aerodynamic method. This method assumes that fluxes can be derived from knowledge of surface temperature and vapour pressure gradients combined with an exchange coefficient. Sensible heat flux density **H** is given as:

$$H = c_p \rho C_H u \left[T_* - T - \frac{g}{c_p}(z - z_0 - z_{0H}) \right]$$

Equation 12.5

where T, is the air temperature measured at height z, c_p is the specific heat capacity of air, g is the gravitational constant, ρ is the density of dry air derived from the standard gas laws, u is the windspeed, C_H is the heat exchange coefficient, and z_0 and z_{0H} are the momentum and heat exchange roughness lengths (**12.1.2**).

The evaporation flux density **E** is given as:

$$E = c_p \rho C_H u \psi (q_{sat} - q)$$

Equation 12.6

where q is the specific humidity at a given height z, and q_{sat} is the saturated vapour pressure at the surface, ψ is a surface resistance factor (**12.1.2**). The latent heat flux density **LE** is calculated as a product of the evaporation rate **E** and latent heat of evaporation or sublimation depending on whether the evaporating surface is snow or water:

$$LE = \begin{cases} L_c E & S \le 0 \\ E(L_f + L_c) & S > 0 \end{cases}$$

Equation 12.7

L_c and L_f is the latent heat of evaporation and fusion respectively.

c) Ground Heat Flux

The ground heat flux density (**G**) is calculated as:

$$G = \frac{2\lambda_{effective}}{z_{soil}}(T_* - T_{soil})$$

Equation 12.8

where T_{soil} is the temperature of the top soil layer and z_{soil} is the depth of the top soil layer, which is set at 0.1 metres. Thermal conductivity ($\lambda_{effective}$) is parameterised as:

$$\lambda_{effective} = \begin{cases} \lambda_{soil}\left[1+\dfrac{S\rho_{snow}^{-1}}{z_{zoil}}\left(\dfrac{\lambda_{Soil}}{\lambda_{snow}}-1\right)\right]^{-1} & S\rho_{snow}^{-1} < \dfrac{z_{soil}}{2} \\ \lambda_{snow} & S\rho_{snow}^{-1} \geq \dfrac{z_{soil}}{2} \end{cases}$$

Equation 12.9

where λ_{snow} is the prescribed thermal conductivity of snow, λ_{soil} is the interactive thermal soil conductivity (see **12.1.5**) and ρ_{snow} is the prescribed density of snow.

The use of an effective parameterisation of thermal conductivity removes the need for a separate snow layer in the model.

12.1.2 AERODYNAMIC EXCHANGE

Atmospheric stability, surface roughness elements and resistance exert a strong control on the magnitude of momentum exchange at the land surface. An adjustment to the turbulent flux is thus required.

The aerodynamic momentum roughness length z_0 is an important determinant of turbulent mixing in the atmosphere, and consequently heat and vapour exchange. The magnitude of z_0 is dependent on the surface type and is calculated interactively in the full MOSES model as a function of canopy height; in the version used here it is prescribed. For shallow snow-covers an effective roughness length is used to parameterise the effect of emergent roughness elements through the snowpack.

The heat exchange coefficient C_H is used to adjust the energy fluxes for atmospheric stability; when the air is unstable and therefore turbulently mixed, energy exchange is a much more efficient process than during stable conditions, when air is poorly mixed and stratified.

The bulk approximation of the latent heat flux density (Equation 12.6) assumes a freely-evaporating surface, either of snow/ice or water. This is generally not the case as the surface acts to resist evaporation through plant stomatal and soil resistance. A moisture resistance factor is thus introduced to adjust for this process.

a) Aerodynamic roughness length

The aerodynamic momentum roughness length is given as:

$$z_0 = \begin{cases} z_{0\,snowfree} & S \le 0 \\ \max\left\{z_{0\,snowfree} - 0.0004S, z_{0\,snow}\right\} & S > 0 \end{cases}$$

Equation 12.10

where z_{0snow} and $z_{0snow\text{-}free}$ are a prescribed roughness length for a snow covered and snow-free surface respectively. S is the mass per unit area of lying snow.

The aerodynamic heat roughness length is assumed to be equal to the evaporation roughness length and is given as:

$$z_{0H} = \frac{z_0}{10}$$

Equation 12.11

b) Heat exchange coefficient

This is achieved by way of a dimensionless Richardson (Ri) number formulation which relates the relative roles of buoyancy (surface temperature gradient) to mechanical forces (wind stress gradient), during turbulent flow (Oke, 1987). Thus, during unstable conditions buoyancy forces dominate leading to a positive Richardson number. During stable and neutral conditions mechanical stress dominates and the Richardson number tends to zero.

The heat exchange coefficient is calculated as:

$$C_H = f_H C_{Hn}$$

Equation 12.12

Where:

$$C_{Hn} = k^2 \left[\ln\left(\frac{z+z_0}{z_0}\right) \ln\left(\frac{z+z_0}{z_{0H}}\right) \right]^{-1}$$

Equation 12.13

is the neutral exchange coefficient, and k is the von Kármán constant, the neutral exchange coefficient is scaled by:

$$f_H = \begin{cases} \left(1+\dfrac{10Ri}{\Pr}\right)^{-1} & Ri \geq 0 \\ 1-10Ri\left(1+10C_{Hn}\dfrac{\sqrt{-Ri}}{f_z}\right)^{-1} & Ri < 0 \end{cases}$$

Equation 12.14

where Pr is the Prandtl number and f_z is a scalar given as:

$$f_z = \frac{1}{4}\left(\frac{z_0}{z+z_0}\right)^{\frac{1}{2}}$$

Equation 12.15

the Prandtl number is used to characterise convection:

$$\Pr = \ln\left(\frac{z+z_0}{z_0}\right)\left[\ln\left(\frac{z+z_0}{z_{0H}}\right)\right]^{-1}$$

Equation 12.16

The Richardson number is calculated as:

$$Ri = \frac{gz}{u^2}\left\{\frac{1}{T}\left[T - T_* + \frac{g}{c_p}\left(z+z_0-z_{0H}\right)\right] + \psi\frac{q-q_{sat}}{q+\varepsilon/(1-\varepsilon)}\right\}$$

Equation 12.17

where ε is the ratio of water vapour and air.

c) *Surface Moisture Resistance*

The moisture resistance factor is the fraction of the flux with only aerodynamic resistance. The full MOSES model calculates ψ dependent on plant functional type, leaf area index, rooting depth and vegetation fractional area. The model assumes there is no resistance to moisture transfer (i.e. free evaporation) when the surface is snow covered. Surface resistance is simulated in the full version of MOSES and is used as a driving variable in the cut-down version when the surface is snow-free ($\psi_{snow\text{-}free}$).

$$\psi = \begin{cases} 1 & S \leq 0 \\ \psi_{snowfree} & S > 0 \end{cases}$$

Equation 12.18

12.1.3 SNOW ALBEDO

Surface albedo is a sensitive variable in snow models. Melt is often driven by shortwave radiation and the albedo is a scalar controlling shortwave absorption. To account for spatial variation in snow-cover MOSES uses an effective albedo (Equation 12.3).

Snow albedo is derived using a prognostic temperature dependent parameterisation of crystal aging. Snow covered fraction is calculated using a simple parameterisation of the snow depth and the momentum roughness length.

a) *Prognostic Snow Albedo*

The effect of snow crystal metamorphism on snow albedo α_{snow} is parameterised in terms of empirically derived grain size (r) dependence:

$$\alpha_{snow} = \alpha_{fresh} - 0.5\left[2E3\left(r^{\frac{1}{2}} - r_{fresh}^{\frac{1}{2}}\right)\right] + 0.09\log\left[\frac{r}{r_{fresh}}\right]$$

Equation 12.19

where α_{fresh} and r_{fresh} are a prescribed parameters of the albedo and grain size of fresh snow respectively. Grain size is time dependent and is given as:

$$r(t+\Delta t) = \left[r(t)^2 + \frac{G_r}{\pi}\Delta t\right]^{\frac{1}{2}} - \left[r(t) - r_{fresh}\right]\frac{P_s \Delta t}{d_0}$$

Equation 12.20

where Δt is the model timestep, and d_0 is the mass of fresh snow required to refresh the albedo. Grain size is limited to a maximum of r_{max}. G_r is an empirical grain area growth rate:

$$G_r = \begin{cases} 0.6 & T_* = T_m \\ 0.06 & T_* < T_m, r < 150 \\ 0.23\times 10^6 \exp\left(\dfrac{-3700}{RT_*}\right) & T_* < T_m, r > 150 \end{cases}$$

Equation 12.21

Grain growth rate is temperature and grain size dependent. The grain size condition is used to differentiate between cold aged snow and cold fresh snow.

b) *Snow covered Fraction*

The snow covered fraction f_{snow} is given as:

$$f_{snow} = \frac{S\rho_{snow}^{-1}}{S\rho_{snow}^{-1} + 10z_0}$$

Equation 12.22

This simple parameterisation of snow depth and a scaled roughness length is used to account for spatial variation in snow-cover. This parameterisation is used to account for small scale variation in snow-cover rather than that associated with

blowing snow and complex topography as seen at the field site. The snow covered fraction only exerts an effect when the snow-cover is very shallow.

12.1.4 SNOWPACK MASS BALANCE

The snowpack mass balance at time t is given simply as:

$$S(t+\Delta t) = S(t) + \Delta t(P_s + M + E)$$

Equation 12.23

where **M** is the snowmelt flux density, $\mathbf{P_S}$ is snowfall and **E** is the evaporation flux density. This simple approach ignores the spatial processes of deposition and accumulation due to wind redistribution and sublimation during blowing snow.

a) Snowmelt flux density

Snowmelt flux density **M** is calculated from Equation 12.1 as:

$$M = \begin{cases} L_f H_{sm} & T_* > 0 \\ 0 & T_* \leq 0 \end{cases}$$

Equation 12.24

where T_* is the skin temperature. Snowmelt is subsequently split between soil infiltration and surface runoff depending on soil conditions. No snowmelt routing is included in the model, and neither is snowmelt allowed to refreeze within the snowpack.

12.1.5 SOIL MODEL

The soil model consists of four layers, set at 0.1, 0.25, 0.65 and 2.00 m depth respectively. The standard parameters used in the soil model are for a loam soil and are inappropriate for the organic peat soils of the study site. The parameters are therefore adjusted to those given by Lloyd *et al.*, (1999) for an Arctic tundra peat soil.

Table 12-1: MOSES Soil parameters for an organic peat soil

	Standard Value	Lloyd *et al.* (1999) Value
Clapp-Hornberger exponent	6.6	4
Soil heat capacity (J K^{-1} m^{-3})	1,190,000	1,000,000
Soil thermal conductivity (W m^{-1} K^{-1})	0.23	0.025
Saturated hydraulic conductivity (kg m^{-2} s^{-1})	0.0047	0.015
Saturated soil water suction (m)	0.049	0.015
Volumetric soil moisture at critical point (m^3 m^{-3})	0.242	0.3
Volumetric soil moisture at saturation (m^3 m^{-3})	0.458	0.8
Volumetric soil moisture at wilting point (m^3 m^{-3})	0.136	0.1

The soil model is used to calculate an interactive soil thermal conductivity λ_{soil} and soil temperature T_{soil}. The soil model is treated as a black box in the subsequent analysis.

12.2 MOSES Snow Model Parameters

MOSES uses a number of parameters to characterise the land surface. These parameters are often only approximations and can show a large degree of spatial and temporal variability. They are set *a priori* according to expert judgement. Table 12-2 gives the default values used in the snow component of the MOSES code.

Table 12-2: Parameters used in the cut-down MOSES snow model.

Parameter	Initial Value
d_0	2.5 kg m^{-2}
r_{fresh}	50 μm
r_{max}	2000 μm
z_{0snow}	5E-4 m
α_0	0.12
α_{fresh}	0.8
λ_{snow}	0.265 W m^{-2} K^{-1}
ρ_{snow}	250 kg m^{-3}

12.3 Model initialisation

The snow model requires certain variables to be given initial values. These values are snow crystal grain size (r), lying snow mass (S), skin temperature (T_*), soil temperature ($\theta_{soil(1)}$, $\theta_{soil(2)}$, $\theta_{soil(3)}$, $\theta_{soil(4)}$) and moisture in each of the four layers.